Development and monitoring of the mechanical and hygrothermal performance of low-carbon materials by smart technology

Manal Bouasria

Normandie Université

THÈSE

Pour obtenir le diplôme de doctorat

Spécialité GENIE CIVIL

Préparée au sein de l'Université de Caen Normandie

Development and monitoring of the mechanical and hygrothermal performance of low-carbon materials by smart technology

Présentée et soutenue par
MANAL BOUASRIA

Thèse soutenue le 26/09/2022 devant le jury composé de		
MME NAIMA BELAYACHI	Maître de conférences HDR, Université d'Orléans	Rapporteur du jury
M. ABDERRAHIM BOUDENNE	Professeur des universités, Université Paris-Est Créteil (UPEC)	Rapporteur du jury
M. MOHAMED-HICHEM BENZAAMA	Maître de conférences, Ecole sup.d'ingénieurs ESITC Caen	Membre du jury
M. JEAN-FRANÇOIS BARDEAU	Directeur de recherche, UNIVERSITE LE MANS	Président du jury

Thèse dirigée par YASSINE EL MENDILI (Laboratoire de cristallographie et sciences des materiaux (Caen)) et VALERIE PRALONG (Laboratoire de cristallographie et sciences des materiaux (Caen))

UNIVERSITÉ CAEN NORMANDIE

ESITC CAEN
Ecole Supérieure d'Ingénieurs des Travaux de la Construction

ED 591 PSIME

RISMA

Remerciements

Je remercie tout d'abord l'ensemble des membres du jury pour le temps et l'intérêt qu'ils ont manifesté pour ce travail. Notamment, je remercie Monsieur Jean-François BARDEAU qui m'a fait l'honneur d'examiner mon travail et de présider le jury de thèse. Je remercie également madame Naima BELAYACHI et monsieur Abderrahim BOUDENNE qui ont accepté d'être rapporteurs de ce travail et pour leurs rapports très précieux.

J'exprime ma reconnaissance à monsieur Franck HENNEQUART pour avoir accepté mon invitation et pour m'avoir accueilli au sein du laboratoire d' ALGAIA pour le stage R&D dans le cadre de ma formation doctorale « compétence pour l'entreprise ».

Je tiens à remercier vivement monsieur Mehdi SALMOUNI ZERHOUNI, monsieur Benaissa CHENNOUFI et monsieur Abdelghani SEBBAR pour le soutien tout au long de mon projet professionnel.

Je remercie mes collègues et toutes les personnes avec qui j'ai partagé mes années d'études et notamment ces années de thèse. Je remercie particulièrement ceux qui m'ont aidé à l'élaboration de mon manuscrit.

Enfin je remercie mes parents Souad et Mohammed sans qui rien de tout ça n'aurait été possible. J'aimerais vous exprimer toute ma gratitude et reconnaissance. Je vous aime du plus bel amour qui soit, je vous dois la vie, je vous dois mon bonheur de vivre, je vous dois l'amour, je vous dois tout ce que je suis. Mes pensées vont également à ma sœur Oumayma et à mon frère Aymane. La fin de ma thèse était particulièrement difficile, je remercie mon frère pour son support et sa présence à mes côtés et je remercie ma sœur pour sa bienveillance et son amour inconditionnel.

TABLE OF CONTENTS

LIST OF FIGURES

LIST OF TABLES

List of standards

NF EN 197-1 : *Cement - Part 1: Composition, specifications and conformity criteria for common cements*

Defines and provides specifications for 2 low short-term strength sulfate-resistant blast furnace cements, 3 distinct low short-term strength blast furnace cements, and 27 different common cements and their constituents. The proportions that must be mixed to create these various products in a range of nine strength classes are included in each cement's description. The requirements that the constituents must satisfy are also included in the definition. The requirements for mechanical, physical, and chemical systems are also included. The conformity criteria and corresponding norms are also specified in this text. The standards for durability are also mentioned.

NF EN 196-1 : *Methods of testing cement - Part 1: Determination of strength*

Outlines the procedure for determining a cement mortar's compressive strength and, optionally, its flexural strength. The procedure applies to ordinary cements as well as other cements and materials for which the standards specify this method. Other types of cement, those with a quick initial setting time, shall not be subject to its application. This technique is used to check whether a cement's compressive strength complies with its specification. Additionally, it is used for the EN 196-1 "CEN standard sand" validation test as well as the validation test of different clamping equipment variations.

Additionally describes the reference equipment and method, as well as the usage of alternative compaction equipment and procedures certified in compliance with this specification. In a dispute, only the reference tools and methods are applied.

NF EN 450-1 : *Fly ash for concrete - Part 1: Definition, specifications and conformity criteria*

Outlines the specifications for siliceous fly ash used as a Type II additive for concrete manufacturing, including the required chemical and physical qualities and quality control processes. This publication states that fly ash can also be utilized in grouts and mortars. This European Standard does not apply to fly ash produced with other types or higher percentages of co-combustion materials than those specified in Clause 4. The practical application of fly ash in the manufacture of concrete, i.e., the

requirements concerning the composition, mixing, placing, curing, etc., of concrete containing fly ash, is outside the scope of this standard.

NF P18-452 : *Concretes - Measuring the flow time of concretes and mortars using a workabilitymeter.*

Discusses the use of a maniabilimeter to measure the flow time of mortars and concretes. It applies to mortars and concretes whose largest aggregate's maximum diameter D max is less than or equal to 12.5 mm. The workability and plasticity of a concrete can be assessed using this method.

NF P15-431 : *Hydraulic binders. Methods for testing cement. Setting test.*

This document is part of a series of standards dealing with procedures or techniques for evaluating cements. It is devoted to the determination of setting time on typical mortar.

ASTM C204 : *Test Methods for Fineness of Hydraulic Cement by Air-Permeability Apparatus.*

Covers the determination of hydraulic cement fineness using the Blaine air-permeability device. The specific surface is the amount of surface area represented as the square centimeters or square meters per kilogram of cement. Two test procedures are provided: Test Method A is the Reference Test Method, which employs manually operated standard Blaine apparatus, whereas Test Method B allows the use of automated apparatus that has proved acceptable performance in compliance with the certification standards of this test method. Although the test method can and has been used to determine the measures of fineness of different materials, it should be noted that, often, relative rather than absolute fineness values are obtained.

NF EN ISO 12572 : *Hygrothermal Performance of Building Materials and Products - Determination of Water Vapour Transmission Properties – Cup Method.*

Outlines a technique based on cup tests for calculating the water vapour permeability of building materials and building products under isothermal conditions. There are various lists of test conditions. All hygroscopic and non-hygroscopic construction materials and products, including insulation materials and those with facings and integral skins, are subject to the general principles. Details of test procedures suitable for various material kinds are provided in the annexes. The outcomes of this approach are appropriate for product specifications as well as design and production control.

Résumé étendu en français

- Introduction

La durabilité et la conception de bâtiments respectueux de l'environnement sont d'une grande importance dans le secteur de la construction. Par conséquent, il est important d'utiliser des matériaux de construction écologiques tels que la construction en terre ou en béton incorporant différents matériaux écologiques. La production de ces nouveaux matériaux alternatifs a trois objectifs : réduire la consommation d'énergie pendant la production, fournir des solutions pour prévenir la consommation de ressources, et réduire l'utilisation de ciment et les émissions de CO_2. Par conséquent, un certain nombre de sous-produits sont potentiellement utilisés dans la construction. C'est notamment le cas des laitiers de haut de fourneau, des cendres volantes, des boues de lavage de graviers ou encore des coquillages.

Pour comprendre les enjeux industriels liés à leur utilisation, il faut d'abord comprendre les limites environnementales et/ou économiques associées à ces matériaux. En effet, ces sous-produits sont considérés comme des déchets difficilement éliminables ou valorisables, et leur valorisation comme composant dans le béton ou comme remblai semble une voie intéressante pour les valoriser en grande quantité.

Les scories de ferronickel de Nouvelle-Calédonie (FNS), sont un sous-produit des procédés pyrométallurgiques utilisés pour produire du ferronickel. Depuis plus de 145 ans, la Société Le Nickel (SLN, Nouvelle-Calédonie) produit sans interruption du nickel à partir de latérites. Avec actuellement près de 25 millions de tonnes disponibles en stock. Actuellement, seulement 8% de la production annuelle de la SLN est actuellement utilisée. Pour minimiser l'impact environnemental, le FNS restant est stocké sur site, ce qui augmente les coûts de stockage de façon exponentielle. Ces scories constituent une ressource utile pour le recyclage. Les FNS de Nouvelle-Calédonie présentent d'excellentes propriétés telles qu'une perméabilité à l'eau élevée, une dureté excellente, une densité élevée, un potentiel de compactage élevé et une grande résistance au feu avec une expansion thermique modérée. Ils sont également exempts de composés dangereux. Par conséquent, ce sous-produit peut être utilisé dans la construction.

Les cendres volantes (FA) qui sont un co-produit des centrales électriques au charbon sont largement utilisées comme liant. La disponibilité mondiale des FA est estimée à

plus de 800 millions de tonnes par an, et la production mondiale est estimée entre 500 et 1 milliard de tonnes par an. Seule une petite partie des FA est recyclée. Le reste est enfoui ou stocké dans le sol. Les propriétés des FA, telles qu'une faible gravité spécifique, une faible perméabilité et un angle de frottement interne élevé, améliorent la capacité portante du sol tout en réduisant la compressibilité et l'affaissement. De plus, les FA fournissent une grande quantité d'aluminosilicate dans le mélange, augmentant ainsi la surface de réaction pour les réactions pouzzolaniques. Selon l'UNICEM, la filière française des graviers produit chaque année environ 6,5 millions de tonnes de boues de lavage des graviers. En raison de ses excellentes propriétés, ce matériau peut être utilisé comme matière première secondaire pour diverses applications. Cependant, les décharges sont généralement exclues du recyclage. Les structures en suspension présentent de nombreux avantages tels qu'une efficacité accrue, des coûts réduits grâce à une consommation réduite d'énergie et de matières premières. De plus, l'utilisation de composants à faible consommation d'énergie disponibles localement profite à l'économie locale en raison de l'augmentation des coûts de construction et de la part de la main-d'œuvre dans la valeur ajoutée. La boue est un mélange de divers minéraux argileux et sa structure est un facteur clé pour déterminer sa durabilité et sa résistance.

Les coquilles de mollusque sont un autre déchet naturel abondant qui peut être utilisé comme matériaux cimentaires supplémentaires (SCM). Par exemple, les coquilles de crépidure (CR), les coquilles d'huîtres et les coquilles de moules sont disponibles en France. Les français sont de grands consommateurs de coquillages en Europe. En France, 191 800 tonnes de moules par exemple sont éliminées chaque année en décharge, en incinérateur ou en déchet environnemental. C'est une opération très coûteuse.

Historiquement, à la fin des années 1700, des coquillages étaient déjà incorporés dans la construction pour créer un type spécifique de matériau de construction appelé "Tabby". Pour faire du tabby, un type de béton spécifique mélangé avec des coquilles d'huîtres sont brûlées pour faire de la chaux, qui est ensuite mélangée avec du sable, de la cendre, des coquilles d'huîtres broyées comme agrégat et de l'eau. Les premiers explorateurs espagnols du XVIe siècle utilisaient des tabby en Caroline du Nord et en Floride. En 1700, les colons anglais employaient des tabby principalement en Géorgie et en Caroline du Sud. Une forme de tabby est utilisée au Maroc aujourd'hui.

- Objectifs

L’objectif de cette thèse est de développer des matériaux à faible impact environnemental. Des essais de caractérisation physique, chimique, hygrothermique et mécanique sont réalisés à différentes échelles. Un prototype a été créé et une preuve de concept sera créée pour vérifier l’efficacité des matériaux bas carbone développés dans cette thèse.

- Contenu du manuscrit

Ce travail de thèse est divisé en trois chapitres. Le premier chapitre est consacré à une étude bibliographique sur (i) l'hydratation du ciment et l'impact de l'utilisation des sous-produits dans les mélanges cimentaires, (ii) les différentes techniques de stabilisation de la terre. La dernière partie présente un état de l’art sur l’utilisation des modèles de réseaux de neurones artificiels dans le domaine de la construction.

Dans le chapitre 2, nous avons d'abord étudié le comportement de mélanges cimentaires incluant des sous-produits. Nous avons substitué le ciment par plusieurs déchets, à savoir les scories de ferronickel (FNS) associé à des coquilles de crépidule (CR) et des cendres volantes (FA) associés à des coquilles de crépidule. Des études mécaniques et hygrothermiques ont été menées à la fois à l’échelle du matériaux (mortier et béton) et aussi sur un prototype à l’échelle du laboratoire. Les propriétés mécaniques du mortier avec une utilisation de FA-CR en substitution du ciment se sont avérées supérieures à celles du mortier ordinaire. Enfin, le mécanisme de l’hydratation du nouveau ciment a été étudié à l'aide de la spectroscopie Raman. Un prototype à base de ce nouveau matériau bas carbone a été développé pour surveiller le comportement hygrothermique avec des modèles de réseaux de neurones artificiels. Les résultats de l'expérience sur le risque de condensation et le développement de moisissures révèlent que le mélange de béton choisi peut empêcher la condensation.

Dans le troisième chapitre, nous nous sommes intéressés à la stabilisation de la construction en terre par un liant cimentaire et ensuite par un liant organique. Le mécanisme de stabilisation de la terre a été étudié à l'aide de techniques d'analyse microstructurale (DRX et spectroscopie Raman). Dans la première partie, nous avons étudié l’efficacité de la boue de lavage de gravier et des coquillages comme matériau de construction en terre non cuite tout en utilisant des cendres volantes comme liant et stabilisateur cimentaire. Nos résultats montrent que ce mélange conduit à une

réduction de la porosité, une augmentation des performances mécaniques, une diminution de la conductivité thermique avec une capacité thermique spécifique plus élevée. Dans la deuxième partie, nous avons utilisé de la poudre d'algues comme stabilisateur de la bauge. Nous avons étudié l'impact de la substitution de la terre par de la poudre d'algues (liant organique). Pour ce nouveau matériau à base d'algues, nous avons observé une amélioration de la capacité de stockage de la chaleur et de la conductivité thermique sans impacter les propriétés mécaniques. Le développement du modèle de réseaux de neurones artificiels pour prédire les propriétés hygrothermiques du prototype terre-algues-fibres a montré une bonne similarité entre les résultats expérimentaux et le modèle développé.

- Chapitre 1. État de l'art - Construction de bâtiments à faible émission de carbone et performance énergétique

Dans ce chapitre nous avons en premier évoqué l'hydratation des ciments et l'influence de l'utilisation des coproduits (laitiers de haut fourneau, cendres volantes, coquillage) sur l'hydratation et le comportement du matériau final. Les principaux éléments du ciment qui réagissent avec l'eau sont les silicates tricalciques Ca_3SiO_5 ($3CaO\text{-}SiO_2$), les silicates dicalciques Ca_2SiO_4 ($2CaO\text{-}SiO_2$), l'aluminate tricalcique $Ca_3AL_2O_6$ ($3CaO\text{-}Al_2O_3$), et l'alumino-ferrite tétracalcique $Ca_4Al_2Fe_2O_{10}$ ($4\ CaO\text{-}Al_2O_3\text{-}Fe_2O_3$). Ils interagissent dans un processus complexe pour produire principalement le silicate de calcium hydraté (C-S-H), la Portlandite (CH), l'ettringite (calcium trisulphoaluminate de calcium hydraté $C_6A\overline{S}_3H_{32}$).

Les scories de ferronickel (FNS) ont une teneur en magnésium plus élevée et une teneur en calcium plus faible que les scories métallurgiques. Leur hydratation est principalement basée sur la réaction pouzzolanique. L'ajout de cendres volantes (FA) au ciment réduit la vitesse d'hydratation, améliore la fluidité des mélanges frais en raison de la forme fine et sphérique des grains et de leur texture vitreuse molle. La réaction pouzzolanique, qui est causée par l'interaction du silicium et de l'aluminium présents dans les cendres volantes avec la portlandite, entraînant ainsi la formation des silicates de calcium hydratées (C-S-H) et des silicates de calcium-aluminium hydratés (C-A-S-H).

Parmi les coquillages présents en France, nous avons identifié les coquilles de *Crepidula fornicata* (CR). Ces coquillages sont invasifs et non comestibles. Le carbonate de calcium (aragonite, $CaCO_3$), qui peut être utilisé comme matériau de

cimentation supplémentaire, est le principal composant des CR. L'aragonite étant plus soluble et métastable que la calcite, le calcium est libéré plus rapidement. D'après la littérature, il a été constaté que lorsque la quantité de poudre de coquille dans les mélanges de béton augmente, l'ettringite et le carboaluminate de calcium augmentent.

Dans un deuxième lieu, nous avons exploré les types de construction en terre et leurs propriétés. Les techniques de construction en terre les plus courantes sont le plâtre, le torchis, la bauge, l'adobe, les briques de terre comprimée et la terre crue. Dans la région de Normandie (France), la technique de construction en terre la plus utilisée est la bauge. La bauge est une technique de construction traditionnelle combinant l'argile, l'eau, le sable et des fibres telles que la paille et le roseau. Les matériaux fibreux tels que le roseau sont généralement utilisés pour réduire le retrait de séchage. Les constructions en bauge ont une longue histoire, notamment en Allemagne. Une couche supplémentaire a été utilisée dans ce type de construction. Pour répondre aux exigences du règlement RE2020 et la recommandation de la COP 21, il a été envisagé de combiner deux couches de murs en matériaux de terre. Un mur isolant à forte teneur en fibres (bauge isolante ou terre allégée) et une couche porteuse à plus forte densité (bauge structurelle) constituent les deux couches. Cependant, la terre est soumise à un tassement différentiel, à une forte compressibilité et à une faible résistance au cisaillement et doit être stabilisée pour améliorer ses propriétés. La méthode de stabilisation chimique est la technique la plus récente à cet effet. La stabilisation chimique consiste à ajouter d'autres matériaux et éléments chimiques au sol pour ajuster ses propriétés, soit par une réaction physico-chimique entre les grains et les matériaux, soit par la production d'une matrice qui lie ou enrobe la terre. On recense comme stabilisateurs les liants minéraux et les liants organiques. Le terme "liants minéraux" désigne toute substance composée de matière minérale. Mélangés à l'eau, les spécimens minéraux forment une pâte qui durcit en un bloc solide par agglomération des grains. Les ciments et les chaux sont les liants les plus utilisés dans la construction en terre crue. Il existe d'autres liants dits alternatifs (cendres volcaniques, géopolymères, gypse) ou sous-produits de diverses industries (laitier de haut fourneau, cendres de bagasse de canne à sucre, cendres volantes, ou cendres de balle de riz) pour remplacer le ciment ou la chaux par une pouzzolane à faible teneur en carbone. Dans les liants bio-organiques, nous retrouvons les polysaccharides, la cellulose, la lignine, les gommes naturelles, les jus de plantes gélatineux et le chitosane. Nous retrouvons aussi les lipides, qui sont des composés

hydrophobes et insolubles dans l'eau. Les graisses animales et les graines de certaines plantes sont les sources les plus courantes de lipides.

- Chapitre 2. Nouveaux liants en remplacement du ciment

Nous avons étudié le comportement des mélanges cimentaires incluant des sous-produits. La réduction de la teneur en ciment dans les composites cimentaires, en particulier lorsque le ciment Portland est partiellement remplacé par des déchets, peut réduire l'impact environnemental des matériaux de construction.

Dans ce chapitre, nous avons étudié deux types de mortiers (et bétons) à faible teneur en carbone basés sur : (i) l'association de scories de ferronickel et de coquillages comme remplacement du ciment et (ii) l'association de cendres volantes et de coquillages comme remplacement du ciment. L'impact de l'incorporation des sous-produits sur les propriétés du mortier a été étudié à l'échelle du matériau et également sur un prototype à l'échelle du laboratoire. Pour des temps de durcissement allant de 2 à 28 jours, les propriétés mécaniques sont étudiées à l'aide d'essais de flexion et de compression à 3 points. La diffraction des rayons X, la microscopie électronique à balayage et la spectroscopie micro-Raman sont utilisées pour caractériser les propriétés microstructurales de ces additifs.

Pour les mortiers avec ajout de FNS, la résistance à la compression en dessous de 10% reste similaire et dépasse même le mortier témoin aux premiers âges mais diminue avec un taux de remplacement supérieur à 10% en poids. Les propriétés mécaniques avec l'ajout de FNS-CR restent similaires ou même légèrement supérieures à celles du mortier standard jusqu'à 20 % en poids. La combinaison de FNS et de CR présente deux avantages majeurs : (i) la teneur élevée en silice du FNS favorise la polymérisation dans la structure C-S-H ; (ii) les ions CO_3^{2-} dissous des coquilles de crépidule favorisent la formation de carboaluminates, réduisant ainsi la porosité du système et augmentent sa résistance.

Néanmoins, l'isolation thermique n'est pas améliorée en raison de la présence de FNS. Pour y remédier, nous avons alors remplacé le ciment cette fois-ci par des cendres volantes (FA) et des CR.

Les propriétés mécaniques du mortier de FA-CR se sont avérées supérieures à celles du mortier témoin avec un taux d'incorporation de FA-CR allant jusqu'à 10%. En conséquence de la réaction pouzzolanique, les teneurs élevées en silice et en calcium

de FA et CR, respectivement, conduisent au développement de gels C-S-H et C-S-A-H supplémentaires, ce qui entraîne une réduction de la porosité et une augmentation des résistances. En outre, à mesure que la quantité de substitution augmente, la conductivité thermique du béton diminue considérablement. Il a été démontré que ces sous-produits ont un réel potentiel pour le remplacement partiel du ciment à un taux de 30 % (FA15-CR15).

- Chapitre 3. Stabilisation chimique de la construction en terre par un liant alternatif

Nous avons étudié le comportement des constructions en terre stabilisées dans le but d'améliorer la cohésion et la résistance de la terre. Dans ce chapitre, nous nous sommes d'abord intéressés à la stabilisation chimique des constructions en bauge par des liants cimentaires et organiques. Dans la première partie, nous avons étudié la possibilité d'utiliser les boues de lavage de gravier et des coquillages à être utilisés comme matériau de construction en terre non cuite, tout en employant des cendres volantes comme liant et stabilisateur cimentaire. Ce mélange innovant de boue de lavage de gravier, de coquilles de *Crepidula fornicata* et de cendres volantes (GMW-FA-CR) a été caractérisé thermiquement et mécaniquement. L'ajout de cendres volantes et de coquilles de crépidule aux boues de lavage de gravier entraîne une augmentation de la résistance à la compression. Ce mélange contient de la silice et du calcium, qui vont tous deux réagir avec les argiles (silicates) pour former du C-S-H et du C-A-C-H par réaction pouzzolanique et ainsi contribue à la réduction de la porosité et à l'augmentation des performances mécaniques. La tobermorite et l'Al-tobermorite sont les principaux produits d'hydratation expliquant les excellentes propriétés des performances mécaniques. Le matériau GMW-FA-CR a une conductivité thermique inférieure et une capacité thermique spécifique supérieure en comparaison à la bauge traditionnelle. En conséquence, l'utilisation des GWM, CR et FA peut contribuer largement à la réalisation des objectifs de développement durable et donc à la réduction des émissions de carbone.

Dans la deuxième partie de ce chapitre, nous avons évalué la possibilité d'utiliser les algues comme stabilisateur pour la construction en bauge. Nous avons étudié l'impact de l'incorporation d'algues à différents niveaux de remplacement à la fois pour la terre allégée et la bauge structurelle. Les murs en bauge ont été analysés pour évaluer la résistance à la compression et les caractéristiques hygrothermiques. Pour la terre

allégée, nous avons observé une amélioration de la capacité de stockage de la chaleur et de la conductivité thermique, sans incidence sur la résistance à la compression. La quantité optimale d'algues permettant de réduire la conductivité thermique de 26% par rapport à la bauge standard est de 20%. L'incorporation de 5% d'algues dans la bauge structurelle a amélioré la résistance à la compression de 22%. L'amélioration des performances mécaniques et hygrothermiques des échantillons de bauge contenant des algues permet de réduire l'épaisseur des murs et donc de fabriquer un matériau de construction écologique, durable et à haut rendement énergétique.

- **Chapitre 4. Modélisation par intelligence artificielle du comportement hygrothermique des bâtiments**

Dans la troisième partie de ce chapitre nous avons présenté la modélisation par des réseaux de neurones artificiels (ANN). Il s'agit de modèles basés uniquement sur des données d'entrée/sortie et n'ont pas d'interprétation physique. Selon la littérature, la modélisation par des réseaux de neurones artificiels, contrairement aux modèles physiques, est un outil efficace pour simuler le comportement hygrothermique des produits de construction avec un nombre mineur d'entrées. Son architecture est séparée en trois types de couches, toutes liées entre elles : la couche d'entrée, qui introduit les entrées du modèle; la couche de sortie, qui récupère les sorties du modèle entraîné; et les couches cachées, qui sont des couches intermédiaires entre les précédentes. L'implémentation du modèle de réseau de neurones artificiel se fait en trois étapes. Le modèle est d'abord entraîné afin de réduire la fonction d'erreur, en comparant entre les résultats expérimentaux et ceux du modèle. L'étape de validation vient ensuite. L'objectif est d'évaluer un modèle qui s'adapte à l'ensemble des données d'entraînement tout en modifiant ses hyperparamètres de manière objective. Dans la dernière étape, les résultats obtenus par le modèle sont évalués pour tester leur adéquation.

La formulation optimale avec un remplacement de 30 % du ciment par du FA-CR est utilisée pour construire un prototype à l'échelle du laboratoire. Le prototype a été développé pour surveiller le comportement hygrothermique à l'aide de modèles de réseaux des neurones artificiels (ANN). Le modèle ANN est entraîné et validé à l'aide des données recueillies par les capteurs sans fil placé sur le prototype (température, humidité relative et luminosité). Le modèle utilisé dans cette recherche comporte huit entrées et deux sorties (température et humidité relative). Les résultats de l'expérience

sur le risque de condensation et le développement de moisissures révèlent que le mélange de béton choisi peut prévenir la condensation. En effet, la teneur élevée en silice, aluminate et calcium du mélange de cendres volantes et de la crépidule réagit avec l'humidité pour générer des hydrates supplémentaires à la suite d'une réaction pouzzolanique, ce qui entraîne une amélioration continue de la résistance.

Les formulations optimales avec des remplacement de 20% d'algues dans la terre allégée et 5% d'algues dans la bauge structurelle ont été utilisés pour la construction d'un prototype à l'échelle du laboratoire. Le prototype a été équipé par des capteurs sans fil pour collecter la température, l'humidité relative et la luminosité. Le développement du réseau neuronal artificiel pour prédire les propriétés hygrothermiques de la structure à deux couches a donné des résultats positifs. Les résultats expérimentaux et prédits par le réseau de neurones artificiels ont montré une bonne similarité.

- Conclusion

Dans cette thèse, nous avons étudié l'efficacité de nouveaux liants cimentaires et bio-organiques. Dans la première partie de ce projet de recherche, nous avons étudié l'effet du remplacement du ciment.

Nous avons commencé par remplacer le ciment par du FNS-CR et avons étudié les propriétés mécaniques et hydrothermiques de la pâte de ciment et du mortier. Les conclusions obtenues peuvent être résumées ci-dessous :

- Une substitution partielle du ciment par un mélange FNS-CR, jusqu'à 30 %, n'a aucun effet sur l'ouvrabilité du mortier à l'état frais. L'ouvrabilité est réduite au-delà de ce taux de substitution en raison de l'absorption importante d'eau par ce mélange FNS-CR.
- L'augmentation de l'addition de FNS-CR dans le ciment entraîne une diminution des résistances à la compression et à la flexion. Par conséquent, l'utilisation de FNS et de CR, qui sont moins denses que le ciment, est limitée à des taux modérés. Néanmoins, les résistances mécaniques restent proches de celles du mortier témoin jusqu'à 20% de substitution du ciment par les FNS-CR.
- A 2 jours de cure, l'ajout de 10% de FNS-CR améliore le comportement mécanique grâce à l'accélération de la prise du ciment.

- La combinaison du FNS et du CR présente deux avantages majeurs : (i) la forte teneur en silice du FNS favorise la polymérisation dans la structure C-S-H ; (ii) les ions CO_3^{2-} dissous provenant du CR induisent la formation de carboaluminates, qui réduisent la porosité du système et augmentent sa résistance.
- Les résultats montrent un potentiel évident pour l'utilisation des sous-produits de FNS-CR comme remplacement partiel du ciment à un taux optimal de 20 %.

Cependant, la résistance thermique n'était pas satisfaisante en raison de la présence de FNS riches en magnésium. Pour remédier à ce problème, nous avons remplacé le FNS par des FA et examiné le comportement du mortier et du béton avec du ciment substitué par du FA et du CR.

L'effet du remplacement partiel du ciment par un mélange de FA et CR sur les propriétés mécaniques et hygrothermiques du mortier et du béton a été examiné. L'utilisation de CR et de FA permet de réaliser d'importantes économies dans la fabrication du ciment. Elle peut contribuer de manière significative à la réalisation des objectifs de développement durable et, par conséquent, à la réduction des émissions de CO_2. En raison de la réaction pouzzolanique, les teneurs élevées en silice et en calcium du FA et du CR, respectivement, conduisent au développement de composants C-S-H et C-S-A-H supplémentaires, ce qui entraîne une réduction de la porosité et une augmentation de la résistance à la compression. En outre, à mesure que la quantité de substitution augmente, la conductivité thermique du béton diminue considérablement. Il a été démontré que ces sous-produits ont un réel potentiel pour le remplacement partiel du ciment à un taux de 30 % (FA15-CR15). Pour la première fois, le modèle ANN est utilisé pour évaluer le comportement hygrothermique d'un prototype en béton. Les modèles physiques du comportement hygrothermique nécessitent un grand nombre de propriétés hygroscopiques du matériau étudié, qui peuvent être difficiles, voire impossibles, à obtenir. Les hyperparamètres peuvent être calculés rapidement grâce à l'optimisation par algorithme génétique. Nous avons pu déterminer la meilleure architecture après avoir étudié la sensibilité du modèle à l'algorithme et au nombre de neurones dans la couche cachée. Les résultats révèlent que le modèle ANN a appris et prédit le comportement hygrothermique du prototype. L'approche proposée permettra aux ingénieurs du bâtiment de diagnostiquer rapidement diverses circonstances et de déterminer le confort hygrothermique du bâtiment.

Le mélange de FA et CR est également utilisé, mais cette fois comme stabilisateur de la boue de lavage de gravier français (GWM) pour la construction en bauge. Les performances thermiques et mécaniques de la boue mélangée à ces sous-produits, ainsi que l'étude des produits hydratés, révèlent des résultats encourageants, qui sont exposés ci-après :

- La combinaison de GWM-FA-CR contribue de manière significative à la réalisation des objectifs de développement durable et, par conséquent, à la réduction des émissions de carbone.
- La tobermorite et l'Al-tobermorite sont les principaux produits d'hydratation responsables des excellentes performances mécaniques de la bauge
- L'augmentation de la résistance à la compression par rapport aux matériaux de construction traditionnels en bauge entraînera une réduction de l'épaisseur des parois en bauge et, par conséquent, une diminution de la quantité de matières premières employées dans ce type de construction.
- L'utilisation de FA et CR présente deux avantages :
    - Les teneurs élevées en silice et en calcium de ces deux sous-produits réagissent avec les argiles, entraînant la formation de systèmes CSH et CASH (tobermorite et Al-tobermorite) par réaction pouzzolanique, et donc la réduction de la porosité et l'augmentation des performances mécaniques.
    - Par rapport aux matériaux de construction traditionnels en bauge utilisés en Normandie, ce nouveau matériau GMW-FA-CR présente une conductivité thermique plus faible et une capacité thermique spécifique plus élevée.

L'évaluation mécanique et hygrothermique des murs en bauge incorporant des algues brunes de type *Laminaria Digitata* a été l'objectif principal de la deuxième partie de ce projet de recherche. Les conclusions obtenues peuvent être résumées ci-dessous :

- Les algues augmentent la capacité de la bauge à stocker la chaleur, son degré d'isolation et sa résistance à la compression.
- L'incorporation de 20 % d'algues dans la couche isolante a réduit la conductivité thermique de 26 %.
- L'incorporation de 5 % d'algues dans la bauge structurelle a amélioré la résistance à la compression de 22 %.

La couche isolante en bauge contenant 20 % d'algues et la bauge structurelle contenant 5 % d'algues ont été utilisés pour la construction d'un prototype à l'échelle

du laboratoire. Ce prototype a été équipé de capteurs sans fil pour mesurer la température, l'humidité relative et la luminosité. Le développement de l'ANN pour prédire les propriétés hygrothermiques de la structure à deux couches a donné des résultats encourageants. Les résultats expérimentaux et prédits par le modèle ANN ont montré une bonne similarité.

Les matériaux avec des algues se sont avérés être efficaces dans la construction en bauge, conduisant à la réduction de l'épaisseur des murs et contribuant à l'économie d'énergie grâce à ses propriétés thermiques. Une conception architecturale optimisée pour les murs intérieurs et/ou extérieurs avec l'utilisation des algues permettra d'obtenir une bonne efficacité énergétique pendant l'hiver et un bon confort pendant l'été.

Dans cette thèse, nous avons montré la possibilité d'utiliser des ressources disponibles pour apporter de nouvelles performances aux constructions en béton et en terre. Les conclusions prouvent également que notre démarche s'inscrit bien dans les objectifs de développement durable et de réduction du CO_2.

INTRODUCTION

The growth of the building industry has led to an increase in cement production on a large scale. The cement production is responsible for a large part of the CO_2 emissions. The European Commission launched the "Green Deal" at the end of 2019 with the intention of putting the European Union (EU) on a path to climate neutrality by 2050. The European Union has drafted a legislation known as the "European Climate Act," that took effect on July 9, 2021, and intends to reduce greenhouse gas emissions in the EU by at least 55% by 2030. Also, to keep up with the RE2020 regulation and to respect the recommendations of the COP 21, it is necessary to reduce energy consumption and to move towards the use of more environmentally friendly materials. My thesis subject is in line with a circular economy approach. The construction industry is resource-intensive and generates around 35% of the total waste generation in the EU. Consequently, it is relevant to use environmentally friendly building materials, such as earthen construction or concrete incorporating a variety of ecological elements. Producing these new alternative materials has three objectives: reducing energy use during production, providing solutions to prevent the consumption of resources such aggregates, and reducing cement usage and CO_2 emissions. Therefore, a number of by-products are potentially used in construction. This is particularly the case for ferronickel slag, fly ash, gravel washing mud or even shells.

To understand the industrial issues associated with their use, it is necessary to first understand the environmental and/or economical limitations associated with these materials. Indeed, these by-products are considered as waste that the elimination or recovery may be challenging, their exploitation as constituents of concrete or earth addition seem to be an interesting way of recovering large quantities.

Ferronickel slag from New Caledonia (FNS), is a by-product of the pyrometallurgical processes used to produce ferronickel. Over 145 years, the Société Le Nickel (SLN, New Caledonia) has been producing nickel from laterites continuously. With a stockpile of more than 25 million tons already in place. Only 8% of the annual FNS production is currently utilized. To minimize the impact on the environment, the remaining FNS is stacked up on site with expansive storage costs. These slags offer a useful resource for recycling. The FNS from SLN exhibit good properties such as high-water permeability, excellent hardness and toughness, high density, high compaction potential, and huge fire resistance with moderate thermal expansion. They are also

free of hazardous compounds. As a result, this by-product can be employed in construction.

Fly ash (FA) has been widely used as a binder material, and it is a waste product of coal-fired power plants. The global availability of FA is predicted to be over 800 million metric tons per year, with annual global production estimated to be between 500 million and one billion tons. Just a small fraction of FA is recycled; the remainder is dumped or stored on the ground. The FA's characteristics, such as low specific gravity, low permeability, and high internal friction angle, enhance earth bearing capacity while reducing compressibility and settlement. Furthermore, FA provides high quantity of alumino-silicates to the mixture, increasing the reactive surface for the pozzolanic reaction.

According to UNICEM, each year, the gravel industry in France generates around 6.5 million tons of gravel wash mud. This material could be exploited as a secondary raw material for a variety of applications due to its excellent properties. However, by dumping it in landfills, it is usually excluded from recycling. Mud construction provides a number of advantages, including lower costs due to increased efficiency and lower energy and raw material use. Furthermore, by exploiting locally available low-energy components, the local economy benefits from enhancings in the labour component of building costs and adding value. Mud is a mixture of different clay minerals whose structure is crucial since it determines the mud's durability and strength.

Seashells are another abundant natural waste material that can be used as SCM. *Crepidula* shells (CR), oyster shells, and mussel shells, for example, are available in France. France is a major consumer of shellfish in Europe. In France, 191 800 tons of seashells are disposed of in landfills, incinerators, or as litter in the environment each year. This is an expensive endeavor.

Marine macroalgae, on the other hand, get to be an issue when the tide recedes and leaves a significant amount of stranded red, green, and brown seaweed on the shores. They cause odor issues around the Normandy coasts, and under extremely unusual circumstances, they can become hazardous as they degrade.

In the late 1700s, seashells were historically incorporated into concrete to create a particular kind of building material called "Tabby" . To construct tabby, a form of concrete, oyster shells are burned to create lime, which is then combined with sand, ash, crushed oyster shells as aggregate, and water. Early Spanish explorers in the 16th

century utilized Tabby in North Carolina and Florida. Around 1700, British colonists primarily employed Tabby in Georgia and South Carolina.

This work is divided into four chapters. The first chapter is dedicated, to a bibliographical study of: (i) the cement hydration and the impact of using co-products in cementitious mixtures, (ii) the different technics of earthen construction and the earth stabilization. In the last part, we introduced the artificial neural network modelling.

The objective of this PhD is to develop new low carbon materials and a new approach to modeling hygrothermal behavior. Within this context, in the second chapter we investigated the hygrothermal, mechanical and thermal behaviors of cementitious mixtures including by-products. First we studied the effect of adding silicon-rich FNS, then the effect of combining FNS with C*repidula* shells for their calcium content. We substituted cement by FNS, by FNS associated with *Crepidula* shell and by the association of FA and *Crepidula* shell.

We looked into the stabilization of soil in order to overcome the consideration of the earthen structures as inferior to more permanent materials due to their poor longevity in an unstabilized state. Experiments to characterize materials are conducted at various scales using physical, chemical, hygrothermal, and mechanical methods. To this end, the third chapter focuses on the stabilization of the earthen constructions. In the first part we added FA and *Crepidula* shell powder to the gravel wash mud as this combination has shown promising results as a cementitious binder. To study its feasibility as an alternative binder, we evaluated the compressive strength and thermal characteristics of unfired cob specimens. In the second part we used algae powder as stabilizer to structural and insulation cob.

Seaweed (as powders, fibers, and byproducts) could be added to soil to reduce environmental contamination and allow for the reuse of waste products. Algae are also well adapted to a variety of stabilizing and gel-forming applications in the food, pharmaceutical, printing, and textile dye industries. The ability of this natural product to gel and texturize is a characteristic that all these sectors have seek.

We used brown algae of the *Laminaria Digitata* type which contain alginates, which are a water-soluble polymer that becomes an insoluble gel when in contact with calcium. At various levels of substitution, we investigated the hygroscopic, thermal, and mechanical performance of insulating and structural cob. A technique comparable to that used in conventional cob construction is employed to prepare the cob materials.

In the fourth chapter, we started with a review on the hygrothermal modelling and we introduced the artificial neural network modelling. The optimal formulation with the best thermal and mechanical agreement for cement with by-products is used to build a lab scaled prototype. And the optimal formulation with the best thermal conductivity for the insulation cob and the best compressive strength for the structural cob is used to build a lab scaled prototype. Thanks to the data (temperature and relative humidity) collected from the wireless sensors placed on the prototypes, we developed an artificial neural network able to model the hygrothermal properties.

Chapter 1. State of the art - Low carbon building construction and energy performance

1.1 Bibliographie

1.1.1 Contexte

The Global Status report (2020) [1] shows that CO_2 emissions from building operations have reached their greatest level yet, at roughly 10 GtCO2, representing 28% of total global energy-related CO_2 emissions. When emissions from the building construction industry are included, this number grew to 38% of total world energy-related Emissions of CO_2 (Figure 1-1). Building operation accounts for 30% of overall final energy consumption, with an additional 5% for the building and construction industry. Buildings presently consume over 55% of global electricity (IEA 2020b) [2]. Building energy consumption was constant in 2019 for the first time since 2012. It should be noted that energy uses due to transporting building materials to construction sites were not included. This field's considerable function results in a continual and significant consumption of natural resources, significant CO_2 emissions, and significant energy usage.

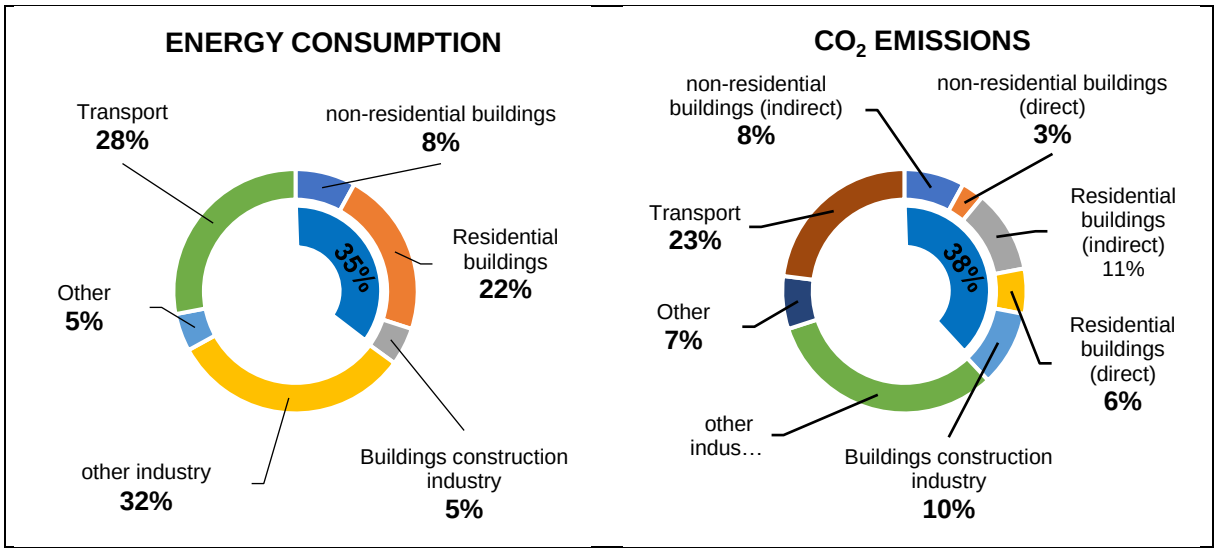

Figure 1-1 Global share of buildings and construction final energy and emissions, 2019

Notes: Buildings construction industry is the portion (estimated) of overall industry devoted to manufacturing building construction materials such as steel, cement and glass. Indirect emissions are emissions from power generation for electricity and commercial heat. Sources: (IEA 2020d; IEA 2020b)

Cement and steel manufacturing account for the majority of emissions from the manufacture of building materials and their construction (see Table 1.1) [2], and their increased use is a major contributor to carbon emissions from buildings. The building construction sector contributes for around 50% of cement consumption and 30% of steel demand. The increased awareness of authorities regarding the reduction of

greenhouse gas emissions tends to improve environmental and energy performance in the building industry, both in terms of materials and design.

These considerations demonstrate the significance of prolonging the life of buildings, minimizing their use, and replacing them with materials with lower carbon emission. Between 40% and 50% of global material resources are exploited for housing, building, and infrastructure [3]. The Climate Accord, which was signed during the COP 21 in Paris in 2015, aims to reduce greenhouse gas emissions. It considers that at least 40% of emissions must be reduced by 2030 [4]. The European commission has raised the target for reducing greenhouse gas emissions to 55% by 2030 [5].

Table 1.1 IEA Buildings operation and construction emissions estimates, 2019

	2019 ($MtCO_2$)	
Buildings use phase	9953	
Coal	496	9% direct emissions
Oil	939	
Natural gas	1663	
Electricity and heat	6855	19% indirect emissions
Buildings construction	130	10% indirect buildings and construction value chain emissions
Construction energy use	130	
Material manufacturing	3430	
Cement and steel manufacturing for construction	2038	
Other	1391	
Buildings and construction value chain	13512	38% of total energy related emissions

Source (IEA 2020b), Adapted from "Energy Perspectives 2020"

The cement production is world widely increased due to the expansion of the construction field. In 2019, the cement production emitted 2.3 $GtCO_2$ [6] and generates a large amount of CO_2, SO_2 and NO_x [7]. The reduction of CO_2 emission in the construction sector has been discussed and many alternatives of cementing systems was enunciated: a) changing from coal to natural gas in the clinker preparation, based on a chemical absorption process able to capture CO_2, b) Promoting clinker dry manufacturing and c) Partially substituting cement by supplementary cementitious materials [8]. The common supplementary cementitious material (SCM) used are fly ash (FA), silica fume, ground granulated blast furnace slag (GGBS), metakaolin, rice husk ash, glass powder and ceramic waste powder [9].

1.1.1.1 Cement hydration

Portland cement is made up of 80% limestone and 20% alumina and silica-rich materials (clay or kaolin). The Table 1.2 below shows the standard raw material composition. The product obtained at the kiln's exit is known as clinker; it is finely crushed with 3 to 5% calcium sulfate (gypsum $CaSO_4$,2(H_2O) or anhydrite) to control the setting, as well as minor secondary ingredients such as blast furnace slag, fly ash, limestone fillers.

Table 1.2 Chief chemical constituents of Portland cement

Calcium oxide (CaO)	65 à 70 %
Silica (SiO_2)	18 à 24 %
Alumina (Al_2O_3)	4 à 8 %
Iron oxide (Fe_2O_3)	1 à 6 %

The main elements of cement that react with water are tricalcium silicates Ca_3SiO_5 ($3CaO\text{-}SiO_2$), dicalcium silicates Ca_2SiO_4 ($2CaO\text{-}SiO_2$), tricalcium aluminate $Ca_3AL_2O_6$ ($3CaO\text{-}Al_2O_3$), and tetra-calcium aluminoferrite $Ca_4Al_2Fe_2O_{10}$ ($4\ CaO\text{-}Al_2O_3\text{-}Fe_2O_3$). They interact in a complex process to produce new chemical components with high mechanical performance. The average quantities of these main components are presented in Table 1.3 [10,11].

Table 1.3 Anhydrous cement composition (Bogue compounds).

Component	Chemical formula	Nominal Formula	Proportion %
Tricalcium silicate (Alite)	$3\ CaO\text{-}SiO_2$	C_3S	40-60
Dicalcium silicate (Belite)	$2CaO\text{-}SiO_2$	C_2S	13-50
Tricalcium aluminate (Celite)	$3CaO\text{-}Al_2O_3$	C_3A	4-11
Tetracalcium aluminoferrite (Ferrite)	$4CaO\text{-}Al_2O_3\text{-}Fe_2O_3$	C_4AF	7-13
Others			7-10

- C_3S : Has a high heat of hydration (500 KJ/Kg). It provides cement with a fast and high resistance.
- C_2S : Has a low heat of hydration (250 kJ/Kg). It allows the cement to reach high resistances in the mid and long term.

- C_3A : has a high heat of hydration during the first few days of hardening (900kJ/Kg). It contributes to the setting of the cement paste, but little to the final strength.
- C_4AF : it has a minor role in the hardening reaction and contributes only to the final strength.

This hydration is influenced mostly by concentrations of Ca^{2+}, OH^-, and SO_4^{2+} in the mixing water, which is known as the dissolution Table 1.3. The amount of alkali sulphate, gypsum, and free lime in the cement impact the concentration of these ions. When the ion saturation level is achieved, the hydrates precipitate. The literature has detailed the various dissolution-precipitation equilibria for the different aqueous phases of Portland cement. Standard cement chemistry acronyms are utilized, C = CaO, S= SiO_2, $\overline{S}$= SO_3, A = Al_2O_3, F = Fe_2O_3, and H = H_2O.

The equation of the C_3S and C_2S phases dissolution:

$$C_3S + 3\ H_2O \rightarrow 3\ Ca^{2+} + H_2SiO_4^{2-} + 4\ OH^- \quad \textbf{1-1}$$

$$C_2S + 3\ H_2O \rightarrow 2\ Ca^{2+} + H_2SiO_4^{2-} + 4\ OH^- \quad \textbf{1-2}$$

The equations of the C_3S and C_2S phases precipitation:

$$x\ Ca^{2+} + H_2SiO_4^{2-} + 2(x-1)\ OH^- + n\ H_2O \rightarrow C_xSH_n \quad \textbf{1-3}$$

$$Ca^{2+} + 2\ OH^- \rightarrow Ca(OH)_2 \quad \textbf{1-4}$$

The dissolution and precipitation reactions of the aluminate phases (C_3A and C_4AF) rely on the presence or absence of sulphates.

- **When there is no sulphate available:**

$$2C_3A + 27H \rightarrow C_4AH_{19} + C_2AH_8 \quad \textbf{1-5}$$

$$C_4AH_{19} + C_2AH_8 \rightarrow 2\ C_3AH_6 \quad \textbf{1-6}$$

- **When sulphate is available:**

$$C_3A + 6\ H_2O \rightarrow 3\ Ca^{2+} + 2\ AlO^{2-} + 12\ OH^- \quad \textbf{1-7}$$

$$29\ H_2O + 6\ Ca^{2+} + 2\ AlO^{2-} + 3SO_4^{2-} + 4\ OH^- \rightarrow (Ca_3Al(OH)_6)2.(SO_4)_3.25H2O \quad \textbf{1-8}$$

The chemical reactions that occur during cement hydration can be summarized by the equations below in equation 1-12 to equation 1-14 [12–14]:

$$C_3S + 5.3\ H \rightarrow C_{1.7}SH_{3.9} + 1.3CH \quad \textbf{1-9}$$

$$C_2S + 4.3H \rightarrow C_{1.7}SH_{3.9} + 0.3CH \quad \textbf{1-10}$$

$$C_3A + 3C\overline{S}H_2 + 26\ H \rightarrow C_6A\overline{S}_3H_{32}\ \text{(ettringite)} \quad \textbf{1-11}$$

$$2C_3A + C_6A\bar{S}_3H_{32} + 4H \rightarrow 3\ C_4A\bar{S}H_{12} \quad \textbf{1-12}$$

$$C_3A + CH + 12\ H \rightarrow\ C_4AH_{13} \quad \textbf{1-13}$$

$$C_4AF + 3\ C\bar{S}H_{2G} + 30\ H \rightarrow C_6A\bar{S}_3H_{32} + CH + FH_3 \quad \textbf{1-14}$$

$$2\ C_4AF + C_6A\bar{S}_3H_{32} + 12H \rightarrow 3\ C_4A\bar{S}H_{12} + 2\ CH + 2\ FH_3 \quad \textbf{1-15}$$

$$C_4AF + 2CH + 10\ H \rightarrow 2C_3(A,F)H_6 \quad \textbf{1-16}$$

The hydration of C_2S and C_3S leads in the creation of portlandite (CH) and C-S-H, as described in equation **1-9** and equation **1-10**. The hydration of C_3A is described in equation **1-11** to equation 1-13, while the hydration of C_4AF is described in equation 1-14 to equation 1-16. Celites and ferrites first interact with gypsum to generate ettringite (trisulphoaluminate (Aft phase)) as shown in equation 1-11 and equation **1-14**. After consumption of gypsum, celites and ferrites interact with ettringite to generate monosulphoaluminates (Afm phase) as shown in equation **1-12** to equation **1-15**, and they produce hydrated calcium aluminate (CAH) and ($C_3(A,F)H_6$) when they interact with portlandite ($Ca(OH)_2$).

1.1.1.2 Classification of cements

The cement types are impacted by the composition of the cements, the Portland cement CEM I is composed of 95% clinker at least, and the cement types CEM II to CEM V are relative to the cements with additions. In the Table 1.4 the different cement types and their content of mineral elements are listed according to the European Standard EN 197-1 [15].

Table 1.4 Composition of the common cements

Main types of cement	Notation	Clinker (%)	Blast furnace slag (%)	Silica fume	Pozzolana		Fly ash		Burnt shale	Limestone	
					Natural	Natural calcined	Siliceous	Calcreceous			
		K	S	D	P	Q	V	W	T	L	LL
Portland	CEM I	95-100	-	-	-	-	-	-	-	-	-
Portland-slag	CEM II/A-S	80-94	6-20	-	-	-	-	-	-	-	-
	CEM II/B-S	65-79	21-35	-	-	-	-	-	-	-	-

Portland-silica fume	CEM II/A-D	90-94	-	6-10	-	-	-	-	-	-	-
Portland pozzolana	CEM II/A-P	80-94	-	-	6-20	-	-	-	-	-	-
	CEM II/B-P	65-79	-	-	21-35	-	-	-	-	-	-
	CEM II/A-Q	80-94	-	-	-	6-20	-	-	-	-	-
	CEM II/B-Q	65-79	-	-	-	21-35	-	-	-	-	-
Portland-fly ash	CEM II/A-V	80-94	-	-	-	-	6-20	-	-	-	-
	CEM II/B-V	65-79	-	-	-	-	21-35	-	-	-	-
	CEM II/A-W	80-94	-	-	-	-	-	6-20	-	-	-
	CEM II/B-W	65-79	-	-	-	-	-	21-35	-	-	-
Portland-burnt shale	CEM II/A-T	80-94	-	-	-	-	-	-	6-20	-	-
	CEM II/B-T	65-79	-	-	-	-	-	-	21-35	-	-
Portland-limestone	CEM II/A-L	80-94	-	-	-	-	-	-	-	6-20	-
	CEM II/B-L	65-79	-	-	-	-	-	-	-	21-35	-
	CEM II/A-LL	80-94	-	-	-	-	-	-	-	-	6-20
	CEM II/B-LL	65-79	-	-	-	-	-	-	-	-	21-35
Portlande-composite	CEM II/A-M	80-88	<----------12-20---------->								
	CEM II/B-M	65-79	<----------21-35---------->								
Blast furnace	CEM III/A	35-64	36-65	-	-	-	-	-	-	-	-
	CEM III/B	20-34	66-80	-	-	-	-	-	-	-	-
	CEM III/C	5-19	81-95						-	-	-
Pozzolana	CEM IV/A	65-89	-	<----------11-35---------->					-	-	-
	CEM IV/B	45-64	-	<----------36-55---------->					-	-	-

Composite	CEM V/A	40-64	18-30	-	18-30	-	-	-	-
	CEM V/B	20-38	31-49	-	31-49	-	-	-	-

1.1.1.3 Calcium silicate hydrate (C-S-H)

When the tricalcium silicates react with water, they react to form and release $H_2SiO_4^{2-}$ ions, Ca^{2+} ions, and OH^- ions, forming hydrated calcium silicates (C-S-H) and portlandite ($Ca(OH)_2$) as seen in **1-3** and 1-4. The CSH is responsible for the strength of hydrated cement. They are obtained by the hydration of Alite and Belite in the cement, but they can also be formed by the hydration of mineral additives. In C-S-H, the C/S ratio ranges from 0.66 to 2 [16], while in Portland cement, it ranges from 1.2 to 2.1 [17], with a mean value of 1.75 [16,18,19]. When a paste incorporates a supplementary cementing materials like silica fume, fly ash, metakaolin, or crushed granulated blast-furnace slag, the mean value drops significantly, to less than one [18].

1.1.1.4 Portlandite (CH)

Portlandite is a hydration product of C_2S and C_3S that is easily identified by its crystalline structure of hexagonal shape. Portlandite, unlike CSH, does not contribute to the mechanical strength of hydrated cement, however, in the presence of pozzolanic materials, it interacts with silica (SiO_2) to form CSH. Portlandite ensures a basic pH in the concrete by acting as a buffer.

1.1.1.5 Hydration of aluminates

In the absence of gypsum, the hydration of aluminates results in hydrogenate C_3AH_6. When sulphates of gypsum are present, the hydrating product is ettringite (calcium trisulphoaluminate hydrate $C_6A\bar{S}_3H_{32}$), and when the gypsum is depleted the ettringite dissolves to form calcium monosulphate hydrate. Long-term hydration of non-hydrated C_3A and C_4AF produces calcium aluminoferrite hydrate.

1.1.2 Influence of the use of co-products in construction

The partial replacement of cement by supplementary cementitious materials, such as blast furnace slag [20], fly ash [21],silica fume [22], marble dust waste [23,24], sea shell [25],stone waste [26], granite dust waste [27] leads to industrial by-products recycling, to the conservation of natural resources, and thus to a reduction of the CO_2 emissions. According to these investigations, the pozzolanic products utilized as

cement substitutes enhanced the characteristics of cement-based products and a number of environmental indicators. Pozzolanic mineral additions enhance the development of strength, the enhancement of rheological characteristics, and the resistance of cementitious materials towards environmental conditions during the period of their service life [28]. Based on several reports, the strength activity index (SAI) of concretes and mortars with high SCM content is given in Table 1.5. The SAI of concrete, according to ASTM C311 [29], is defined as the ratio of the compressive strength of specimens containing SCM and the control specimen without SCM.

Table 1.5 Compressive strength of mixes with SCM

SCM	Replacement (%)	Water/binder	SAI (%)			Additives	Sources
			7 days	28 days	90 days		
FA	40	0,47	64	64	65	-	[30]
	45	0,33	79	57	91	SP	[31]
	50	0,4	51	71	78	-	[32]
	50	0,55	45	77	85	SP	[33]
	50	0,5	27	47	89	SP	[34]
GGBS	40	0,35	87	104	116	SP	[35]
	40	0,28	99	101	104	SP	[36]
	50	0,55	92	106	112	SP	[33]
	50	0,35	80	99	104	SP	[35]
	50	0,5	64	92	127	-	[34]
CWP	40	0,34	85	81	88	SP	[37]
	40	0,35	76	99	107	SP	[38]
	50	0,4	52	61	62	SP	[39]
	60	0,35	63	88	94	SP	[38]
	60	0,48	70	75	81	-	[40]

SP – Superplasticizer;

The compressive strength generally decreases with the increase of cement replacement rates using various SCMs. Through a pozzolanic reaction, the silica and alumina in SCMs react with C-H in cement. However, as replacement levels of SCMs rise, unreacted silica and alumina are present because the C-H concentration is insufficient due to the decreased cement content. The ratio of water to binder (w/b) and particle size have a significant influence on the mix performance. For concretes with

significant pozzolan content, additives like superplasticizers can guarantee low w/b ratios. The main disadvantage of substituting large amounts of cement by pozzolans is their slow strength improvement. Low early strength can be problematic in some building types that call for high early strength and can have a large negative impact on the construction industry's economy [41]. The use of concretes containing significant volumes of SCMs has the advantage of being able to be employed in mass concrete to reduce potential temperature cracking [42]. This is related to the slow reaction rate of the pozzolanic reaction, which results in a lower heat of hydration [42,43].

In comparison to studies on mechanical and durability properties, there has been little research on the thermal properties of cementitious composites using recycled materials [44]. Studies on concrete with cement replaced by blast furnace slag, Fly ash, and silica fume have shown that thermal conductivity decreases as the replacement rates rise [45–49]. Abdalla et al. [50] investigated the effect of replacing Portland cement with sugar cane bagasse (SCBA) in proportions ranging from 10% to 50% in concrete manufacture. The data show that increasing the replacement of SCBA has resulted in a decrease in thermal conductivity. Both Chindaprasirt et al. [51] and Sargam et al. [52] reported a similar observation. The study by Bostanci (2020) [53] found that mixes containing 5% and 10% marble dust had reduced thermal conductivity values of 20.7% and 36.7%, respectively, when compared to the control mixture. In the Demirboga investigation [48], fly ash and blast furnace slag were used to replace cement to varying degrees (from 50% to 70%). Fly ash and blast furnace slag reduced thermal conductivity by 54 and 21% for the mortar and 60 and 31% for the cement paste, respectively. Giannakou and Jones [54] showed that a 30% Fly Ash concentration resulted in a 38% reduction in thermal conductivity. However, it is important to consider that having ashes of different sources influences their chemical composition. The influence of the chemical composition of the ash on the thermal conductivity is minimal compared to that of the physical structure, yet it does indirectly affect the thermal conductivity [55].

1.1.2.1 Blast furnace slag

Slags are by-product of the industrial processes of ores and recycled metals. The most frequent varieties are steel slag, foundry slag, blast furnace slag, copper slag, and ferronickel slag. For the production of every ton of ferronickel, around 12 to 14 tons of ferronickel slag (FNS) is generated [56]. In terms of metallurgical slag discharge,

ferronickel slag is currently a significant challenge because of its huge volumes landfilled and its limited utilization rate [57]. FNS is obtained from the extraction of nickel [58]. Its annual production is estimated to be 30 million tons in China, representing more than 20% of worldwide ferronickel slag production [57,59], estimated by about 2 million tons in Korea [58], and about 1.6 million tons by société Le Nickel (SLN) with a stockpile of 25 million tons [60]. only 6-10% of accessible slags are incorporated in cement or concrete mixtures as pozzolanic additives [61,62]. Ferronickel slag stacking and landfilling use a lot of land, harm the environment, and can transfer (launch) certain concentrate components into groundwater and surface water [57].

Ferronickel slag has a higher magnesium content and a lower calcium content than metallurgical slags. These attributes are challenging, they lead to a low stability and activity index of the building materials [57]. FNS was used as a fine aggregate substitute in mortar and concrete [63], as a substitute of Portland cement in concrete [64–68] and also as substitute for natural aggregates in road layers [69].

FNS is comparable to cement , its most dominant chemical elements are CaO, SiO2, Al2O3 and MgO [70]. Its hydration is mostly based on the pozzolanic reaction as described in the equation**1-17** given by Gartner [8] to produces hydration product [71]. Thus, when FNS is added to a cementitious mixture, the properties of cement are enhanced. The hydration products fill the porosities, resulting in improved mechanical characteristics of cementitious mixtures.

$$A_xS_y + mCH + nH \rightarrow C-S-H + C-A-H \qquad \textbf{1-17}$$

Because of the minimal quantity of toxic metals leaching from it, the FNS from New Caledonia is environmentally safe for use in concrete [56]. Yet, unlike blast furnace slag or fly ash, FNS was primarily employed as aggregate substitute in concrete. Some issues with durability have been reported [68,72–74]. The presence of a significant amount (>30%) of magnesium oxide in FNS limits its use as cementitious material. The hydration reaction of MgO caused an expansion after 2 years of treatment [75].

1.1.2.2 Fly ash

The primary byproduct of coal combustion is fly ash (FA). It is a heterogeneous material composed of SiO_2, Al_2O_3, Fe_2O_3, and CaO. The chemical properties of FA are influenced by the characteristics of the burned coal as well as the storage and handling

methods used. The pozzolanic reaction produces CSH when fly ash reacts with portlandite (equation **1-18**).

$$SiO_2 + x.Ca(OH)_2 + y.H_2O \rightarrow C_xSH_{x+y} \quad \textbf{1-18}$$

The substitution of cement by FA will modify the physiochemical properties of the concrete. It has been reported that adding FA to cement concrete reduces the hydration rate [76], improves the flowability of fresh mixtures due to the fine and spherical form of the grains and their soft vitreous texture. As a result, a relatively small amount of water may be necessary for the same workability [77]. Few studies have been performed [78] on the thermal performance of concretes incorporating FA, which show a potential high insulation characteristics of these concrete mix containing FA. Cement mixes containing FA take more time to set than standard concrete. The slow hydration reaction of FA and the reduction of cement concentration are to responsible for this behaviour [79]. Due to matrix densification, which inhibits internal hydration from evaporating, , the drying shrinkage decreases as FA substitution increases [80,81]. Additionally, it was observed that early FA incorporation results in a reduction in compressive strength. However, over time, the strength difference between concrete incorporating FA and ordinary concrete tends to diminish. The pozzolanic reaction, which is caused by the interaction of the silicon and aluminium present in FA with the portlandite, results in the formation of calcium-silicate-hydrates (C-S-H) and calcium-alumina-silicate-hydrates (C-A-S-H). Fly ash's pozzolanic contribution is minimal at advanced ages because the pozzolanic reaction is relatively sluggish [82]. According to Berry et al [83] fly ashes have a function of space filler and lead to the formation of ettringite in the early stages (AFt). At long-term, they serve primarily as silico-aluminate binders in the hydration reaction. When silica-rich materials are utilized, the reaction products, primarily calcium silicate hydrates (C-S-H) with lower Ca/Si ratios [17,18].

Fly ash (FA) was shown to be available on a global scale in the range of 800 million Mt per year, with an estimated global production of between 500 million and one bt per year [86],[87]. FA is primarily deposited on the surface and only a small portion is recycled. Due to their potentially hazardous trace element concentration, FA storage poses a major risk to ecosystems and human health [80].

1.1.2.3 *Crepidula* Shell

Nearly 200,000 t of seashells are incinerated in France or left to rot in the environment [88]. We identified the invasive and inedible *Crepidula fornicata* shells (CR) among

these seashells. Calcium carbonate (Aragonite, $CaCO_3$), which is suited for use as supplemental cementing material, is the primary component of CR. Since aragonite is more soluble and is metastable in comparison to calcite, calcium is released more rapidly. Several research [89] explored the possibility of replacing cement with shells. It was found that as the amount of shell powder in the concrete mixtures increased, the ettringite and calcium carboaluminate increase. This contributes to partially explain how shells participate in the formation of hydration products. The effectiveness of CR shells was attributed to the liberation of CO_3^{2-} ions, which led to the formation of carboaluminates and the reduction of the porosity of porosity, which increased mechanical strengths [90]. Wang et al [91] demonstrated that concrete's water absorption increases with calcium carbonate content and that concrete with a higher cockle shell ash content has more porous properties. Furthermore, Bentz et al [78] demonstrated that the incorporation of FA into concrete improved thermal conductivity compared to standard concrete. The use of Si-rich materials in blended cement can enhance later age strength but decrease early age strength due to the need for activation and gradual hydration.

There have been attempts to use calcium-rich elements in ternary mixed cements to increase their strength at an early age. Numerous studies have demonstrated the advantages of mixing silica and calcium carbonate (such as limestone) in concrete or mortar. Indeed, silica-rich materials will enhance later strengths while calcium carbonate filler will enhance early concrete strength, resulting in optimal strength growth [90].

1.2 Earthen construction

1.2.1 Introduction

Earth construction is one of the oldest and most widely used building techniques [92]. It is found in many parts of the world Figure 1-2 and has been the main building material in the ancient civilizations [92] cities such as Harappa (Pakistan), Atal-Huyuk (Turkey), Marrakech (Morocco), Duheros (España), Akhlet-Aton (Egypt), Babylon (Iraq), Jericho (Palestine), Chan-Chan (Peru) and others [93–95]. Earth has the ability to maintain higher thermal mass potential and indoor humidity than most alternative building materials [96]. It absorbs odours and noise, does not spread toxic substances, and adjusts hygrometry naturally. The heat that accumulates throughout the day in the building's thick and dense walls is dissipated during the night creating comfortable interiors. This definition simplifies the physical and technical behaviour of a large porous material in which linked hygrothermal processes coexist at a microstructural scale and are influenced by pore network architecture.

Figure 1-2 In orange, the regions of distribution of the raw earth constructions. The dots indicate the main architectural sites inscribed on the UNESCO World Heritage List

The granulometries of the material vary widely, which influenced the techniques utilized. The extraction is chemical-free, creates no waste or pollution, and consumes extremely low energy. If it hasn't been "stabilized" with cement, it can also be recycled indefinitely. Earth can be applied directly to build walls or used in the form of building blocks, cob, rammed earth, Daub, and compressed earth [97].

1.2.1.1 Type of earthen construction

There are several techniques using raw soil. Each one of these techniques arose from a diversity of geographical conditions, lifestyles, customs, and climates, as well as the resources available. The five most common construction techniques are adobe, cob, wattle and daub, rammed earth and compressed earth bricks (CEB). Guillaud and Houben [98] have schematically listed the twelve main techniques in the so-called "wheel" of earth construction techniques (Figure 1-3).

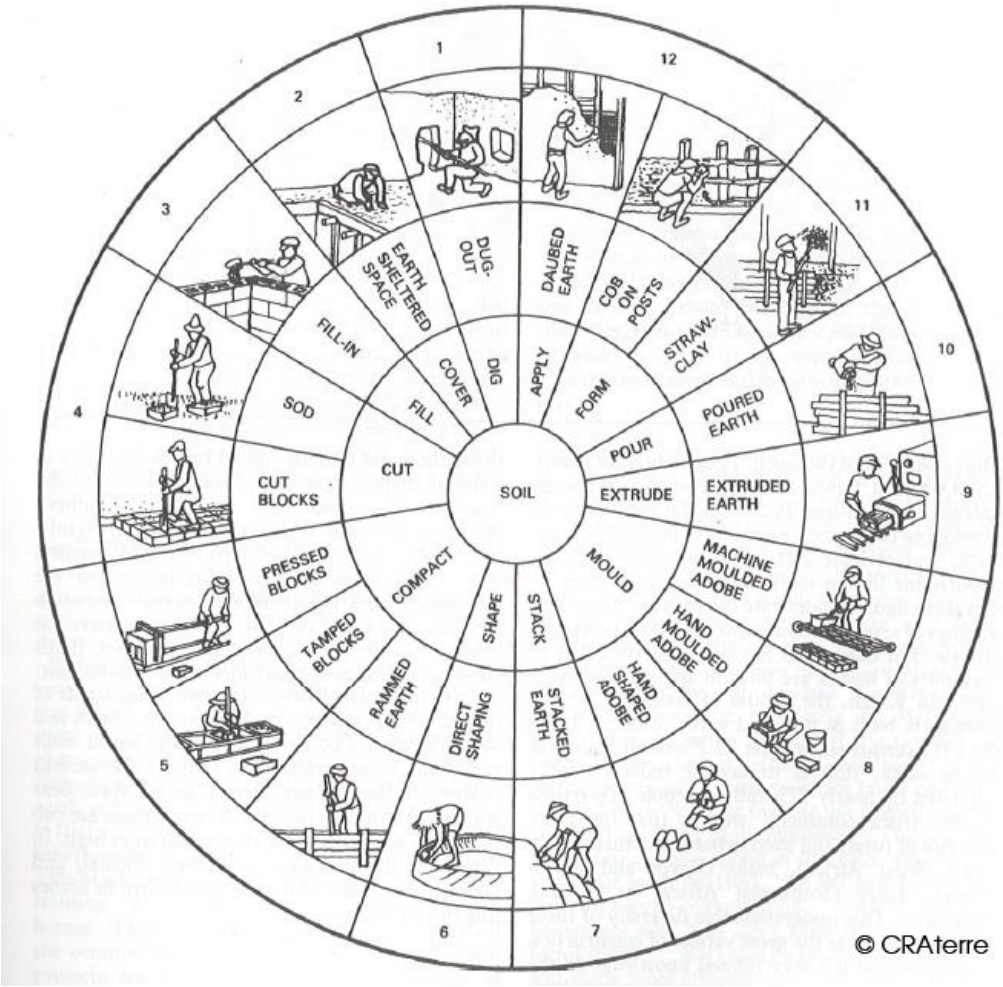

Figure 1-3 Wheel of earthen construction techniques [98]

1.2.1.1.1 Adobe

The adobe employs a very clayey materials that are manufactured in a liquid form (approximately 30% water content). It is a handcrafted method of producing blocks shaped by hand or in wooden or metal molds [99]. After hardening in the sunlight, these blocks will be placed in a masonry with mud from the same earth as the mortar. The resulting blocks are utilized as a supporting or filler material.

Figure 1-4 Production of adobe bricks [100]

1.2.1.1.2 Cob

The earth used for cob construction is comparable to that of adobes, and it is prepared similarly. The manufacturing method is artisanal: it entails hand modeling walls in advance, using earthen balls. The clayey material can be supplemented with vegetable fibers or straw [101]. The resulting walls are usually load-bearing.

Figure 1-5 Cob wall construction [102]

1.2.1.1.3 Wattle and daub

Wattle and daub composite is thought to be the first composite material ever invented. The wood is weaved into a lattice and covered in an earth mixture consisting of moist soil, clay, sand, animal dung, and straw (Figure 1-6). The primary component is the same as cob, It is usually sprayed or coated on a wood or bamboo frame after fibers have been added [101]. It is therefore a filler, with the wood structure providing the carrying function.

Figure 1-6 Wattle and daub filling of a wood-frame construction [103]

The heavy wattle and daub composite is made of a lot of soil and a small amount of straw, used as a load-bearing element. Its density is 1400 kg/m^3 dry and 1800 kg/m^3 wet. The thermal conductivity of this material is approximately 1,05 W/(m.K). The lightened wattle and daub composite is made of a high amount of straw and low quantity of soil Its density is between 300 kg/m^3 and 400 kg/m^3 and its thermal conductivity is from 0,12 to 0,15 W/(m.K) [104].

1.2.1.1.4 Rammed earth

This method employs a sandy or gravelly material with a clay percentage from 5 to 20% [105,106]. To build walls, the traditional artisanal method consists of manually compacting the soil between two wooden benches forming a formwork, through using rammers. The adobe walls have horizontal stripes that correspond to the branches, giving them a hefty appearance as shown in Figure 1-7.

Figure 1-7 Rammed-earth construction [107]

1.2.1.1.5 Compacted earth bricks

The compacted earth bricks (CEB) are made of a sandy-clay soil with a maximum element size of 20 mm (Figure 1-8). These bricks can be used for load bearing or filling purposes. The CEB materials are formed by manual, hydraulic, or mechanical presses with static, dynamic, or vibro-compression. CEB have the advantages of reducing wall thickness while maintaining the same properties as other approaches and allowing a variety of building styles [108].

Figure 1-8 Compressed earth blocks produced for the construction of model houses in Karaveddy, Manmunai West, Batticaloa. (Source: Jaime Royo Olid, EU Delegation 2017)

1.2.1.1.6 Self-compacted earth

Also known as site concrete or earth concrete. This material is elaborated from a mixture similar to adobe soil, liquid enough to be poured between two waterproof benches without compaction, as traditional cement concrete (Figure 1-9). Cement concrete and poured earth both use similar components. The difference between them are the proportions of the base materials and their origin, both of which have an impact on their environmental footprint. Cement is added to moulded earth to allow it to "hold" once the mould is removed, not to improve its mechanical strength. It would not harden without cement, and the mixture would take several weeks to dry. For almost the same density, the cement proportion range from 3 to 5%, which is about three times less than traditional concrete. Poured earth walls have a mechanical resistance between 2 and 4 MPa, whereas adobe has a mechanical resistance from 1 to 2 MPa. Today, the stabilization of poured earth with cementitious or chemical materials are the subject of an increasing number of investigations and research.

Figure 1-9 Self-compacted earth (source: Mathieu Neuville)

1.2.1.2 Lightened earth

Lightened earth is a non-load-bearing thermal and acoustic insulation method combining the techniques of ramming earth and cob. It is made up of a clay matrix that coats vegetable or mineral particles. The resulting construction material retains its straw appearance (Figure 1-10). This material has a number of physical characteristics depending on the density of the dry mix and the characteristics of the raw material, including thermal insulation, thermal inertia, acoustic insulation, and a good hygroscopic behaviour [109].This material has a number of physical characteristics depending on the density of the dry mix and the characteristics of the raw material thermal, including thermal insulation, thermal and hygrometric inertia, acoustic insulation, adsorption and desorption [109].

Figure 1-10 Lightened earth wall [110]

In summary, the earthen construction material can be classified into three categories: compacted earth, moulded earth, and fibered earth. The Table 1.6 summarizes the

raw earth's main properties. The hygroscopic, mechanical, and thermal characteristics of the hardened state are mostly influenced by the same characteristics: total porosity, pore size distribution, clay content, clay specific surface area and cation exchange capacity. In general, the soil has a higher capability for water vapor retention than current building materials. Moisture transport through the earth envelope enables the building's humidity to be maintained, which can ensure a good comfort for the occupants. Fibered earth can be used to provide a higher level of insulation than earth alone [111,112].

Table 1.6 Overview of the main soil properties

Properties		Units	Compacted earth	Molded earth	Fibred earth
[113–120]	Clay content	%	5 - 30	20 - 40	-
	Plasticity index PI	%	5 - 30	15 - 35	-
	Initial water content w_{ini}	%	5 - 15	15 - 35	-
Dry density ρ [111,113–115,117–119,121–131]		kg/m^3	1600 - 2300	1200 - 2100	200 - 1200
water content w [119,122,132–134]		%	0,5 - 5		
Water vapour diffusion resistance factor μ [119,122,131,133,135–138]			2 à 13		
Compressive strength [113–115,117–119,123–127,137,139]		MPa	0,4 - 4 (~1.5)	0,4 - 5	<1,2
Specific heat capacity Cp [119,122,129,132,135,140–143]		J/(kg.K)	500 à 1100 (~850)		
Thermal conductivity λ [111,116,119,121–124,127–131,137,138,143–147]		W/(m.K)	0,5 - 1,7	0,25 - 1,5	0,06 - 0,3

The techniques of earthen construction in France vary according to regional habits and traditions. In their book on earthen construction, Houben and Guillaud [148] summarized several production procedures. The earthen construction allows for a wide range of applications, depending on the techniques and the type of earth used. The common earth construction techniques are **ground-based plaster, Wattle and daub, cob, adobe, compressed earth bricks, and Rammed earth.** The soil is brought together by the dynamic or static compaction of the material, which gives the compacted earth certain strengths. While the drying of the clays gives the moulded

earth its strength. In Normandy region (France), the common earth construction technique used is cob. Cob is a traditional building technique combining clay, water, sand and fibers such as straw and reed [121]. Fibrous materials such as reed are typically used to reduce drying shrinkage in earth material and to provide the good thermal properties. Indeed, earth is subject to differential settlement, high compressibility and low shear strength and must be stabilized to improve its properties. The chemical stabilization method is the most recent technique for this purpose [149].

1.2.2 Raw earth stabilization for construction

The suitable materials in construction must be long-lasting. The buildings are designed to last at least 50 years. Earthen structures have traditionally been considered inferior to more permanent materials such as stones and baked clay bricks due to their poor longevity in an unstabilized state [150]. The addition of stabilizers to earth walls can improve their water and abrasion resistance. Plant and animal stabilizers (ferments, blood, urine, cow dung, horse manure) can be used for this purpose. Houben and Guillaud [98] classified stabilization procedures into three different types: mechanical, physical, and chemical. The mechanical stabilization is the compaction of a material which leads to a change in its density, permeability, mechanical strength, porosity, and compressibility. The term "physical stabilization" involves changes of the texture of materials. This includes the controlled mixing of various soil fractions or natural soils, as well as the incorporation of fibers into the soil. Chemical stabilization is the process of adding other materials and chemical elements to the soil to adjust its properties, either through a physical-chemical reaction between the grains and the materials or by producing a matrix that binds or coats the soil.

1.2.2.1 Binders overview

1.2.2.1.1 Mineral binders

The term "mineral binders" refers to any substance made up of mineral matter. When mixed with water, mineral specimens form a paste that hardens into a solid block by agglomerating grains. The majority of the mineral binders are synthetic, only natural pozzolans are exempt to this, but they only have a binding effect in the presence of lime, which is artificial. Cements and limes are the most popular binders used in raw earth building. They exist other binders known as alternative binders (volcanic ashes, geopolymers, gypsum) or by-products of various industries (blast furnace slag, fly ash,

sugarcane bagasse ash or rice husk ash) to replace cement or lime with a low carbon pozzolan.

1.2.2.1.2 Bio-organic binders

1.2.2.1.2.1 Polysaccharides

Polysaccharides are sugar polymers with monosaccharides or oses as monomers (glucose, galactose ...). Polysaccharides must be prepared to enable long chains break away from their organized structure in order to interact with soil (traditionally by maceration). When combined with water, the hydroxyl groups produce "hydrogels," which are cross-linked polymers with a hydrophilic structure that absorb water without dissolving [151]. When the hydrogels are mixed with soil and water, they coat the surface of the soil particles and bind them together to give the stabilizing effect [152]. Figure 1-11 shows that particles of stabilized soil by gellan gum are bound together by gels that form web-like matrices. Polysaccharides exist in a wide range of forms and can be classified into subfamilies based on their origin.

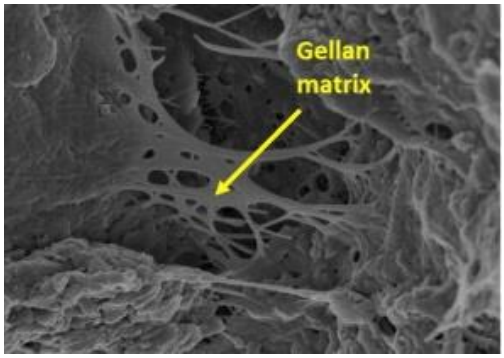

Figure 1-11 Scanning electron microscope (SEM) of stabilized soil by gellan gum

- **Starches**

Starches are one of the most significant organic compounds found in plants, and they serve as a source of sustenance for organisms. Starches gel at temperatures above 60°C in a hydrated environment.

- **Seaweed extracts**

Algae are chlorophyll-containing plants. We distinguish blue algae, green algae, red algae, and brown algae based on their extra pigments [153]. Some extracts of these algae have industrial applications in several fields due to its special attributes (food, pharmaceutical, cosmetics and biotechnology) [154]. Agar Agar and carrageenan are two more biopolymers derived from red algae. Alginate is a polysaccharide obtained by dilution in an acid from brown algae in the form of alginic acid. It's also available as

an alginate salt, most often as sodium alginate. Alginate is a hydrophilic agent that forms a gel in the presence of a number of salts. Its polymer's chains are made up of a series of fundamental monomers called - L-guluronic (G) and - D-mannuronic (M). Gelation is more significant in alginates with a high guluronic fraction (FG). Table 1.7 gives the chemical compositions of alginates according to the species of brown algae [155].

Table 1.7 Chemical composition of alginates varies according to brown seaweed species.[155]

Space	F_G	F_M
Laminaria digitata	0,41	0,59
Laminaria hyperborea (leaf)	0,49	0,51
Laminaria hyperborea (stem)	0,63	0,37
Durvillea Antarctica	0,32	0,68
Acophyllum nodosum	0,39	0,61
Lessonia nigrescens	0,41	0,59
Macrocystis pyrifera	0,42	0,58

- **Cellulose and lignin**

Unlike cellulose, lignin is a biopolymer that does not belong to the polysaccharide family, but its practically systematic coexistence with cellulose in higher plants leads to its consideration. Cellulose is found in almost pure form in the cell walls of cotton seed hairs (about 95 %), but it is found in wood at 40 to 50 %, hemp at 70 %, and flax at 80 %, which explains the economic relevance of these fibers [156]. The macromolecules of cellulose gather together in a cluster of fibers in their normal state, wrapped by a layer of hemicellulose and lignin, with the lignin ensuring the stiffness of fibers.

The soil is stabilized by either adding straw or rice husk, or by adding domestic animal excrements that have been allowed to ferment in a humid setting before utilization. The maceration of vegetal fibers leads to their decomposition by micro-organisms. The microorganisms first absorb the sugars and then, by their extracellular enzymes, attack the easily degradable biopolymers (pectin, starch, cellulose...). Thus the contact surface between the clays and these microscopic fibers becomes greater [157].

- **Natural gums**

Natural gums are mostly plant secretions that help heal wounds, with the exception of xanthan gum, produced by bacteria. These Gums have a thickening property and are

used to stabilize raw earth plaster. Fabaceae (acacias) generate gum Arabic, which is widely used in West Africa.[158].

- **Gelatinous plant juices**

Gelatinous plant juices are viscous liquids made by soaking specific plant parts in water. These plant extracts, which are made up of polysaccharides, generate a viscous solution practically instantaneously when they meet water. The banana tree's leaves and stalks, the agaves, the cactus, and the aloe are all counted. The thick liquid formed by the soaking of stems, bark, or roots of specific plants (liana) improves the resistance to shrinkage of earthen plasters [158]. The gels affect the fresh properties of soil and the dry process of the plaster. The drying process could be a slightly slower and more homogeneous, which reduces the formation of cracks [157]. Moreover, these gels become a real glue for the mineral particles as the water evaporates during drying.

- **Chitosan**

Chitosan is a polysaccharide of animal origin. It is a by-product of the crustacean and cephalopod industries [159]. It is made by deacetylating chitin from the shells of shrimps and other crustaceans, and it is widely produced in Asia (India, China) where crustacean manufacturing is popular.

1.2.2.1.2.2 Lipids

The fat matter of living creatures is made up of lipids. They are hydrophobic compounds that are insoluble in water. Animal fats and the seeds of some plants are the most common sources of lipids. At normal temperature, oils are liquid, waxes are solid, and fats are in the middle. For example, linseed oil, kapok oil, shea butter, and wild grape oil are used mostly for preparing topcoats or for surface treatment [158].

Therefore, the incorporation of seaweed minerals or seaweed ash in the earth construction can be explored. Seaweed is an environmentally friendly material because it is naturally occurring and stores carbon. These seaweeds also contribute to limiting ocean acidification and deoxygenation as well as other impacts related to global climate change [160]. The incorporation of stranded seaweed (powders, fibers and co-products) into soil could lead to the reuse of waste materials, limit environmental contamination and at the same time reduce the cost of earth and its impact on the environment while maintaining or improving the properties of the soil [112].

1.2.2.2 Stabilization of raw earth for construction

Stabilization is defined as a change in physical and chemical properties of earth [161]. The addition of biopolymer as stabilization of earth lead to a change in its density and its porosity and thus have an influence on earth properties. The density, for example, can be impacted by the stabilization process and consequently affect the mechanical resistance as well as the thermal behaviour. Additionally, the porosity has an impact on material structure, directly affecting capillarity and water resistance, and indirectly affecting durability, mechanical, and hygrothermal characteristics. Biopolymers have the capacity to transform the pore size distribution through various mechanisms, including filling the tiniest pore, enhancing soil particle packing by binding them together, or changing the rheology properties [162–164]. When we integrate additives, a lower bulk density is not necessarily indicative of higher porosity, as voids in the mixture can be filled by lighter additives [165]. Raw earth stabilization seeks to improve the mechanical and durability properties of the material and allow it to be more resistant to mechanical and climatic pressures. Danso et al [166] classify stabilization methods into three categories: fiber reinforcement, binders, and a combination of the fibers-binders. Compaction and texture adjustment are also considered as mechanical and physical stabilization. Most of the research conducts a simple compressive strength measurement to assess the effectiveness of stabilization. For several reasons, comparing the compressive strengths achieved by different publications is problematic, the values vary depending on the manufacturing method, curing condition, specimen form, and test procedure [167,168]. There are several testing methodologies available to quantify the uniaxial compressive strength, but they do not produce the same outcomes for the same types of materials [168]. The following sections focus on binder-based stability.

1.2.2.2.1 Stabilization with mineral binders

Table 1.8 summarizes few findings from literature on soil stabilization with mineral and alternative binders using various techniques.

Table 1.8 Literature synthesis on mineral stabilization of different types of construction

CCR: Calcium Carbide Residue, CaO: Calcium Oxide (Quicklime), $Ca(OH)_2$: Calcium Hydroxide (Slaked lime).

	Stabilizer	Type	Ref	cure (days)	Quantity (%)	Compressive strength (MPa)
Min era	Cement	CEB	[169]	-	0	1
					5	1

						7	1,3
						10	2,0
				[170]	21	0	1.4
						8	8.2
				[171]	28	0	0.6
						4	1.5
						8	5.6
						12	6
			Adobe	[172]	-	0	2,2
						2	2,6
						4	2,8
						8	3
						12	3,2
			Rammed Earth	[173]	28	0	3,82
						10	6,47
			Self-compacted earth	[174]	7	0	1.3
						5	1.6 - 3.8
					28	0	1.7
						5	2.5 - 6
					90	0	2
						5	2,5 - 8
	Lime	$Ca(OH)_2$	CEB	[175]	28	0	0,6
						10	16,5
		Not specified		[169]	-	0	1,0
						5	0,6
						7	0,8
						10	1,3
		$CaO + CA(OH)_2$	Adobe	[176]	-	0	2,3
						4	3,2
						6	3,3
						8	3,4
						10	3,5
						12	3,2
	Lime		Rammed earth	[177]	28	0	0.6
						2	1
						3	1.2
						5	1.2
						6	1.1
Alternative minerals	Volcanic ash		CEB	[178]	7,28,56, 90	5	0,5-1,2
						10	0,5-1,8
						15	0,5-2,6
						20	0,5-3,1
				[175]	-	0	0,6

	Lime – Sugar cane bagasse ash			7, 14, 28	20			17,7–20,8–21,3
	Gypsum	Adobe	[179]	-	0			1
					5			1,2
					10			3
					15			4,5
					20			4,6
					25			4,8
	Phosphogypsum			-	5			1,1
					10			3
					15			3
					20			4
					25			4,5
	Gypsum		[169]	-	0			1
					10			2,4
	calcium carbide and fly ash Ratio 2/3 = CCR/FA		[180]	28, 60	0			0,3
					3			1,3
					6			2,1 - 2,5
					9			3 - 3,8
					12			3,5 - 5,2
					15			3,5 - 5,8
	Limestone filler (LF), metakaolin (MTK)	Self-compacted rammed earth	[181]	28	Cement 10%	MTK	2	9,1
						LF	1,5	
						MTK	3	11
						LF	1,5	
						MTK	5,5	10,8
	Fly ash		[120]	3,7,28	10			0,5 – 1,1 – 2,8
					15			0,8 – 1,1 – 3,5
					20			0,9 – 1,4 – 4,3
					25			0,9 – 1,3 – 4,9
	Phosphogypsum				2			0,49 – 1 – 4
					5			0,55 – 1 – 4,2
					10			0,5 – 0,8 – 3
					15			1 – 1 – 3,2
	Quicklime				3			1,1 – 1,2 – 4,4
					5			1,1 – 1,4 – 4,5
					8			1,2 – 1,3 – 4,5
					10			1,2 – 1,6 – 4,6

The compressive strength of an unstabilized earth ranges can be found in Table 1.6 . In the best-case scenarios, the stability of up to 10% cement allows these figures to be multiplied by a factor of 2 to 3 [182]. Mineral stabilizers slightly improve the compressive strength of earth. For example, in the research of Alam et al [169] and

Dao et al [172], compressive strengths increased from 1 MPa to 2 MPa with 10% of cement and from 2,2 MPa to 3,2 MPa with 12% of cement, respectively. However, neither of these studies used wet curing, which might explain the low compressive strengths. In comparison to the studies of Sore et al [170] and Tran et al [171], they produced greater strengths from 1,4 MPa to 8.2 MPa with 8% of cement and from 0,6 MPa to 6 MPa with 12% of cement with a 21-day and 28-day wet cure, respectively. The slight rise in compressive strengths with the addition of cement (often in significant amounts) is consistent with the results of Van Damme and Houben [182]. Their research shows that, in most cases, cement stabilization is not beneficial both mechanically and environmentally. Indeed, cement provides very low mechanical impact at a significant environmental cost. Alavéz-Ramrez et al [175] showed that the stabilization with lime provides an enhanced performance compared to other investigations. In the other investigations, regardless of the lime amount (up to 12%) or the type of lime utilized, the increase in dry compressive strength is quite low [169,176,177]. The compressive strength increase was most likely due to the progressive densification of the matrix due to a chemical reaction between lime and silica and alumina available in the soil, resulting in the formation of calcium silicate hydrate (CSH) and calcium-aluminium silicate hydrate (CAH), which are the main products of the hydration of Portland cement [112]. The results of Alavéz-Ramrez et al [175] on the use of alternative mineral stabilization seem also unusual. Indeed, the specimen achieves up to 21,3 MPa for compressive strength with 20% lime mixture and sugarcane bagasse ash. All the studies show that the required time to achieve the best strengths are rather long, which corresponds to the mechanism of pozzolanic binders' action, which have slow kinetics when compared to Portland cement. The findings of Hossain and Mol [178] regarding soil stabilization reveal an increase in the compressive strength with the inclusion of volcanic ash ranging from 1.2 to 3.1 after 90 days of curing time.

In the study conducted by Gu and Chen [120], the elaborated samples were stabilized by cement and different minerals additions (fly ash, phosphogypsum, quicklime). After 28 days of curing time, samples containing 2–5% phosphogypsum (PG) showed a higher compressive strength than those containing 10–15 % PG. The maximum mechanical strength was found in stabilized loess with 5% PG, due to the participation of PG in the hydration kinetic and the promotion of the formation of a C-S-H gel. The addition of 20% FA increased the compressive strength after 28 days of curing. FA is

an alkali-activated substance that may react with cement to form C-S-H gels and C-A-S-H through pozzolanic reaction. The calcium and alumina originating from FA combines with the clay elements (SiO_2 and aluminum silicates), resulting in the creation of both tobermorites and Al-tobermorite. When 25% FA was added, the unconfined compressive strength at 28d decreased marginally. Since the active ingredient of FA cannot be fully reacted, excess FA would reduce soil particle cohesiveness.

1.2.2.2.2 Stabilization with organic binders

Table 1.9 summarizes some findings of compressive strength from literature on soil stabilization with organic binders. Some binders are introduced in liquid form or as a water-diluted form.

Table 1.9 Literature synthesis on organic stabilization of different types of construction
CaO: Calcium Oxide (Quicklime), $Ca(OH)_2$: Calcium Hydroxide (Slaked lime), NaOH: Sodium hydroxide, GDL : Glucono-Delta Lactone, HMP-Na : Sodium Hexametaphosphate.

	Type	Binder	Quantity (%)	Activation	fibers (%)	Compressive strength (MPa)
[183]	CEB	Alginate	0%	0,5% Lignum (Guayacan resin)	0 - 0,25 of wool	2,23 – 3,05
			19,5 (dissolved)		0,25 - 0,50 of wool	4,44- 4,37
			19,75		0	3,77
[184]	CEB	Used cooking oil	0%	-	-	1
			1%	4% CaO		2.5
				0,1% NaOH + 4% CaO		2.9
[185]	adobe	Carageenan dissolved	0%	-		2.1
			0,5%			3.9
[186]	adobe	Xanthan Gum	0%			0.4
			1%			3.7
[187]	Soil	guar gum	0,5			1,6
			1			2,1
			1,5			3,3
			2			4
			3			4,2
		xanthan gum	0,5			2,1
			1			2,5
			1,5			3
			2			3,5
			3			4,2
		Cement	8%			3,1

[188]	Self-compacted earth	Starch	0%	-		3
			1%	Heating at 120°C		4-7
[189]	Self-compacted earth	Alginates	0%	-		-
			0,5%	0,075% CaCO3, 0,275% GDL, HMP-Na		2,5
[190]	Adobe	Chitosan	0%	-		2,1
			3%			4,64

In most cases, organic binders are used in association with activating agents. Pinel et al [189] have shown that in addition to a calcium source, regulating agents such as HMP-Na and GDL are necessary for a good efficiency of the alginate as seen in the Figure 1-12. Alhaik et al [188], by studying eleven starches, they showed that depending on the source and the industrial treatment of the starch as well as the nature of the soil, the results were very different. The mixture with fibers, and even mineral binders (lime) makes it difficult to identify the effect specific to the organic binders [188]. Muguda et al [187] showed that a biopolymer content of 1.5–2.0% was able to generate a similar compressive strength than a soil stabilized by 8.0% of cement. The findings of Galán-Marín [183] showed that the alginate improved the compressive strength of CEB from 2.23 to 3.77 MPa. The addition of wool without alginate increases slightly the compressive strength from 2.23 to 3.05. However, combining wool and alginate raises soil resistance to 4.44 MPa [183].

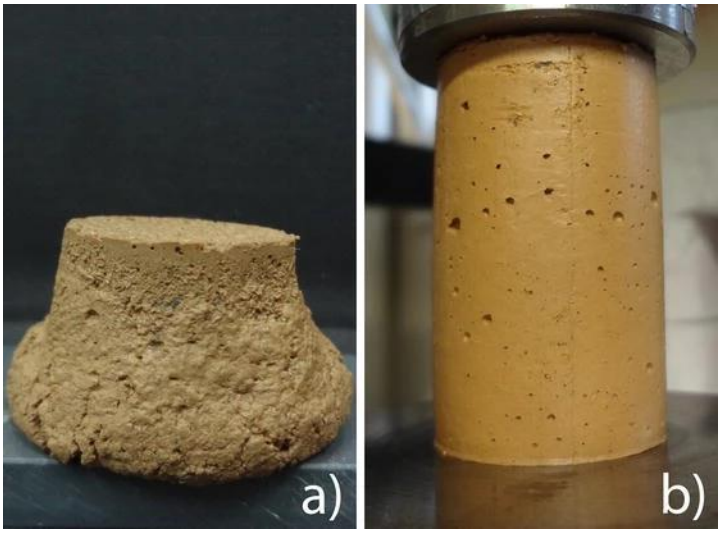

Figure 1-12 Mortar specimens demoulded 24 h after pouring and without drying, a) mixture with no GDL (binder phase containing SHMP, alginate) and b) optimal composition (containing SHMP, alginate and GDL) [189]

1.2.2.2.3 Effect of binder on the thermal performance

Regardless of the method used, thermal conductivity is determined by the inherent properties of the material (water content and dry bulk density). The apparent density has a significant impact on heat conductivity with the same water content. This is related to the solid-state heat propagation principle. Indeed, heat is transmitted between solid-state particles. The existence of gaps corresponding to the porosity of less dense materials causes a break in the heat transmission. Mineral binders reduce the optimal density of compaction of pressed/compacted materials (CEB or rammed earth). The consequence of mineral binders is the substantial decrease or not of heat conductivity. This is supported by the findings of Liuzzi et al. [191], which found that adding 5% of lime reduces the dry bulk density from 1992 kg/m^3 to 1843 kg/m^3, lowering the thermal conductivity from 1.2 W/(K.m) to 0.88 W/(K.m). Other production processes, such as adobe, might result in a different dry bulk density evolution after stabilization. Indeed, adobes are porous materials, and adding a binder can assist to plug these porosities, improving the material's density. Thus, some studies conducted on adobes showed an increase in thermal conductivity with 8-12% cement addition [172],[192] and also with lime addition [192]. However, for addition rates less than 8%, both authors showed thermal conductivity values close to those of the unstabilized material. The thermal conductivity values appear unaffected by stabilization at lowest cement adding rates. Concerning, the stabilization by organic binders, Pinel et al [189] investigated their impact on the material's hygrothermal performance. The results showed that the thermal conductivity decreases from 1.9 W/(K.m) for the unstabilized soil to 1.4 W/(K.m) for the combination with 1% alginate and regulating agent. The hygrothermal properties are more likely to be studied when fibers are used as a soil stabilizer. Fibers lower density, increase porosity and thereby reduce thermal conductivity. [193,194]. Laborel-Préneron et al[195] found that the thermal conductivity of raw earth decreases when stabilized with 6% barley straw and goes from 0.57 W m to 0.14 W/(K.m). According to the findings of Ashor et al [196], the thermal conductivity decreased by about 53% and 54.4%, respectively, compared to earth bricks without fiber reinforcement with the incorporation of barley and wheat straw fibers in amounts ranging from 0 to 3%.

1.3 Conclusion

Construction, and more specifically the building materials industry, is presenting more and more local and eco-friendly material-based solutions as a response to the issues

surrounding sustainable development. This chapter has drawn up a report on the behaviour of concrete containing supplemental cementitious materials. According to these investigations, the pozzolanic products utilized as cement substitutes enhanced the characteristics of cement-based products and a number of environmental indicators. In this thesis, the mains SCM used are FNS, FA and shell powder of *Crepidula fornicata*. The addition of FNS to a cementitious mixture enhance the properties of cement. The hydration products fill the porosities, resulting in improved mechanical characteristics of cementitious mixtures. The addition of FA to cement concrete reduces the hydration rate, improves the flowability of fresh mixtures. The Studies performed on the thermal performance of concretes incorporating FA, show a potential high insulation characteristic. Fly ash's pozzolanic contribution is minimal at advanced ages because the pozzolanic reaction is relatively sluggish. The strength differential between concrete containing fly ash and conventional concrete tends to decrease with time. According to the studies that investigated the substitution cement with shells, the amount of ettringite and calcium carboaluminate increased with the addition of shell powder. Studies have demonstrated the advantages of mixing silica and calcium carbonate (such as limestone) in concrete or mortar. Indeed, silica-rich materials will enhance later strengths while calcium carbonate filler will enhance early concrete strength, resulting in optimal strength growth. In line with this, we integrated these various SCMs in the next sections of this thesis to optimize a formulation with favorable mechanical and thermal properties. This chapter also highlighted the methods used to stabilize earthen structures. Among these techniques is the cob, an ancestral raw earth construction style that is common in Normandy. The usage of alginates was identified as one of the systems. Given the alarming amounts of algae present on the Normandy coast, this appears to be interesting. The interaction of polymers called alginates result in gelling and precipitation occurrences at room temperature. They interact with cations like Ca^{2+} that may be emitted from the earth itself. In the following we developed a biodegradable, low cost and low quantity biobased material. We investigated the functional performance, hydric and thermal properties of the cob stabilised with algal powder.

1.4 References

[1] United Nations Environment Programme, 2020, 2020 Global Status Report for Buildings and Construction: Towards a Zero-emission, Efficient and Resilient Buildings and Construction Sector, Nairobi.

[2] 2020, “Energy Technology Perspectives 2020,” Energy Technology Perspectives, p. 400.

[3] De Wit, M., Hoogzaad, J., Ramkumar, S., Friedl, H., and Douma, A., The Circularity Gap Report.

[4] 2015, “The Paris Protocol.”

[5] 2021, “Fit for 55”: Delivering the EU’s 2030 Climate Target on the Way to Climate Neutrality.

[6] 2019, “Direct CO2 Emissions from Selected Heavy Industry Sectors,” IEA [Online]. Available: https://www.iea.org/data-and-statistics/charts/direct-co2-emissions-from-selected-heavy-industry-sectors-2019.

[7] Rashad, A. M., 2013, “A Comprehensive Overview about the Influence of Different Additives on the Properties of Alkali-Activated Slag – A Guide for Civil Engineer,” Construction and Building Materials, **47**, pp. 29–55.

[8] Gartner, E., 2004, “Industrially Interesting Approaches to ‘Low-CO2’ Cements,” Cement and Concrete Research, **34**(9), pp. 1489–1498.

[9] Nwankwo, C. O., Bamigboye, G. O., Davies, I. E. E., and Michaels, T. A., 2020, “High Volume Portland Cement Replacement: A Review,” Construction and Building Materials, **260**, p. 120445.

[10] Saleh, H. M., and Eskander, S. B., 2020, “18 - Innovative Cement-Based Materials for Environmental Protection and Restoration,” New Materials in Civil Engineering, P. Samui, D. Kim, N.R. Iyer, and S. Chaudhary, eds., Butterworth-Heinemann, pp. 613–641.

[11] Baron, O., 1996, Durabilité des bétons.

[12] Meinhard, K., and Lackner, R., 2008, “Multi-Phase Hydration Model for Prediction of Hydration-Heat Release of Blended Cements,” Cement and Concrete Research, **38**(6), pp. 794–802.

[13] Liu, C., and Zhang, M., 2021, “Effect of Curing Temperature on Hydration, Microstructure and Ionic Diffusivity of Fly Ash Blended Cement Paste: A Modelling Study,” Construction and Building Materials, **297**, p. 123834.

[14] Nicolas, V., Sorelli, L., Sudret, B., Yalamas, T., and Gagné, R., 2012, “Uncertainty Propagation of a Multiscale Poromechanics-Hydration Model for Poroelastic Properties of Cement Paste at Early-Age,” Probabilistic Engineering Mechanics, p. 1.

[15] 2012, “NF EN 197-1. Cement - Part 1 : composition, specifications and conformity criteria for common cements.”

[16] Nonat, A., 2004, “The Structure and Stoichiometry of C-S-H,” Cement and Concrete Research, **34**(9), pp. 1521–1528.

[17] Richardson, I. G., and Groves, G. W., 1993, “Microstructure and Microanalysis of Hardened Ordinary Portland Cement Pastes,” Journal of Materials Science, **28**(1), pp. 265–277.

[18] Richardson, I. G., 1999, “The Nature of C-S-H in Hardened Cements,” Cement and Concrete Research, **29**(8), pp. 1131–1147.

[19] Richardson, I. G., 2000, “The Nature of the Hydration Products in Hardened Cement Pastes,” Cement and Concrete Composites, **22**(2), pp. 97–113.

[20] Liu, J., Qin, Q., and Yu, Q., 2020, “The Effect of Size Distribution of Slag Particles Obtained in Dry Granulation on Blast Furnace Slag Cement Strength.”

[21] Mehta, A., Siddique, R., Ozbakkaloglu, T., Uddin Ahmed Shaikh, F., and Belarbi, R., 2020, “Fly Ash and Ground Granulated Blast Furnace Slag-Based Alkali-Activated Concrete: Mechanical, Transport and Microstructural Properties,” Construction and Building Materials, **257**, p. 119548.

[22] Xu, W., Zhang, Y., and Liu, B., 2020, “Influence of Silica Fume and Low Curing Temperature on Mechanical Property of Cemented Paste Backfill,” Construction and Building Materials, **254**, p. 119305.

[23] Gülmez, N., 2021, “Performance of Marble Powder on Cementitious Composites Including Waste Steel Chips as an Additive,” Construction and Building Materials, **312**, p. 125369.

[24] Prošek, Z., Nežerka, V., and Tesárek, P., 2020, “Enhancing Cementitious Pastes with Waste Marble Sludge,” Construction and Building Materials, **255**, p. 119372.

[25] Tayeh, B. A., Hasaniyah, M. W., Zeyad, A. M., Awad, M. M., Alaskar, A., Mohamed, A. M., and Alyousef, R., 2020, “Durability and Mechanical Properties of Seashell Partially-Replaced Cement,” Journal of Building Engineering, **31**, p. 101328.

[26] Singh, M., Saini, B., and Chalak, H. D., 2020, “Long Term Evaluation of Engineered Cementitious Composite Containing Stone Slurry Powder,” Construction and Building Materials, **264**, p. 120183.

[27] Danish, A., Mosaberpanah, M. A., Salim, M. U., Fediuk, R., Rashid, M. F., and Waqas, R. M., 2021, “Reusing Marble and Granite Dust as Cement Replacement in Cementitious Composites: A Review on Sustainability Benefits and Critical Challenges,” Journal of Building Engineering, **44**, p. 102600.

[28] Quedou, P. G., Wirquin, E., and Bokhoree, C., 2021, “Sustainable Concrete: Potency of Sugarcane Bagasse Ash as a Cementitious Material in the Construction Industry,” Case Studies in Construction Materials, **14**, p. e00545.

[29] 2022, “ASTM-C311. Standard Test Methods for Sampling and Testing Fly Ash or Natural Pozzolans for Use in Portland-Cement Concrete.”

[30] Hemalatha, T., Mapa, M., George, N., and Sasmal, S., 2016, “Physico-Chemical and Mechanical Characterization of High Volume Fly Ash Incorporated and Engineered Cement System towards Developing Greener Cement,” Journal of Cleaner Production, **125**, pp. 268–281.

[31] Kate, G. K., and Thakare, S. B., 2017, “An Experimental Study of High Strength-High Volume Fly Ash Concrete for Sustainable Construction Industry,” IOP Conf. Ser.: Mater. Sci. Eng., **225**(1), p. 012247.

[32] Panesar, D. K., Kanraj, D., and Abualrous, Y., 2019, “Effect of Transportation of Fly Ash: Life Cycle Assessment and Life Cycle Cost Analysis of Concrete,” Cement and Concrete Composites, **99**, pp. 214–224.

[33] Gholampour, A., and Ozbakkaloglu, T., 2017, “Performance of Sustainable Concretes Containing Very High Volume Class-F Fly Ash and Ground Granulated Blast Furnace Slag,” Journal of Cleaner Production, **162**, pp. 1407–1417.

[34] Sakthivel, T., Gettu, R., and Pillai, R. G., 2019, “Compressive Strength and Elastic Modulus of Concretes with Fly Ash and Slag,” J. Inst. Eng. India Ser. A, **100**(4), pp. 575–584.

[35] Samad, S., Shah, A., and Limbachiya, M. C., 2017, “Strength Development Characteristics of Concrete Produced with Blended Cement Using Ground Granulated Blast Furnace Slag (GGBS) under Various Curing Conditions,” Sādhanā, **42**(7), pp. 1203–1213.

[36] Megat Johari, M. A., Brooks, J. J., Kabir, S., and Rivard, P., 2011, “Influence of Supplementary Cementitious Materials on Engineering Properties of High Strength Concrete,” Construction and Building Materials, **25**(5), pp. 2639–2648.

[37] El-Dieb, A. S., and Kanaan, D. M., 2018, “Ceramic Waste Powder an Alternative Cement Replacement – Characterization and Evaluation,” Sustainable Materials and Technologies, **17**, p. e00063.

[38] El-Dieb, A. S., Taha, M. R., Abu-Eishah, S. I., El-Dieb, A. S., Taha, M. R., and Abu-Eishah, S. I., 2018, The Use of Ceramic Waste Powder (CWP) in Making Eco-Friendly Concretes, IntechOpen.

[39] Rani, D. M. S., “A Study on Ceramic Waste Powder,” A Study on Ceramic Waste Powder.

[40] Samadi, M., Huseien, G. F., Mohammadhosseini, H., Lee, H. S., Abdul Shukor Lim, N. H., Tahir, M. M., and Alyousef, R., 2020, “Waste Ceramic as Low Cost and Eco-Friendly Materials in the Production of Sustainable Mortars,” Journal of Cleaner Production, **266**, p. 121825.

[41] Gupta, S., 2016, “Effect of Content and Fineness of Slag as High Volume Cement Replacement on Strength and Durability of Ultra-High Performance Mortar,” Journal of Building Materials and Structures, **3**(2), pp. 43–54.

[42] Du, H., and Tan, K. H., 2014, “Waste Glass Powder as Cement Replacement in Concrete,” Journal of Advanced Concrete Technology, **12**(11), pp. 468–477.

[43] Rahhal, V., and Talero, R., 2004, “Influence of Two Different Fly Ashes on the Hydration of Portland Cements,” Journal of Thermal Analysis and Calorimetry, **78**(1), pp. 191–205.

[44] Adesina, A., 2021, “Overview of the Influence of Waste Materials on the Thermal Conductivity of Cementitious Composites,” Cleaner Engineering and Technology, **2**, p. 100046.

[45] Sun, Y., Gao, P., Geng, F., Li, H., Zhang, L., and Liu, H., 2017, “Thermal Conductivity and Mechanical Properties of Porous Concrete Materials,” Materials Letters, **209**, pp. 349–352.

[46] Kim, K.-H., and Jeon, S.-E., 2003, “An Experimental Study on Thermal Conductivity of Concrete,” Cement and Concrete Research, **33**(3), pp. 363–371.

[47] 2003, “Influence of Mineral Admixtures on Thermal Conductivity and Compressive Strength of Mortar,” Energy and Buildings, **35**(2), pp. 189–192.

[48] Demirboğa, R., 2003, “Thermo-Mechanical Properties of Sand and High Volume Mineral Admixtures,” Energy and Buildings, **35**(5), pp. 435–439.

[49] Xiao, J. Z., Song, Z. W., and Zhang, F., 2010, “An Experimental Study on Thermal Conductivity of Concrete,” Journal of building materials.

[50] Abdalla, T. A., Koteng, D. O., Shitote, S. M., and Matallah, M., 2022, “Mechanical and Durability Properties of Concrete Incorporating Silica Fume and a High Volume of Sugarcane Bagasse Ash,” Results in Engineering, **16**, p. 100666.

[51] Chindaprasirt, P., Sujumnongtokul, P., and Posi, P., 2019, “Durability and Mechanical Properties of Pavement Concrete Containing Bagasse Ash,” Materials Today: Proceedings, **17**, pp. 1612–1626.

[52] Sargam, Y., Wang, K., and Alleman, J. E., 2020, “Effects of Modern Concrete Materials on Thermal Conductivity,” Journal of Materials in Civil Engineering, **32**(4), p. 04020058.

[53] Bostanci, S. C., 2020, “Use of Waste Marble Dust and Recycled Glass for Sustainable Concrete Production,” Journal of Cleaner Production, **251**, p. 119785.

[54] Giannakou, A., and Jones, M. R., 2002, “Potential of Foamed Concrete to Enhance the Thermal Performance of Low-Rise Dwellings,” Innovations and Developments In Concrete Materials And Construction, Thomas Telford Publishing, pp. 533–544.

[55] Rezaei, H. R., Gupta, R. P., Bryant, G. W., Hart, J. T., Liu, G. S., Bailey, C. W., Wall, T. F., Miyamae, S., Makino, K., and Endo, Y., 2000, “Thermal Conductivity of Coal Ash and Slags and Models Used,” Fuel, **79**(13), pp. 1697–1710.

[56] Saha, A. K., and Sarker, P. K., 2017, “Sustainable Use of Ferronickel Slag Fine Aggregate and Fly Ash in Structural Concrete: Mechanical Properties and Leaching Study,” Journal of Cleaner Production, **162**, pp. 438–448.

[57] Xi, B., Li, R., Zhao, X., Dang, Q., Zhang, D., and Tan, W., 2018, “Constraints and Opportunities for the Recycling of Growing Ferronickel Slag in China,” Resources, Conservation and Recycling, **139**, pp. 15–16.

[58] Cho, B.-S., Kim, Y.-U., Kim, D.-B., and Choi, S.-J., 2018, “Effect of Ferronickel Slag Powder on Microhydration Heat, Flow, Compressive Strength, and Drying Shrinkage of Mortar,” Advances in Civil Engineering, **2018**, p. e6420238.

[59] Gu, Y., Li, J.-L., Peng, J.-K., Xing, F., Long, W.-J., and Khayat, Kamal. H., 2020, “Immobilization of Hazardous Ferronickel Slag Treated Using Ternary Limestone Calcined Clay Cement,” Construction and Building Materials, **250**, p. 118837.

[60] “Le Nickel - SLN Ferronickel Slag - FNS: a promising construction material for the Pacific Region,” SLN [Online]. Available: https://sln.eramet.com/. [Accessed: 12-Apr-2022].

[61] Agnihotri, A., and Ramana, P. V., 2022, “GGBS: Fly-Ash Evaluation and Mechanical Properties within High Strength Concrete,” Materials Today: Proceedings, **50**, pp. 2404–2410.

[62] Long, W.-J., Peng, J., Gu, Y., Li, J., Dong, B., Xing, F., and Fang, Y., 2021, “Recycled Use of Municipal Solid Waste Incinerator Fly Ash and Ferronickel Slag for Eco-Friendly Mortar through Geopolymer Technology,” Journal of Cleaner Production, **307**, p. 127281.

[63] Liu, Q., Chen, S., Lin, W., Qi, A., and Chen, Z., 2020, “Experimental Behaviors of Prefabricated Members Made of Ferronickel Slag Concrete,” Construction and Building Materials, **261**, p. 120519.

[64] Saha, A. K., and Sarker, P. K., 2016, “Expansion Due to Alkali-Silica Reaction of Ferronickel Slag Fine Aggregate in OPC and Blended Cement Mortars,” Construction and Building Materials, **123**, pp. 135–142.

[65] Saha, A. K., and Sarker, P. K., 2017, “Compressive Strength of Mortar Containing Ferronickel Slag as Replacement of Natural Sand,” Procedia Engineering, **171**, pp. 689–694.

[66] Nguyen, Q. D., Khan, M. S. H., Castel, A., and Kim, T., 2019, “Durability and Microstructure Properties of Low-Carbon Concrete Incorporating Ferronickel Slag Sand and Fly Ash,” J. Mater. Civ. Eng., **31**(8), p. 04019152.

[67] Saha, A. K., and Sarker, P. K., 2020, “Mitigation of the Potential Alkali–Silica Reaction of FNS Using Ground FNS as a Supplementary Binder,” Advances in Cement Research.

[68] Saha, A. K., and Sarker, P. K., 2018, “Durability of Mortar Incorporating Ferronickel Slag Aggregate and Supplementary Cementitious Materials Subjected to Wet–Dry Cycles,” Int J Concr Struct Mater, **12**(1), p. 29.

[69] Wang, G., Thompson, R. G., and Wang, Y., 2011, “Hot-Mix Asphalt That Contains Nickel Slag Aggregate: Laboratory Evaluation of Use in Highway Construction,” Transportation Research Record, **2208**(1), pp. 1–8.

[70] Xu, Z., Gao, J., Zhao, Y., Li, S., Guo, Z., Luo, X., and Chen, G., 2022, “Promoting Utilization Rate of Ground Granulated Blast Furnace Slag (GGBS): Incorporation of Nanosilica to Improve the Properties of Blended Cement Containing High Volume GGBS,” Journal of Cleaner Production, **332**, p. 130096.

[71] Balamuralikrishnan, R., and Saravanan, J., 2021, “Effect of Addition of Alccofine on the Compressive Strength of Cement Mortar Cubes,” Emerging Science Journal, **5**(2), pp. 155–170.

[72] Saha, A. K., Khan, M. N. N., and Sarker, P. K., 2018, “Value Added Utilization of By-Product Electric Furnace Ferronickel Slag as Construction Materials: A Review,” Resources, Conservation and Recycling, **134**, pp. 10–24.

[73] Saha, A. K., and Sarker, P. K., 2018, “Durability Characteristics of Concrete Using Ferronickel Slag Fine Aggregate and Fly Ash,” Magazine of Concrete Research, **70**(17), pp. 865–874.

[74] Saha, A. K., and Sarker, P. K., 2020, “Effect of Sulphate Exposure on Mortar Consisting of Ferronickel Slag Aggregate and Supplementary Cementitious Materials,” Journal of Building Engineering, **28**, p. 101012.

[75] Du, C., 2005, “A Review of Magnesium Oxide in Concrete,” **27**(12), pp. 45–50.

[76] Yu, J., Lu, C., Leung, C. K. Y., and Li, G., 2017, “Mechanical Properties of Green Structural Concrete with Ultrahigh-Volume Fly Ash,” Construction and Building Materials, **147**, pp. 510–518.

[77] Rashad, A. M., 2015, “A Brief on High-Volume Class F Fly Ash as Cement Replacement – A Guide for Civil Engineer,” International Journal of Sustainable Built Environment, **4**(2), pp. 278–306.

[78] Bentz, D., Peltz, M., Durán-Herrera, A., Valdez, P., and Juárez, C., 2011, “Thermal Properties of High-Volume Fly Ash Mortars and Concretes,” Journal of Building Physics, **34**(3), pp. 263–275.

[79] Durán-Herrera, A., Juárez, C. A., Valdez, P., and Bentz, D. P., 2011, “Evaluation of Sustainable High-Volume Fly Ash Concretes,” Cement and Concrete Composites, **33**(1), pp. 39–45.

[80] Tang, S. W., Cai, X. H., He, Z., Shao, H. Y., Li, Z. J., and Chen, E., 2016, “Hydration Process of Fly Ash Blended Cement Pastes by Impedance Measurement,” Construction and Building Materials, **113**, pp. 939–950.

[81] Yang, E.-H., Yang, Y., and Li, V. C., 2007, “Use of High Volumes of Fly Ash to Improve ECC Mechanical Properties and Material Greenness,” MJ, **104**(6), pp. 620–628.

[82] Lam, L., Wong, Y. L., and Poon, C. S., 2000, “Degree of Hydration and Gel/Space Ratio of High-Volume Fly Ash/Cement Systems,” Cement and Concrete Research, **30**(5), pp. 747–756.

[83] Berry, E. E., Hemmings, R. T., and Cornelius, B. J., 1990, “Mechanisms of Hydration Reactions in High Volume Fly Ash Pastes and Mortars,” Cement and Concrete Composites, **12**(4), pp. 253–261.

[84] Escalante-Garcia, J.-I., and Sharp, J. H., 2004, “The Chemical Composition and Microstructure of Hydration Products in Blended Cements,” Cement and Concrete Composites, **26**(8), pp. 967–976.

[85] Lothenbach, B., Scrivener, K., and Hooton, R. D., 2011, “Supplementary Cementitious Materials,” Cement and Concrete Research, **41**(12), pp. 1244–1256.

[86] Ahmaruzzaman, M., 2010, “A Review on the Utilization of Fly Ash,” Progress in Energy and Combustion Science, **36**(3), pp. 327–363.

[87] Bakharev, T., 2005, “Geopolymeric Materials Prepared Using Class F Fly Ash and Elevated Temperature Curing,” Cement and Concrete Research, **35**(6), pp. 1224–1232.

[88] 2019, “Chiffres Clés de La Filière Pêche et Aquaculture En France” [Online]. Available: https://www.franceagrimer.fr/Actualite/Filieres/Peche-et-aquaculture/2019/Chiffres-cles-de-la-filiere-peche-et-aquaculture-en-France-en-2019. [Accessed: 08-Oct-2021].

[89] Tayeh, B. A., Hasaniyah, M. W., Zeyad, A. M., and Yusuf, M. O., 2019, “Properties of Concrete Containing Recycled Seashells as Cement Partial Replacement: A Review,” Journal of Cleaner Production, **237**, p. 117723.

[90] Bouasria, M., Khadraoui, F., Benzaama, M.-H., Touati, K., Chateigner, D., Gascoin, S., Pralong, V., Orberger, B., Babouri, L., and El Mendili, Y., 2021, “Partial Substitution of Cement by the Association of Ferronickel Slags and Crepidula Fornicata Shells,” Journal of Building Engineering, **33**, p. 101587.

[91] Wang, J., Liu, E., and Li, L., 2019, “Characterization on the Recycling of Waste Seashells with Portland Cement towards Sustainable Cementitious Materials,” Journal of Cleaner Production, **220**, pp. 235–252.

[92] Jaquin, P., 2012, “12 - History of Earth Building Techniques,” Modern Earth Buildings, M.R. Hall, R. Lindsay, and M. Krayenhoff, eds., Woodhead Publishing, pp. 307–323.

[93] Hanelt, D., Wiencke, C., and Bischof, K., 2003, “Photosynthesis in Marine Macroalgae,” Photosynthesis in Algae, A.W.D. Larkum, S.E. Douglas, and J.A. Raven, eds., Springer Netherlands, Dordrecht, pp. 413–435.

[94] Lemesle, S., Mussio, I., Rusig, A.-M., Menet-Nédélec, F., and Claquin, P., 2015, “Impact of Seaweed Beachings on Dynamics of Δ15N Isotopic Signatures in Marine Macroalgae,” Marine Pollution Bulletin, **97**(1), pp. 241–254.

[95] Pereira, L., 2021, “Macroalgae,” Encyclopedia, **1**(1), pp. 177–188.

[96] Allinson, D., and Hall, M., 2010, “Hygrothermal Analysis of a Stabilised Rammed Earth Test Building in the UK,” Energy and Buildings, **42**(6), pp. 845–852.

[97] Lekshmi, M. s., Vishnudas, S., and Nair, D. G., 2017, “An Investigation on the Potential of Mud as Sustainable Building Material in the Context of Kerala,” International Journal of Energy Technology and Policy, **13**(1–2), pp. 107–122.

[98] Houben, H., and Guillaud, H., 1994, Earth Construction: A Comprehensive Guide, London : Intermediate Technology Publications.

[99] Olivier, M., and Mesbah, A., 2016, “Introduction à la construction en terre,” p. 7.

[100] “Adobe” [Online]. Available: https://www.approche-ecohabitat.org/images/Ecopole/Materiautheque/Construction/C5_Adobe_v2.pdf .

[101] Houben, H., and Guillaud, H., 2006, Traité de construction en terre, Parenthèses Editions.

[102] “Mur de Bauge” [Online]. Available: http://totem-terre-couleurs.fr/maconnerie-terre/mur-de-bauge.html. [Accessed: 21-May-2022].

[103] “Wattle & Daub,” Lowimpact.org [Online]. Available: https://www.lowimpact.org/topics/wattle-daub/. [Accessed: 21-May-2022].

[104] 2018, Guide Des Bonnes Pratiques de La Construction En Terre Crue_TORCHIS_2018.

[105] Lin, H., Zheng, S., Lourenço, S. D., and Jaquin, P., 2017, “Characterization of Coarse Soils Derived from Igneous Rocks for Rammed Earth,” Engineering geology, **228**, pp. 137–145.

[106] François, B., Palazon, L., and Gerard, P., 2017, “Structural Behaviour of Unstabilized Rammed Earth Constructions Submitted to Hygroscopic Conditions,” Construction and Building Materials, **155**, pp. 164–175.

[107] says, J. S., “Rammed Earth Construction,” MaterialDistrict [Online]. Available: https://materialdistrict.com/article/rammed-earth-construction/. [Accessed: 21-May-2022].

[108] Houben, H., Rigassi, V., and Gamier, P., 1996, Compressed Earth Blocks: Production Equipment, CDI CRATerre-EAG., CDI, Brussels, Belgium.

[109] Guide Des Bonnes Pratiques de La Construction En Terre Crue_TERRE_ALLEGEE_2018.

[110] Nicolas, “LES CLOISONS EN TERRE PAILLE,” Autoconstruction de notre maison Bois Paille Terre [Online]. Available: http://autoconstruction-bois-paille-terre.fr/2020/08/les-cloisons-en-terre-paille.html. [Accessed: 29-May-2022].

[111] Gomes, M. I., Faria, P., and Gonçalves, T. D., 2018, “Earth-Based Mortars for Repair and Protection of Rammed Earth Walls. Stabilization with Mineral Binders and Fibers,” Journal of Cleaner Production, **172**, pp. 2401–2414.

[112] Laborel-Préneron, A., Aubert, J. E., Magniont, C., Tribout, C., and Bertron, A., 2016, “Plant Aggregates and Fibers in Earth Construction Materials: A Review,” Construction and Building Materials, **111**, pp. 719–734.

[113] Heath, A., Walker, P., Fourie, C., and Lawrence, M., 2009, “Compressive Strength of Extuded Unfired Clay Masonry Units,” Proceedings of The Ice - Construction Materials, **162**, pp. 105–112.

[114] Hall, M., and Djerbib, Y., 2004, “Rammed Earth Sample Production: Context, Recommendations and Consistency,” Construction and Building Materials, **18**(4), pp. 281–286.

[115] Kouakou, C., and Morel, J.-C., 2009, “Strength and Elasto-Plastic Properties of Non-Industrial Building Materials Manufactured with Clay as a Natural Binder,” Applied Clay Science, **44**, pp. 27–34.

[116] Maniatidis, V., Walker, P., Heath, A., and Hayward, S., 2007, “Mechanical and Thermal Characteristics of Rammed Earth,” Bangalore, India, pp. 205–211.

[117] Pkla, A., Mesbah, A., Rigassi, V., and Morel, J.-C., 2003, “Comparaison de méthodes d’essais de mesures des caractéristiques mécaniques des mortiers de terre,” Materials and Structures, **36**, pp. 108–117.

[118] Vega, P., Juan, A., Guerra, M. I., Morán, J. M., Aguado, P. J., and Llamas, B., 2011, “Mechanical Characterisation of Traditional Adobes from the North of Spain,” Construction and Building Materials, **7**(25), pp. 3020–3023.

[119] Laborel-Préneron, A., Magniont, C., and Aubert, J.-E., 2018, “Hygrothermal Properties of Unfired Earth Bricks: Effect of Barley Straw, Hemp Shiv and Corn Cob Addition,” Energy and Buildings, **178**, pp. 265–278.

[120] Gu, K., and Chen, B., 2020, “Loess Stabilization Using Cement, Waste Phosphogypsum, Fly Ash and Quicklime for Self-Compacting Rammed Earth Construction,” Construction and Building Materials, **231**, p. 117195.

[121] Goodhew, S., Boutouil, M., Streiff, F., Le Guern, M., Carfrae, J., and Fox, M., 2021, “Improving the Thermal Performance of Earthen Walls to Satisfy Current Building Regulations,” Energy and Buildings, **240**, p. 110873.

[122] Colinart, T., Vinceslas, T., Lenormand, H., Menibus, A. H. D., Hamard, E., and Lecompte, T., 2020, “Hygrothermal Properties of Light-Earth Building Materials,” Journal of Building Engineering, **29**, p. 101134.

[123] Laurent, J.-P., 1987, “Propriétés Thermiques Du Matériau Terre,” Cahiers du CSTB, **Cahier 2156**, p. 17 pages.

[124] Laurent, J.-P., Quenard, D., and Sallée, H., 1984, “Caractérisation Thermique Du Matériau Terre.,” Actes de Colloques, pp. 67–88.

[125] Goodhew, S., Griffiths, R., Short, D., and Watson, L., 2000, “Some Preliminary Studies of the Thermal Properties of Devon Cob Walls,” Terra 2000, 8th Inter Conf on the study and conservation of earthen architecture, pp. 139–143.

[126] Bui, Q.-B., and Morel, J.-C., 2009, “Assessing the Anisotropy of Rammed Earth,” Construction and Building Materials, **23**(9), pp. 3005–3011.

[127] Ávila, F., Puertas, E., and Gallego, R., 2021, “Characterization of the Mechanical and Physical Properties of Unstabilized Rammed Earth: A Review,” Construction and Building Materials, **270**, p. 121435.

[128] El Azhary, K., Raefat, S., Laaroussi, N., and Garoum, M., 2018, “Energy Performance and Thermal Proprieties of Three Types of Unfired Clay Bricks,” pp. 495–502.

[129] El Fgaier, F., Lafhaj, Z., Antczak, E., and Chapiseau, C., 2016, “Dynamic Thermal Performance of Three Types of Unfired Earth Bricks,” Applied Thermal Engineering, **93**, pp. 377–383.

[130] Röhlen, U., and Ziegert, C., Construire en terre crue : construction, rénovation, finitions.

[131] Labat, M., Magniont, C., Oudhof, N., and Aubert, J.-E., 2016, “From the Experimental Characterization of the Hygrothermal Properties of Straw-Clay Mixtures to the Numerical Assessment of Their Buffering Potential,” Building and Environment, **97**, pp. 69–81.

[132] Laurent, J.-P., 1986, “Contribution à La Caractérisation Thermique Des Milieux Poreux Granulaires : Optimisation d’outils de Mesure « in-Situ » Des Paramètres

Thermiques, Application à l'étude Des Propriétés Thermiques Du Matériau Terre," thesis.

[133] Bourgès, A., 2003, Study on the Physical-Mechanical Properties on Artificial Adobe and Determination of the Water Influence.

[134] Hansen, E. J. de P., and Hansen, K. K., 2002, "Unfired Clay Bricks – Moisture Properties and Compressive Strength: 6th Symposium on Building Physics in Nordic Countries," Proceedings of the 6th Symposium on Building Physics in the Nordic Countries, Skipnes AS, Trondheim, Norway, pp. 453–460.

[135] 2020, "NF EN 1745. Masonry and Masonry Products - Methods for Determining Thermal Properties."

[136] Collet, F., 2004, "CARACTERISATION HYDRIQUE ET THERMIQUE DE MATERIAUX DE GENIE CIVIL A FAIBLES IMPACTS ENVIRONNEMENTAUX," thesis, INSA Rennes.

[137] Alassaad, F., Touati, K., Levacher, D., and Sebaibi, N., 2021, "Impact of Phase Change Materials on Lightened Earth Hygroscopic, Thermal and Mechanical Properties," Journal of Building Engineering, **41**, p. 102417.

[138] Niang, I., Maalouf, C., Moussa, T., Bliard, C., Samin, E., Thomachot-Schneider, C., Lachi, M., Pron, H., Mai, T. H., and Gaye, S., 2018, "Hygrothermal Performance of Various Typha–Clay Composite," Journal of Building Physics, **42**(3), pp. 316–335.

[139] Bahar, R., Benazzoug, M., and Kenai, S., 2004, "Performance of Compacted Cement-Stabilised Soil," Cement and Concrete Composites, **26**(7), pp. 811–820.

[140] Azeredo, G., Morel, J.-C., and Barbosa, N. P., 2007, "COMPRESSIVE STRENGTH TESTING OF EARTH MORTARS," Journal of Urban and Environmental Engineering, **1**(1), pp. 26–35.

[141] Jaquin, P., Augarde, C., Gallipoli, D., and Toll, D., 2009, "The Strength of Unstabilised Rammed Earth Materials," Géotechnique, **59**, pp. 487–490.

[142] Maniatidis, V., and Walker, P., 2008, "Structural Capacity of Rammed Earth in Compression," Journal of Materials in Civil Engineering, **20**(3), pp. 230–238.

[143] Abanto, G. A., Karkri, M., Lefebvre, G., Horn, M., Solis, J. L., and Gómez, M. M., 2017, "Thermal Properties of Adobe Employed in Peruvian Rural Areas: Experimental Results and Numerical Simulation of a Traditional Bio-Composite Material," Case Studies in Construction Materials, **6**, pp. 177–191.

[144] Goodhew, S., and Griffiths, R., 2004, "Analysis of Thermal-Probe Measurements Using an Iterative Method to Give Sample Conductivity and Diffusivity Data," Applied Energy, **77**(2), pp. 205–223.

[145] Goodhew, S., and Griffiths, R., 2005, "Sustainable Earth Walls to Meet the Building Regulations," Energy and Buildings, **37**, pp. 451–459.

[146] Medjelekh, D., Ulmet, L., and Dubois, F., 2017, "Characterization of Hygrothermal Transfers in the Unfired Earth," Energy Procedia, **139**, pp. 487–492.

[147] Brouard, Y., Belayachi, N., Hoxha, D., Ranganathan, N., and Méo, S., 2018, "Mechanical and Hygrothermal Behavior of Clay – Sunflower (Helianthus Annuus) and Rape Straw (Brassica Napus) Plaster Bio-Composites for Building Insulation," Construction and Building Materials, **161**, pp. 196–207.

[148] “Traité de construction en terre,” Editions Parenthèses [Online]. Available: https://www.editionsparentheses.com/traite-de-construction-en-terre. [Accessed: 26-Apr-2022].

[149] Medvey, B., and Dobszay, G., 2020, “Durability of Stabilized Earthen Constructions: A Review,” Geotech Geol Eng, **38**(3), pp. 2403–2425.

[150] Heathcote, K. A., “An Investigation into the Erodibility of Earth Wall Units,” p. 272.

[151] Brax, M., Buchmann, C., and Schaumann, G. E., 2017, “Biohydrogel Induced Soil–Water Interactions: How to Untangle the Gel Effect? A Review,” Journal of Plant Nutrition and Soil Science, **180**(2), pp. 121–141.

[152] Chang, I., Prasidhi, A. K., Im, J., and Cho, G.-C., 2015, “Soil Strengthening Using Thermo-Gelation Biopolymers,” Construction and Building Materials, **77**, pp. 430–438.

[153] Quero, J.-C., Du Buit, M. H., Fonteneau, J., Labastie, J., Laborde, J.-L., Morandeau, G., and Vayne, J.-J., 1992, “Observations ichtyologiques effectuées en 1991,” Annales de la Société des Sciences Naturelles de la Charente-Maritime, **8**(1), pp. 51–57.

[154] Srinivasan, R., 2013, “CHAPTER 4:Natural Polysaccharides as Treatment Agents for Wastewater,” Green Materials for Sustainable Water Remediation and Treatment, pp. 51–81.

[155] Andersen, T., Strand, B. L., Formo, K., Alsberg, E., and Christensen, B. E., 2011, “Chapter 9:Alginates as Biomaterials in Tissue Engineering,” Carbohydrate Chemistry, pp. 227–258.

[156] “Chimie Du Bois - - Tatjana Stevanovic, Dominique Perrin (EAN13 : 9782880747992),” EPFL Press [Online]. Available: https://www.epflpress.org/produit/448/9782880747992/chimie-du-bois. [Accessed: 29-Apr-2022].

[157] Vissac, A., Bourgès, A., Gandreau, D., Anger, R., and Fontaine, L., 2017, Argiles & Biopolymères - Les Stabilisants Naturels Pour La Construction En Terre.

[158] Laetitia Fontaine and Romain Anger, 2013, Projet PaTerre+. Interactions argiles/biopolymères: patrimoine architectural en terre et stabilisants naturels d’origine animale et végétale. Rapport final.

[159] Kolypczuk, L., 2010, Chitine et Chitosan.

[160] Pien, S., Brebion, J., Jacquette, J. M., Rusig, A.-M., Lefebvre, V., Dehail, M., Mussio, I., and Maine, L., 2016, Etude de l’algue Invasive Sargassum Muticum En Vue d’une Exploitation et d’une Valorisation En Normandie. Normandi.

[161] Danso, H., Martinson, D. B., Ali, M., and Williams, J. B., 2015, “Physical, Mechanical and Durability Properties of Soil Building Blocks Reinforced with Natural Fibres,” Construction and Building Materials, **101**, pp. 797–809.

[162] Millogo, Y., Morel, J.-C., Aubert, J.-E., and Ghavami, K., 2014, “Experimental Analysis of Pressed Adobe Blocks Reinforced with Hibiscus Cannabinus Fibers,” Construction and Building Materials, **52**, pp. 71–78.

[163] Latifi, N., Horpibulsuk, S., Meehan, C. L., Abd Majid, M. Z., Tahir, M. M., and Mohamad, E. T., 2017, “Improvement of Problematic Soils with Biopolymer—An Environmentally Friendly Soil Stabilizer,” Journal of Materials in Civil Engineering, **29**(2), p. 04016204.

[164] Millogo, Y., Aubert, J.-E., Séré, A. D., Fabbri, A., and Morel, J.-C., 2016, “Earth Blocks Stabilized by Cow-Dung,” Mater Struct, **49**(11), pp. 4583–4594.

[165] Achenza, M., and Fenu, L., 2006, “On Earth Stabilization with Natural Polymers for Earth Masonry Construction,” Mater Struct, **39**(1), pp. 21–27.

[166] Danso, H., Martinson, B., Ali, M., and Mant, C., 2015, “Performance Characteristics of Enhanced Soil Blocks: A Quantitative Review,” Building Research & Information, **43**(2), pp. 253–262.

[167] Aubert, J. E., Maillard, P., Morel, J. C., and Al Rafii, M., 2016, “Towards a Simple Compressive Strength Test for Earth Bricks?,” Mater Struct, **49**(5), pp. 1641–1654.

[168] Morel, J.-C., Pkla, A., and Walker, P., 2007, “Compressive Strength Testing of Compressed Earth Blocks,” Construction and Building Materials, **21**(2), pp. 303–309.

[169] Alam, I., Naseer, A., and Shah, A. A., 2015, “Economical Stabilization of Clay for Earth Buildings Construction in Rainy and Flood Prone Areas,” Construction and Building Materials, **77**, pp. 154–159.

[170] Omar Sore, S., Messan, A., Prud’homme, E., Escadeillas, G., and Tsobnang, F., 2018, “Stabilization of Compressed Earth Blocks (CEBs) by Geopolymer Binder Based on Local Materials from Burkina Faso,” Construction and Building Materials, **165**, pp. 333–345.

[171] Tran, K. Q., Satomi, T., and Takahashi, H., 2018, “Improvement of Mechanical Behavior of Cemented Soil Reinforced with Waste Cornsilk Fibers,” Construction and Building Materials, **178**, pp. 204–210.

[172] Dao, K., Ouedraogo, M., Millogo, Y., Aubert, J.-E., and Gomina, M., 2018, “Thermal, Hydric and Mechanical Behaviours of Adobes Stabilized with Cement,” Construction and Building Materials, **158**, pp. 84–96.

[173] Raavi, S. S. D., and Tripura, D. D., 2020, “Predicting and Evaluating the Engineering Properties of Unstabilized and Cement Stabilized Fibre Reinforced Rammed Earth Blocks,” Construction and Building Materials, **262**, p. 120845.

[174] Ouellet-Plamondon, C. M., and Habert, G., 2016, “Self-Compacted Clay Based Concrete (SCCC): Proof-of-Concept,” Journal of Cleaner Production, **117**, pp. 160–168.

[175] Alavéz-Ramírez, R., Montes-García, P., Martínez-Reyes, J., Altamirano-Juárez, D. C., and Gochi-Ponce, Y., 2012, “The Use of Sugarcane Bagasse Ash and Lime to Improve the Durability and Mechanical Properties of Compacted Soil Blocks,” Construction and Building Materials, **34**, pp. 296–305.

[176] Millogo, Y., Hajjaji, M., and Ouedraogo, R., 2008, “Microstructure and Physical Properties of Lime-Clayey Adobe Bricks,” Construction and Building Materials, **22**(12), pp. 2386–2392.

[177] Ciancio, D., Beckett, C. T. S., and Carraro, J. A. H., 2014, “Optimum Lime Content Identification for Lime-Stabilised Rammed Earth,” Construction and Building Materials, **53**, pp. 59–65.

[178] Hossain, K. M. A., and Mol, L., 2011, “Some Engineering Properties of Stabilized Clayey Soils Incorporating Natural Pozzolans and Industrial Wastes,” Construction and Building Materials, **25**(8), pp. 3495–3501.

[179] Degirmenci, N., 2008, “The Using of Waste Phosphogypsum and Natural Gypsum in Adobe Stabilization,” Construction and Building Materials, **22**(6), pp. 1220–1224.

[180] Siddiqua, S., and Barreto, P. N. M., 2018, “Chemical Stabilization of Rammed Earth Using Calcium Carbide Residue and Fly Ash,” Construction and Building Materials, **169**, pp. 364–371.

[181] Matos, A. M., and Varum, H., 2022, “Self-Compacting Earth-Based Composites: Mixture Design and Multi-Performance Characterisation,” Buildings, **12**(5), p. 612.

[182] Van Damme, H., and Houben, H., 2018, “Earth Concrete. Stabilization Revisited,” Cement and Concrete Research, **114**, pp. 90–102.

[183] Galán-Marín, C., Rivera-Gómez, C., and Petric, J., 2010, “Clay-Based Composite Stabilized with Natural Polymer and Fibre,” Construction and Building Materials, **24**(8), pp. 1462–1468.

[184] Camões, A., Eires, R., and Jalali, S., 2012, “Old Materials and Techniques to Improve the Durability of Earth Buildings,” International Council on Monuments and Sites (ICOMOS). International Committee on Vernacular Architecture (CIAV).

[185] Nakamatsu, J., Kim, S., Ayarza, J., Ramírez, E., Elgegren, M., and Aguilar, R., 2017, “Eco-Friendly Modification of Earthen Construction with Carrageenan: Water Durability and Mechanical Assessment,” Construction and Building Materials, **139**, pp. 193–202.

[186] Chang, I., Im, J., Prasidhi, A. K., and Cho, G.-C., 2015, “Effects of Xanthan Gum Biopolymer on Soil Strengthening,” Construction and Building Materials, **74**, pp. 65–72.

[187] Muguda, S., Booth, S. J., Hughes, P. N., Augarde, C. E., Perlot, C., Bruno, A. W., and Gallipoli, D., 2017, “Mechanical Properties of Biopolymer-Stabilised Soil-Based Construction Materials,” Géotechnique Letters, **7**(4), pp. 309–314.

[188] Alhaik, G., Ferreira, M., Dubois, V., Wirquin, E., Tilloy, S., Monflier, E., and Aouad, G., 2017, “Enhance the Rheological and Mechanical Properties of Clayey Materials by Adding Starches,” Construction and Building Materials, **139**, pp. 602–610.

[189] Pinel, A., Jorand, Y., Olagnon, C., Charlot, A., and Fleury, E., 2017, “Towards Poured Earth Construction Mimicking Cement Solidification: Demonstration of Feasibility via a Biosourced Polymer,” Mater Struct, **50**(5), p. 224.

[190] Aguilar, R., Nakamatsu, J., Ramírez, E., Elgegren, M., Ayarza, J., Kim, S., Pando, M. A., and Ortega-San-Martin, L., 2016, “The Potential Use of Chitosan as a Biopolymer Additive for Enhanced Mechanical Properties and Water Resistance of Earthen Construction,” Construction and Building Materials, **114**, pp. 625–637.

[191] Liuzzi, S., Hall, M. R., Stefanizzi, P., and Casey, S. P., 2013, “Hygrothermal Behaviour and Relative Humidity Buffering of Unfired and Hydrated Lime-Stabilised Clay Composites in a Mediterranean Climate,” Building and Environment, **61**, pp. 82–92.

[192] Saidi, M., Cherif, A. S., Zeghmati, B., and Sediki, E., 2018, “Stabilization Effects on the Thermal Conductivity and Sorption Behavior of Earth Bricks,” Construction and Building Materials, **167**, pp. 566–577.

[193] Randazzo, L., Montana, G., Hein, A., Castiglia, A., Rodonò, G., and Donato, D. I., 2016, “Moisture Absorption, Thermal Conductivity and Noise Mitigation of Clay

Based Plasters: The Influence of Mineralogical and Textural Characteristics," Applied Clay Science, **132–133**, pp. 498–507.

[194] Santos, T., Nunes, L., and Faria, P., 2017, "Production of Eco-Efficient Earth-Based Plasters: Influence of Composition on Physical Performance and Bio-Susceptibility," Journal of Cleaner Production, **167**, pp. 55–67.

[195] Laborel-Préneron, A., Aubert, J.-E., Magniont, C., and Bertron, A., 2015, Influence of Straw Content on the Mechanical and Thermal Properties of Bio-Based Earth Composites.

[196] Ashour, T., Korjenic, A., Korjenic, S., and Wu, W., 2015, "Thermal Conductivity of Unfired Earth Bricks Reinforced by Agricultural Wastes with Cement and Gypsum," Energy and Buildings, **104**, pp. 139–146.

Chapter 2. New Binders as substitution of cement

2.1 Preface

The building material that is produced in the greatest volume worldwide is concrete. Due to its significant relevance in the current sustainability evaluation, it is evident that the manufacture of the cement required for its fabrication is held responsible for about 7% of the global CO_2 emissions. This truth, however, is nothing new: perceptions of the concerns of resource preservation, climate change, and sustainability are currently strongly influenced by social and political factors. Additionally, the importance of concrete building and, by extension, the concrete block sector, should not be overlooked in this context.

Aside from the development and use of progressively clinker-efficient cements, there is great potential for advanced binders such as carbosilicate, calcium hydrosilicate binders and geopolymers. Most of these binders have been used for a long time and are regaining attention in research and practice due to their minimal environmental impact, particularly the potential for CO_2-capture. However, in some circumstances, their reliability in terms of performance and durability still has to be validated.

This chapter highlights the advantages and disadvantages of using novel binders originating from industrial by-products in conjunction with the construction of low carbon concrete in the future.

In this chapter we investigated two types of low carbon concretes based on: (i) the association of ferronickel slag and seashells as cement replacement and (ii) the association of fly ash and seashells as cement replacement. The effect of cement replacement on the mechanical and hygrothermal properties of concretes was also explored.

Part I : The potential of Ferronickel slags and Crepidula shell as substitution of Portland Cement

Abstract

Reduced cement content in cementitious composites, particularly when Portland cement is partially replaced by wastes, can reduce the environmental impact of construction materials. In this study, cement is replaced with ferronickel slags (FNS) and shell by-products while maintaining interesting characteristic. FNS with *Crepidula fornicata* shells (CR) are excellent candidates for substituting a portion of Portland cement since they have interesting physical and chemical properties and are widely available.

The impact of incorporating FNS and CR on mortar mechanical properties is investig ated in this study. X-Ray diffraction, Scanning Electron Microscopy, and Micro-Raman spectroscopy are used to characterize the microstructures of these additives. Mortars are made up of various combinations of FNS-CR and Portland cement. Fresh mortar surface area, workability, and setting times are examined. For curing time ranging from 2 to 28 days, mechanical properties are investigated using 3-point bending and compressive tests. In the fresh state, replacing cement with FNS-CR by up to 20% wt.% has no impact on mortar properties. FNS-CR addition lead to an increase of the setting times in the hardened state. Mechanical properties remain similar or even slightly larger than those of the standard mortar with up to 20 wt% of FNS-CR incorporation.

2.2 Introduction

As the most commonly used material in the world, cement production significantly increases CO_2 emissions [1]. The global demand for construction materials is about 4.65 billion tons per year, producing about 4 billion tons of CO_2 [2]. This can add up to 7% to the overall anthropogenic footprint [3]. The CO_2 footprint will be greatly reduced by the increased use of alternative cementetious material in the cement manufacturing process. As a result, the development of new supplementary cementitious materials (SCM) has generated more questions than answers.

A potential alternative is the recycling of waste, specifically waste from industrial byproducts, as additives [4]. Slag, a byproduct of the pyrometallurgical processes used to produce ferro-nickel, is one of these products [5–9]. Over 145 years, the Société Le Nickel (SLN, New Caledonia) has been producing nickel from laterites continuously [10,11]. With a stockpile of more than 25 million tons already in place, SLN generates around 1.6 million tons of FNS annually [12]. Only 8% of the annual FNS production is currently utilized [7]. To minimize the impact on the environment, the remaining FNS is stacked up on site with expansive storage costs [13,14]. These slags offer a useful resource for recycling. The FNS from SLN exhibit good properties such as high water permeability, excellent hardness and toughness, high density, high compaction potential, and huge fire resistance with moderate thermal expansion [12]. They are also free of hazardous compounds. As a result, this byproducts can be employed in construction [12]. Slag recycling creates additional value to cement's characteristics in the construction sector [15]. FNS will become an economic resource as a result of SLN. SLAND, a commercial product, is exported to Australia for use as SCM [12], while FNS is used as a base binder for road construction [16]. However, if their physicochemical properties are suitable, FNS can be used as cementitious binder [17,18].

Seashells are another abundant natural waste material that can be used as SCM. *Crepidula* shells (CR), oyster shells, and mussel shells, for example, are available in France. France is a major consumer of shellfish in Europe. In France, 191,800 tons of *Crepidula*, oyster or clam shells are disposed of in landfills, incinerators, or as litter in the environment each year [19]. This is an expensive endeavor.

In the late 1700s, seashells were historically incorporated into concrete to create a particular kind of building material called "Tabby." To construct tabby, a form of

concrete, oyster shells are burned to create lime, which is then combined with sand, ash, crushed oyster shells as aggregate, and water. Early Spanish explorers in the 16th century utilized Tabby in North Carolina and Florida. Around 1700, British colonists primarily employed Tabby in Georgia and South Carolina [20]. For 50 years, investigations on the use of seashells as SCM have shown that ground seashells can be used in mortars as aggregate or cement substitution [21,22]. In comparison to the control mortar, mortars that use seashells as partial replaement of cement can exhibit appropriate strength and reduced thermal conductivity. The calcium carbonate ($CaCO_3$) content of seashells is around 95%, which is comparable to the calcium carbonate content of the limestone used to manufacture Portland cement [23]. Calcium carbonate, or $CaCO_3$, which can be used as SCM, forms a major part of *Crepidula* shells. Portland cement may contain up to 35% of $CaCO_3$ or limestone, according to the standard EN 197-1 [24]. Due to its limited solubility, $CaCO_3$ powder mostly serves as an inert filler when the replacement level is more than 5%. The usage of carbonate powder in the cement industry is restricted by its inert nature and low reactivity [25]. The use of slags in mortar or concrete can enhance late-age strength but reduces early-age strength due to slow hydration and the need for alcaline activation. Attempts have been made to incorporate carbonate in ternary blended cements to enhance early strength. Various studies show that combining calcium carbonate originating from limestone and slag in concrete or mortar is advantageous. Indeed, the calcium carbonate binder improves early strength while the slag improves late strength, resulting in optimised strength development [26,27].

The association of *Crepidula fornicata* shells and ferronickel slag as a partial replacement in mortar is the main topic of this work. An experimental investigation of the soundness and compressive strength of mortars made with this combination is performed for that purpose. Multiple mortar mix with various substitution proportions of slags and CR shells are prepared and tested to failure.

2.3 Materials and Methods

2.3.1 Materials

2.3.1.1 Cement

The cement used in this investigation is a CEM I 52.5 N manufactured by Calcia according to the standard EN 197-1 [24]. The density of cement is 3.2 g.cm-3, and the Blaine fineness is 4100 $cm^2.g^{-1}$. The clinker ratio is 95%, and the mineralogical composition is as follows: C_3S = 74%, C_2S = 12%, C_3A = 11%, SO_3 = 2.7 %, S^{2-} < 0.02 %, and Na_2O = 0.06 % Table 2.1 shows the chemical composition of the cement.

Table 2.1 Chemical composition of CEM I 52.5 N cement as determined by Energy Dispersive X-Ray spectroscopy.

Component	SiO_2	CaO	Al_2O_3	Fe_2O_3	MgO	SO_3	K_2O	Na_2O	Loss on Ignition
wt.%	19.5	63.2	4.8	3.5	1.5	2.7	0.6	0.1	4.1

2.3.1.2 Sand

The sand used in this study is a French normalized sand manufactured by SOCIETE NOUVELLE DU LITTORAL according to the EN 196-1 standard [28]. It is derived from natural quartz sand (99% of silica). The sand grains are rounded and uncrushed.

2.3.1.3 Ferronickel slag

The Société le Nickel-ERAMET provided the ferronickel slags (SLN, New Caledonia). The granulated slag has approximately 4 mm-sized particles. Using high energy ball milling for 30 minutes, the raw FNS grains are reduced to powder (< 63 µm). The slag's Blaine fineness is 6700 $cm^2.g^{-1}$, and its specific gravity is 2.92 $g.cm^{-3}$.

2.3.1.4 *Crepidula fornicata* shells

The CR shells were collected from a fish corporation in Normandy (France), which are ground, and screened on site. The raw *Crepidula fornicata* shells grains are dried at 120°C and ground to powder (<63 µm) using high energy ball milling for 30 min. CR shells have a specific gravity of 2.73 $g.cm^{-3}$ and a Blaine fineness of 8140 $cm^2.g^{-1}$. On an industrial scale with vast volumes of shells, processes range from open air drying (direct, indirect, mixed, and hybrid solar dryers) to gas dryers. By replacing the use of fossil fuels or chemical fertilizers with a superior heat source from parallel processes like methanization, drying costs have been greatly reduced. This strategy offers fresh opportunities for development in this field.

2.3.1.5 Mortars design

According to EN 196-1 [28], all mortars elaborated have a water on cement ratio (W/C) of 0.5 and a sand to cement ratio of 3. The mortars were filled into prismatic moulds after they had been mixed (40 x 40 x 160 mm^3). After pouring each layer, the moulds were exposed to 60 hits on a vibrating table to expel the air. The moulds were then placed in a specially designed confined room with a temperature of 20 °C and a relative humidity of 90%. The mortar samples were demoulded 24h after fabrication and stored at controlled room temperature until testing. In this study, nine mortar mixtures were produced (Table 2.2). FNS has been used to replace cement at a rate of 0%, 10%, 15%, and 30% by weight. Furthermore, the cement has been replaced with a mixture containing equal proportions of FNS and CR in the ranges of 10%, 20%, 30%, 40%, and 60% by weight.

Table 2.2 Composition of the different mortar specimens

Sample	Mass substitution rate of cement by FNS (wt.%)	Mass substitution rate of cement by *Crepidula* (wt.%)
CM	0	0
FNS10	10	0
FNS15	15	0
FNS30	30	0
FNS5-CR5	5	5
FNS10-CR10	10	10
FNS15-CR15	15	15
FNS20-CR20	20	20
FNS30-CR30	30	30

2.3.2 Technical characterization

The elemental compositions were obtained using X-ray fluorescence (XRF) spectroscopy and Scanning Electron Microscope (SEM). XRF spectra were recorded using an Inel Equinox 3500 spectrometer (equipped with a Cu microfocus source, a multilayer parabolic mirror in the primary beam and an Amptek X123SDD silicon). Drift detectors were placed vertically 10 mm above the sample to ensure high sensitivity even for low atomic number elements). Data were collected with an integration time of 400 s.

A scanning electron microscope (SEM; SUPRA ™ 55 SAPPHIRE; Carl Zeiss, Jena, Germany) with an energy dispersive spectrometer was used for imaging and elemental analysis (EDS). Prior to examinations at a voltage of 20 kV, the samples were carbon coated.

ICP-OES was used to analyse the major elements, whereas ICP-MS was used to evaluate the trace elements (As-Zr) (Analyses conducted in SARM/CRPG laboratory, Nancy).

X-Ray Diffraction : An incident beam Ge (111) monochromator on a D8 Advance Vario 1 Bruker instrument (2-circles diffractometer, -2 Bragg-Brentano mode) was used to collect the XRD diagram using copper radiation (λ = 1.54059). From 10° to 80°, the X-ray diffraction pattern of soil is acquired for 1sec at each 0.01° step (16 h/scan). The LaB6 standard powder (NIST SRM-660b) was used to calibrate for the instrumental contribution [29]. Quantification and crystalline phase identification were done with the Full-Pattern Search-Match (FPSM) technique and the Crystallography Open Database [30]. There are numerous stages to refine the diffraction patterns of the samples analysed. Knowledge of the chemical composition is required in order to assign all phases of such a pattern. As a result, elemental studies using XRF and EDS were carried out. After the initial chemical analysis, the average crystallite sizes for each phase were estimated using the online Full Profile Search Match fitting process (http://nanoair.dii.unitn.it:8080/sfpm/). Crystal structure information can be found in the Crystallography Open Database (COD). The automatic identification of crystal phases as a first list is the basis of these quantifications. Micro-Raman is then used to generate a more comprehensive list of probable phase candidates due to its much higher sensitivity at the micron scale. Finally, the Rietveld quantification was done with the MAUD software [31].

A Thermo Scientific Raman microscope (Thermo Fisher Scientific DXR) with a green laser (532 nm) as an excitation source with a 900 lines/mm diffraction grating. In a backscattering geometry and at room temperature, we used a 50X long-distance objective to focused the laser beam onto the surface. The data were obtained over a 50-2200 cm-1 range. In order to assess the OH and the H_2O stretching mode region and the C-S-H species and ettringite, the spectral ranges from 3200 to 4000 cm^1. The laser's spot diameter was calculated to be 0.8 µm, with a spectral resolution of 3 cm^{-1}. Raman spectra were acquired twice with a low laser power (2 mW) and a 120-s integration time. As basic fitting functions, we employed the Origin software and Gaussian curves. By comparing the obtained Raman spectra to those in the Raman Open Database ROD [32], the mineral compositions were established.

The thermal conductivity was measured using a NETZSCH Heat Flow Meter device (Model HFM 436 Lambda). The samples have prismatic dimensions of 30x30x7 cm^3 and are positioned between the cooling plate and the heater plate; heat passes from the heater plate through the sample to the cooling plate, where it is transported away. A Peltier cryostat adjusts the cooling and heater plate temperatures to create a temperature gradient of 10 ÷ 40°C from the heater plate across the specimen.

2.3.3 Test methods

2.3.3.1 Specific surface area

Using the Blaine air permeability apparatus and the ASTM C-204 test procedure [33], the specific surface area of each cement mix elaborated in this investigation was measured.

2.3.3.2 Fresh properties of mortars

Workability tests were performed in accordance with the NF P18-452 standard [34]. The testing device consists of a removable wall that divides a compartment into two unequal volumes. The time it takes for the mortar to flow from the big compartment to the smaller one under the impact of the imposed vibration is measured in the test. All mortar mixtures' initial and final setting times were also measured. These tests involve measuring the time required for a plunger assembly weighing 1000 g to penetrate the material. According to the NF P 15-431 standard [35], when there is 2.5 mm between the plunger's end and the base plate, the initial setting time is applicable.

2.3.3.3 Mechanical properties of hardened mortars

According to EN 196-1 standard [28], compressive and three-point bending tests were used to determine the mechanical properties of the mortars on all specimens aged between 2 and 28 days. The 3-point bending and compression tests were carried out on specimens of 4x4x16 cm^3 concurrently at constant rates of 0.05 kN/sec and 2.4 kN/sec, respectively. For the 3-point bending, the specimen is loaded until it ruptures by being put on the press frame with 100 mm between the two supports. The equation 2-1 is used to calculate the flexural strength.

$$R_f = \frac{3.F_{fmax}.L}{2.b^3} \qquad \textbf{2-1}$$

$F_{f,max}$ [N] = Maximum bending load at rupture,

L [mm] = Distance between supports,

b [mm] = Side of the square section of the specimen.

After the flexural test, the two pieces of the splintered specimen underwent the compression test. The equation 2-2 used to calculate the compressive strength.

$$R_c = \frac{F_{c,max}}{A} \quad \textbf{2-2}$$

$F_{c,max}$ [N] = Maximum compressive load at rupture.

A [mm^2] = Area of the test specimen's cross-section

2.4 Results and discussion

2.4.1 Microstructural characterization of FNS

The FNS's chemical and mineralogical characteristics are significant elements that influences its recovery. The elemental analyses of FNS powder are shown in Table 2.3.

Table 2.3 Chemical composition of FNS as measured by ICP-MS and ICP-OES. d.l.: detection limit.

Oxide	(wt.%)	Element	µg/g	Element	µg/g	Element	µg/g	Element	µg/g
SiO_2	51.67	As	d.l	Hf	0.22	Ta	0.06	Nd	1.48
Al_2O_3	2.29	Ba	16.24	In	d.l	Th	0.44	Sm	0.34
Fe_2O_3 (FeO)	12.58 (11.3)	Be	0.24	Mo	2.15	U	0.16	Eu	0.08
MnO	0.46	Bi	d.l	Nb	0.38	V	65	Gd	0.36
MgO	31.56	Cd	d.l	Ni	665	W	d.l	Tb	0.06
CaO	0.31	Co	61	Pb	1.34	Y	3.31	Dy	0.41
Na_2O	0.50	Cr	7932	Rb	1.41	Zn	236	Ho	0.09
K_2O	0.03	Cs	0.17	Sb	0.22	Zr	8.37	Er	0.27
TiO_2	0.04	Cu	9.19	Sc	24	La	1.53	Tm	0.05
P_2O_5	d.l	Ga	0.63	Sn	0.45	Ce	2.49	Yb	0.29
Total	99.44	Ge	0.16	Sr	13	Pr	0.37	Lu	0.05

The FNS slag sample contains approximately 52 wt.% of SiO_2, 32 wt.% of MgO, and 12.6 wt.% of Fe_2O_3. The significant proportion of the iron is divalent iron (FeO: 11.3 wt.%). Minor elements include 2.3 wt. % of Al_2O_3, approximately 0.5 wt.% of Na_2O and MnO, 0.3 wt. of % CaO, and 0.4 wt. % of total water. CO_2 levels are low (0.16 wt.%). Other minor elements such as K_2O and TiO_2 are present at very low porcentage 0.04 wt.%. The highest trace element values are approx 7900 ppm of Cr, 670 ppm of Ni,

260 ppm of Zn, 65 ppm of V, 61 ppm of Co, and 20 ppm of Sc. As, Cd, U, and Th values are reported to be relatively low (Table 2.3).

The FNS sample's XRD pattern can be reasonably refined using four main phases (Figure 2-1 and Table 2.4). Quantitative phase assessment using Rietveld refinement reveals that the two major phases are quartz and forsterite.

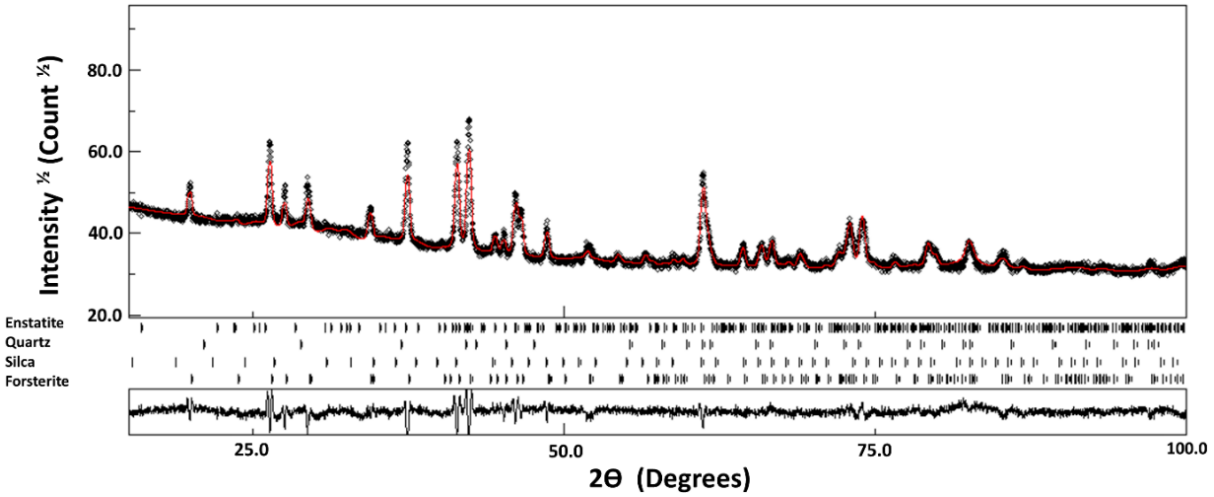

Figure 2-1 FNS X-ray diffraction pattern refined with MAUD software. The calculated pattern (red line) overlays the observed profile (black dots). At the bottom is the difference curve ($I_{obs} - I_{calc}$).

Table 2.4 Mineralogical composition of FNS with the refined lattice parameters, unit cell volume, average diameter, and microstrain <ε2>1/2 were all refined. On the last digit, one standard deviation is indicated by parenthesis.

Phases	COD reference	V (%)	Lattice type + Space group	Lattice parameters (Å)	⟨D⟩ (nm)	$\langle\varepsilon^2\rangle^{1/2}$
Forsterite Mg_2SiO_4	9000319	39.5 (4)	Orthorhombic Pbnm	a=4.751 (1) b=10.202 (1) c=5.968 (2)	834 (20)	$6\ 10^{-4}$
Enstatite Mg_2SiO_3	9014117	7.2 (2)	Orthorhombic Pbca	a=18,595 (1) b=8,797 (1) c=5,231 (1)	253 (15)	$1\ 10^{-3}$
SiO_2	1011097	11.6 (4)	Cubic P213	a=9,423 (1)	121 (10)	0
Quartz	9000594	41.7 (5)	Trigonal $P3_221$	a=5,641 (2) c=5,247 (2)	92 (4)	$1\ 10^{-4}$

Our fits below 2 (GoF = 1.76) are satisfactory, and it quantitatively ensure our experimental diagram with agreement factors Rwp = 3.9 % and RB = 2.5 %.

The XRD diagram of the FNS shows that quartz (41.7%), forsterite (39.5%), silica (11.6%), and enstatite (7.2%) are the main minerals. Regardless of the size of the particles, these phases were found in every batch of slag powder.

The Raman spectroscopy confirm that Forsterite $(Mg,Ni)_2SiO_4$, quartz (SiO_2), silica (SiO_2) and enstatite $(Mg,Fe)_2SiO_3$ are the primary constituents of FNS, with traces of chromite ($FeCr_2O_4$), calcite ($CaCO_3$), and akaganeite (β-$FeO_{1-2x}(OH)_{1+x}Cl_x$) (Figure 2-2 and Figure 2-3). During cooling and solidification, quartz is created in silica-rich scories. With a melting point of 1890 °C, forsterite exhibits great thermal stability [36,37]. Forsterite is reported to occured at low temperatures via the reaction of silica with MgO [36]. Forsterite reacts also with SiO_2 to create enstatite ($MgSiO_3$) when there is an excess of quartz and silica [38].

Figure 2-2(a) illustrates the Raman spectrum of the silica structure. With six Gaussians, refinement was possible (Table 2.5). The degree of silicate tetrahedra polymerization significantly describes the structure of the vitreous silicate network. It is defined by the abundance of different Qn species, where Q_n refers to a tetrahedron connected to n adjacent tetrahedra by bridging oxygen atoms (n from 0 to 4). Q_0 represents an isolated monomer, Q_1 and Q_2 represent chains, and Q_3 and Q_4 represent interconnected structures.

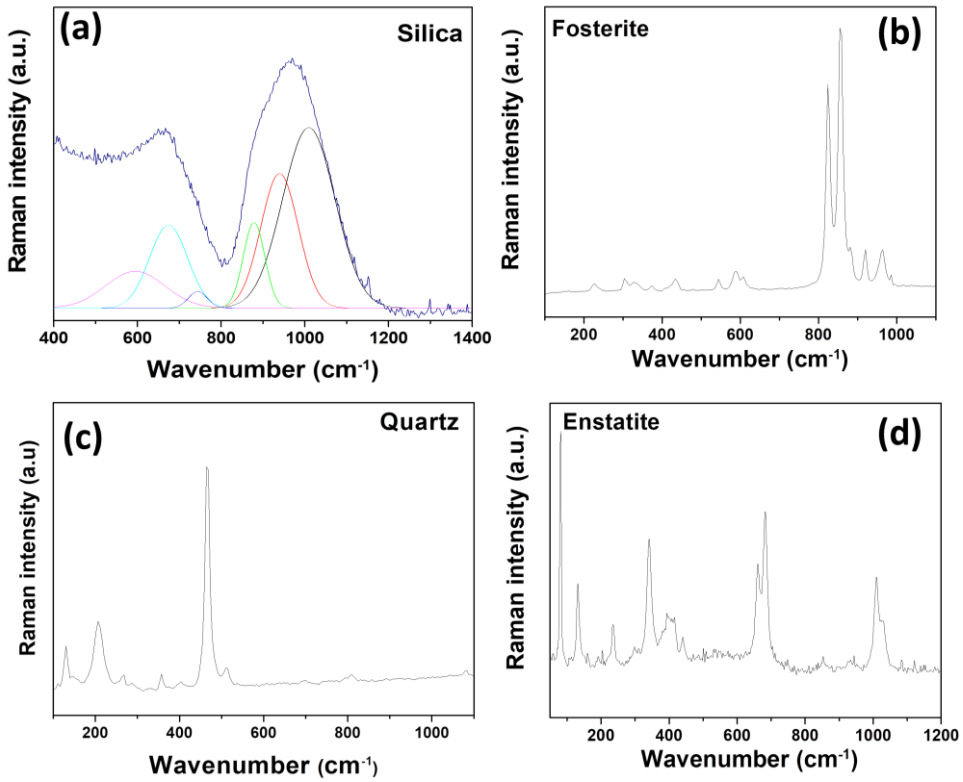

Figure 2-2 Raman spectra of : (a) vitreous silica, (b) forsterite, (c) quartz and (d) enstatite.

Table 2.5 Raman vibration modes of vitreous silica.

Peaks	Vibration mode	Center
1	Q_3	1010
2	Q_2	940
3	Q_1	880
4	Si–O stretching	750
5	O—(Ca, Mg, Si)—O bending	675
6	O—(Mg, Si)—O bending	595

The Raman spectrum of vitreous silica is characterized by broad vibration modes. The vibration modes of the Q_1, Q_2, and Q_3 species are centred at 880, 940, and 1010 cm^{-1}, respectively. The vibration modes of twisting and stretching modes of the Si-O-Si bonds are responsible for the band at 595 cm^{-1} [39–41]. A poorly crystalline calcium-magnesium silicate is responsible for the vibration mode at 675 cm^{-1} [42,43]. The stretching vibration Si–O with a dominating Si motion is assigned to the band at 750 cm^{-1} [40]. The Q_3/Q_2 ratio is high, indicating an increase in the number of Q_3 silicon sites and a high degree of polymerization. In general, higher polymerization levels in vitreous-like structures result in higher compressive strength [44,45].

For forsterite, the vibration modes in the 800-1100 cm^{-1} region are assigned to SiO_4 internal stretching vibrational modes (Figure 2-2b) [45]. A doublet with bands at 818 and 848 cm^{-1} and with different relative intensities that depend on the crystal orientation are observed in the Raman spectrum of forsterite in this wavenumber region. The SiO_4 tetrahedra's coupled symmetric and asymmetric vibrations generate these vibration bands. The internal bending vibrational modes of SiO_4 are observed in the 400–800 cm^{-1} region. Lattice modes contributing to bands below 400 cm^{-1} and are dominated by SiO_4 tetrahedral rotations and octahedral coordinated cation translations (magnesium motion) in the crystal lattice [46,47]. When cement is partially replaced by slag, forsterite may play an significant role. It is well known that cementitious materials can achieve early strength and durability when the binder contains a large amount of magnesium [48].

According to symmetric stretching of the oxygen in six-membered SiO_4 tetrahedra, the quartz Raman spectrum (Figure 2-2c) exhibits prominent α-phase Raman mode at 462 cm^{-1} [49]. In addition, the band found at 805 cm^{-1} is attributed to the Si–O stretching

motions within tetrahedral SiO_4 units. Raman bands below 300 cm^{-1} wavenumber is contributed to complex translations and rotations of the SiO_4 tetrahedra.

Enstatite's Raman spectra (Figure 2-2d) can be separated into five regions [41,50–52]: (i) The Si-O stretching vibrations associated with the non-bridging Si-O bonds are assigned to bands in the 800-1100 cm^{-1} wavenumber region; (ii) the Si-O stretching vibrations of the bridging O atoms are assigned to vibration modes in the wavenuber region between 650 and 750 cm^{-1}; (iii) the bending O-Si-O modes are observed in the wavenumber region between 500 and 600 cm^{-1}; (iv) two vibration modes attributed to the Mg-O octahedron modes (375 to 500 cm^{-1}); and (v) the vibration modes assigned to the Fe-O octahedron in the wavenumber between 225 and 350 cm^{-1}).

- Minor phases detected only by Raman spectroscopy.

The Raman spectrum of chromite (Figure 2-3 (a)) shows various bands associated with the stretching vibrations of the Fe-O and Cr-O [53]. The symmetric stretching $A_{1g}(v_1)$ vibrational mode is responsible for the broad and intense band at 780 cm^{-1}. The two bands at 485 and 730 cm^{-1} correspond to $E_g(v_2)$ and $F_{2g}(v_4)$ modes, respectively. The broad and intense band at 590 cm^{-1} is attributed to $F_{2g}(v_3)$ mode.

Figure 2-3 (b) illustrates the Raman spectrum for akaganeite (β-$FeO_{1-2x}(OH)_{1+x}Cl_x$) [54], with vibration bands at 308, 390, 535, and 720 cm^{-1}. El Mendili et al. [55] reported similar Raman characteristics. Akaganeite forms in high-chlorine environments and, low-pH (3–4) with temperatures around 60°C, such as hot springs and volcanic deposits [56]. Akaganeite has a monoclinic crystal structure and is always ionized with Cl^-. According to Keller [57], akaganeite can contain up to 6% chloride by weight. It also forms preferentially in environments with high Fe^{2+} and Cl^- concentrations when compared to lepidocrocite and goethite. The presence of akaganeite in FNS may be due to slag cooling with seawater.

The Raman spectrum of calcium carbonate (calcite structure) exhibits four Raman bands (156, 282, 712, and 1088 cm^{-1}) (Figure 2-3 (c)) [58]. The A_{1g} mode is assigned to the intense Raman band at 1088 cm^{-1}. The internal E_g mode is observed at 712 cm^{-1}, while the external E_g and lattice modes are observed at 282 and 156 cm^{-1}, respectively.

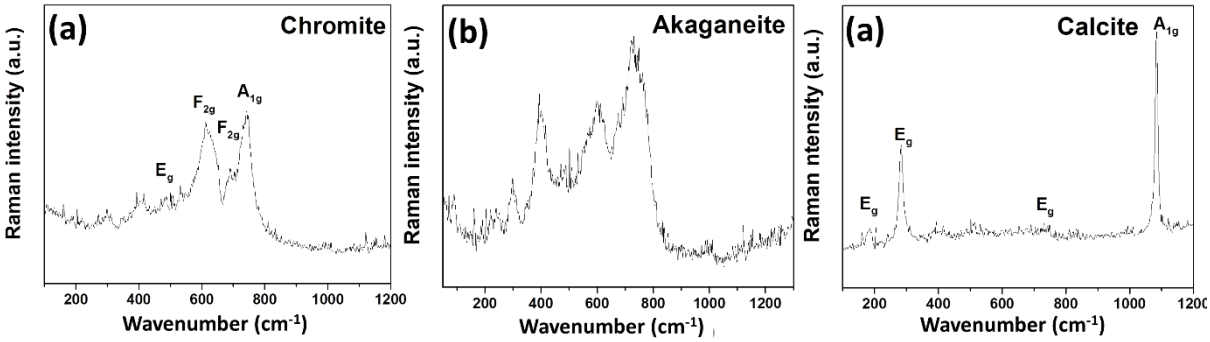

Figure 2-3 Raman spectra of (a) chromite, (b) akaganeite and (c) calcite.

In recent years, the use of quartz as SCM has increased [59]. Indeed, quartz powder can reduce the mixture's initial porosity, increasing the final strength. Furthermore, the reactivity of quartz in an alkaline environment, such as that produced by cement and lime, is very low. When mixed in required proportions, quartz improves the properties of both fresh and hard concrete, including durability, permeability, and compressive flexural and tensile strengths [59,60].

The presence of vitreous silicates with a high degree of polymerization results in increased compressive strength. Furthermore, it is known that magnesium-rich binder can lead to early strength development and cementitious material durability.

All of these findings indicate that FNS additive has the potential to produce a high-performance mortar.

2.4.2 Microstructural characterization of CR shell

The chemical compositions of *crepidula fornicata* shells determined by EDS analyses are shown in Table 2.6. Calcium is the most abundant element in the *crepidula*, with traces of Na, Si, S, Mg, and Al.

Table 2.6: Chemical composition of CR (wt.%) obtained from EDS measurements

**Oxygen and Carbon measured by EDS are taken with caution as low precision; d.l.: detection limit*

Element	(wt.%)
O	36.65* ± 3.4
C	7.44* ± 0.8
Ca	53.72 ± 1.4
Na	0.59 ± 0.06
S	0.45 ± 0.04
Mg	0.53 ± 0.05
Si	0.35 ± 0.04
Al	0.28 ± 0.04
Cl	d.l
Total	100,00

Different Raman spectra for the *crepidula fornicata* powder were collected and compared from various locations. All of the investigated locations produced the same spectrum and vibration modes. Figure 2-4 shows the obtained Raman spectrum of CR powder. The spectrum is consistent with an orthorhombic carbonate phase. Raman lines with low wavenumbers (113, 151, 181, 208, 250, and 263 cm^{-1}) are associated with external optical or lattice modes and result from interactions between CO_3^{2-} ions and Ca^{2+}. The internal modes of the CO_3^{2-} group are assigned the high-wavenumber vibrational modes v_4 at 701 and 710 cm^{-1}, v_2 at 856 cm^{-1}, v_1 at 1086 cm^{-1}, and v_3 at 1461 cm^{-1} [61].

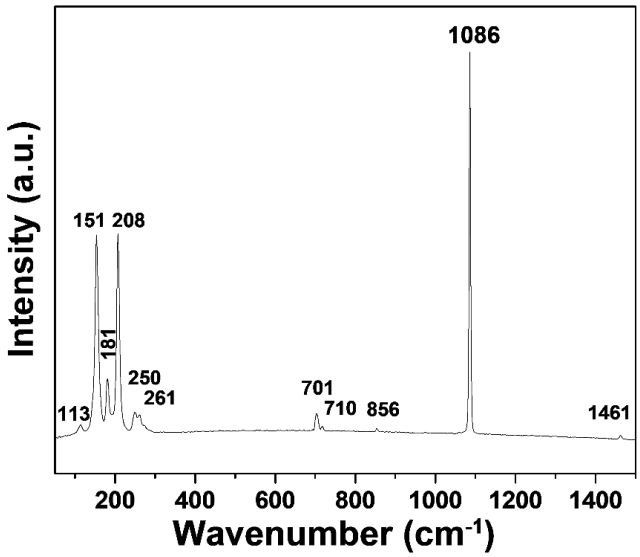

Figure 2-4 Raman spectrum of *Crepidula fornicata*.

2.4.3 Mortar mixture properties

2.4.3.1 Specific surface area

The specific surface area (SSA) of the slag-cement powder is greatly increased by the addition of FNS (Figure 2-5). This behavior results from FNS having a larger Blaine specific surface than cement (6700 cm^2/g versus 4100 cm^2/g). However, the two SSAs that compose this increase in SSA are not simply combined linearly (Figure 2-5). It suggests that combining cement with the initial specific surface of FNS may have caused some blockage. With such a low substitution rate, there is likely less FNS particle interaction during mixing, which accounts for the blockage that is clearly visible for FNS10.

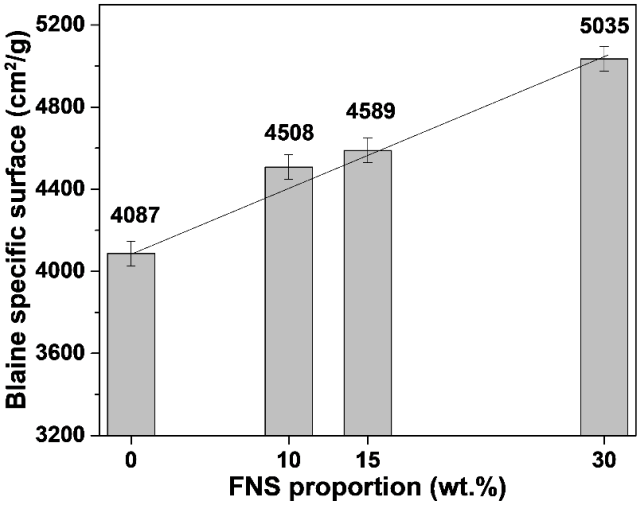

Figure 2-5 Evolution of the Blaine specific surface area (SSA) of the cements elaborated with FNS.

The SSA of the slag-cement powder is significantly raised by the inclusion of FNS and CR shells (Figure 2-6). This behavior is further brought on by the fact that FNS and CR have greater Blaine specific surfaces than cement (4100 cm^2/g for cement, 6700 cm^2/g for FNS, and 8140 cm^2/g for CR shells). The resultant SSA increase is a straightforward linear combination with this new mixture (Figure 2-6).

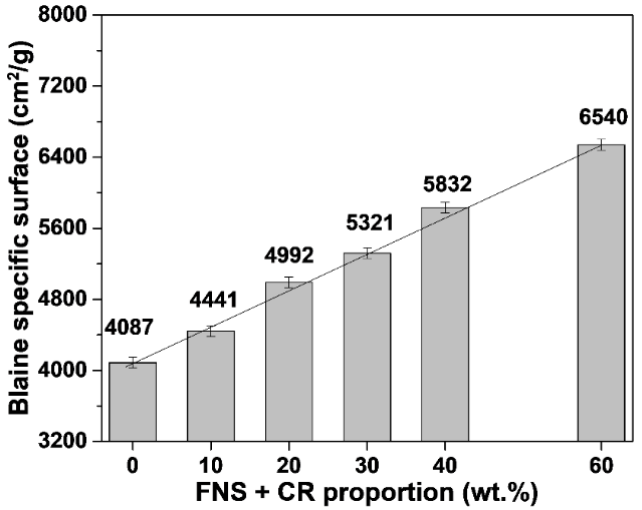

Figure 2-6 Evolution of the Blaine specific surface area (SSA) of the cements elaborated with FNS and CR.

2.4.3.2 Density of mortars

The bulk density were measured after 2 and 28 days (Figure 2-7). The density of all mixes increased with increasing curing time up to 28 days (Figure 2-7). When compared to the control mortar, gradually increasing the cement replacement content reduces mortar density throughout the aging process. Because the densities of slag and CR shells are slightly lower than those of control cement, an overall density decrease with the addition of FNS and CR is expected. However, after 2 days the

density decrease is more significant than after 28 days. This shows that with curing time, there is further densification and less porosity.

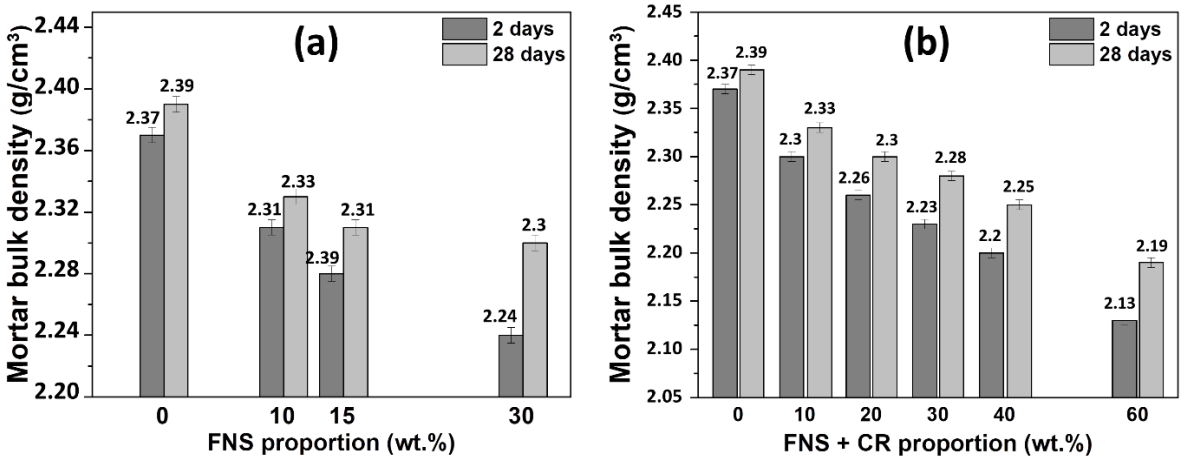

Figure 2-7 Variation of the bulk density of the mortars with different substitution levels by FNS and FNS+CR shells after 2 and 28 days of curring.

2.4.3.3 Workability and setting time of fresh mortars

FNS Slag has no impact on the flow times for any composition of FNS-cement, according to the conclusions of the flowability experiments. Indeed, a flow time between 6 and 7 s is observed for all specimens with FNS. The flow time values range between 6 and 8 s for mixtures that contain FNS and CR up to 30 wt.%. However, this flow time increases to more than 10 s for higher proportions, i.e. 40% and 60%.

The evolution of setting time as a function of FNS and FNS+CR mixture proportions is represented in Figure 2-8. The minimum initial setting time for CEM I 52.5 should be greater than 60 minutes. All mortar combinations' initial and final setting times, as shown in Figure 2-8, fall within limits needed for the cement class being employed. Samples with only FNS addition indicate that the increase in initial and final setting times is gradual when compared to the control sample. While these times typically decrease by 4% for a 10% of FNS addition, they increase by up to 9% at a 15% of FNS substitution. At higher FNS substitution levels, setting times eventually increase in comparison with the control sample. The initial setting time is accelerated by the addition of up to 15% of FNS. The initial and final setting times are increased at 30% of FNS incorporation. The initial and final setting times were found to be retarded by 2 and 14 minutes, respectively, compared to the control mix at a cement substitution level of 30 %. However, FNS addition setting times below 30% are not significantly affected. All samples' setting times are in accordance with the NF P 15-431 standard [35].

The final setting times of FNS+CR mixed with mortar were high compared to the control paste. The control paste's final setting time was 320 minutes. FNS and CR increased this value to 325 and 395 minutes, respectively, by substituting 10% and 60% of the mortar. The presence of high quantity of calcium provided by CR is known to cause the increase in setting time. As a result, the final setting time will increase at a high proportion of cement substitution by the calcium originating from CR shells. Despite the observed variability for the initial setting time, the setting time with "FNS + CR" increases almost continuously.

When using FNS addition, no or slight setting time increase was recorded. Considering the constant environmental conditions and the use of the same cement, it is possible that the decrease in initial setting times is due to low Ca-containing FNS, which reduces the hydration rate at an early age. Indeed, increasing the FNS rate in cement increases the spacing between hydrated cement particles, reducing capillary bridge formation and postponing the formation of an interconnected network between the particles [62].

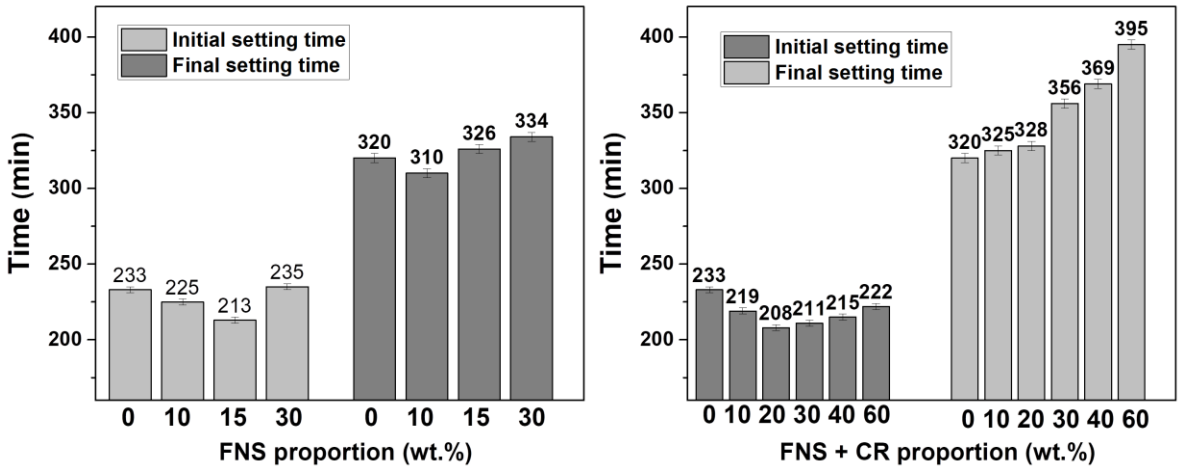

Figure 2-8 Setting time of FNS and FNS-CR pastes.

2.4.3.4 Compressive and flexural strength of mortars

Figure 2-9 illustrates the average compressive strengths of mortar mix after 2, 7, 14, and 28 days of curing. For all mixtures, the compressive strength increases with age. Compressive strength decreases with replacement rate above 10% of FNS substitution (Figure 2-9(a)). After 2 and 7 days of curing, the maximum compressive strength values are obtained for the FNS10 mixture.

When FNS levels are low, it appears to act more at early age. Indeed, at 7 days, the compressive strength of the FNS10 mortar mixture increases and surpasses that of the control mortar by 5%. Below 10% of FNS substitution, a significant increase in non-

evaporable water occurs early in the aging process due to the binder effect, and later in the aging process due to slag hydration. The binder effect cannot overcome the diluting impact brought on by the significant addition of slow-reacting slag particles at higher replacement rates [63]. At early curing ages, FNS10 performs as a nucleating agent with a higher compressive strength.

This phenomenon is attributed to the reaction between portlandite and active silica originating from FNS leading to the formation of additional hydrated calcium silicates products (C–S–H).

After 28 days of curing, the compression strength values of all FNS-cement mortar compositions are greater than 42.5 MPa. This value, classified as CEM II 42.5, is suitable for applications in the building and construction industry.

Figure 2-9(b) shows the evolution of compressive strenght as function of FNS-CR addition. The maximum compressive strength at young curing time was obtained for FNS-CR mixtures with a 10% substitution of cement (FNS5-CR5). This is due to its microstructural reinforcement and ability to fill pore or voids [64]. As a result, CR improves the microstructure and strength of mortar at an early stage. The compressive strengths obtained after 14 and 28 days for all FNS-CR cement mix are relatively low compared to the control mortar. The compression values of mortars incorporating up to 20% FNS-CR remain very close to those of the control mortar. However, the results obtained for cement mortar mixes containing FNS-CR are still suitable for use in the construction industry.

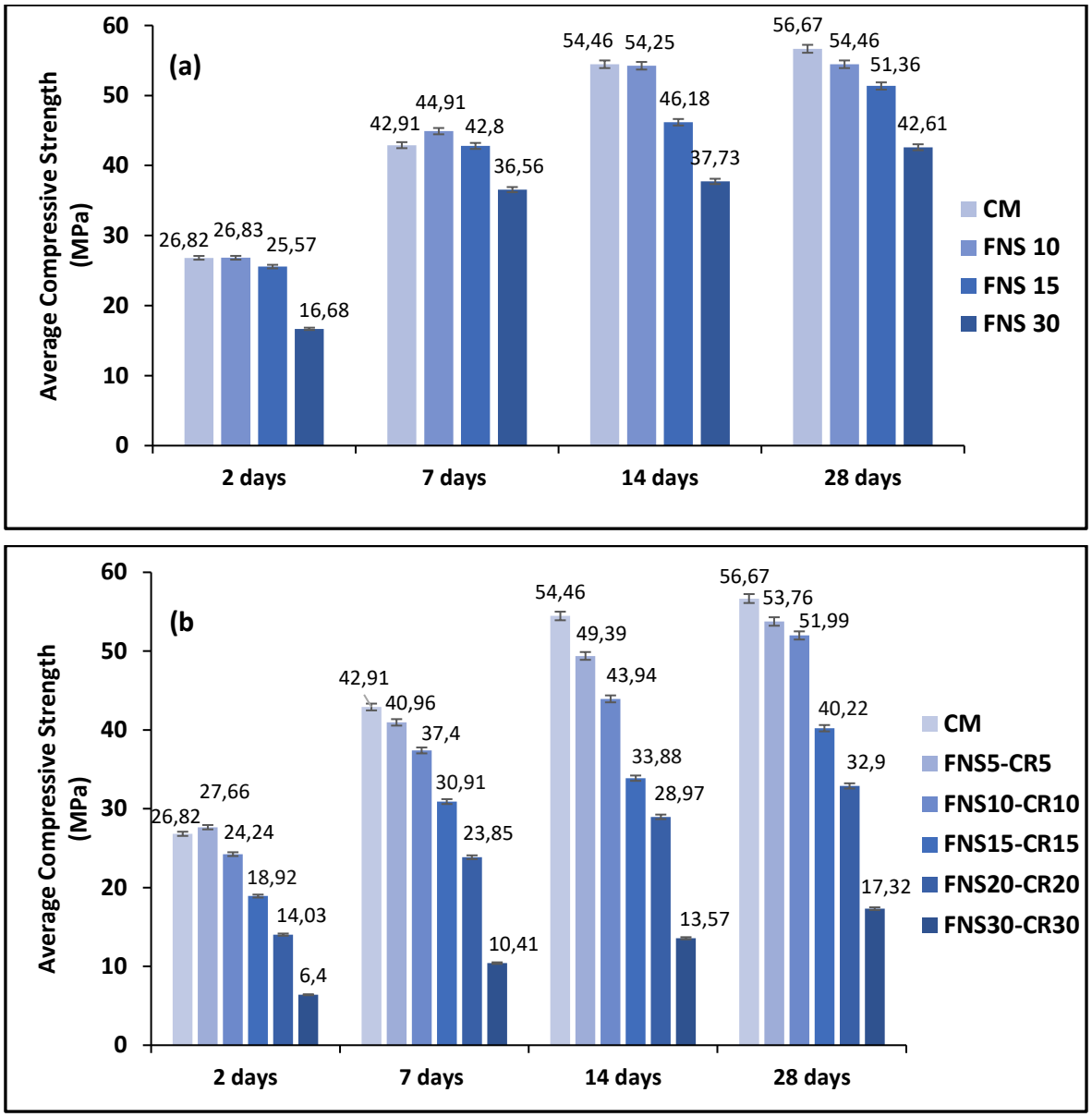

Figure 2-9 Compressive strength values obtained after different curing times of the mixtures with: (a) FNS and (b) FNS-CR.

When the FNS replacement rate is up to 15%, the flexural tensile strengths are lower than the control mortar (Figure 2-10a). This effect is due to the slower pozzolanic reactivity because of FNS [65]. In contrast, the FNS10 specimen's flexural tensile strengths on all curing days are slightly higher than those of other mixes, including the control mix. The FNS10 mortar's flexural tensile strengths at 2 and 28 days enhanced by 1 and 4 %, respectively, in comparison to the control mortar.

These findings agree with those obtained for the setting times. Indeed, the hydration process was accelerated at low FNS incorporation rates, especially at 10%. This resulted in an increase in mechanical strength, particularly at a young age.

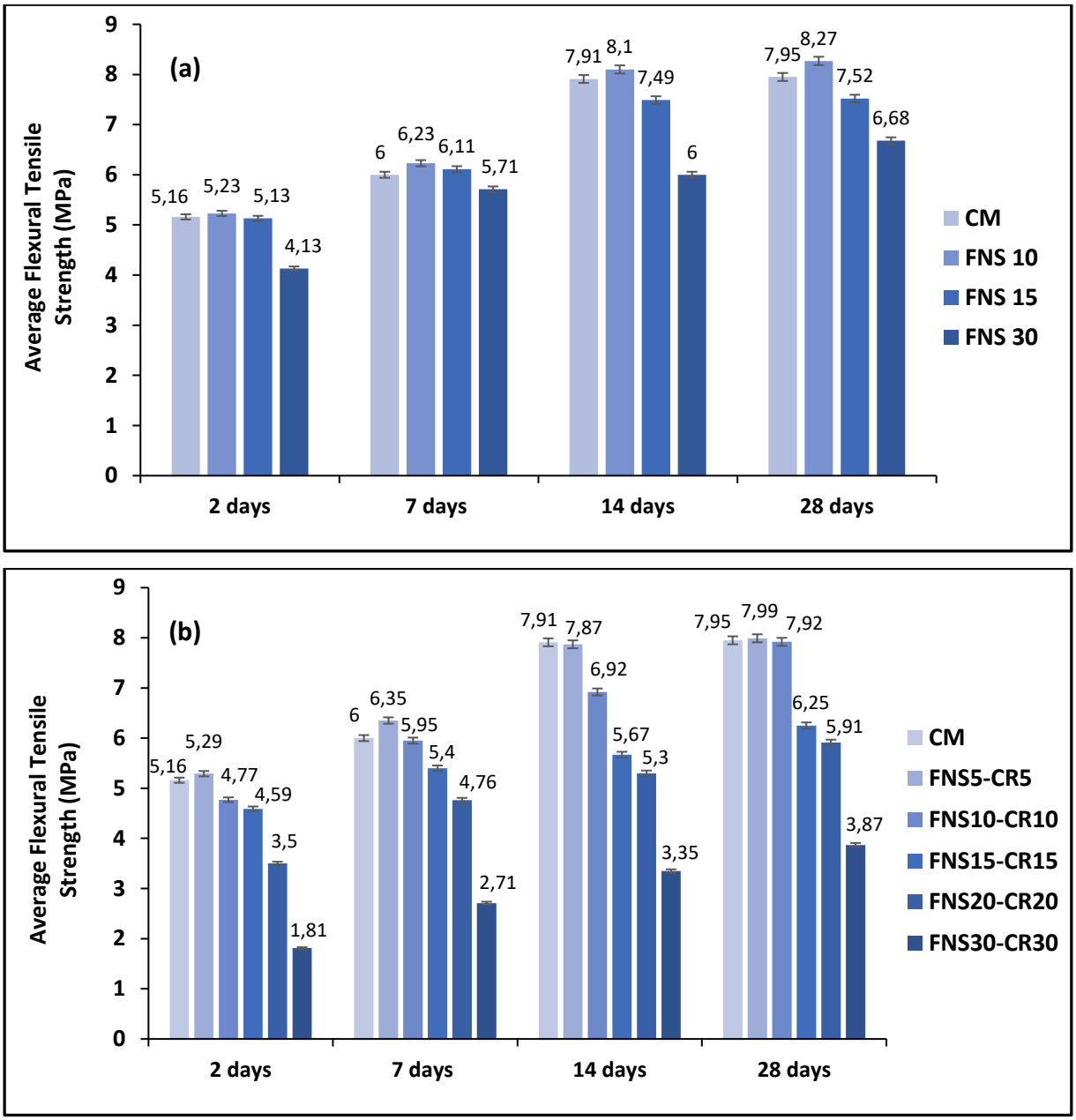

Figure 2-10 Flexural strength values obtained after different curing times of the mixtures with: (a) FNS and (b) FNS-CR.

The flexural and compressive strengths of the various FNS-CR mortars are significantly linked (Figure 2-10b). All specimens have the same hardening kinetics between 2 and 28 days. After 28 days of curing, the maximum flexural strength values were measured at 10% FNS-CR partial substitution. When the substitution rate exceeds 30%, the flexural strengths remain very low in comparison to mixtures with a low substitution rate. Flexural strengths are very close to the control mortar for the low substitution rate. However, at 28 days, those with 10% FNS-CR partial substitution remain slightly higher than the control mortar, 7.99 MPa for FNS5-CR5 specimen and 7.95 MPa for control mortar.

2.4.3.5 Raman analyses of mortars

After 28 days of aging, Raman analyses of the mortar surface of control mortar reveal the presence of C-S-H and calcite (Figure 2-11). In the case of the FNS5-CR5 mortar, Raman spectroscopy reveals the presence of ettringite on the mortar surface in addition to C-S-H and calcite.

Calcite exhibits the four expected Raman bands. The A_{1g} mode with the highest intensity is present at 1085 cm-l [58]. At 713 and 1435 cm^{-1}, two sets of doubly degenerated internal E_g modes are observed, and external E_g and lattice modes are observed at 283 and 155 cm^{-1}.

The Raman spectra of C-S-H systems have received considerable attention [66,67]. Si–O stretching vibration is responsible for the most intense vibration band at 670 cm^{-1}. The lattice vibrations of Ca-O polyhedra were assigned to the bands present in the low wavenumber region (100-360 cm^{-1}). The twisting and stretching of the Si–O–Si vibration modes generates the band at 445 cm^{-1}. The bands between 850 and 1100 cm^{-1} correspond to the symmetric stretching modes of Qn species in silicate (Si–O). The H_2O stretching modes are assigned to the bands with high range wavenumbers (2800-3600 cm^{-1}). When examining the Raman spectra of C-S-H produced on a regular mortar surface and in the FNS5-CR5, it is found that the Ca–O polyhedra vibration modes significantly increase their intensity and shift to low wavenumber. This phenomenon is attributed to the presence of *Crepidula* shells, which provide high amount of calcium leading to an increased ordering of the calcium environment of C-S-H structutre and thus increasing the degree of polymerization. When compared to a control mortar, the specimen Raman spectra of FNS5-CR5 reveal a decrease in Q_1 (880-890 cm^{-1}) and an increase in Q_3 (1080 cm^{-1}). In the case of the FNS05-CR05 mortar, this variation can be explained by the cross-linking of silica layers. The Q_2 species (1000–1020 cm^{-1}) in the FNS–CR specimen split into two distinct bands at 1006 and 1015 cm^{-1}. This finding supports the hypothesis that the number of the silica tetrahedrons Q_{2p} (pairing) and Q_{2b} (bridging) modified the length of the Si–O–Si chain [68]. This is associated to the significant amount of silica supplied by FNS. Indeed, the excess of calcium hydroxide reacts with the silicates originating from FNS to produce additional C-S-H.

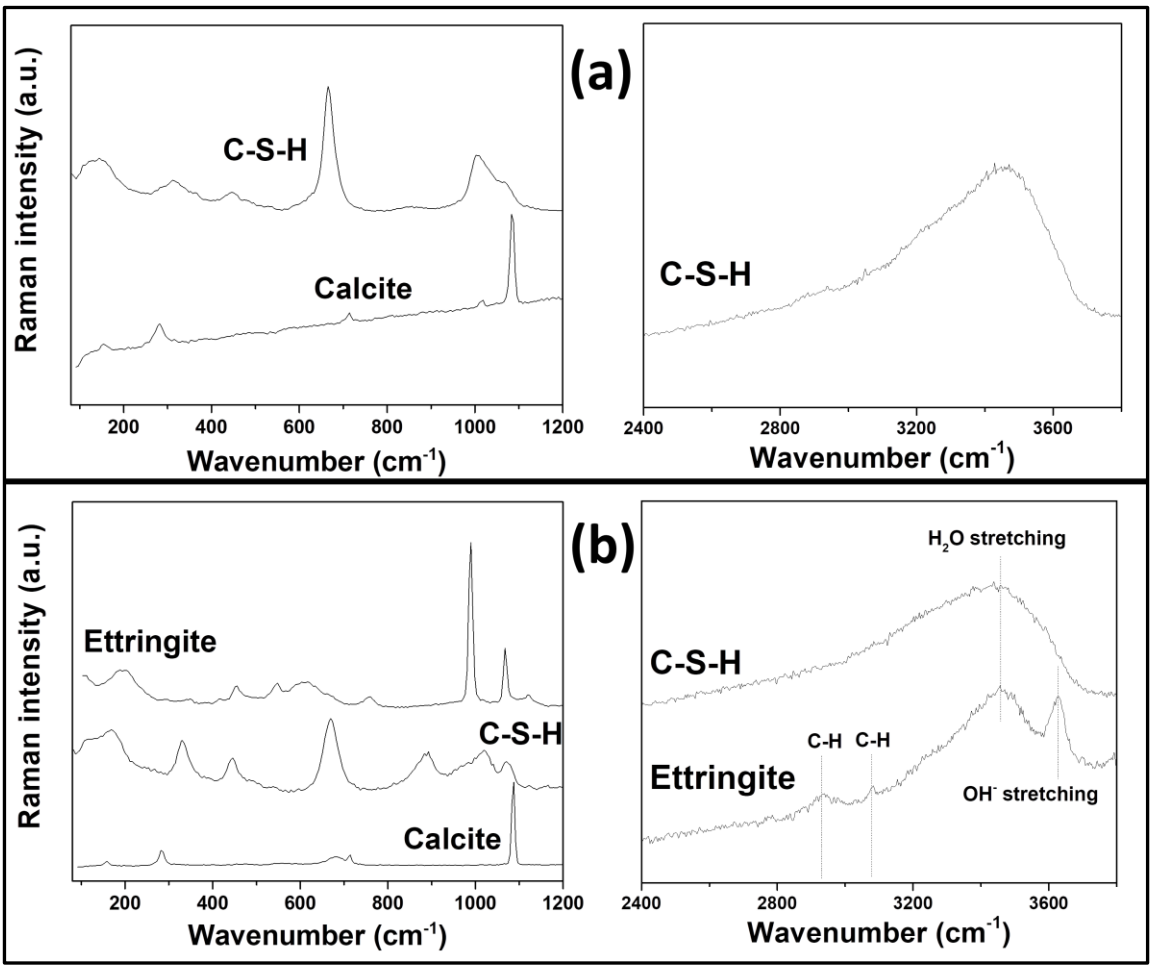

Figure 2-11 Raman spectra recorded for the mortars after 28 days of aging: (a) ordinary mortar, (b) FNS5-CR5 mortar.

The Raman spectrum of ettringite shows the presence of the intense vibration bande at 988 cm^{-1}, which has been assigned as the $v_1(SO_4)$ vibration mode [58]. Furthermore, the Raman spectrum reveals also the presence of relatively weak bands at 1113 cm^{-1} for $v_3(SO_4)$, 615 cm^{-1} for $v_4(SO_4)$, 545 cm^{-1} for Al-OH stretch, 450 cm^{-1} for $v_2(SO_4)$, and 345 cm^{-1} for Al-OH rotation and translation) [69]. The spectrum continuity in the high wavenumber range exhibits two features: a sharp band at 3629 cm^{-1} attributed to the OH stretching vibration of the OH units, and a broad and large band at around 3500 cm^{-1} attributed to water stretching vibrations. The presence of the weaker band 1080 cm^{-1} produced by C-O stretching in the carbonate groups present in calcium-carbonate, due to a mixture of calcite and aragonite, indicates that the ettringite has undergone carbonation. This contributes to the development of tricarboaluminate. The presence of the C-H vibrations at 2930 cm^{-1} and 3060 cm^{-1}, clearly supports the formation of tricarboaluminates.

The crystal structure of aragonite originating from CR is a planar configuration of Ca and O atoms with significantly larger density and strength than limestone powder [70]. At 25 °C, the measured solubility ($LogK_{sp}$) of aragonite in water is -8.336, resulting in the formation of Ca^{2+} and CO_3^{2-} ions [70,71]. In this case, the dissolved CO_3^{2-} ions can participate in hydration reactions of the aluminate phases. As a result, carboaluminates were formed rather than sulfoaluminates, which stabilized the ettringite formed at early ages [72,73]. Carboaluminates have higher volumes and stiffness than sulfoaluminates [73–75] , allowing for further decreases in porosity while increasing final product strengths.

In comparison to fly ash or blast furnace slag, there are very few studies on the use of FNS as SCM. The FNS used in this study is originating from the processing of nickel laterite ore. The FNS contains low iron oxide and high MgO. This is advantageous since a high proportion of MgO in cements (binders) reduces shrinkage-cracking in concrete. This magnesium-rich cement can cause autogenous expansion during early curing times and compensate for concrete contraction due to shrinkage and cold weather [76]. X-ray diffraction and Raman analysis also revealed the presence of MgO in the form of forsterite and enstatite (Figure 2-1 and Figure 2-2). Enstatite and forsterite are stable and chemically inert [37]. Forsterite and enstatite, which contain MgO, do not participate in the hydration event that creates expanding $Mg(OH)_2$ [36,37]. The presence of FNS retarded the hydration process in FNS blended concrete, according to Katsiotis et al. [77]. Additionally, the authors noted that the pozzolanic reaction of FNS resulted in an increase in compressive strength during later stages of curing. The primary cause of the reduction in expansion is thought to be the consumption of portlandite by the pozzolanic reaction of FNS.

Quartz has become incredibly common as a pozzolanic material in recent years [70]. The hydrated calcium silicate (C–S–H), which gives hydrated cement pastes their strength, is created when pozzolanic materials combine with hydrated calcium hydroxide. Quartz, when added in a certain ratio, enhances the durability, permeability, and compressive, flexural, and tensile strengths of both fresh and hard concrete [70,71].

The vitreous-like silica, which is also present in the FNS, is highly polymerized. This result is significant for using this compound as a cement substitution because the above-mentioned structure implies that the silicate will achieve stiffness, strength, and

density over time. The silica in FNS reacted at later age, forming supplementary calcium silicate hydrate (C-S-H) gel and increasing the density of the silicate microstructure [78]. In general, higher polymerization levels in vitreous structures result in higher compressive strength [79,80].

2.4.3.6 Thermal conductivity of concrete mixes

The thermal conductivity of the concrete samples showed an increasing trend with the increasing content of FNS and CR, as shown in Figure 2-12. This is due to the high magnesium content of FNS. These initial results are intriguing and demonstrate that the substitution of cement with ferronickel slag and *Crepidula* can increase the thermal conductivity of concrete.

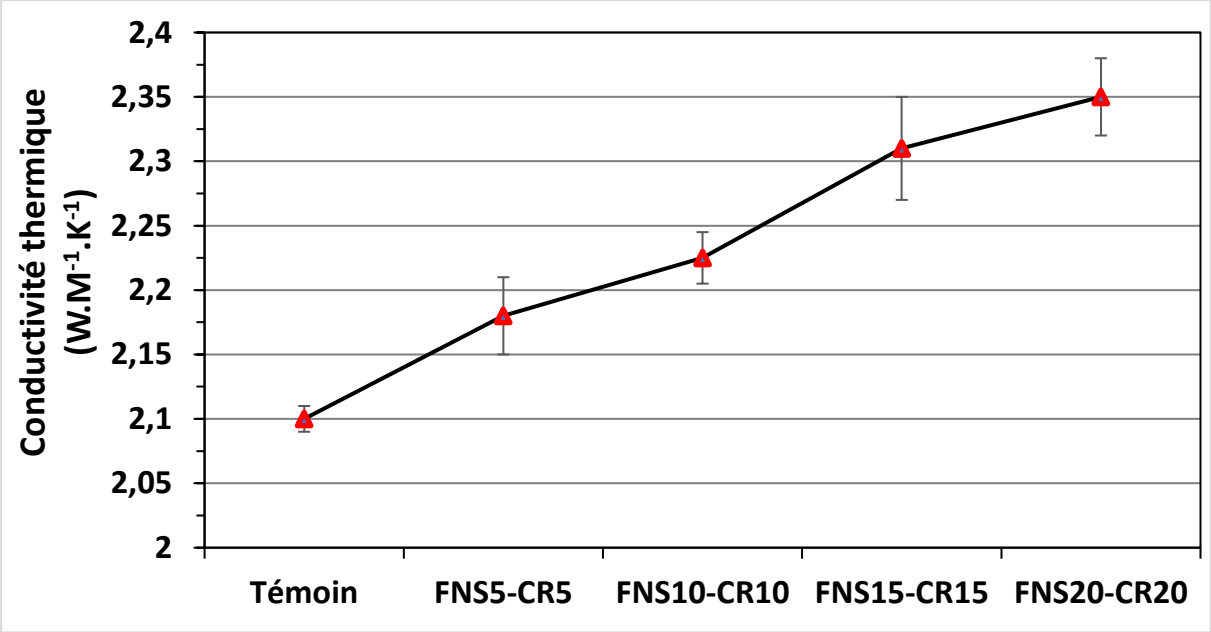

Figure 2-12 Variation of the thermal condictivity of the concretes elaborated with different FNS+CR proportion after 28 days of curing. Error bars are standard deviation calculated for 3 replicates.

2.5 Conclusions

The effects of cement replacement by FNS and FNS+CR on the cement paste and mortar properties were studied at different percentage. The following conclusions can be drawn:

- A partial substitution of cement by FNS-CR mix, up to 30%, has no effect on the workability of mortar in its fresh state. Workability is reduced above this substitution rate due to the water absorption of these admixtures with high SSA.

- Increasing FNS-CR addition in cement results in lower compressive and flexural strengths. As a result, the use of these less dense substitutes, which are less dense than cement, is limited to moderate rates.
- However, mechanical strengths remain close to those of the control mortar at up to 20% substitution by FNS+CR.
- At 2 days curing time, the addition of 10% FNS-CR improves mechanical behavior due to the cement setting acceleration at the same rate.
- The Raman analysis show that the combination of FNS and CR has two major advantages: (i) FNS's high silica content promotes polymerization in the C-S-H structure; (ii) the *Crepidula* shells' dissolved CO_3^{2-} ions induce the formation of carboaluminates, which reduce the system's porosity and increase its strength.
- The excess of calcium hydroxide reacts with the silicates originating from FNS to produce additional C-S-H and C-S-A-H.
- The results show a clear potential for using FNS-CR wastes as a partial replacement for cement at an optimal rate of 20%.

Nevertheless, the thermal study of these mixtures showed that the thermal insulation is not improved by the presence of FNS. Indeed, the thermal conductivity increased with high rates of cement substitution by FNS.

Part II: The potential of Fly Ash and *Crepidula* shell as substitution of Portland Cement

Abstract

The goal of this research is to determine how a clever mixture of waste materials, fly ash, and *Crepidula* shells affects the performance of mortar and concrete based on partial cement substitution. Fly ash and *Crepidula* are used to substitute cement in the proportions of 10, 20, 30 and 40% by weight. The following three steps are the subject of this research: (i) determine the optimal compression and hygrothermal behavior formulation, (ii) construct a prototype and monitor hygrothermal behavior with sensors, and (iii) collect data and develop a neural network model to model the prototype's hygrothermal behavior. The mechanical properties of the fly ash-*Crepidula* mortar were proven to be higher than the control mortar with a fly ash-*Crepidula* incorporation rate of up to 10%. Furthermore, replacing cement with fly ash and *Crepidula* shells improves concrete's thermal conductivity.

2.6 Introduction

The increase of the building industry has resulted in a worldwide increase in cement production. Cement manufacture released 2.3 GtCO2 [81] in 2019 and produces a lot of CO_2, SO_2, and NO_x [82]. The reduction of CO_2 emissions in the construction sector has been discussed, and several cementing system alternatives have been proposed: a) switching from coal to natural gas in clinker preparation, based on a CO_2 capture by chemical absorption process, b) encouraging clinker dry manufacturing, and c) partially substituting cement with supplementary cementitious materials (SCM) [83]. The use of SCM such as blast furnace slag [84], fly ash [85], and silica fume [86] to partially substitute cement results in the recycling of industrial by-products, the conservation of natural resources, and consequently a reduction in CO_2 emissions.

The global availability of fly ash (FA) is predicted to be over 800 million metric tons per year, with annual global production estimated to be between 500 million and one billion tons [87,88]. Just a small fraction of FA is recycled; the remainder is dumped or stored on the ground. Because of its potentially harmful trace element content, FA storage poses a major threat to human health and ecosystems [89]. FA is a heterogeneous compound made up of the chemical components SiO_2, Al_2O_3, Fe_2O_3, and CaO that is produced as a by-product of coal burning. The qualities of the burned coal, as well as the procedures employed for processing and storage, have an impact on the chemical properties of FA. FA in the cement had an effect on the physical and chemical properties of the concrete. Due to the tiny and spherical shape of the particles as well as their smooth vitreous texture, it has been claimed that adding FA to cement concrete reduces hydration heat [90] and improves the fluidity of fresh mixtures. As a result, a smaller volume of water is required for the same workability [91]. Few investigations have been published on the thermal conductivity behavior of concrete with FA [92]. When compared to regular concrete, cement mixes with FA have a longer setting time. FA's sluggish pozzolanic reactions and the decrease in cement concentration are the causes of this phenomenon [93]. Because of matrix densification, which slows the evaporation of the internal hydration [94], drying shrinkage tends to decrease as FA substitution increases [89]. The inclusion of FA at a young age was also demonstrated to reduce compressive strength. However, the strength difference between FA-concrete and standard concrete tends to shrink with time. The pozzolanic reaction occurs when the silica and alumina in the FA combine with the portlandite to create calcium-silicate-hydrates (CSH) and calcium-alumina-silicate-hydrates (CASH).

However, the pozzolanic reaction is sluggish, and the pozzolanic contribution of fly ash at advanced ages is insignificant [95]. Fly ashes, according to Berry et al. [96], have the physical effect of a space binder in the early stages and are responsible for the development of ettringite (AFt). In the long term, they serve mostly as silico-aluminate binders in the hydration reaction. When silica-rich materials (SCMs) are utilized, the reaction products, mostly in the form of calcium silicate hydrates (CSH), have lower calcium-to-silica ratios (c/s) [97,98].

The use of a calcium-rich product is one of the strategies for improving the early-stage resilience of concrete based on FA substitution for cement. Molluscan shells are a common waste product in coastal locations and nations with significant seafood consumption [21], and they are among the numerous wastes in nature. Nearly 200,000 tons of shells are burnt in France or end up as garbage in the environment [19]. *Crepidula fornicata* shells (CR), an invasive and inedible species, were discovered among these seashells. Calcium carbonate (Aragonite, $CaCO_3$) is the major component of CR, which makes it an excellent additional cementing ingredient. Aragonite is more metastable than calcite and has a higher solubility, resulting in faster calcium release. Several studies [21] have looked into the use of shells as a cement substitute. When the amount of shell powder in the concrete mixtures was raised, the levels of ettringite and calcium carboaluminate grow as well. This helps to understand how shell helps hydration products to precipitate [99]. The liberation of CO_3^{2-} ions, which leads to the creation of carboaluminates and the reduction of concrete porosity, increases the flexural and compressive strengths of CR shells [100]. Wang et al. [99] found that concrete water absorption rises with $CaCO_3$ level and that concrete containing more cockle shell ash has better porous characteristics. In addition, Bentz et al. [92] shown that adding FA to concrete improved the thermal conductivity behavior when compared to plain concrete.

The inclusion of silica-rich components in blended cement can improve later age strength but lower early age strength due to the necessity for activation and progressive hydration. Calcium-rich materials have been used to improve the strength of ternary mixed cements at an early stage. Combining calcium carbonate (like limestone) with silica in concrete or mortar has been demonstrated to be advantageous in several studies. Indeed, calcium carbonate enhances early concrete strength, while silica-rich ingredients enhance later strength, resulting in optimal strength growth [100].

The effect of FA (silicate-rich) and CR (calcium carbonate) cement replacement on the mechanical and hygrothermal properties of concrete was explored in this study.

2.6.1 Materials and samples preparation

2.6.1.1 Cement

The cement used is a CEM I 52.5 N made in accordance with the NF EN 197-1 [24] standard norm. The blaine finesses are 4100 cm2/g and the density is 3.2 g/cm3. The mineralogy composition is C_3S = 74 %, C_2S = 12%, C_3A = 11%, SO_3 = 2.7%, S^{2-} < 0.02% and Na_2O = 0.06% with clinker accounting for 95 %. Table 2.7 shows the chemical composition.

Table 2.7 : Chemical composition of CEM I 52.5 N cement in weight percent as determined by EDX spectroscopy.

Component	SiO_2	CaO	Al_2O_3	Fe_2O_3	MgO	SO_3	K_2O	Na_2O	Loss on Ignition
wt.%	19.5	63.2	4.8	3.5	1.5	2.7	0.6	0.1	4.1

2.6.1.2 Sand

We used a normalized sand in accordance with the standard norm NF EN 196-1 [28], which was sold in a polyethylene container containing 1350 g of natural rounded quartz grains.

2.6.1.3 Fly ash

With an absolute density of 2.8 g/cm^3 and Blaine finesses of 3950 cm^2/g, we selected Fly Ash (FA) class F from coal-fired power plants, which was also certified as compliant with the standard norm NF EN 450-1 [101]. No further processing was required because the FA was powdered and spherical. Table 2.8 shows the chemical makeup of the product. FA contains larnite, portlandite, gehlenite, calcite, and calcium oxide, quartz, and corundum in tiny amounts [102].

Table 2.8 Chemical composition of fly ash (by weight.%) obtained by Energy Dispersive X-Ray spectroscopy

Component	SiO_2	Al_2O_3	Fe_2O_3	MgO	MnO_2	CaO	SO_3	TiO_2	Cl	P_2O_5	Na_2O	K_2O
wt.%	53.3	23.6	8.5	3.0	0.5	5.1	1.1	1.0	0.1	0.2	0.6	3.0

2.6.1.4 *Crepidula fornicata* shells

Due to its overabundance throughout the French and Brittany coasts, CR is an invasive species that poses a threat to halieutic resources. These shells were gathered from a fish factory in Normandy that had already been processed (France). The raw shells

were baked in the oven for at least 24 hours to remove any remaining organics before being processed to powder. 2.73 g/cm^3 and 8140 cm^2/g, respectively, are the specific gravity and Blaine fineness.

Table 2.9 shows the chemical composition of CR powder as determined by Energy-Dispersive X-ray Spectroscopy (EDS). The most abundant element is calcium. There are additional residues of Na, Si, S, Mg, and Al (0.6 wt%), according to the analysis.

Table 2.9 Chemical composition of CR (by wt.%) obtained from EDS measurements on ground CR powders

*O and C contents are taken with caution as low precision; d.l.: detection limit

Element	O	C	Ca	Na	S	Mg	Si	Al	Cl	Total
(wt.%)	36.6* ± 3.4	7.4* ± 0.8	53.7 ± 1.4	0.6 ± 0.1	0.5 ± 0.1	0.5 ± 0.1	0.4 ± 0.1	0.3 ± 0.1	d.l	100,00

Aragonite has a rhombohedral symmetry and a Raman spectra featuring vibrational modes in the low-wavenumber range (154, 190, 208, and 274 cm^{-1}) due to interactions between CO_3^{2-} ions and Ca^{2+}. The internal modes of the CO_3^{2-} group are assigned to the vibrational modes v_4 at 701 cm^{-1} and 710 cm^{-1}, v_2 at 856 cm^{-1}, v_1, at 1086 cm^{-1}, and v_3 at 1461 cm^{-1} [61].

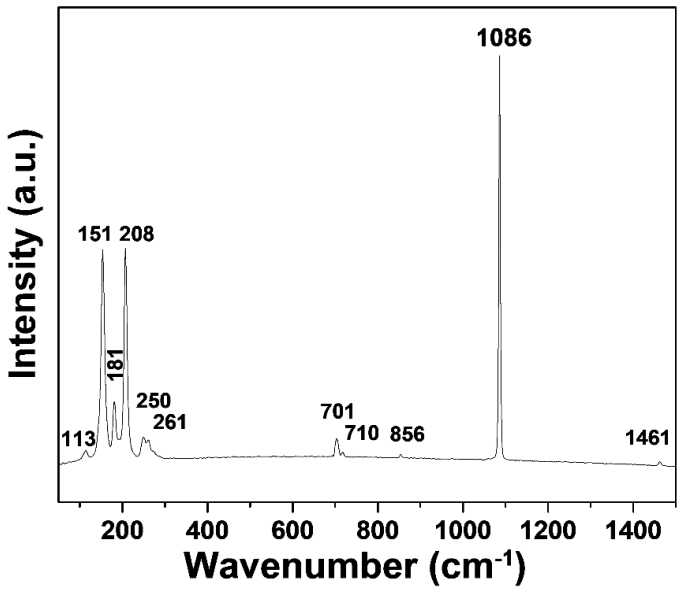

Figure 2-13 Raman spectrum of CR shell.

2.6.1.5 Mortars mix design

According to the standard norm [28], all mortars elaborated have a water on cement ratio (W/C) of 0.5 and a sand to cement ratio of 3. The mortars were filled into prismatic

molds after they had been mixed (40 x 40 x 160 mm3). After pouring each layer, the molds were exposed to 60 hits on a vibrating table to expel the air. The molds were then placed in a specially designed confined room with a temperature of 20°C and a relative humidity of 90%. The mortar samples were demolded 24h after fabrication and stored at controlled room temperature until testing. five different mortars are prepared, including the usual mortar (Table 2.10). FA and CR were used in equal amounts to replace cement, at rates of 10%, 20%, 30% and 40%, respectively.

Table 2.10. Substitution ratio of the different mortar mixtures

Sample	Mass substitution rate of cement by FA (%)	Mass substitution rate of cement by CR (%)
CM	0	0
FA5-CR5	5	5
FA10-CR10	10	10
FA15-CR15	15	15
FA20-CR20	20	20

2.6.2 Characterization techniques

Energy Dispersive X-Ray spectroscopy (SUPRATM 55, SAPPHIRE; Carl Zeiss, Jena, Germany) was used to analyze the elements. All Raman spectra were obtained using a Thermo Scientific microscope (DXR Raman, ThermoFisher Scientific Inc., MA, USA) and a 532 nm laser as an excitation source at room temperature. As basic fitting functions, Origin software and Gaussian curves are employed. Direct comparison with Raman spectra provided in the Raman Open Database [32] was used to identify the mineral compositions.

2.6.3 Test methods

2.6.3.1 Specific surface area

The Blaine air permeability apparatus was used to determine the specific surface area of each cement mixture utilized in this investigation, according to the ASTM C-204 test procedure [33].

2.6.3.2 Thermal conductivity

Five concretes were made in 30x30x7 cm^3 prismatic molds for the thermal analysis: a control concrete (CC) and four concretes containing fly ash and *Crepidula* (FA-CR) with mass incorporation rates of 10%, 20%, 30%, and 40%, respectively. On a vibration table, all of the concrete sample were compressed. They were demolded after 24 hours

and then cured for 28 days at 20°C with a relative humidity of 95 %. Table 2.11 shows the composition of the various concrete combinations.

Table 2.11 Composition of the different concrete mixes (Kg m^{-3})

	CC	FA5-CR5	FA10-CR10	FA15-CR15	FA20-CR20
Cement	350	332,5	315	297.5	280
Fine sand 0/3	756	756	756	756	756
Gravel 3/8	980	980	980	980	980
FA+CR	0	17,5	35	52.5	70
Water	175	175	175	175	175

A Heat Flow meter system was used to measure thermal conductivity (HFM 436 Lambda, NETZSCH). The tested samples are placed between the cooling plate and the heating plate, with prismatic dimensions of 30x30x7 cm^3. A Peltier cryostat controls the temperature of the cooling and heating plates.

2.6.3.3 Fresh properties of mortars

The mortar maniabilimeter was used to measure the workability of the mixes, as recommended by the French standard NF P18-452 [34]. The test is used to determine the mortar's dynamic workability under the influence of forced vibration. The time it takes for the mortar to flow out of the huge compartment and reach the level line is measured in this test as shown in the Figure 2-14.

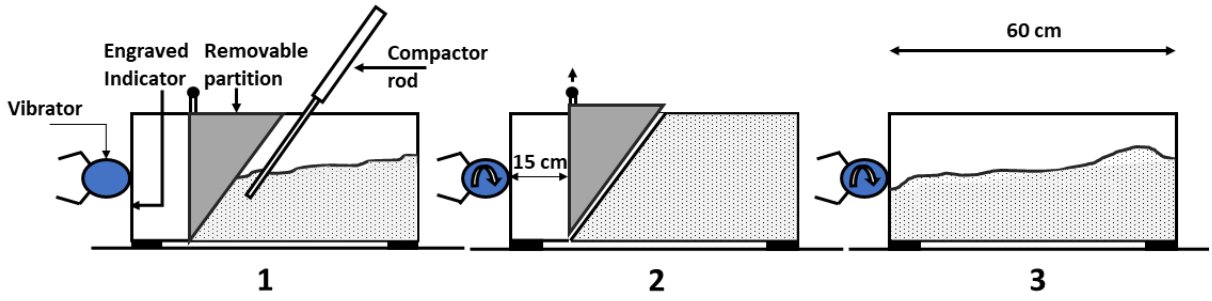

Figure 2-14 Maniabilimeter's operating principles

For all mixtures, we measured the initial and final setting times according to the standard norm NF P15-431 [35]. It is crucial to ascertain the water content required for a standardized paste consistency before beginning the setting time test. The Vicat apparatus was equipped with a 10 mm diameter plunger for this purpose, and the consistency was considered normalized when the plunger penetrated to a depth of 6 ± 1 mm. The plunger is then modified by a needle of 1.13 diameter fixed to the

moveable component of the Vicat apparatus for the initial setting time. When the gap between the mould base and the plunger is d=4 mm, the initial setting time is effective. When the needle insertion is less than 0.5 mm, the final setting time is reached by rotating the mould and using the needle with annular attachment.

2.6.3.4 Mechanical properties of hardened mortars

An electromechanical press from the IGM Company was used to test the mechanical resistance of the normalized mortar after 2 and 28 days of curing. The 3-point bending and compression tests were carried out concurrently at constant rates of 0.05 kN/sec and 2.4 kN/sec, respectively.

2.7 Results and discussion

2.7.1 Experimental results

2.7.1.1 Specific surface area and mortars density

The combination of CR shells and FA considerably enhances the cement powder's specific surface area (SSA) (Figure 2-15). Indeed, C*repidula* shells have a higher Blaine finess than cement and FA (8140 cm^2/g for CR, 4087 cm^2/g for cement, and 3950 cm^2/g for FA). Figure 2-15a shows that the increase in Blaine finesses is not a simple linear regression, showing a blockage of the initial specific surface of CR *Crepidula* shells by mixing with cement at 5% CR replacement. The higher fineness of CR compared to cement is likely to be the cause of the obstruction, as the CR shell particles can act as a nucleation site for the hydration products [100].

With increasing curing time from 2 to up to 28 days, an increase in bulk density is observed for all mortar mixes (Figure 2-15b). At all curing times, increasing the CR and FA fraction resulted in a progressive decrease in mortar density. This is due to lower CR and FA densities when compared to CEM I. The decline is more pronounced after 2 days than after 28 days, as seen in Figure 2-15b. This effect is due to increased densification, which leads to a low porosity of samples over time.

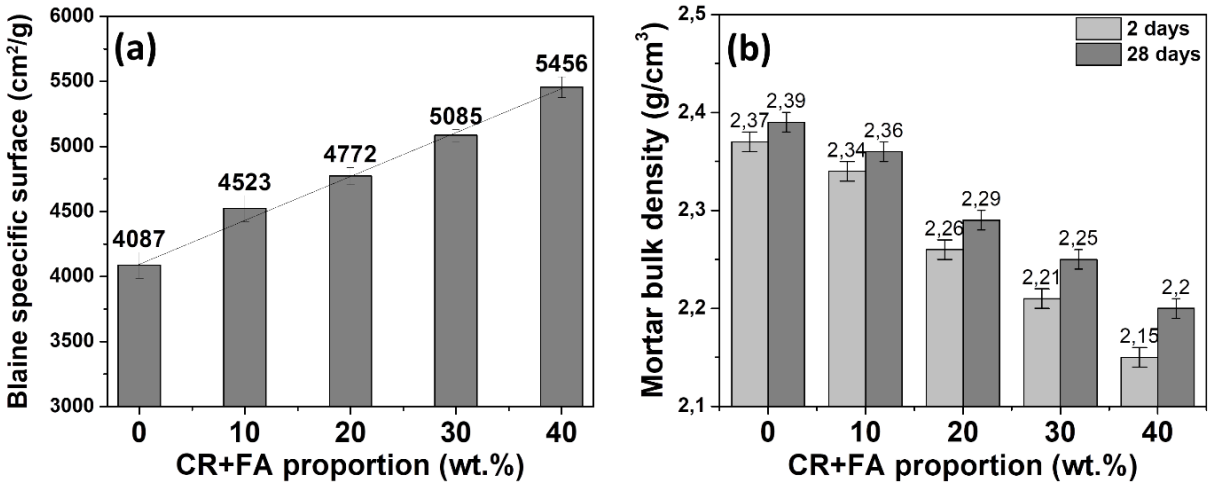

Figure 2-15 (a) Variation of the Blaine specific surface area (SSA) of the cements elaborated with different CR+FA proportion. (b) Evolution of the bulk density of the mortars with different substitution of cement by CR shells and FA after 2 and 28 days of curing. Error bars are standard deviation calculated for 3 replicates.

2.7.1.2 Normal consistency

With the increasing percentage level of FA-CR up to 20%, the mortars demand more water for normal consistency (Table 2.12). Indeed, with the subtitution of 10% of FA-CR, the amount of water required for the paste's typical consistency fell significantly, then increase for further FA-CR incorporation. Despite the greater surface area of CR, which requires more water, the results of mortar consistency with 5% of FA-CR are slightly low. Furthermore, the presence of FA reduced water demand, allowing consistency to be managed within limits.

Table 2.12 Water contents for normal consistency of paste with different concentrations of CR and FA.

Sample	Water contents for normal consistency of paste (wt.%)
CM	33
FA5-CR5	32
FA10-CR10	34
FA15-CR15	35
FA20-CR20	36

2.7.1.3 Workability and setting time of fresh mortars

Figure 2-16a shows the variation of flow time of mixes integrating various FA-CR addition rates. The flow time dropped initially up to a level rate of 20%, then increase with larger FA-CR concentrations. The surface area of CR is extremely large. As a result, CR can play the role of a binder between the cement and FA grains, resulting in a shorter flow time [103]. However, if more than 10% CR is added to the mixture, the water demand is increasing, resulting in increased viscosity, yield stress, and, as a result, the high flow time [103]. The initial and final setting times of cement paste with various FA and CR ratios are presented in Figure 2-16b. In comparison to the control paste, the results reveal that increasing the FA-CR content by 20% slightly reduced the initial and final setting times. The FA-CR, for example, increased the initial and final setting times by 10 and 35 minutes, respectively, at a 10% cement replacement level. Setting times are not considerably altered below 30% FA-CR addition. The decrease in setting time is expected, and it is related to the finer CR particles, which result in a considerable increase in the number of nucleation sites. It is well known that adding more nanomaterial to mortar promotes the development of more hydration products, which accelerates the hydration reactions [104,105]. Nevertheless, lowering the FA-CR rate in cement below 30% increases the separation between hydrated cement particles, delaying the development of capillary bridges and, as a result, the development of an interlocking network between the particles [72]. Nonetheless, the setting periods of all pastes are consistent with the NF P15-431 standard [35].

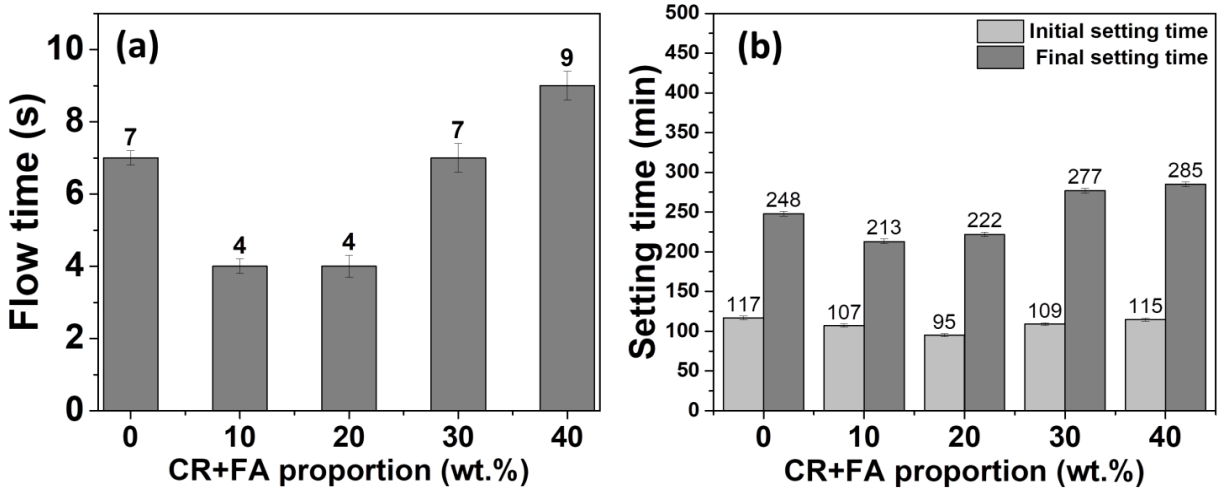

Figure 2-16 (a) Flow time and (b) CR-FA mortars setting time.

2.7.1.4 Thermal conductivity of concrete mixes

The thermal conductivity of the concrete samples showed a considerable decrease trend when FA and CR content increased, as shown in Figure 2-17. The slope of the drop in thermal conductivity between the control concrete and the concrete with 10% FA+CR is greater, and the slope of the decrease in thermal conductivity gets less above 10% substitution level.

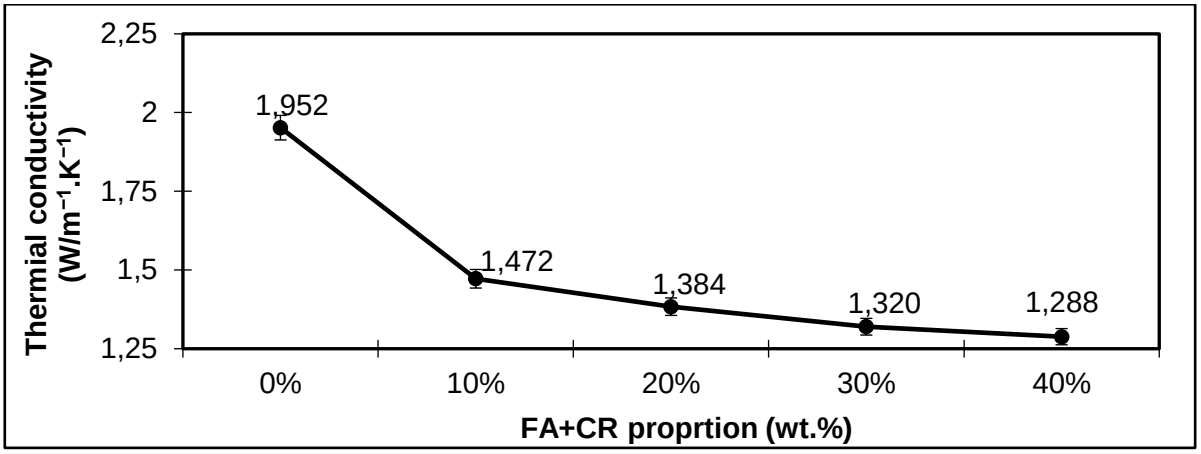

Figure 2-17 Variation of the thermal condictivity of the concretes elaborated with different CR+FA proportion after 28 days of curing. Error bars are standard deviation calculated for 3 replicates.

These first findings are intriguing, demonstrating that substituting fly ash and *Crepidula* for cement can increase concrete's thermal insolation.

2.7.1.5 Mechanical strength of mortar

The compressive strengths of mortars mix after 2, 7, 14, and 28 days of curing are shown in Figure 2-18a. The compressive strength of the mortar are enhanced with time, regardless of the composition considered. The results also demonstrate that replacing 10% of the cement with CR+FA resulted in largest strength for all curing times when compared to control mortar. Indeed, the FA5-CR5 mortar's compressive strength improves over time, surpassing the control mortar by 8% and 4% at 2 and 28 days, respectively. Afterwards, a 10% replacement of FA-CR produces the maximum compressive strength at 28 days, with a value of 59 MPa. The compressive strength decreased with the replacement rate above 10% FA-CR substitution and remains superior to 28 MPa. Finally, the results obtained for cement mortar mixes containing FA-CR are still suitable for use in the construction industry.

Particularly specific combinations with mixed FA and calcium carbonate systems (such as limestone and CR) showed a compressive strength gain as compared to the CM.

When FA and $CaCO_3$ are mixed, the strength increase, particularly at low concentrations [106].

The interaction of the $CaCO_3$ particles with the FA and cement hydration phases results in the creation of carboaluminates at the expense of monosulphate, and consequently, the hydration products increase the compressive strength [107]. Li et al, Péra et al, Shaikh and Supit [107–109] found that CR can react with tricalcium silicate, accelerate the hardening and development of initial strength in mortar. FA also adds more aluminates to the system, lowering the sulfate/aluminate ratio and amplifying the CR's effect. Furthermore, poor dispersion due to CR particle agglomeration in the wet mix and van der Waals forces in the cement could be responsible for the lower compressive strength produced with a larger FA-CR component [107].

The evolution of flexural tensile strengths is similar with those of compressive strengths, as shown in Figure 2-18b. Indeed, the flexural tensile strength of the mortar containing 10% FA-CR is higher than that of all specimen mixes and for all curing days, including the control mortar. The flexural tensile strengths of the 10% FA-CR specimen improve by 3% and 1%, respectively, as compared to the control mix at 2 and 28 days. The loss in flexural tensile strength as level replacement increases is most likely owing to increased CR finesses and subsequent CR particle agglomeration at high proportions. Aggregation of CR particles destabilizes the system by limiting the production of uniform hydrated microstructures, resulting in a reduction in strength [107,110]. Thus, it is recommended to use FA-CR powder with a low replacement rate (up to 10%) to achieve best compressive and flexural strength.

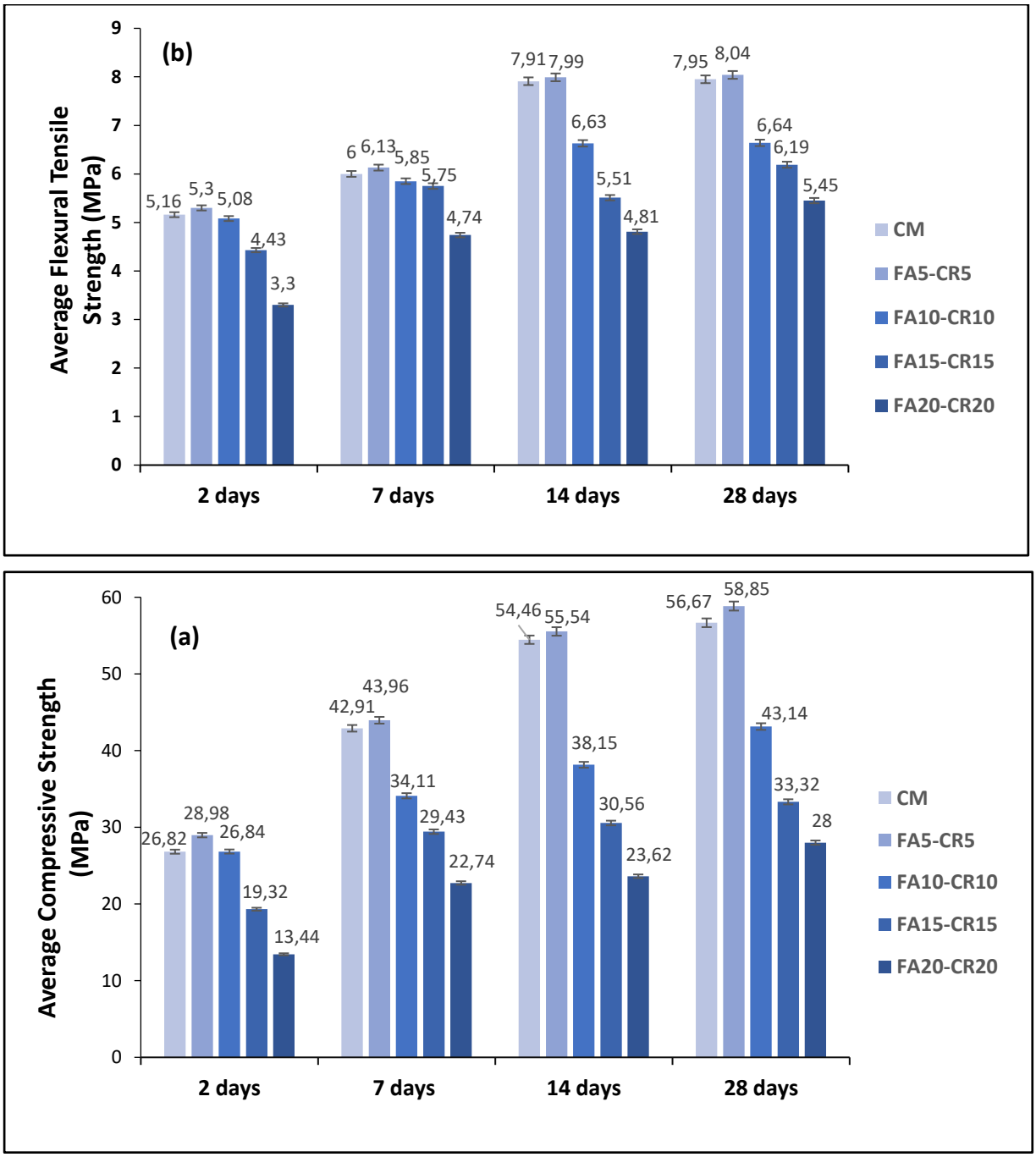

Figure 2-18 (a) Average compressive strength at different ages of the mixtures with different CR+FA proportion. (b) Average flexural strength at different ages of the mixtures with different CR+FA proportion.

2.7.1.6 Analyses of mortars by Raman spectroscopy

Only the C-S-H phase is present in the hydrated structures developped on the control mortar after 28 days, according to Raman analysis (Figure 2-19). In the case of fly ash and C*repidula* mix mortars, Raman spectra show also the presence of tricarboaluminate in addition to C-S-H. In addition to these phases, the Raman analyses reveal also the presence of quartz (originating from sand) as well as calcite

for the control mortar and a mixture of calcite and aragonite for the FA-CR mortars, in addition to the hydrate phases. Nevertheless, in order to understand the mechanism of cement hydration, we only investigated the hydrated phases.

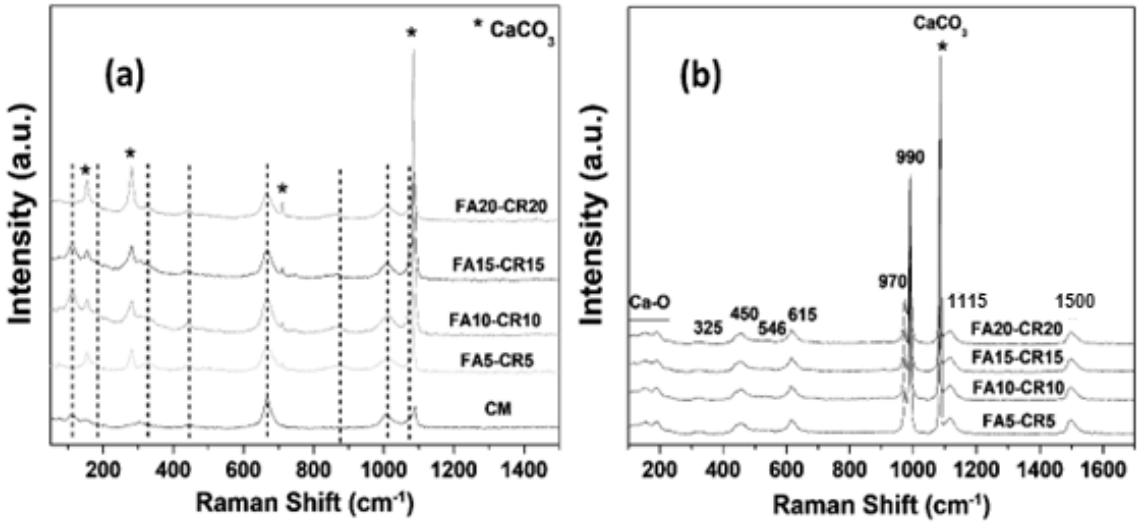

Figure 2-19 Raman spectrum of the mortar mixture after 28 days of curring time: (a) CSH, (b) Carbo-aluminate.

Raman spectroscopy has been used extensively to investigate the nature of the hydrated C-S-H and C-S-A-H structures generated during cement hydration [67,111]. All C-S-H Raman spectra demonstrate the presence of the most strong vibration mode at 670 cm^{-1}, which is related to the Si–O stretching vibration (Figure 2-19a). The vibration modes assigned to the Ca O polyhedra's lattice vibrations are present at low wavenumbers (< 350 cm^{-1}). The Si–O–Si twisting and stretching modes are attributed to the band at 440 cm^{-1}. The Q_n symmetric stretching modes of silicate Si-O are assigned to the bands between 850 and 1100 cm^{-1}, where Q refers to the SiO_4 tetrahedron and n to the number of oxygen shared with neighbouring tetrahedral. Q0 denotes a solitary monomer, Q_1 and Q_2 chains, and Q_3 and Q_4 interconnected structures, respectively. Only the Q_1, Q_2, and Q_3 species are found in our mortars, and they are centered at 880, 1010, and 1075 cm^{-1}, respectively.

When examining the Raman spectra of C-S-H produced on a regular mortar surface and in the FNS-CR specimen, it is found that the Ca–O polyhedra vibration modes significantly increase their intensity and shift to low wavenumber. This phenomenon is attributed to the presence of *Crepidula* shells, which provide high amount of calcium leading to an increased ordering of the calcium environment of C-S-H structure and thus increasing the degree of polymerization.

In the FA-CR specimens, the Q_2 symmetric stretching modes of silicate (1005-1020 cm^{-1}) separated into two bands at 1007 and 1016 cm^{-1}, according to the Raman spectra. This finding supports the hypothesis that the number of the silica tetrahedrons Q_{2p} (pairing) and Q_{2b} (bridging) modified the length of the Si–O–Si chain [68]. This is associated to the significant amount of silica supplied by FA. Indeed, the excess of calcium hydroxide reacts with the silicates originating from FA to produce additional C-S-H, resulting in a reduction in porosity and increased strengths.

The Raman spectra demonstrate that the C-O stretching in the $CaCO_3$ group becomes more prominent as the CR content increases. This demonstrates that at high CR proportions, the amount of undissolved $CaCO_3$ becomes highly critical, resulting in an increase in nonpozzolanic materials, which explains the observed reduction in compressive and flexural strengths above 20% cement substitution.

The Raman spectra of carbo-aluminates found in FA-CR specimens (Figure 2-19b) show the presence of the intense vibration bandes at 970 and 990 cm^{-1}, which have been assigned as the $v_1(SO_4)$ vibration mode [58,112]. Furthermore, the Raman spectrum reveals also the presence of relatively weak bands at 1113 cm^{-1} for $v_3(SO_4)$, 615 cm^{-1} for $v_4(SO_4)$, 546 cm^{-1} for Al-OH stretching mode, 450 cm^{-1} for $v_2(SO_4)$, and 345 cm^{-1} for Al-OH rotation and translation) [112]. The presence of the weaker band 1086 cm^{-1} produced by C-O stretching in the carbonate groups present in calcium-carbonate, due to a mixture of calcite and aragonite, indicates that the ettringite has undergone carbonation. This contributes to the development of tricarboaluminate. The dissolved CO_3^{2-} ions from CR take part in hydration reactions and react with the aluminates supplied by FA. As a result, carboaluminates stabilized the ettringite developed at an early age [72]. Carboaluminates are denser than sulfoaluminates, with larger volumes and stiffness [74,75], resulting in increased porosity reduction and faster hardening and strength development in mortar.

2.8 Conclusions

The effect of partial cement replacement with an FA and CR mix on the mechanical and thermal properties of mortar and concrete is examined. The use of CR and FA will result in significant cost savings in cement manufacturing. It has the potential to significantly contribute to the attainment of sustainable development goals and, as a result, the reduction of CO_2 emissions.

- The replacement of cement with 10% of CR+FA resulted in largest compressive strength for all curing times when compared to control mortar
- The flexural tensile strength of the mortar containing 10% FA-CR is higher than that of all specimen mixes and for all curing days, including the control mortar.
- The Raman analysis show that the combination of FA and CR has two major advantages: (i) FA's high silica content promotes polymerization in the C-S-H structure; (ii) the *Crepidula* shells' dissolved CO_3^{2-} ions induce the formation of C-S-A-H, resulting in a reduction in porosity and increased strengths.
- The results show a clear potential for using FA-CR wastes as a partial replacement for cement at an optimal rate of 30%.

Furthermore, as the substitution amount is increased, the concrete's thermal conductivity reduces dramatically. It has been demonstrated that these by-products have a real potential for partial cement replacement at a rate of 30 % (FA15-CR15).

2.9 References

[1] Andrew, R. M., 2018, "Global CO_2 Emissions from Cement Production, 1928–2017," Earth System Science Data, **10**(4), pp. 2213–2239.

[2] The European Cement Association (CEMBUREAU), 2017, *Activity Report*, first ed, Belgium.

[3] Malhotra, V., 2000, "Role of Supplementary Cementing Materials in Reducing Greenhouse Gas Emissions," *Concrete Technology for a Sustainable Development in the 21st Century*, E & FN SPON, London, pp. 226–235.

[4] Siddique, R., 2008, *Waste Materials and By-Products in Concrete*, Springer-Verlag Berlin Heidelberg.

[5] Sakoi, Y., Aba, M., Tsukinaga, Y., and Nagataki, S., 2013, "Properties of Concrete Used in Ferronickel Slag Aggregate," Tokyo, Japan, p. 6.

[6] Higuera, P., 2019, *Évaluation Technico-Économique Des Débouchés de Valorisation Des Scories de Nickel. Territoire : Nouvelle-Calédonie*, IAE Nantes—Économie & Management Université de Nantes, Nantes, France,.

[7] Tangahu, B. V., Warmadewanthi, I., Saptarini, D., Pudjiastuti, L., Tardan, M. A. M., and Luqman, A., 2015, "Ferronickel Slag Performance from Reclamation Area in Pomalaa, Southeast Sulawesi, Indonesia," ACES, **05**(03), pp. 408–412.

[8] Sun, J., Wang, Z., and Chen, Z., 2018, "Hydration Mechanism of Composite Binders Containing Blast Furnace Ferronickel Slag at Different Curing Temperatures," J Therm Anal Calorim, **131**(3), pp. 2291–2301.

[9] Katsikaris, K., Voutsas, E., Magoulas, K., Andronikos, G., and Stamataki, S., 2002, "Recycling Ferrous-Nickel Slag in Blast Cleaning," Waste Manag Res, **20**(3), pp. 269–278.

[10] Ibrahim, E., Barnabé, P., Ramanaidou, E., and Pirard, E., 2018, "Mapping Mineral Chemistry of a Lateritic Outcrop in New Caledonia through Generalized Regression Using Sentinel-2 and Field Reflectance Spectra," International Journal of Applied Earth Observation and Geoinformation, **73**, pp. 653–665.

[11] Ashok, D., Dalvi, D., Gordon, D. W., Mr, B., and Osborne, R. C., 2004, "The Past and the Future of Nickel Laterites," *PDAC 2004 International Convention, Trade Show & Investors Exchange March 7-10*, p. 18.

[12] "Le Nickel - SLN Ferronickel Slag - FNS: a promising construction material for the Pacific Region," SLN [Online]. Available: https://sln.eramet.com/. [Accessed: 12-Apr-2022].

[13] Nguyen, Q. D., Khan, M. S. H., Castel, A., and Kim, T., 2019, "Durability and Microstructure Properties of Low-Carbon Concrete Incorporating Ferronickel Slag Sand and Fly Ash," J. Mater. Civ. Eng., **31**(8), p. 04019152.

[14] Saha, A. K., and Sarker, P. K., 2017, "Sustainable Use of Ferronickel Slag Fine Aggregate and Fly Ash in Structural Concrete: Mechanical Properties and Leaching Study," Journal of Cleaner Production, **162**, pp. 438–448.

[15] Anastasiou, E., Georgiadis Filikas, K., and Stefanidou, M., 2014, "Utilization of Fine Recycled Aggregates in Concrete with Fly Ash and Steel Slag," Construction and Building Materials, **50**, pp. 154–161.

[16] Olofinnade, O., Ede, A., Ndambuki, J., and Bamigboye, G., 2016, "Structural Properties of Concrete Containing Ground Waste Clay Brick Powder as Partial Substitute for Cement."

[17] Saha, A. K., and Sarker, P. K., 2018, “Durability of Mortar Incorporating Ferronickel Slag Aggregate and Supplementary Cementitious Materials Subjected to Wet–Dry Cycles,” Int J Concr Struct Mater, **12**(1), p. 29.

[18] Rahman, M. A., Sarker, P. K., Shaikh, F. U. A., and Saha, A. K., 2017, “Soundness and Compressive Strength of Portland Cement Blended with Ground Granulated Ferronickel Slag,” Construction and Building Materials, **140**, pp. 194–202.

[19] 2019, “Chiffres Clés de La Filière Pêche et Aquaculture En France” [Online]. Available: https://www.franceagrimer.fr/Actualite/Filieres/Peche-et-aquaculture/2019/Chiffres-cles-de-la-filiere-peche-et-aquaculture-en-France-en-2019. [Accessed: 08-Oct-2021].

[20] Sickels-Taves, L. B., and Sheehan, M. S., 1999, *The Lost Art of Tabby Redefined: Preserving Oglethorpe’s Architectural Legacy*, Architectural Conservation Press, Southfield, MI.

[21] Tayeh, B. A., Hasaniyah, M. W., Zeyad, A. M., and Yusuf, M. O., 2019, “Properties of Concrete Containing Recycled Seashells as Cement Partial Replacement: A Review,” Journal of Cleaner Production, **237**, p. 117723.

[22] Mohammad, W. A. S. B. W., Hazurina Othman, N., Ibrahim, M. H. W., Rahim, M. A., Shahidan, S., and Rahman, R. A., 2017, “A Review on Seashells Ash as Partial Cement Replacement,” Materials Science and Engineering Conference Series, **271**(1), p. 012059.

[23] Mosher, S., Cope, W. G., Weber, F. X., Shea, D., and Kwak, T. J., 2012, “Effects of Lead on Na^+, K^+-ATPase and Hemolymph Ion Concentrations in the Freshwater Mussel Elliptio Complanata,” Environ Toxicol, **27**(5), pp. 268–276.

[24] 2012, “NF EN 197-1. Cement - Part 1 : composition, specifications and conformity criteria for common cements.”

[25] Taylor, H. F. W., 1997, *Cement Chemistry*, Thomas Telford.

[26] Menendez, G., Bonavetti, V. L., Donza, H., Trezza, M., and Irassar, E. F., 2002, “Ternary Blended Cement for High-Performance Concrete,” Brazil.

[27] Tan, Z., De Schutter, G., Ye, G., and GAO, Y., 2013, “The Effect of Limestone Powder Addition on Strength of Slag Blended Cement,” Nanjing, China, pp. 1888–1898.

[28] 2016, “NF EN 196-1. Methods of testing cement - Part 1: Determination of strength.”

[29] Caglioti, G., Paoletti, A., and Ricci, F. P., 1958, “Choice of Collimators for a Crystal Spectrometer for Neutron Diffraction,” Nuclear Instruments, **3**(4), pp. 223–228.

[30] Gražulis, S., Daškevič, A., Merkys, A., Chateigner, D., Lutterotti, L., Quirós, M., Serebryanaya, N. R., Moeck, P., Downs, R. T., and Le Bail, A., 2012, “Crystallography Open Database (COD): An Open-Access Collection of Crystal Structures and Platform for World-Wide Collaboration,” Nucleic Acids Res, **40**(Database issue), pp. D420-427.

[31] Lutterotti, L., Matthies, S., Wenk, H.-R., Schultz, A. S., and Richardson, J. W., 1997, “Combined Texture and Structure Analysis of Deformed Limestone from Time-of-Flight Neutron Diffraction Spectra,” Journal of Applied Physics, **81**(2), pp. 594–600.

[32] El Mendili, Y., Vaitkus, A., Merkys, A., Gražulis, S., Chateigner, D., Mathevet, F., Gascoin, S., Petit, S., Bardeau, J.-F., Zanatta, M., Secchi, M., Mariotto, G., Kumar, A., Cassetta, M., Lutterotti, L., Borovin, E., Orberger, B., Simon, P., Hehlen, B., and Le Guen, M., 2019, "Raman Open Database: First Interconnected Raman–X-Ray Diffraction Open-Access Resource for Material Identification," J Appl Crystallogr, **52**(3), pp. 618–625.

[33] 2018, "ASTM C204. Test Methods for Fineness of Hydraulic Cement by Air-Permeability Apparatus."

[34] 2017, "NF P18-452. Concretes - Measuring the flow time of concretes and mortars using a workabilitymeter."

[35] 1994, "NF P15-431. Hydraulic binders. Methods for testing cement. Setting test."

[36] Kosanović, C., Stubičar, N., Tomašić, N., Bermanec, V., and Stubičar, M., 2005, "Synthesis of a Forsterite Powder by Combined Ball Milling and Thermal Treatment," Journal of Alloys and Compounds, **389**(1), pp. 306–309.

[37] Abdi Maghsoudlou, M. S., Ebadzadeh, T., Sharafi, Z., Arabi, M., and Zahabi, K. R., 2016, "Synthesis and Sintering of Nano-Sized Forsterite Prepared by Short Mechanochemical Activation Process," Journal of Alloys and Compounds, **678**, pp. 290–296.

[38] Michel, R., Ammar, M. R., Simon, P., De Bilbao, E., and Poirier, J., 2014, "Behaviour of Olivine Refractories at High Temperature: Agglomeration in a Fluidized Bed Reactor," Refractories Worldforum, **6**, pp. 95–98.

[39] Galeener, F. L., 1982, "Planar Rings in Vitreous Silica," Journal of Non-Crystalline Solids, **49**(1), pp. 53–62.

[40] Matson, D. W., Sharma, S. K., and Philpotts, J. A., 1983, "The Structure of High-Silica Alkali-Silicate Glasses. A Raman Spectroscopic Investigation," Journal of Non-Crystalline Solids, **58**(2), pp. 323–352.

[41] McMillan, P., 1984, "Structural Studies of Silicate Glasses and Melts-Applications and Limitations of Raman Spectroscopy," American Mineralogist - AMER MINERAL, **69**, pp. 622–644.

[42] Deng, C.-S., Breen, C., Yarwood, J., Habesch, S., Phipps, J., Craster, B., and Maitland, G., 2002, "Ageing of Oilfield Cement at High Humidity: A Combined FEG-ESEM and Raman Microscopic Investigation," J. Mater. Chem., **12**(10), pp. 3105–3112.

[43] Martínez-Ramírez, S., Frías, M., and Domingo, C., 2006, "Micro-Raman Spectroscopy in White Portland Cement Hydration: Long-Term Study at Room Temperature," Journal of Raman Spectroscopy, **37**, pp. 555–561.

[44] Ma, H., Zhu, H., Yi, C., Fan, J., Chen, H., Xu, X., and Wang, T., 2019, "Preparation and Reaction Mechanism Characterization of Alkali-Activated Coal Gangue–Slag Materials," Materials (Basel), **12**(14), p. 2250.

[45] El Mendili, Y., Chateigner, D., Orberger, B., Gascoin, S., Bardeau, J.-F., Petit, S., Duée, C., Le Guen, M., and Pilliere, H., 2019, "Combined XRF, XRD, SEM-EDS, and Raman Analyses on Serpentinized Harzburgite (Nickel Laterite Mine, New Caledonia): Implications for Exploration and Geometallurgy," ACS Earth Space Chem., **3**(10), pp. 2237–2249.

[46] Takei, H., 1978, "Growth of Fayalite (Fe2SiO4) Single Crystals by the Floating-Zone Method," Journal of Crystal Growth, **43**(4), pp. 463–468.

[47] Kolesov, B. A., and Geiger, C. A., 2004, “A Raman Spectroscopic Study of Fe–Mg Olivines,” Phys Chem Minerals, **31**(3), pp. 142–154.

[48] Chopelas, A., 1991, “Single Crystal Raman Spectra of Forsterite, Fayalite, and Monticellite,” American Mineralogist, **76**, pp. 1101–1109.

[49] Lin, C.-C., 2004, “Pressure-Induced Polymorphism in Enstatite (MgSiO3) at Room Temperature: Clinoenstatite and Orthoenstatite,” Journal of Physics and Chemistry of Solids, **65**(5), pp. 913–921.

[50] Sharma, S. K., Simons, B., and Yoder, H. S., 1983, “Raman Study of Anorthite, Calcium Tschermak’s Pyroxene, and Gehlenite in Crystalline and Glassy States,” American Mineralogist, **68**(11–12), pp. 1113–1125.

[51] McMillan, P. F., and Hofmeister, A. M., 1988, “Infrared and Raman Spectroscopy,” *Spectroscopic Methods in Mineralogy and Geology*, De Gruyter, pp. 99–160.

[52] Farmer, V. C., 1974, “Orthosilicates, Pyrosilicates, and Other Finite-Chain Silicates,” *The Infrared Spectra of Minerals*, Mineralogical Society, London, pp. 285–303.

[53] Reddy, B. J., and Frost, R. L., 2005, “Spectroscopic Characterization of Chromite from the Moa-Baracoa Ophiolitic Massif, Cuba,” Spectrochim Acta A Mol Biomol Spectrosc, **61**(8), pp. 1721–1728.

[54] Réguer, S., Dillmann, P., and Mirambet, F., 2007, “Buried Iron Archaeological Artefacts: Corrosion Mechanisms Related to the Presence of Cl-Containing Phases,” Corrosion Science, **49**(6), pp. 2726–2744.

[55] El Mendili, Y., Abdelouas, A., Ait Chaou, A., Bardeau, J.-F., and Schlegel, M. L., 2014, “Carbon Steel Corrosion in Clay-Rich Environment,” Corrosion Science, **88**, pp. 56–65.

[56] Scheinost, A. C., 2005, “Metal Oxides,” *Encyclopedia of Soils in the Environment*, D. Hillel, ed., Elsevier Academic Press, pp. 428–438.

[57] Keller, P., 1969, “Vorkommen, Entstehung und Phasenumwandlung von β-FeOOH in Rost,” Materials and Corrosion, **20**(2), pp. 102–108.

[58] Ait Chaou, A., Abdelouas, A., Mendili, Y. E., Bouakkaz, R., Utsunomiya, S., Martin, C., and Bourbon, X., 2015, “Vapor Hydration of a Simulated Borosilicate Nuclear Waste Glass in Unsaturated Conditions at 50 °C and 90 °C,” RSC Adv., **5**(79), pp. 64538–64549.

[59] Rashad, A. M., and Zeedan, S. R., 2012, “A Preliminary Study of Blended Pastes of Cement and Quartz Powder under the Effect of Elevated Temperature,” Construction and Building Materials, **29**, pp. 672–681.

[60] Lin, R.-S., Wang, X.-Y., and Zhang, G.-Y., 2018, “Effects of Quartz Powder on the Microstructure and Key Properties of Cement Paste,” Sustainability, **10**(10), p. 3369.

[61] Gillet, P., Biellmann, C., Reynard, B., and McMillan, P., 1993, “Raman Spectroscopic Studies of Carbonates Part I: High-Pressure and High-Temperature Behaviour of Calcite, Magnesite, Dolomite and Aragonite,” Physics and Chemistry of Minerals, **20**, pp. 1–18.

[62] Lizarazo-Marriaga, J., Claisse, P. A., and Ganjian, E., 2011, “Effect of Steel Slag and Portland Cement in the Rate of Hydration and Strength of Blast Furnace Slag Pastes,” J. Mater. Civil. Eng, **23**(2), pp. 153–160.

[63] Castellano, C. C., Bonavetti, V. L., Donza, H. A., and Irassar, E. F., 2016, "The Effect of w/b and Temperature on the Hydration and Strength of Blastfurnace Slag Cements," Constr. Build. Mater, **111**, pp. 679–688.

[64] Abinaya, S., and Venkatesh, S., 2016, "An Effect on Oyster Shell Powder ' s Mechanical Properties in Self Compacting Concrete," Int. J. Innov. Res. Sci. Eng. Technol, **5**, pp. 11785–11789.

[65] Papadakis, V. G., Antiohos, S., and Tsimas, S., 2002, "Supplementary Cementing Materials in Concrete: Part II: A Fundamental Estimation of the Efficiency Factor," Cement and Concrete Research, **32**(10), pp. 1533–1538.

[66] Kirkpatrick, R. J., Yarger, J. L., McMillan, P. F., Ping, Y., and Cong, X., 1997, "Raman Spectroscopy of C-S-H, Tobermorite, and Jennite," Adv. Cem. Based Mater, **5**(3), pp. 93–99.

[67] Garbev, K., Stemmermann, P., Black, L., Breen, C., Yarwood, J., and Gasharova, B., 2007, "Structural Features of C–S–H(I) and Its Carbonation in Air—A Raman Spectroscopic Study. Part I: Fresh Phases," Journal of the American Ceramic Society, **90**(3), pp. 900–907.

[68] Grangeon, S., Claret, F., Roosz, C., Sato, T., Gaboreau, S., and Linard, Y., 2016, "Structure of Nanocrystalline Calcium Silicate Hydrates: Insights from X-Ray Diffraction, Synchrotron X-Ray Absorption and Nuclear Magnetic Resonance," J Appl Crystallogr, **49**(Pt 3), pp. 771–783.

[69] Deb, S., Manghnani, M., Ross, K., Livingston, R., and Monteiro, P., 2003, "Raman Scattering and X-Ray Diffraction Study of the Thermal Decomposition of an Ettringite-Group Crystal," Phys. Chem. Miner, **30**, pp. 31–38.

[70] Othman, N. H., Abu Bakar, B. H., Don, M. M., and Johari, M. A. M., 2013, "Cockle Shell Ash Replacement for Cement and Filler in Concrete," Malaysian. J. Civil. Eng, **25**, pp. 201–211.

[71] Plummer, L. N., and Busenberg, E., 1982, "The Solubilities of Calcite, Aragonite and Vaterite in CO2-H2O Solutions between 0 and 90°C, and an Evaluation of the Aqueous Model for the System CaCO3-CO2-H2O," Geochimica et Cosmochimica Acta, **46**(6), pp. 1011–1040.

[72] Matschei, T., Lothenbach, B., and Glasser, F. P., 2007, "The Role of Calcium Carbonate in Cement Hydration," Cement and Concrete Research, **37**(4), pp. 551–558.

[73] Cost, V. T., Matschei, T., Shannon, J., and Howard, I. L., 2014, "Extending the Use of Fly Ash and Slag Cement in Concrete through the Use of Portland-Limestone Cement."

[74] De Weerdt, K., Ben Haha, M., Le Saout, G., Kjellsen, K. O., Justnes, H., and Lothenbach, B., 2011, "Hydration Mechanisms of Ternary Portland Cements Containing Limestone Powder and Fly Ash," Cem. Concr. Res, **41**(3), pp. 279–291.

[75] Moon, J., Oh, J. E., Balonis, M., Glasser, F. P., Clark, S. M., and Monteiro, P. J. M., 2012, "High Pressure Study of Low Compressibility Tetracalcium Aluminum Carbonate Hydrates 3CaO·Al2O3·CaCO3·11H2O," Cement and Concrete Research, **42**(1), pp. 105–110.

[76] Zhang, T., Vandeperre, L. J., and Cheeseman, C. R., 2014, "Formation of Magnesium Silicate Hydrate (M-S-H) Cement Pastes Using Sodium Hexametaphosphate," Cement. Concr. Res, **65**, pp. 8–14.

[77] Katsiotis, N. S., Tsakiridis, P. E., Velissariou, D., Katsiotis, M. S., Alhassan, S. M., and Beazi, M., 2015, "Utilization of Ferronickel Slag as Additive in Portland Cement: A Hydration Leaching Study," Waste Biomass Valor, **6**(2), pp. 177–189.

[78] Lemonis, N., Tsakiridis, P. E., Katsiotis, N. S., Antiohos, S., Papageorgiou, D., Katsiotis, M. S., and Beazi-Katsioti, M., 2015, "Hydration Study of Ternary Blended Cements Containing Ferronickel Slag and Natural Pozzolan," Construction and Building Materials, **81**, pp. 130–139.

[79] Ma, Z., Tang, Q., Yang, D., and Ba, G., 2019, "Durability Studies on the Recycled Aggregate Concrete in China over the Past Decade: A Review," Advances in Civil Engineering, **2019**, p. e4073130.

[80] Wu, C., Chen, W., Zhang, H., Yu, H., Zhang, W., Jiang, N., and Liu, L., 2017, "The Hydration Mechanism and Performance of Modified Magnesium Oxysulfate Cement by Tartaric Acid," Construction and Building Materials, **144**, pp. 516–524.

[81] 2019, "Direct CO2 Emissions from Selected Heavy Industry Sectors," IEA [Online]. Available: https://www.iea.org/data-and-statistics/charts/direct-co2-emissions-from-selected-heavy-industry-sectors-2019.

[82] Rashad, A. M., 2013, "A Comprehensive Overview about the Influence of Different Additives on the Properties of Alkali-Activated Slag – A Guide for Civil Engineer," Construction and Building Materials, **47**, pp. 29–55.

[83] Gartner, E., 2004, "Industrially Interesting Approaches to 'Low-CO2' Cements," Cement and Concrete Research, **34**(9), pp. 1489–1498.

[84] Liu, J., Qin, Q., and Yu, Q., 2020, "The Effect of Size Distribution of Slag Particles Obtained in Dry Granulation on Blast Furnace Slag Cement Strength."

[85] Mehta, A., Siddique, R., Ozbakkaloglu, T., Uddin Ahmed Shaikh, F., and Belarbi, R., 2020, "Fly Ash and Ground Granulated Blast Furnace Slag-Based Alkali-Activated Concrete: Mechanical, Transport and Microstructural Properties," Construction and Building Materials, **257**, p. 119548.

[86] Xu, W., Zhang, Y., and Liu, B., 2020, "Influence of Silica Fume and Low Curing Temperature on Mechanical Property of Cemented Paste Backfill," Construction and Building Materials, **254**, p. 119305.

[87] Ahmaruzzaman, M., 2010, "A Review on the Utilization of Fly Ash," Progress in Energy and Combustion Science, **36**(3), pp. 327–363.

[88] Bakharev, T., 2005, "Geopolymeric Materials Prepared Using Class F Fly Ash and Elevated Temperature Curing," Cement and Concrete Research, **35**(6), pp. 1224–1232.

[89] Tang, S. W., Cai, X. H., He, Z., Shao, H. Y., Li, Z. J., and Chen, E., 2016, "Hydration Process of Fly Ash Blended Cement Pastes by Impedance Measurement," Construction and Building Materials, **113**, pp. 939–950.

[90] Yu, J., Lu, C., Leung, C. K. Y., and Li, G., 2017, "Mechanical Properties of Green Structural Concrete with Ultrahigh-Volume Fly Ash," Construction and Building Materials, **147**, pp. 510–518.

[91] Rashad, A. M., 2015, "A Brief on High-Volume Class F Fly Ash as Cement Replacement – A Guide for Civil Engineer," International Journal of Sustainable Built Environment, **4**(2), pp. 278–306.

[92] Bentz, D., Peltz, M., Durán-Herrera, A., Valdez, P., and Juárez, C., 2011, “Thermal Properties of High-Volume Fly Ash Mortars and Concretes,” Journal of Building Physics, **34**(3), pp. 263–275.

[93] Durán-Herrera, A., Juárez, C. A., Valdez, P., and Bentz, D. P., 2011, “Evaluation of Sustainable High-Volume Fly Ash Concretes,” Cement and Concrete Composites, **33**(1), pp. 39–45.

[94] Yang, E.-H., Yang, Y., and Li, V. C., 2007, “Use of High Volumes of Fly Ash to Improve ECC Mechanical Properties and Material Greenness,” MJ, **104**(6), pp. 620–628.

[95] Lam, L., Wong, Y. L., and Poon, C. S., 2000, “Degree of Hydration and Gel/Space Ratio of High-Volume Fly Ash/Cement Systems,” Cement and Concrete Research, **30**(5), pp. 747–756.

[96] Berry, E. E., Hemmings, R. T., and Cornelius, B. J., 1990, “Mechanisms of Hydration Reactions in High Volume Fly Ash Pastes and Mortars,” Cement and Concrete Composites, **12**(4), pp. 253–261.

[97] Escalante-Garcia, J.-I., and Sharp, J. H., 2004, “The Chemical Composition and Microstructure of Hydration Products in Blended Cements,” Cement and Concrete Composites, **26**(8), pp. 967–976.

[98] Lothenbach, B., Scrivener, K., and Hooton, R. D., 2011, “Supplementary Cementitious Materials,” Cement and Concrete Research, **41**(12), pp. 1244–1256.

[99] Wang, J., Liu, E., and Li, L., 2019, “Characterization on the Recycling of Waste Seashells with Portland Cement towards Sustainable Cementitious Materials,” Journal of Cleaner Production, **220**, pp. 235–252.

[100] Bouasria, M., Khadraoui, F., Benzaama, M.-H., Touati, K., Chateigner, D., Gascoin, S., Pralong, V., Orberger, B., Babouri, L., and El Mendili, Y., 2021, “Partial Substitution of Cement by the Association of Ferronickel Slags and Crepidula Fornicata Shells,” Journal of Building Engineering, **33**, p. 101587.

[101] 2012, “NF EN 450-1. Fly ash for concrete - Part 1 : definition, specifications and conformity criteria.”

[102] El Mendili, Y., Bouasria, M., Benzaama, M.-H., Khadraoui, F., Le Guern, M., Chateigner, D., Gascoin, S., and Bardeau, J.-F., 2021, “Mud-Based Construction Material: Promising Properties of French Gravel Wash Mud Mixed with Byproducts, Seashells and Fly Ash as a Binder,” **14**(20), p. 6216.

[103] Esping, O., 2008, “Effect of Limestone Filler BET(H2O)-Area on the Fresh and Hardened Properties of Self-Compacting Concrete,” Cement and Concrete Research, **7**(38), pp. 938–944.

[104] Gutteridge, W. A., and Dalziel, J. A., 1990, “Filler Cement: The Effect of the Secondary Component on the Hydration of Portland Cement: Part 2: Fine Hydraulic Binders,” Cement and Concrete Research, **20**(6), pp. 853–861.

[105] Marzouki, A., Lecomte, A., Beddey, A., Diliberto, C., and Ouezdou, M. B., 2013, “The Effects of Grinding on the Properties of Portland-Limestone Cement,” Construction and Building Materials, **Complete**(48), pp. 1145–1155.

[106] Georgescu, M., and Saca, N., 2009, “PROPERTIES OF BLENDED CEMENTS WITH LIMESTONE FILLER AND FLY ASH CONTENT,” scientific bulletin, **71**, p. 12.

[107] Shaikh, F. U. A., and Supit, S. W. M., 2014, “Mechanical and Durability Properties of High Volume Fly Ash (HVFA) Concrete Containing Calcium Carbonate (CaCO3) Nanoparticles,” Construction and Building Materials, **70**, pp. 309–321.

[108] Li, W., Huang, Z., Zu, T., Shi, C., Duan, W. H., and Shah, S. P., 2016, “Influence of Nanolimestone on the Hydration, Mechanical Strength, and Autogenous Shrinkage of Ultrahigh-Performance Concrete,” Journal of Materials in Civil Engineering, **28**(1), p. 04015068.

[109] Péra, J., Husson, S., and Guilhot, B., 1999, “Influence of Finely Ground Limestone on Cement Hydration,” Cement and Concrete Composites, **21**(2), pp. 99–105.

[110] Li, G., 2004, “Properties of High-Volume Fly Ash Concrete Incorporating Nano-SiO2,” Cement and Concrete Research, **34**(6), pp. 1043–1049.

[111] Bouasria, M., Babouri, L., Khadraoui, F., Chateigner, D., Gascoin, S., Pralong, V., Benzaama, M.-H., Orberger, B., and El Mendili, Y., 2020, “Insight into the Partial Replacement of Cement by Ferronickel Slags from New Caledonia,” European Journal of Environmental and Civil Engineering, **0**(0), pp. 1–19.

[112] Livingston, R. A., Monteiro, P. J. M., Deb, S. K., Manghnani, M. H., and Ross, K., 2003, “Raman Scattering and X-Ray Diffraction Study of the Thermal Decomposition of an Ettringite-Group Crystal,” Physics and Chemistry of Minerals, **30**(1), pp. 31–38.

Chapter 3. Chemical stabilization of earthen construction by alternative binder

Preface

Earthen building materials are typically stabilized for two reasons. One of them is improving the group cohesiveness and strength of soils that would otherwise be unsatisfactory for construction. The other is to improve the material's resistance to water-induced erosion, or durability. Durability is crucial for any material used in construction for obvious reasons; a building's life cycle is typically estimated to be 50 years, although we generally utilize them for much longer. Earthen constructions can withstand a variety of climatic conditions, if the appropriate soil is chosen, the proper precautions are taken, and adequate maintenance is given. The latter offers the oldest justification for not using earth in construction: the labour-intensive nature of maintaining soil makes it uneconomical from a time and money standpoint, and those with the means tend to choose for more durable materials. In regions where human labour is expensive and where buildings that require any type of ongoing upkeep are frequently considered outdated, this argument has gained traction.

Earth stabilization methods used in construction are classified into three categories: mechanical, physical, and chemical. Mechanical stabilization corresponds to material compaction that causes changes in density, mechanical strength, compressibility, permeability, and porosity. Physical stabilization is the process of changing the texture of a material. This includes the controlled mixing of different grain fractions or natural soils, as well as the incorporation of fibers into the soil. Chemical stabilization involves the addition of other materials and chemicals that alter the properties of the soil, either through a physicochemical reaction between the particles and the materials by creating a matrix that binds the grains.

This chapter focuses on the chemical stabilization of cob construction by cementitious and organic binder.

Part I: Alternative mud-based construction material: Promising properties of French gravel wash mud mixed with by-products, seashell and fly ash as alternative binder

Abstract

Each year, the French gravel industry produces about 6.5 million tons of gravel wash mud. This material seems to have a great deal of potential, but it needs to be thoroughly characterized before it can be used as a construction material. Otherwise, it will be removed from the value chain by being disposed of in landfills. We investigated the suitability of gravel wash mud and seashells for unfired earth construction material while employing fly ash as a binder and cementitious stabilizer. The innovative mixture of gravel wash mud, *Crepidula fornicata* shells, and fly ash was thermally and mechanically characterized. The addition of fly ash and *Crepidula* shells to gravel wash muds results in increased silica and calcium content, which both will react with clays to form C-S-H and C-A-C-H by pozzolanic reaction. Accordingly, the use of GWM, CR and FA can contribute extensively to the achievement of the sustainable development goals and thus the reduction of the carbon emission.

Keywords: earthen construction; gravel wash mud; by-products; Mineral stabilization; alternative binder; thermal properties; mechanical performance.

3.1 Introduction

Earth is one of the world's oldest and most commonly employed construction materials [1]. In ancient cities such as Harappa (Pakistan), Marrakech (Morocco), Akhlet-Aton (Egypt), Jericho (Palestine), Chan-Chan (Peru), Duheros (España), Atal-Huyuk (Turkey), Babylon (Iraq) and others, raw earth was the primary building material [1–4]. Earth-based construction materials have progressively regained their importance and are becoming a vital feature of sustainable construction [5] after being eclipsed by the architecture of the fossil fuel consumption era in previous centuries. Furthermore, earth has outstanding properties to retain a more stable and higher interior humidity level, as well as a higher thermal mass potential, than most other construction materials [6]. Earth building construction is certainly the most efficient and cost-effective solution to address housing issues with a low resource demand.

Mud is a fine-grained soil substance mixed with water. It has a high level of sustainability as a building material [7–10]. One of the fundamental principles of sustainable construction is to employ locally available resources, which is a feature of mud all over the world. After all of the qualities have been verified and approved, and the necessary materials have been added, almost any sort of mud can be utilized for construction. Gravel Wash Muds (GWM) and waste mud from gravel quarries are two mud materials that have recently been studied [11,12]. GWM is made up of damp deposits that form during gravel extraction and sand and gravel aggregate washing.

According to UNICEM, the national quarry industry and construction materials organization in France, aggregate demand reached 435 million tons in 2019, with concrete accounting for 27% of this total [13]. Aggregates are employed in the construction of civil engineering, road, and building projects. According to UNICEM [13], the French gravel sector produces each year around 6.5 million tons of gravel wash mud. This material could be exploited as a secondary raw material for a variety of applications due to its excellent properties [11,12,14]. However, by dumping it in landfills, it is usually removed from recycling.

Mud construction, according to Zami and Lee [15], provides a number of advantages, including lower costs due to increased efficiency and lower energy and raw material use. Furthermore, by exploiting locally available low-energy components, the local economy benefits by enhancing the labor component of building costs and adding value. Mud is a mixture of different clay minerals whose structure is crucial since it

determines the mud's durability and strength. Clay minerals are natural composites made up of layered hydrated alumino-silicates that can be divided into four groups: kaolin, illite, smectite, and chlorite [16]. The smectite group has a very expandable crystal structure (upon hydration and heavy element absorption), whereas the non-expandable clays are illite, kaolin, and chlorite. In interaction with water, expendable clays experience substantial volume changes (swelling and shrinking) [17]. As a result of the evaporation of water, significant shrinkage and cracking may occur.

By combining by-products with raw earth or GWM components, a technically possible green-like operation can be achieved. It does not, in reality, necessitate final combustion of the components, hence avoiding the associated GHG emissions. It can also eliminate the problem of clay mineral shrinkage and cracking [18]. As a result, by substituting such by-products for traditional building materials, the construction sector can make significant environmental progress in comparison to the existing scenario [19]. The current study focuses on using by-products materials as an additive to earth for construction in order to adapt earthen construction to local and modern contexts. Villamizar et al., [20] in Colombia, for example, investigated the mechanical characteristics of compressed earth blocks after adding coal ash and cassava peels. They demonstrated that coal-ash may be used to stabilize compacted earth blocks, and that using cassava peels massively improved the dry strength of the composites. Lima et al., [21] in Brazil incorporated sugarcane bagasse ash as an additive to compressed earth blocks as a result of industrial procedures. Such additives do not impact mechanical characteristics, according to their compressive strength and absorption tests.

Thomas et al., [22] demonstrated the feasibility of using clayey soil and crushed oyster shell powder for producing unfired rammed earth brick using Rice Husk Ash as a binder. For a 10% replacement of clayey soil by shell, conventional unfired bricks have a higher compressive strength. The calcium carbonate in oyster shells combines with alumino-silicates and silicate-rich pozzolanic materials to produce hydraulic products such as calcium aluminate silicate hydrates (C-A-S-H) and calcium silicate hydrates (C-S-H) [23–25]. The alumina-siliceous amorphous phases of the examined materials influence the pozzolanicity and hence the mechanical performances of these hydraulic compounds, increasing their durability and stability.

High compressibility, differential settlements, and low shear strength characterize clayey earth soils, which must be stabilized to improve their mechanical performance. Chemical stabilization is a strategy that has only lately been proposed [26]. The stabilization of soil by fly ash (FA) has recently become more studied [27–29]. FA has been widely used as a binder material, and it is a waste product of coal-fired power plants. France produces between 2 and 3 million tons of FA annually [30]. FA's characteristics, such as low specific gravity, low permeability, and high internal friction angle, enhance earth bearing capacity while reducing compressibility and settlement [27–29]. Furthermore, fly ash provides high quantity of alumino-silicates to the mixture, increasing the reactive surface for the pozzolanic reaction [27,28]. These supplementary alumino-silicates can also react with calcium hydroxide derived from *Crepidula* shells or clays [27,28,31].

Mud can be placed straight to walls for masonry construction or in the form of mud bricks for construction. Cob, rammed earth, Daub, and compressed earth are among of the most common earth or mud wall construction techniques [32]. The most typical earth construction technique in our region (Normandy, France) is cob (Bauge in French), which comes from the Old English word meaning "a piece of rounded mass". This is a construction process that uses hand-formed earthen clods combined with vegetable fibers [33].

The feasibility of Gravel Wash Mud (GWM) with *Crepidula fornicata* shell and Fly ash as an alternative binder for unfired cob material is investigated in this study. An experimental evaluation of the compressive strength of cob specimens generated with this combination is conducted for this purpose. The analysis of the produced hydrated products and the thermal characteristics are also explored.

3.2 Materials and methods

3.2.1 Materials and samples preparation

3.2.1.1 Gravel wash mud

The gravel wash mud was gathered from a sand and gravel company's decantation basin, which was handled by Lafarge-Holcim granulat (located at Yville-sur-Seine and Anneville-Ambourville in Normandy, France). At the Sablons quarry, the Lafarge gravel industry generates around 200 tons of gravel wash mud annually. The water content of the GWM is roughly 75% by weight. To eliminate the physisorbed water, the GWM samples were dried in an oven at 105°C for 6 hours before being crushed into a fine

powder. This GWM is currently being landfilled and will not be recycled back. However, this material has a great potentiality, therefore it needs to be thoroughly characterized before it can be used as an alternative construction material.

3.2.1.2 Vegetable fibers

In traditional cob, natural fibers are employed as reinforcement materials. In this study, we used readily available and inexpensive wheat straws, which have modest environmental implications. Furthermore, only residual straws are used to avoid ILUC effects and to keep their valorization as renewable and CO_2 emission neutral as possible. The thermal conductivity of straw fibers is between 0.035 and 0.054 $W.m^{-1}.K^{-1}$ [33]. The physical properties of the wheat straws used in this investigation (supplied by farmers from Laulne, Normandy) are listed in Table 3.1.

Table 3.1 Properties of wheat straw used in this study.

Diameter (mm)	Length (cm)	Density ($Kg.m^{-3}$)	Initial water content (%)	Tensile strength (MPa)
1-4	10-58	1910 ± 5	10.7	23.9 ± 3.5

3.2.1.3 Fly ash

The fly ash (FA) used is class F, which is originating from coal-fired power plants and has an absolute density of 2840 kg/m^3 and a Blaine fineness of 3950 cm^2/g, according to the EN 450-1 standard [34]. The FA by-products were supplied by SURSCHISTE suppliers in Hornaing, France, who produce approximately 120,000 tons of FA per year. The FAs used are spherical grain powders that don't need to be processed further. Table 3.2 shows their chemical composition.

Table 3.2 Chemical composition of fly ash in terms of weight %, as determined by energy dispersive X-ray spectroscopy.

Component	SiO_2	Al_2O_3	Fe_2O_3	CaO	MgO	K_2O	SO_3	TiO_2	Na_2O	MnO_2	P_2O_5	Cl
wt.%	53.3	23.6	8.5	5.1	3.0	3.0	1.1	1.0	0.6	0.5	0.2	0.1

3.2.1.4 *Crepidula* fornicata shells

Crepidula fornicata shells (CR) are an invasive gastropod species that has proliferated on the coastlines, causing harm to halieutic resources. A fishing industry in Normandy supplied the ground CR shells for this study. The raw shells were dried in a 105°C oven for at least 24 hours before being processed into powders in our lab using a 63 micron sieve. 2730 $kg.m^{-3}$ and 8140 $cm^2.g^{-1}$ are the specific gravity and Blaine fineness of CR, respectively. In a previous chapter, the chemical composition of CR powders was

evaluated using Energy-Dispersive X-ray Spectroscopy (EDS) [35]. The most abundant cation is calcium. The presence of residues of Na, Si, S, Mg, and Al (0.6 wt%) is also revealed by EDS.

3.2.1.5 Mixture design

We designed a formulation trying to keep the Ca/Si ratio between 1.2 and 2.1 for efficient generation of calcium silicate hydrates. to get the best mechanical and thermal properties. The 5 cm long straw cuttings were added at random and combined with the remaining components until a homogeneous composite was achieved. The straw content is 2% and the water content is 18% by weight, according to the standard procedure [36].

For mechanical and thermal examinations, the optimal mix (GWM-FA-CR) was filled into prismatic moulds (30 x 30 x 4 cm^3) and cylindrical moulds (11 cm in diameter and 22 cm in height). The GWM-FA-CR is mixed dry by hand initially. Water is added to the GWM-FA-CR and stirred until it achieves a liquid state. The PROVITEQ Concrete Mixer is then used to progressively add the cheap wheat straws for 120 s. The mix is manually crushed and maintained at constant temperature of 20 °C for 24 hours. After that, the mixture is manually compacted in moulds that have been prepared and lubricated. Taking into account the amount of water, the total mass required to fill the mould is 2.628 kg. The moulds are left at ambient temperature for 48 hours (20 °C) before being placed in a 40°C oven for additional 48 hours. They take 28 days for the drying process to complete.

Three duplicates of each selected composition were made. The cob samples are stored under ambient conditions (20 °C and 50 % of relative humidity) after this drying period (Figure 3-1). Once equilibrium is established, i.e. when the mass difference between two daily weightings is less than 0.1 %, the samples are then characterized. At room temperature (20 °C), this equilibrium is usually established within 48 hours. It's worth noting that no cracking was observed, and all specimens shrank at a very low rate (less than 1 %) after 28 of curing days. The mix's measured specific gravity is 1910 $kg.m^{-3}$. For comparison, we made a standard cob material with a specific gravity of 1843 $kg.m^{-3}$, similar to that explored in the CobBauge project [33] and a specific gravity close to that of our GMW-CR-FA sample.

Table 3.3 The GMW-FA-CR mix's composition.

Mix	GWM	FA	CR	Fiber	Water
Mass (%)	50	25	5	2	18

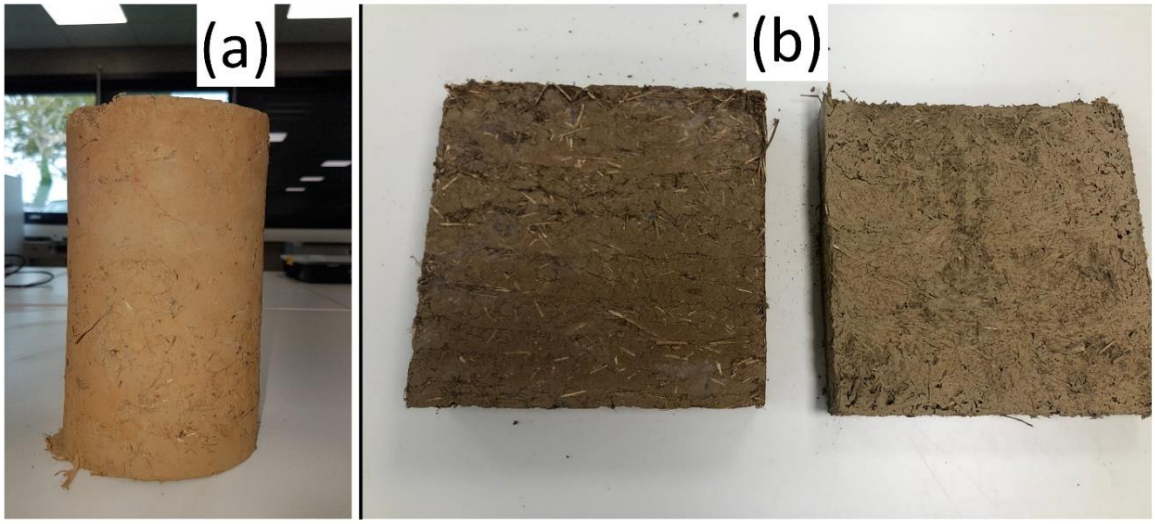

Figure 3-1 (a) Cob samples used for mechanical tests (Ø 11 cm x 22 cm) and (b) used for thermal analysis (30×30×4 cm^3).

3.2.2 Experimental techniques

3.2.2.1 X-ray fluorescence and scanning electron microscope

The elemental composition of Soil and FA were obtained using X-ray fluorescence (XRF) spectroscopy and Scanning Electron Microscope (SEM). XRF spectra were recorded using an Inel Equinox 3500 spectrometer (equipped with a Cu microfocus source, a multilayer parabolic mirror in the primary beam and an Amptek X123SDD silicon). Drift detectors were placed vertically 10 mm above the sample to ensure high sensitivity even for low atomic number elements). Data were collected with an integration time of 400 s.

A scanning electron microscope (SEM; SUPRA ^{TM} 55 SAPPHIRE; Carl Zeiss, Jena, Germany) with an energy dispersive spectrometer was used for imaging and elemental analysis (EDS). Prior to examinations at a voltage of 20 kV, the samples were carbon coated.

3.2.2.2 Raman spectroscopy

A Thermo Scientific Raman microscope (Thermo Fisher Scientific DXR) with a green laser (532 nm) as an excitation source with a 900 lines/mm diffraction grating. In a backscattering geometry and at room temperature, we used a 50X long-distance

objective to focused the laser beam onto the surface. The data were obtained over a 50-2200 cm^{-1} range. The laser's spot diameter was calculated to be 0.8 m, with a spectral resolution of 3 cm^{-1}. Raman spectra were acquired twice with a low laser power (2 mW) and a 120-s integration time. As basic fitting functions, we employed the Origin software and Gaussian curves. By comparing the obtained Raman spectra to those in the Raman Open Database ROD [37], the mineral compositions were established.

3.2.2.3 X-Rays Diffraction

XRD: An incident beam Ge (111) monochromator on a D8 Advance Vario 1 Bruker instrument (2-circles diffractometer, -2Θ Bragg-Brentano mode) was used to collect the XRD diagram using copper radiation (λ = 1.54059 nm). From 10° to 80°, the X-ray diffraction pattern of soil is acquired for 1second at each 0.01° step (16 h/scan). The LaB6 standard powder (NIST SRM-660b) was used to calibrate the instrumental contribution [38]. Quantification and crystalline phase identification were done with the Full-Pattern Search-Match (FPSM) technique and the Crystallography Open Database [39]. There are numerous stages to refine the diffraction patterns of the samples analysed. Knowledge of the chemical composition is required in order to assign all phases of such a pattern. As a result, elemental studies using XRF and EDS were carried out. After the initial chemical analysis, the average crystallite sizes for each phase were estimated using the online Full Profile Search Match fitting process (http://nanoair.dii.unitn.it:8080/sfpm/). Crystal structure information can be found in the Crystallography Open Database (COD). The automatic identification of crystal phases as a first list is the basis of these quantifications. Micro-Raman is then used to generate a more comprehensive list of probable phase candidates due to its much higher sensitivity at the grain scale. Finally, the Rietveld quantification was done with the MAUD software [40].

3.2.2.4 Thermogravimetric analysis

The thermogravimetric analyses of cob specimens have been performed on 60-80 mg of powders deposited in an alumina pan at a heating rate of 10 °C/min from room temperature to 900 °C in an Ar flowing medium (50 mL/min) using the NETZSCH instrument (STA 449 F5 Jupiter).

3.2.2.5 Heat Flow Meter

The thermal conductivity was measured using a NETZSCH Heat Flow Meter device (Model HFM 436 Lambda). The samples have prismatic dimensions of 30x30x7 cm^3 and are positioned between the cooling plate and the heater plate; heat passes from the heater plate through the sample to the cooling plate, where it is transported away. A Peltier cryostat adjusts the cooling and heater plate temperatures to create a temperature gradient of 10 ÷ 40°C from the heater plate across the specimen.

3.2.2.6 Permeability

The dry cup method was used to measure water vapor permeability in accordance with the standard NF EN ISO 12572 [41]. The water vapour permeability of a material is its ability to allow vapour to pass through when subjected to a pressure of water vapour flow. this parameter represents the ratio of the amount of water vapor flowing through a material per unit of time, thickness and the difference in vapour pressure on each side of the material. This test requires the creation of relative humidity gradients between two sides of a specimen that is completely sealed from inside the cup (0% RH) to the outside (50% RH). After this, the daily mass variance must be monitored until it becomes constant. After the initial non-linear phase of the test is eliminated, the slope of the regression line relating the mass of the sample cup as a function of time is used to calculate the steady-state flow of water vapour (G) through the sample. The equation 3-1 is used to calculate the flux density of the vapour (g).

$$g = \frac{G}{A} \qquad \textbf{3-1}$$

A = Surface area of the exposed sample.

The water vapour resistance (Z) can be calculated from the water vapour permeance, as shown in equation 3-2. The latter is based on the partial pressure differential of the water vapor between the sample's sides (ΔP_v).

$$Z = \frac{1}{W} = \frac{\Delta P_v}{g} \qquad \textbf{3-2}$$

The water vapour resistance of the air layer in the cup (Za) is determined by equation 3-3.

$$Z_a = \frac{d_a}{\delta_a} \qquad \textbf{3-3}$$

δ_a = Water vapour permeability of the air at atmospheric pressure.
(equal to 2×10^{-10} $kg.m^{-1}.s^{-1}.Pa^{-1}$).

d_a = Thickness of the air layer.

Equation 3-4 is used to determine the adjusted water vapour permeance Wc.

$$W_c = \frac{1}{Z - Z_a} \quad \textbf{3-4}$$

The water vapour permeability (δ) is calculated using equation3-5.

$$\delta = W_c \times e \quad \textbf{3-5}$$

e = Thickness of the sample

The equation 3-6 is used to get the water vapour resistance factor of the sample.

$$\mu = \frac{\delta_a}{\delta} \quad \textbf{3-6}$$

3.2.2.7 Sorption-desorption

The Dynamic Vapor Sorption (DVS) technique is used to study the interaction of solids with vapor. The sorption isotherms of mixtures are investigated in this work according to ISO 12571 [41]. The tests were conducted using typical samples of 10 g collected from Ø11 cm x 22 cm cylindrical samples. The samples are first dried to reach a consistent weight with less than 0.1% mass variance. The samples are then exposed to a relative humidity range of 10% to 90% over the course of five stages, with the test temperature remaining constant at 23°C. During the test, the samples were weighed automatically every 20 minutes. Equilibrium is considered to be reached for each moisture content when the variance in sample mass is less than 0.01% after 120 minutes. The determination of the isothermal sorption curves occurs discontinuously in a series of steps that involve raising and then decreasing relative humidity.

3.2.2.8 Differential Scanning Calorimetry

The ability of a substance to hold thermal energy is characterized by its specific heat capacity (Cp). Cp measurements are taken using a Differential Scanning Calorimetry technique (DSC, NETZSCH STA 449 F3) in accordance with ISO 11357-4 [42]. Data is continually recorded from -20 °C to 40 °C at a heating rate of 1 °C/min. This method is based on the difference in heat flux exchanged between a reference sample and our sample, keeping them at the same temperature throughout a scan.

3.2.2.9 Specific surface area

The BET method was used to measure the specific surface area of the cob specimens [43], and the absolute density was determined using a Helium pycnometer (Accupyc II 1340). It allows an accurate measurement of the solid phase volume of a sample with a known mass. Indeed, the measurement principle is to introduce helium into a known-

pressure reference chamber and then extend this gas into the chamber containing the sample by measuring the sample's new pressure. Because helium has a tiny atomic diameter and quickly enters pores, this measuring method is appropriate for porous substances with open porosity.

3.2.2.10 Porosity

Apparent porosity of cob samples was measured using the gravimetric method (ISO 5017 [43]). Since earth-based materials cannot be tested with water, these physical characteristics are measured by submerging small samples in a non-wetting oil. Therefore, in this experiment, de-aromatised petroleum was utilised. The samples are dried in an oven at 105°C until they reach a constant mass, which is when the difference between two weights being less than 0.05%. Then, this mass is regarded as the dry mass. The samples were then immersed in liquid for at least 24 hours while being kept under vacuum in a desiccator, allowing the liquid to replace the air in the pores. They were then weighed after they were submerged in oil and again after being removed from the oil. Through a difference in mass between the saturated and dry states, this approach can be used to determine both the density of the sample and the volume of the initial oil-filled voids. As a result, equation 3-7 gives the accessible porosity p0 while equation 3-8 gives the bulk density.

$$p_0 = \frac{M_a - M_s}{M_a - M_h} \quad \textbf{3-7}$$

$$\rho_{sp} = \frac{M_s}{M_a - M_h} \times \rho_h \quad \textbf{3-8}$$

- M_s = Mass of the dry specimen,
- M_h = Mass of the saturated specimen weighed in oil,
- M_a = Mass of the saturated specimen weighed in air,
- ρ_{sp} = Bulk density of the specimen,
- ρ_h = Bulk density of oil.

3.2.2.11 Mechanical strength

The compressive test was performed on cylindrical samples with dimensions of Ø11 cm x 22 cm in accordance with the standard NF EN-12390-3 [44]. The uniaxial compression test was performed on a 100 kN INSTRON SCHENCK press. The testing was conducted at a controlled force with an applied loading rate of 0.05 kN/s.

3.3 Results and discussion

3.3.1 Microstructural properties of gravel wash mud

The principal oxides present in the GWM material are silicon oxide, iron oxide, calcium oxide, and aluminum oxide (Table 3.4).

Table 3.4 Chemical and physical and characteristics of GWM

Oxide composition	**%**
Silicon dioxide (SiO_2)	61.3
Ferric oxide (Fe_2O_3)	10.2
Calcium oxide (CaO)	10.1
Aluminum oxide (Al_2O_3)	9.8
Magnesium oxide (MgO)	2.9
Sodium oxide (Na_2O)	0.1
Potassium oxide (K_2O)	1.8
Sulfur trioxide (SO_3)	<0.1
Phosphorus Pentoxide (P_2O_5)	<0.1
Cl^-	0.11
Physical and hygrothermal properties	
Specific surface ($cm^2.g^{-1}$)	4120
Absolute density ($kg.m^{-3}$)	925
Water vapor permeability ($kg.m^{-1}.s^{-1}.Pa^{-1}$)	2.4×10^{-11}
Thermal conductivity ($W.m^{-1}.K^{-1}$)	0.935 ± 0.01

The grain size distribution of GWM powder (Figure 3-2) has d10 and d90 values of 3.67 and 46.33 m, respectively, as measured by laser diffraction. Approximately 98 % of all particles have a diameter of less than 63 µm.

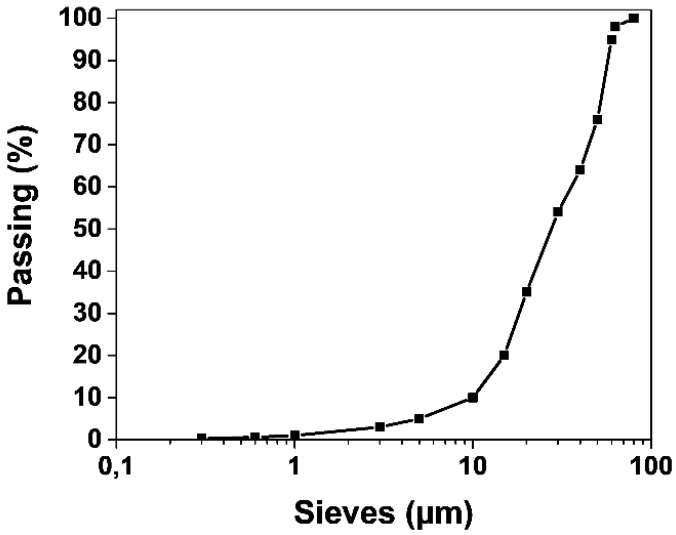

Figure 3-2 Grain size distribution of GWM sample.

EDS analysis primarily characterizes elements and thus the mineralogical composition in term of crystalline phases it is essential to understand the potential of GWM. Si atoms, for example, can be found in quartz and/or clays, two phases that operate very differently when combined with water and mineral addition. The online Full Profile Search Match fitting process (FPSM, http://nanoair.dii.unitn.it:8080/sfpm/) was used to do a preliminary quick phase analysis.

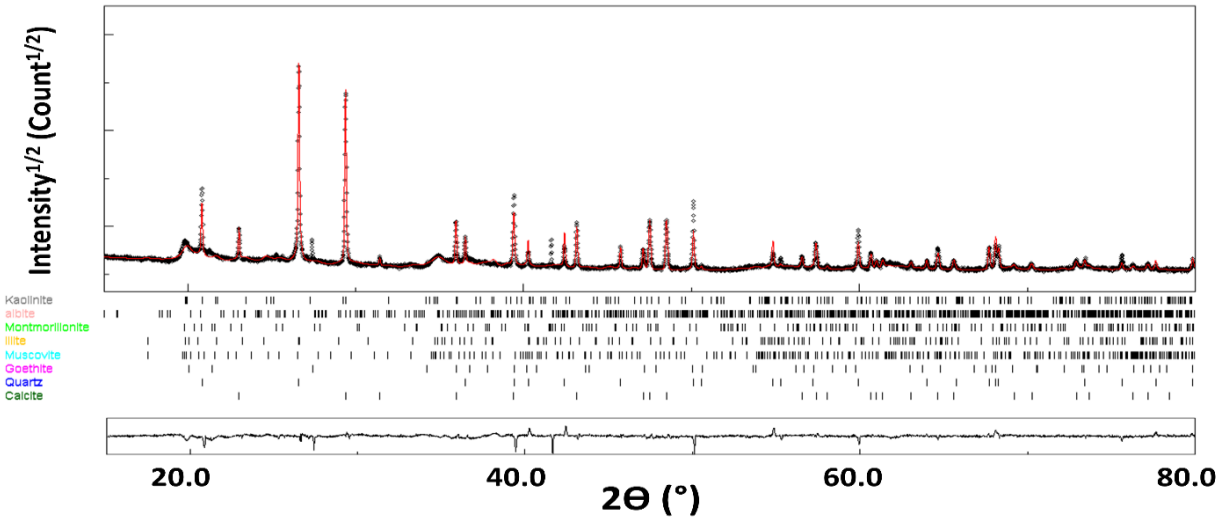

Figure 3-3 GWM X-ray diffraction pattern refined with MAUD software. The calculated pattern (red line) overlays the observed profile (black dots). At the bottom is the difference curve ($I_{obs} - I_{calc}$).

The FPSM tests all possible crystalline phase from the COD Database (limited to the EDS-detected elements) using a Rietveld fitting process, resulting in an ordered list of candidates for further quantification. The GWM sample's XRD pattern is then Rietveld-fitted, taking into consideration the phase identification. Using eight primary phases, a

typical XRD pattern of the GWM sample can be refined (Figure 3-3 and Table 3.5). The agreement factors R_{wp} = 4.7 %, R_B = 3.6 %, and a quality of our Fits of less than 2 (GoF = 1.7) all show that our analyses are reliable. During this step, the microstrain values are also fitted, and they remain low throughout the phases.

Table 3.5 Mineralogical composition with the refined lattice parameters, unit cell volume, average diameter, and microstrain $<\varepsilon^2>^{1/2}$ were all refined. On the last digit, one standard deviation is indicated by parenthesis

Phases	COD reference	V (%)	Lattice type + Space group	Lattice parameters (Å)	⟨D⟩ (nm)	$\langle\varepsilon^2\rangle^{1/2}$
Calcite $CaCO_3$	1547347	30.8 (3)	Trigonal R-3c:H	a=4.987 (1) c=17.056 (2)	392 (20)	8. 10^{-4}
Quartz SiO_2	1526860	14.3 (2)	Trigonal $P3_221$	a=4,915 (2) c=5,407 (2)	219 (10)	4. 10^{-4}
Albite $NaAlSiO_3O_8$	1556999	2.3 (2)	Triclinic P1	a=8,166 (1) b=12,845 (1) c=7,188 (1) α=94.240 (1) β=116.590 (1) γ=87.715	30 (5)	6. 10^{-3}
Kaolinite $Al_2Si_2O_5(OH)_4$	1011045	12.8 (2)	Monoclinic Cc:b1	a=5,246 (1) b=8,886 (1) c=14,672 (1) β=100.565 (1)	26 (5)	6. 10^{-4}
Illite $(K,H_3O)(Al,Mg,Fe)_2(Si,Al)_4O_{10}[(OH)_2,(H_2O)]$	2300190	16.1 (4)	Monoclinic C2/m:b1	a=5,171 (1) b=8,942 (1) c=10,229(1) β=100.683 (1)	70 (5)	2. 10^{-4}
Goethite α-FeO(OH)	2211652	2.4 (3)	Orthorhombic Pbnm:cab	a=4,579 (1) b=9,945 (1) c=2,998 (1)	21 (1)	6. 10^{-4}
Montmorillonite $(Na,Ca)_{0.3}(Al,Mg)_2Si_4O_{10}(OH)_2$	1100106	14.8 (2)	Monoclinic C2/c:b1	a=5,451 (1) b=9,067 (1) c=10,255(1) β=100.780 (1)	125 (4)	6. 10^{-4}
Muscovite $KAl_2(AlSi_3O_{10})(F,OH)_2$	1100011	6.7 (4)	Monoclinic C2/c:b1	a=5,183 (1) b=9,006 (1) c=20,186(1) β=95.702 (1)	89 (5)	2. 10^{-3}

The XRD diagram is indexed by the following major phases, according to quantitative phase analysis using Rietveld refinement: calcite (30.8 %), montmorillonite (14.8 %), quartz (14.3 %), illite (16.1 %), and kaolinite (12.8 %), with traces of goethite, albite, and muscovite.

Muscovite (also known as common mica) is an aluminum and potassium hydrated phyllosilicate mineral. It has a near-perfect basal cleavage, resulting in remarkably thin laminae (sheets) that are frequently elastic in nature [45]. Albite ($NaAlSi_3O_8$) is a feldspar mineral (silicate group family), which can contain traces of K, Ca, and Mg [46]. Goethite is a mineral species that is a polymorph of the compound FeO(OH) [45]. It is a variety of iron (III) oxyhydroxide.

Kaolinite is a mineral species consisting of hydrated aluminum silicate that belongs to the phyllosilicate subgroup [45].

Illite refers to a class of non-swelling clay minerals. The illites are made up of three layers of phyllosilicates, one layer of aluminum, and two layers of silicate. They are structurally similar to micas (muscovite, biotite) and other silicates (feldspar, feldspathoids, orthosis, and others) from which they are formed through bisiallitization, a reaction that occurs when water molecules are attacked under certain temperature and pressure conditions [45].

Montmorillonite is an aluminum silicate and hydrated magnesium mineral. Montmorillonite is a 2/1 clay that is also known as TOT (Tetrahedron / Octahedron / Tetrahedron). This means that a montmorillonite sheet has three layers: an octahedral layer of $Al(OH^-)_5O$ and two tetrahedral layers of SiO_4 [45]. One of the most prominent characteristics of montmorillonites is their high swelling capacity, which results from H_2O insertion between the tetrahedral layers. In contact with water, montmorillonite creates a stable suspension of colloidal particles. The ability of montmorillonite to swell and shrink poses serious geotechnical issues, resulting in significant lateral displacement at the foundations due to variations in subsoil humidity.

The interfoliar spaces of some clays can be expanded. This property is due to the incorporation of some cations (Na^{2+}, Ca^{2+}, etc.), which allows for the compensation of permanent charge deficits. The expandable species are those with charges ranging from 0.3 to 0.8, which includes the smectites subclass. The water incorporated via the hydrated cations allows the crystalline structure to swell. The swelling is amplified by the high humidity level.

Montmorillonite is the only expandable species present in our GWM at a rate of 14.8%. The presence of muscovite, kaolinite, albite, and illite in the GWM sample will influence the shrinkage properties. Given of their narrow intermolar space, these crystals have few water molecules between their layers [47]. As a result, when submerged in water, they exhibit slight intracrystalline swelling [47]. These three types of sludge shrink much less during drying than swelling smectite clays like montmorillonite [47].

3.3.2 Physical and chemical properties of GWM-FA-CR

3.3.2.1 Compressive strength of GWM-FA-CR

The analysis shows that the GWM-FA-CR specimen exhibited high strengths after 28 days of curing than standard cob building materials (Table 3.6). GWMs are known to have differential settlements and low shear strength and must be stabilized to enhance their properties. One of the most recent techniques for this purpose is stabilization through the use of FA addition. This by-product has recently gained popularity [27–29]. FA has been widely used as a binder material. FA properties such as low specific gravity, low permeability, and high internal friction angle enhance earth bearing capacity while decreasing settlement and compressibility [27,29]. Furthermore, FA introduces additional calcium and alumino-silicates into the system, increasing the activated surface and then the pozzolanic reaction [27,28]. The additional aluminosilicates can also interact with calcium derived from clay and *Crepidula* shells [27,28,31]. The formation of calcium silicates and aluminosilicate hydrates will be confirmed in the following section dedicated to Raman and XRD characterization analyses of GWM-FA-CR specimen.

Table 3.6 Compressive strength of standard cob and GWM-FA-CR specimens after 28 days of curing.

Sample	Compressive strength (MPa)
GWM-FA-CR	5.38 ± 0.23
Standard Cob	2.03 ± 0.02
Cob materials from literature	1.42-1.52

3.3.2.2 Analyses of GWM-FA-CR sample using XRD

The XRD diagram of GWM-FA-CR specimen is refined using 7 major phases (Figure 3-4 and Table 3.77). Rwp = 7.8 percent and RB = 9.7 percent (GoF = 1.55) are the agreement factors.

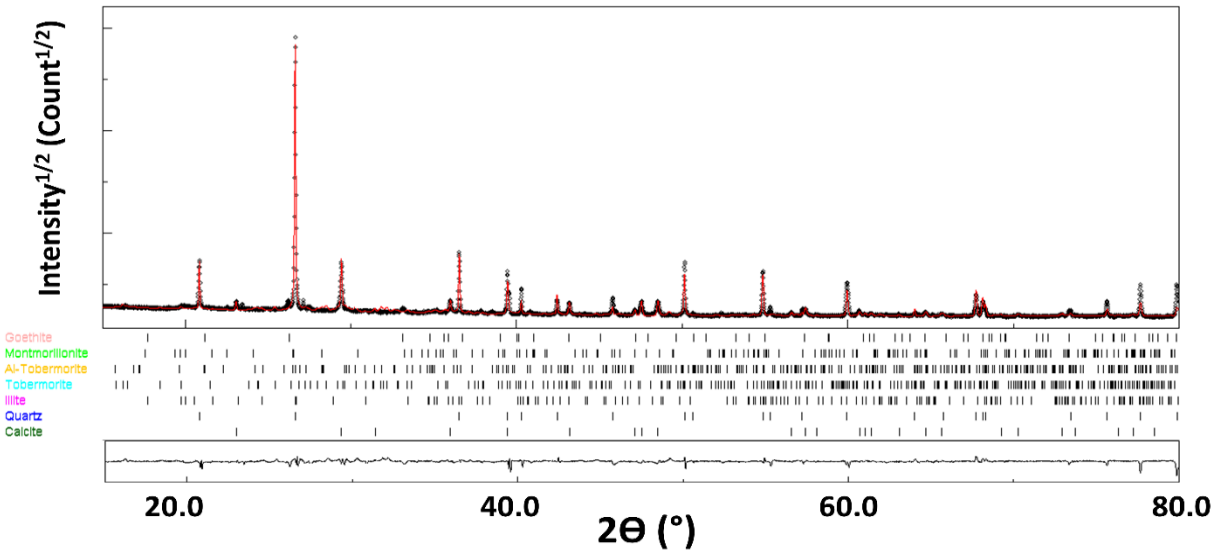

Figure 3-4 Refined X-ray diffraction diagram of GWM-FA-CR specimen using MAUD software. The calculated profile (red line) overlays the observed pattern (coarse line). On the same scale, the difference curve (I_{obs} -I_{calc}) is shown at the bottom.

Table 3.7 Mineralogical composition of GWM-FA-CR sample with the refined lattice parameters, unit cell volume, average diameter, and microstrain $<\varepsilon^2>^{1/2}$ were all refined. On the last digit, one standard deviation is indicated by parenthesis.

Phases	COD reference	V (%)	Lattice type + Space group	Lattice parameters (Å)	⟨D⟩ (nm)	$\langle\varepsilon^2\rangle^{1/2}$
Calcite $CaCO_3$	1547347	26.3 (5)	Trigonal R-3c:H	a=4.984 (1) c=17.047 (2)	308 (20)	8. 10^{-4}
Quartz SiO_2	1526860	22.3 (3)	Trigonal $P3_221$	a=4,913 (2) c=5,404 (2)	690 (10)	5. 10^{-4}
Montmorillonite $(Na,Ca)_{0.3}(Al,Mg)_2Si_4O_{10}(OH)_2$	1100106	6.4 (2)	Monoclinic C2/c:b1	a=5,441 (1) b=9.003 (1) c=10,250(1) β=100.323 (1)	66 (4)	6. 10^{-4}
Illite $(K,H_3O)(Al,Mg,Fe)_2(Si,Al)_4O_{10}[(OH)_2,(H_2O)]$	2300190	7.1 (3)	Monoclinic C2/m:b1	a=5,183 (1) b=8,986 (1) c=10,171(1) β=100.50 (1)	66 (5)	1. 10^{-4}
Tobermorite $Ca_5Si_6O_{16}(OH)_2{\cdot}4H_2O$	9005498	19.5 (3)	Monoclinic Cm:c2	a=6,806 (3) b=7,402 (3) c=22,390 (3) γ=124.345 (3)	58 (1)	5. 10^{-4}
Al-tobermorite $Al_{0.5}Ca_{4.9}H_{10.7}O_{22}Si_{5.5}$	1527001	15.6 (3)	Monoclinic Cm:c2	a=6,770 (3) b=7,359 (3) c=22,227 (3) γ=123.770 (3)	43 (4)	6. 10^{-2}
Goethite α-FeO(OH)	2211652	2.6 (3)	Orthorhombic Pbnm:cab	a=4,588 (1) b=10,093 (1) c=2,984 (1)	19 (1)	6. 10^{-4}

According to quantitative phase analysis, the GWM-FA-CR sample is dominated by calcite, quartz, tobermorite, and Al-tobermorite. In addition to these phases, montmorillonite, illite, and goethite derived from GWM are found in small quantities. As

a result, some of these phases did not react with the components of FA and CR. Calcium from GWM and seashells reacts with aluminosilicates originating from GWM and silica from FA to form new hydrated phases, i.e. tobermorite and Al-tobermorite. Tobermorite ($Ca_{4+x}(Al_ySi_{6-y})O_{15+2x-y}\cdot 5H_2O$, x and y are ranging from 0 to 1) has an orthorhombic symmetry with a basal spacing of 11 Å , [48]. Tobermorite has a high capacity for cation exchange and a high selectivity for Aluminum [49] Silicon is substituted by Aluminum in both bridging and non-bridging tetrahedron sites [50,51]. In the presence of raw materials, such as fly ash and/or phases from the CaO-SiO2-H2O system [52–54], Al-substituted forms of tobermorite are produced.

3.3.2.3 DSC analysis of GWM and GWM-FA-CR samples

The GWM and GWM-FA-CR samples' derivative thermogravimetry calorimetry (DTG) skeletons are presented in Figure 3-5. Evaporation and dehydration of free water are responsible for the mass loss between 100 and 130 °C. The evaporation of physiosorbed water and dehydration of the C-S-H gel are related to the DTG peak in the GWM-FA-CR from 85 to 100 °C [55]. The dehydration of C-A-S-H type reaction products is indicated by the other peak at 130 °C [56] , while the dehydration of portlandite is shown by the peak above 460 °C [57]. The evaporation of hygroscopic water between the clay particles corresponds to the first endothermic peak in the GWM sample, which occurs around 110 °C [58].

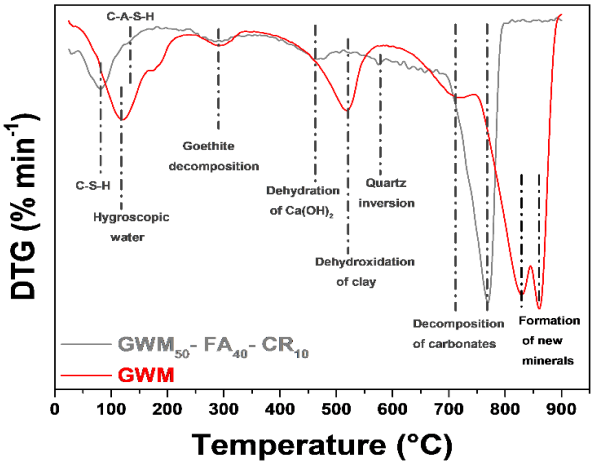

Figure 3-5 DTG curves of GWM and GWM-FA-CR samples after 28 days of curing time.

The dehydration of the clay minerals is responsible for the mass loss between 500 and 560 °C [59,60]. When comparing the GWM-FA-CR sample to the GWM sample, we can notice that the clay dehydration peaks are much weaker. This behaviour is related to the clay minerals' interaction with FA and CR, resulting in the formation of CSH and CASH hydrated products. The dissolution of hydroxides, such as goethite, is

responsible for the mass loss at 295 °C [61]. There is also a discrete endothermic peak around 575 °C. The allotropic transformation of into -α into β-quartz [62] is responsible for this peak.

The dissolution of calcium carbonates produces endothermic peaks around 720 °C with a large disparity noticeable in the DSC curve [63]. It is worth noting that these endothermic peaks are substantially asymmetric, implying that the dissolution kinetic accelerates with increasing temperature until the carbonates are depleted. CO_2 is released into the atmosphere as a result of carbonate decomposition.

The degradation of clay minerals is connected with exothermic DTA peaks above 800 °C, which are only found in the GWM sample. They will combine to generate a new spinel-like mineral [64].

3.3.2.4 Raman analyses of GWM-FA-CR

Raman investigations of the hydrated compounds formed in the GWM-FA-CR after 28 days revealed that tobermorite and Al-tobermorite are present in the sample (Figure 3-6). The Raman spectra indicate also the existence of quartz and calcite in addition to the C-S-H and C-S-A-H phases [65,66]. It is worth noting that no traces of aragonite were found in the sample after 28 days. This is most likely due to the complete dissolution of this calcium carbonate structure. At 25 °C, aragonite's solubility ($LogK_{sp}$) in water is -8.336 ± 0.020, resulting in the generation of Ca^{2+} and CO_3^{2-} ions [67]. As a result, dissolved Ca^{2+} ions will take an active part in the hydration processes, which will contribute to the emergence of new C-S-H and C-A-S-H phases.

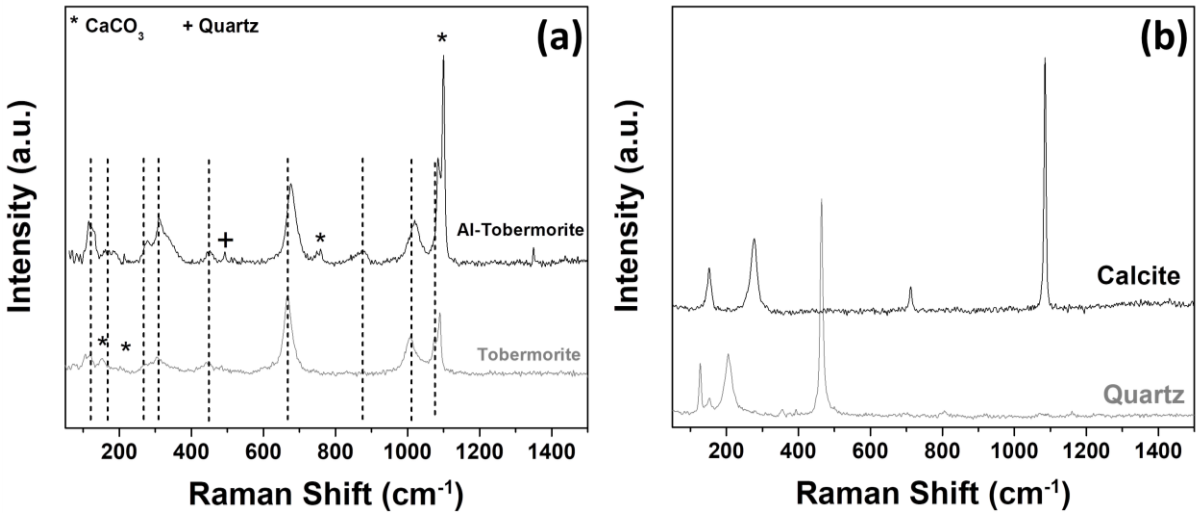

Figure 3-6 Raman spectra of (a) the hydrated phases detected in the GMW-FA-CR mixture after 28 days of curing time : CSH and CASH, (b) calcite and quartz.

Raman spectroscopy has been used extensively to identify the nature of the hydrated C-S-H and C-S-A-H structures [68,69]. The strongest vibration mode due to the Si–O stretching vibration at 665 cm^{-1} is present in all Raman spectra of tobermorite (Fig. 6a). At low wavenumbers (350 cm^{-1}), the vibration modes attributed to the lattice vibrations of Ca-O polyhedra are apparent. The Si–O–Si twisting and stretching modes are responsible for the band near 440 cm^{-1}. The Qn symmetric stretching modes of silicate Si-O are ascribed to the bands in the 850-1100 cm^{-1} wavenumber range, where Q indicates the SiO_4 tetrahedron and n the number of oxygens shared with nearby tetrahedra (n=1 to 4). Q_0 symbolizes a single monomer, Q_1 and Q_2 to chains, and Q_3 and Q_4 to interconnected structures, respectively. Only the Q_1, Q_2, and Q_3 species are present in our CSH and CASH systems, and they are localized at 880, 1010, and 1075 cm^{-1}, respectively.

The Raman spectra in the GWM-FA-CR specimen show that the Q_2 species (1005-1020 cm^{-1}) split into two bands at 1007 and 1016 cm^{-1}, indicating the modulation of the Si–O–Si chain length by a change in the number of silica tetrahedron Q_{2p} (pairing) and Q_{2b} (bridging) [70]. The Q_2 split is mostly due to a high silicon originating from fly ash. As a result of the pozzolanic reaction, the silicates provided by FA combine with the excess calcium hydroxide from CR and GWM to generate additional C-S-H gel, resulting in a reduction of the porosity and enhanced the mechanical performance of the material.

The presence of the C-O stretching vibration mode in the $CaCO_3$ group can also be seen in the Raman spectra at 1085 cm^{-1}.

We can notice that the positions of the vibration modes in Al-tobermorite are shifted to higher wavenumbers than in tobermorite. The substitution of Al in tobermorite produces this effect. Indeed, when Al is substituted for Tobermorite, the cell parameters are slightly reduced compared to pure Tobermorite (Table 3.7). Due to the larger radius of Al^{3+} relative to Si^{4+} [71], the Al substitution increases the (002) interplanar crystal spacing. In addition, Al increased the degree of polymerization of the silicate chains in tobermorite [71].

Low-basic calcium silicate hydrates and alumino-silicate hydrates (tobermorite and Al-tobermorite) are the major hydration products which explain the high mechanical performance properties of GMW-FA-CR specimen.

3.3.2.5 Thermal conductivity and density of GMW-FA-CR

For the GMW-FA-CR specimen, the thermal conductivity is reduced to two-thirds of that of the standard cob (Table 3.8), with 0.58 $W.m^{-1}.K^{-1}$ for standard cob and 0.35 $W.m^{-1}.K^{-1}$ for GMW-FA-CR. This clearly shows that incorporating FA and CR into an earth can improve the thermal insulation properties of the cob construction material.

Table 3.8 Thermal conductivity and density of standard cob and GWM-FA-CR sample after 28 days of curing compared to literature cob building materials.

Sample	Density ($kg.m^{-3}$)	Thermal conductivity ($W.m^{-1}.K^{-1}$)
GMW-FA-CR	1910 ± 5	0.35 ± 0.03
Standard Cob	1843 ± 5	0.58 ± 0.02
Cob materials from literature [33,36,71,72]	1200-2000	0.47-0.93

This is unusual behaviour because the density of the standard cob is lower than that of GMW-FA-CR. Indeed, it is known that when the density increases, the thermal conductivity increase. The addition of FA and CR is then responsible of the significant changes in the thermal carriers in the GMW-FA-CR material. However, additional research is necessary to fully comprehend the phenomenon that affects this behavior. As a result, we have not pursued further research into the properties of this combination.

3.3.2.6 Moisture sorption isotherm of standard cob and GMW-FA-CR

The Figure 3-7 shows the difference in mass as a function of humidity for the cob and the GWM-FA-CR specimens. The moisture sorption curves for the cob and GMW-FA-CR specimens are similar in shape and conform to a sigmoid. These curves are classified as Type II-isotherms by the IUPAC (International Union of Pure and Applied Chemistry) [73]. The mass difference value between the cob and the GWM-FA-CR specimen has decreased. The decrease in porosity and differences in phase fractions (i.e. clay minerals) between the cob and the GMW-FA-CR sample might be attributable to two main reasons. Indeed, given that the former material contains more clay minerals, it is expected to have a larger absorption capacity [74]. The inclusion of FA and aragonite from CR on the GWM resulted in a decrease in clayey minerals in the GWM-FA-CR. Furthermore, the porosity of the GWM-FA-CR composite is only two-thirds that of standard cob (Table 3.9), reducing the mass differential even more.

Table 3.9. Porosity of the standard cob and the GWM-FA-CR mix.

Sample	Standard Cob	GMW-FA-CR
Porosity	61 %	42 %

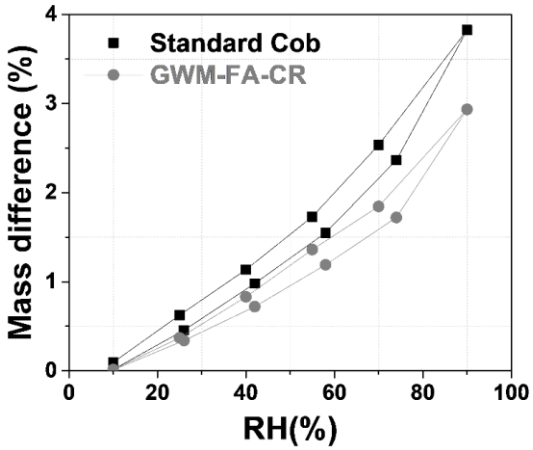

Figure 3-7 Moisture sorption isotherm of the standard cob material compared to the GWM-FA-CR mix at room temperature.

3.3.2.7 Specific heat capacity of standard cob and GWM-FA-CR

Figure 3-8 shows the specific heat capacity curves of the GWM-FA-CR and cob specimens. The specific heat capacity (C_p) values were found to be between 925 and 1250 $J.kg^{-1}.K^{-1}$, which is extremely high when compared to the standard cob specimen (between 200 and 600 $J.kg^{-1}.K^{-1}$). This demonstrates that the GWM sample performed better than the conventional cob.

A material with a greater specific heat capacity value is required in construction applications. In the construction industry, the specific thermal capacity of materials is critical for determining the indoor comfort of the building's occupants. In the summer, high-thermal-capacity walls maintain rooms cool for a long period. They keep heat in buildings for longer in the winter.

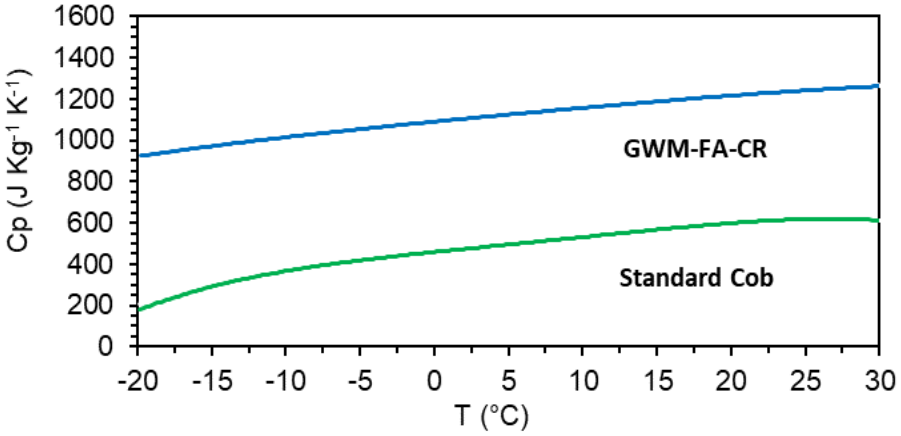

Figure 3-8 Evolution of the C_p of the standard cob material and the GWM-FA-CR mix as function of temperature.

3.3.2.8 Thermal insulating wall with GWM-FA-CR

Cob buildings have a long history, particularly in Germany [75]. A supplementary layer is used in this kind of construction. The first layer is a structural wall made of traditional cob, while the second layer is a thermal insulating wall made of lightened earth (Figure 3-9). To achieve this objective, we have decided to examinate the thermal and mechanical performance of a thermal insulating material made from a GWM-FA-CR mix with reed fibers (length between 4 and 6 cm). The reed content employed is 25%, according to the standard bibliography approach [33].

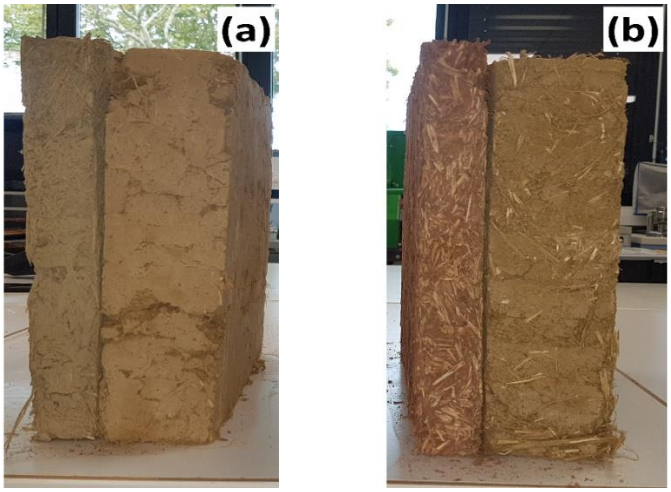

Figure 3-9 Cob walls with two layers : (a) GWM-FA-CR mixture and (b) standard cob.

The thermal conductivity of the light earth specimens prepared using GWM-FA-CR mix is 0.112 $W.m^{-1}.K^{-1}$ at 20°C, as shown in Table 10. Thermal conductivity ranges from 0.157 $W.m^{-1}.K^{-1}$ at 10°C to 0.148 $W.m^{-1}.K^{-1}$ at 40°C for standard insulating cob material. These findings showed that using the GWM-FA-CR resulted in a decrease in thermal conductivity when compared to conventional lightened earth. Furthermore, we demonstrate that this GWM-FA-CR mixture can improve the compressive strength of earth-insulating materials.

Table 3.10 Thermal conductivity and compressive strenght of GWM-FA-CR with 25% of reed fiber after 28 days of curing compared to typical lightened earth materials from the literature.

Sample	Compressive strength (MPa)	Thermal conductivity ($W.m^{-1}.K^{-1}$)
GMW-FA-CR + 25% reed straw	0.140 ± 0.01	0.112 ± 0.005
Standard Cob insulating wall [26]	0.079 ± 0.01	0.157 ± 0.005

In conclusion, the findings suggest that GWM, which is considered as waste, can be used for both structural and thermal insulating walls, as well as having the ability to

improve the thermal and mechanical properties of earth insulating materials by adding FA and CR.

This exploratory research focuses on an aluminosilicate-based material with highly promising chemical and mineralogical properties. Its appropriateness for earth building without further additions was not attainable due to the presence of swelling clay in terms of performance criteria.

It is worth noting that EDS, XRF, and X-ray investigation of distinct GWM powders from 12 different quarries in Normandy revealed that the predominant crystalline phases detected were quartz and muscovite, followed by illite and kaolinite as clay minerals, hematite, and the amorphous components (Table 3.10). However, there was a quick strength improvement, with the maximum attainable compressive strength after 3 weeks of drying being around 5 MPa for all specimens prepared with GMW, 25% FA, and 5% CR. Furthermore, regardless of the source of GWM, this addition reduces the content of swelling clays.

Table 3.11 Chemical and mineralogical properties of different GWM specimens.

Chemical analyses (in weight. %)	Mineralogical composition
SiO_2: from 41 to 78 %	Quartz: from 10 to 25 %
Al_2O_3 : from 6 to 15 %	Kaolinite: from 8 to 20 %
Fe_2O_3: from 5 to 12.5 %	Calcite: from 23 to 35 %
CaO: from 3 to 16 %	Illite: from 11 to 19 %
MgO: from 0.6 to 3.6 %	Smectites: from 10 to 28 %
Na_2O < 0.2 %	Feldspaths: from 0 to 5 %
K_2O: from 1 to 2.1 %	Plagioclases: from 0 to 1 %
SO_3 < 0.1	Iron oxyhydroxides: from 1 to 6 %
P_2O_5 < 0.1	Micas: from 2 to 9 %
Cl^- < 0.2 %	Swelling clays: from 9 to 18 %

3.4 Conclusion

The effect of using fly ash and *Crepidula* shells mix as stabilizer of mud is discussed in this research. The thermal and mechanical performance of French gravel wash mud mixed with by-products, seashell and fly ash as binder, as well as the study of the hydrated products, reveal some encouraging results, which are summarized as follows:

- The combination of French gravel wash mud, seashells, and fly ash can significantly contribute to the achievement of sustainable development goals and, as a result, carbon emission reduction.
- Tobermorite and Al-Tobermorite are the main hydration products justifying the excellent mechanical performance properties.
- The increased compressive strength compared to traditional cob building materials will result in a reduction in cob wall thickness and, as a result, a decrease in the amount of raw materials employed in cob construction.
- There are two advantages to using fly ash and seashells:
  - The high silica and calcium contents of these materials react with clays, resulting in the formation of CSH and CASH systems as a result of pozzolanic reaction, and thus the reduction in porosity and the increase of mechanical performances.
  - When compared to the traditional cob construction materials used in Normandy, the GMW-FA-CR has a lower thermal conductivity and a higher specific heat capacity.

Part II: Earth based building prototype incorporating stranded algae: Mechanical performance and smart hygrothermal modelling

Abstract

Once the tide recedes and leaves a significant amount of stranded seaweed on the coast the marine macroalgae pose a serious threat to the area. Through this work, we considered a large-scale application of stranded macroalgae in building construction. We studied the impact of incorporating seaweed at various replacement levels for the lightened and structural cob. Earth wall specimens were analysed to evaluate their compressive and hygrothermal characteristics. For the lightened earth we observed an improve in the heat storage capacity and the thermal conductivity without negatively impacting the compressive strength. The optimal amount of algae that reduced the thermal conductivity by 26% compared to standard cob is 20%. The enhanced mechanical and hygrothermal performance of cob specimens including algae make the reduction of the walls thickness possible. Consequently, to the creation of environmentally friendly, sustainable, energy-efficient construction materials.

Keywords: earth construction; algae; mechanical and hygrothermal performance; artificial neural network; smart modelling.

3.5 Introduction

Earth construction has been around for ten thousand years ago, and many ancient earthen architectures, such as the Egyptian pyramid, the Great ziggurats of Iran and the Great Wall of China, are still standing today [76,77]. The use of soil as a principal construction material is known as earthen construction. It can be seen of as a stand-alone natural construction philosophy or as a set of techniques that add high hygrothermal, durability, and environmental sustainability to more traditional modern building approaches [6,26,33,78–80]. Earth building is being used by communities and individuals all over the world to reduce their contributions to climate change and global warming [81]. Adobe or mud brick, rammed earth, cob, poured earth, and pressed earth are some of the earth-building methods that use soil as a construction material [32].

The most popular earth-building technique in Normandy (France) is cob (Bauge in French), which combines clay, sand, water, and fibers [26,33,78]. Straw and occasionally tiny stones are placed into a sandy soil for cob construction [33]. The quantity of fibers in a fresh cob is normally between 20 and 30 kg/m^3, with a fiber length of 30-50 cm [82]. The sandy soil is mixed with water until it reaches a plastic consistency, and the straw fibers are then worked underfoot by livestock hooves. The cob is then stacked into 1.0-1.2 m high walls and let to dry. When the masses have the correct moisture content, the wall faces are cut vertically with a spade [82]. The density of the traditional cob is typically between 1200 and 1700 kg/m^3 [33,83]. Given that cob uses locally accessible soils-fibers and requires very little water and energy, traditional cob making is ecologically friendly, inexpensive, and sustainable.

Many environmental factors can have an impact on the structural behavior of cob constructions. Increased water content (due to rising damp or a damaged roof) reduces material strength while also causing putrefaction of the fibers [82]. Insects and rodents can tunnel deep into cob walls due to the high fiber content [82]. All of these elements wreak havoc on the overall structural integrity of cob walls. In addition, differential settlements, poor shear strength, and excessive compressibility characterize clayey earth used traditionally for cob construction, which must be stabilized to improve its mechanical performance [78]. Chemical or mineral stabilization is a new way for accomplishing this [26,78].

Cementitious binders such as Portland cement, fly ash and silica fume can be used to stabilize soil. When these binders are added to the soil-water or soil-fiber-water complex, they lead to a series of short and long-term chemical reactions that stimulate flocculation of the soil elements, resulting in significant increases in composite stiffness and shear strength [78,84–86]. Cementitious binders are well acknowledged as not being environmentally sustainable, despite their effectiveness in terms of stability. Their use is frequently associated by considerable energy and carbon emissions footprints [87–89]. Synthetic or natural polymers, resins, and sulfonated oils, as documented in the scientific literature, are promising replacement materials capable of meeting both geotechnical performance and sustainability requirements [90–93].

The introduction of polymers, like traditional cementitious binders, can also contribute to the flocculation and the hydration of clay particles through a variety of clay–polymer interaction mechanisms, including: (a) van der Waals or hydrogen bonding, (b) charge neutralization (via electrostatic attraction), and (c) cationic bridging for neutral, cationic, and anionic polymers [94–96]. Among the commercially available polymer-based soil stabilizers, those generated from natural resources, i.e., biopolymers, appear to have a variety of intriguing soil physical properties, exceeding synthetic counterparts in terms of sustainability [87]. Sodium alginate is a linear polysaccharide found in the cell walls of brown and red algae and representing between 20 and 60% of the algae dry matter [97]. Alginate is a block copolymer consisting of two connected anionic monomers β-D-mannuronic acid and α-L-guluronic acid residues that is well suited for a variety of stabilizing and gel-forming applications in the textile dyes, culinary, pharmaceutical, and printing sectors [98]. All of these sectors have one common factor, i.e. the gelling and texturizing properties of alginates [98]. Alginate's geotechnical applications have been limited to natural soils, and include improving soil compaction efficiency, increasing soil shear strength/stiffness, and controlling soil erosion [99–101]. These studies' findings, while promising, are still limited, particularly in the context of clay soil stabilization and only a few research on the use of alginate as a stabilizing component for earth construction have been reported [26]. Dove [102] investigated the use of alginate derived from the *Laminaria hyperborea* algae as a binding agent in the production of earth bricks. According to its findings, the addition of algae stem product enhanced the compressive and flexural strength of the earth bricks.

Algae bricks have also been used in the construction of houses in Mexico. Indeed, seeing the proliferation of brown algae (Sargassum) in the region, the inhabitants had the idea of making 2000 bricks with 20 tons of seaweed, clays, chopped straws and water [103]. The bricks were dried in the sun and then assembled like traditional bricks.

Throughout history, algae have been used in Denmark [104]. There, some houses have been built with seaweed-based insulation and a roof made of dried Algae piled up between them in order to obtain a suitable waterproofing of the houses. Algae allows these houses to be durable over time since they do not degrade for 200 years. Because of their abundance and their thermal and acoustic insulation capabilities, algae are environmentally friendly materials.

Since the end of the 20th century, a phenomenon of "green tide" has appeared on the coasts of Britany and Western France [105]. A green tide is the name given to a proliferation of green algae that can cover the coastline, as the concentration of specimens is high. The algae in question belongs to the genus Ulva. During the period from May to September, the natural conditions such as the luminosity or the high temperature of water are favorable to the development of green, brown, and red algae [106]. But the main cause of this proliferation remains the abundant contribution of nitrates [107] from the rivers to the ocean. These nitrates are nutritive elements for the algae and strongly accentuate their development.

Stranded algae and the rafts formed by algal remaining on the water surface are a frequent problem for Normandy shellfish farming, but they also pose a risk to naval activity [108]. The algae are dangerous during their decomposition forming a crust that releases gases [108]. They form toxic gas that has a strong odour and is responsible for several human and animal deaths in Brittany. As the algae accumulate, the health and environmental consequences become more dramatic. To remedy this problem, communities collect the stranded algae or push them back into the sea [106]. Farmers also harvest the algae for use as fertilizer. Despite this, a significant amount of algae is not exploited and/or not collected [106]. On a global level, the world is experiencing the largest sea of sargassum algae, which measures over 8850 km [109]. Scientists have dubbed it the 'Great Atlantic Sargassum Belt'. This huge mass of brownish algae is expanding every year and covers now an area from Africa to the Caribbean. It weighs more than 20 million tons and extends from the Gulf of Mexico to the West coast of Africa.

In this part, we studied the mechanical and hygrothermal performance of cob walls based on earth incorporating vegetal fiber and *Laminaria digitata* algae at different substitution level. The cob materials are prepared using techniques comparable to that utilized in traditional German and England cob construction [33,75]. Indeed, there is a strong tradition for cob building in these two countries. A supplementary layer is used in this construction style. To meet construction rules, a combination of two walling layers made of earth materials was considered. Insulation wall with a high fiber content and a load bearing layer with a greater density make up the two layers. All of the examined mechanical performance, thermal conductivity, and heat capacity of cob walls are evaluated at laboratory scale. This enables the selection of the maximum thermal performance cob combination for the construction of building prototype based on soil-fiber-algae mixes with optimal mechanical performance and high hygroscopic properties, which implies less heat loss and the reduction of the cob walls thickness.

biobased walls [110–113].

3.6 Methodology and Experimental Investigations

3.6.1 Materials and samples preparation

3.6.1.1 Algae

Laminaria digitata is the type of stranded algae investigated in this study. At low tides, *Laminaria digitata* macroalgae (Figure 3-10a) were collected from the Normandy coast (Courseuille sur Mer). Raw *Laminaria digitata* algae were dried in an oven at 40 °C for at least 24 hours before being crushed to powder through a 63-micron sieve (Figure 3-10b). The water content of fresh algae is roughly 78 wt.% [26]. At 20 °C, *Laminaria digitata* has a thermal conductivity of 0.073 $W.m^{-1}.K^{-1}$ [26]. K, Na, Ca, and Mg are the predominant four metal cations in *Laminaria digitata*, in this order: K>Na>Ca>Mg, followed by Sr, Fe, Al, Zn, and As, with traces of Ba, Cu, Cr, Ni, Pb, and Mo [26]. The amount of iodine is comparable to that of calcium and magnesium (Table 3.12). The biochemical analysis shows that *Laminaria digitata* has an average protein content of 7.9 ±1.3 % and the proportion of alginate is 29.3 ± 2.4 % of the dry weight [26]. The density of the *Laminaria digitata* after drying was 136 $Kg.m^{-3}$

Table 3.12 Chemical composition of *Laminaria digitata* algae.

Element	Al	As	Ba	Ca	Cu	Cr	Fe	K	I	Mg	Mo	Na	Ni	Pb	Sr	Zn
Mg/kg	63	21	6.3	8731	3.6	0.8	127	35491	8762	7637	0.3	24863	0.5	0.4	856	48

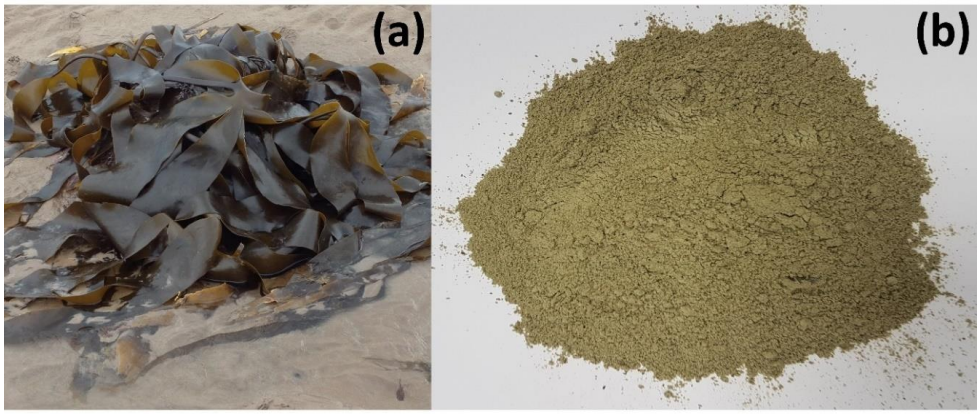

Figure 3-10 (a) Stranded *Laminaria digitata* algae and (b) *prepared Laminaria digitata* powder.

3.6.1.2 Vegetal fibers

As reinforcing and insulator components, natural fibers were used. Farmers from Laulne (Normandy) supplied the fiber utilized in this investigation. Flax straws were utilized for the Structural Cob (It is undervalued because it is derived from the cultivation of oilseed flax or because it is of poor quality for the textile industry). The thermal conductivity of flax straw is between 0.035 and 0.054 $W.m^{-1}.K^{-1}$ [114]. We utilized reed fiber to construct the lightening clay wall. They are easily available and relatively inexpensive. In comparison to synthetic reinforcing materials, their commercialization might have a reduced ecological footprint due to their entirely biodegradable characteristics and CO_2 neutrality. The use of reed as an insulating material is fundamentally acceptable. Reed fibers have a thermal conductivity of around 0.05 $W.m^{-1}.K^{-1}$ [115]. Table 3.13 summarizes the physical properties of reed and flax straw fibers.

Table 3.13 Physical properties of reed and flax straw fibers.

	Diameter (mm)	Density (kg m^{-3})	Initial water content (%)	Tensile strength (MPa)
Flax straw	1-4	1408 ± 5	5,8	112 ± 5
Reed	1-4	1294 ± 5	8.5	117 ± 9

3.6.1.3 Structural cob

The soil used for structural cob was collected in Lieusaint carry, Normandy and is typical of silty soil. The structural earth used in this study contains mainly silicon, aluminum, iron and sodium as the major cations (Table 3.14). The XRD analysis is very important to achieve the mineralogical composition of soil (Figure 3-11). For instance, Si atoms can be found in quartz or clays, two phases with quite distinct properties when used in Cob. The online Full Profile Search Match fitting process

(FPSM, http://nanoair.dii.unitn.it:8080/sfpm/) was used to do a preliminary quick phase analysis. The soil's XRD pattern is then Rietveld-fitted, with the preceding phase identification taken into account. The general R-factors indicate the overall goodness of fit between the model and experimental data (Rwp = 5,1% and Rb = 4,0%, giving goodness of fit of 1,63). The microstrain values are also fitted during this step and remain low for all the phases.

Table 3.14 Chemical composition of structural soil in weight obtained by XRF measures.

Element	Wt.%
Silicon dioxide (SiO_2)	65.89
Aluminum oxide (Al_2O_3)	14.23
Ferric oxide (Fe_2O_3)	6.65
Magnesium oxide (MgO)	4.08
Potassium oxide (K_2O)	2.17
Titanium dioxide (TiO_2)	2.08
Calcium oxide (CaO)	1.27
Sodium oxide (Na_2O)	1.11
Manganese oxide (MnO)	0.16
Phosphorus Pentoxide (P_2O_5)	0.14
Sulfur trioxide (SO_3)	<0.1
Loss on ignition	2.26

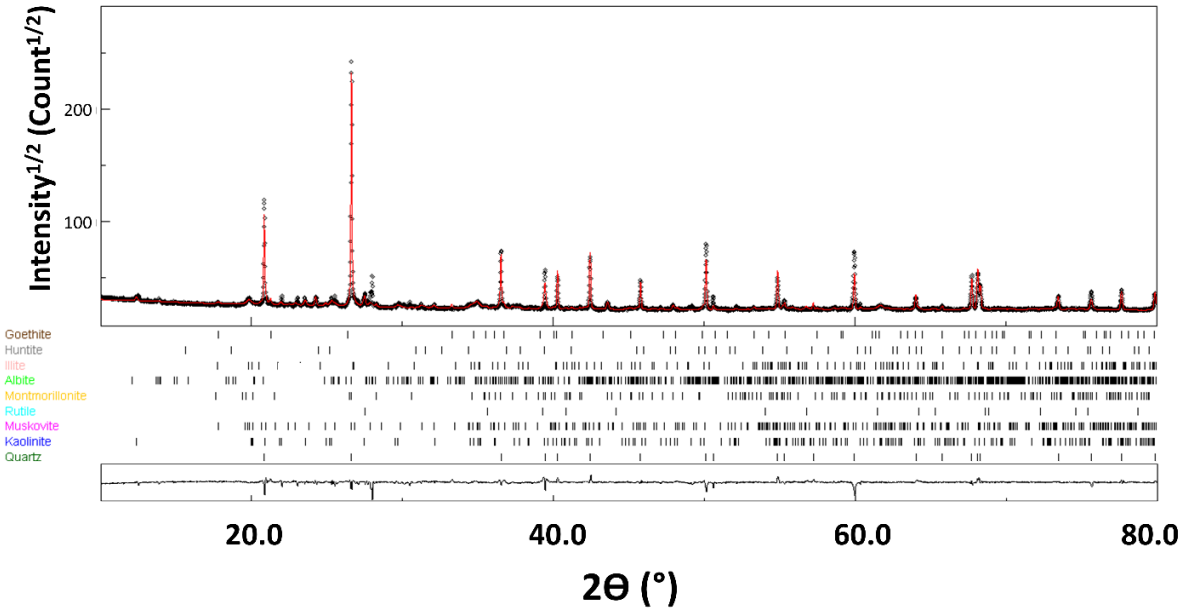

Figure 3-11 XRD pattern of structural soil. On top of the observed profile, the computed pattern (red line) is superimposed (black dots). At the bottom is the difference curve ($I_{obs} - I_{calc}$).

The XRD diagram is adjusted by the main major phases: quartz (54.8 %), muscovite (26.2 %), montmorillonite (6.9 %), and albite (4.2 %), with minor occurrences of

goethite, Kaolinite, illite, rutile, and huntite, according to the quantitative phase identification using Rietveld refinement (Figure 3-11, Table 3.15). Montmorillonite is the only expandable species discovered in our soil, with a rate of 6.9%. The amount of muscovite, albite, kaolinite, and illite in our soil will affect its shrinkage qualities. These crystals have few water molecules between their layers due to their tiny interfoliar space [47]. As a result, they have little intercrystalline swelling when submerged in water [116]. When compared to smectite clays like montmorillonite, these four species shrink significantly less when dried [117]. The first weather-resistant mineral to form is quartz. Mica, feldspars, iron oxy-hydroxides, and limonite are some of the other minerals that can be found in minor amounts [118]. In conclusion, the soil utilized for structural cob is typical of silty soil. It is composed of unaltered minerals such as quartz grains and silicates (micas, feldspars, smectites and serpentines).

Table 3.15 Refined values of lattice parameters, unit cell volume, average diameter and microstrain $<\varepsilon^2>^{1/2}$ used. One standard deviation is indicated in parenthesis on the last digit.

Phases	COD reference	V (%)	Lattice type + Space group	Lattice parameters (Å)	⟨D⟩ (nm)	$\langle\varepsilon^2\rangle^{1/2}$
Quartz SiO_2	1526860	54.8 (5)	Trigonal $P3_221$	a=4,914 (2) c=5,405 (2)	492 (10)	5. 10^{-4}
Muscovite $KAl_2(AlSi_3O_{10})(F,OH)_2$	1100011	26.2 (5)	Monoclinic C2/c:b1	a=5,194 (1) b=9,005 (2) c=19,995(1) β=95.782 (1)	35 (5)	6. 10^{-3}
Montmorillonite $(Na,Ca)_{0.3}(Al,Mg)_2Si_4O_{10}(OH)_2$	1100106	6.9 (2)	Monoclinic C2/c:b1	a=5,386 (2) b=9,039 (2) c=10,196(2) β=100.457 (2)	111 (6)	6. 10^{-4}
Albite $NaAlSiO_3$	1556999	4.2 (2)	Triclinic P1	a=8,166 (1) b=12,845 (1) c=7,188 (1) α=94.240 (1) β=116.590 (1) γ=87.715	43 (5)	6. 10^{-3}
Kaolinite $Al_2Si_2O_5(OH)_4$	1011045	2.1 (3)	Monoclinic Cc:b1	a=5,185 (1) b=8,885 (1) c=14,526 (1) β=100.662 (1)	78 (5)	6. 10^{-4}
Goethite α-FeO(OH)	2211652	2.0 (3)	Orthorhombic Pbnm:cab	a=4,579 (1) b=9,945 (1) c=2,998 (1)	21 (1)	6. 10^{-4}
Rutile	1532819	1.6 (3)	Tetragonal	a=4.582 (1)	92 (5)	8. 10^{-4}

TiO_2			P42/mnm	c=3.014 (2)		
Illite $(K,H_3O)(Al,Mg,Fe)_2(Si,Al)_4O_{10}[(OH)_2,(H_2O)]$	2300190	1.1 (2)	Monoclinic C2/m:b1	a=5,197 (1) b=8,961 (1) c=10,159(1) β=100.970 (1)	100 (5)	6. 10^{-4}
Huntite $Mg_3Ca(CO_3)_4$	1000046	1.1 (2)	Trigonal R32:H	a=9,502 (2) c=7,821 (2)	123 (5)	8. 10^{-4}

3.6.1.4 Clay for insulated cob

The clay used in this study was also collected in Lieusaint carry, Normandy. Table 3.16 shows the chemical composition and physical characteristics of the soil. Quartz, albite, Kaolinite and calcite composed the clay (Figure 3-12 and Table 3.17). Kaolinite and albite provide the clay its moldability when it is combined with water [119]. To eliminate the absorbed water, the clay was dried in an oven at 105°C for 48 hours before being milled to a fine powder.

Table 3.16 Chemical composition and mechanical properties of lightened earth.

Element	**Wt.%**
Silicon dioxide (SiO_2)	59.73
Aluminum oxide (Al_2O_3)	20.25
Ferric oxide (Fe_2O_3)	6.09
Calcium oxide (CaO)	5.33
Magnesium oxide (MgO)	3.16
Sodium oxide (Na_2O)	0.1
Potassium oxide (K_2O)	2.05
Sulphur trioxide (SO_3)	<0.1
Phosphorus Pentoxide (P_2O_5)	<0.1
Cl^-	0.18
Loss on ignition	3.10
Physical properties	
Plasticity limit (%)	42.5
Plasticity index (%)	15.3
Absolute density ($g.cm^{-3}$)	2.73

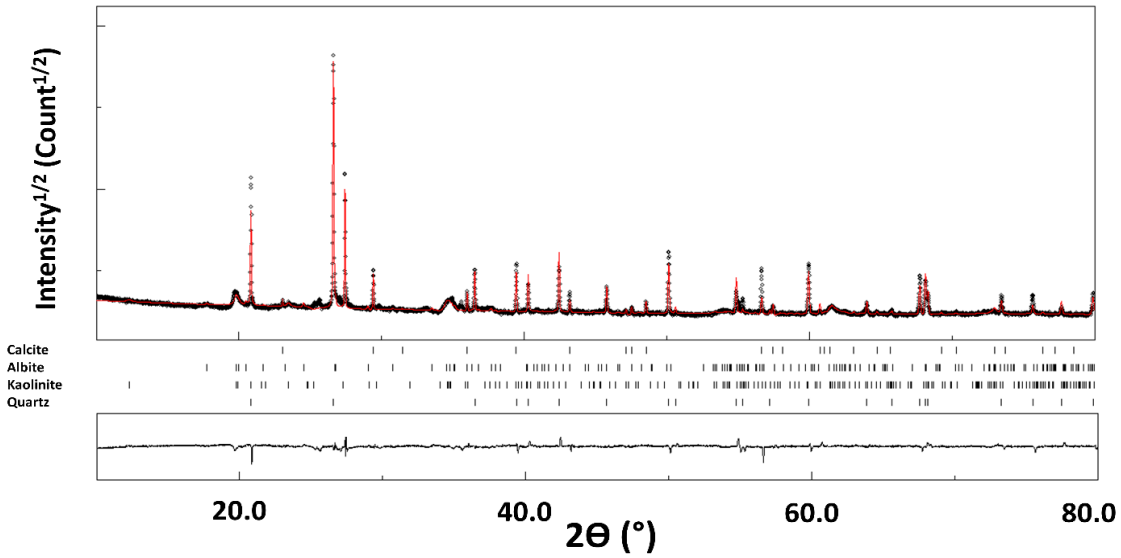

Figure 3-12 XRD pattern of structural soil. On top of the observed profile, the computed pattern (red line) is superimposed (black dots). At the bottom is the difference curve ($I_{obs} - I_{calc}$).

Table 3.17 Refined values of lattice parameters, unit cell volume, average diameter and microstrain $<\varepsilon^2>^{1/2}$ used. One standard deviation is indicated in parenthesis on the last digit.

Phases	COD reference	V (%)	Lattice type + Space group	Lattice parameters (Å)	⟨D⟩ (nm)	$\langle\varepsilon^2\rangle^{1/2}$
Quartz SiO_2	1526860	40.6 (2)	Trigonal $P3_221$	a=4,914 (1) c=5,406 (1)	426 (10)	5. 10^{-4}
Kaolinite $Al_2Si_2O_5(OH)_4$	1011045	32.3 (2)	Monoclinic C2/c:b1	a=5,251 (1) b=8,916 (2) c=14,538 (1) β=99.336(1)	29 (5)	6. 10^{-3}
Albite $NaAlSiO_3$	1556999	15.1 (2)	Monoclinic C2/c:b1	a=5,197 (2) b=8,961 (2) c=10,159 (2) β=100.97 (2)	100 (6)	6. 10^{-4}
Calcite $CaCO_3$	1547347	10.1 (3)	Trigonal R-3c:H	a=4.985 (1) c=17.050 (2)	754 (10)	6. 10^{-4}

3.6.1.5 Sand

The sand used in the structural cob is a natural French sand produced by the Société des Sablières du Cotentin (SABCO, Lieusaint, FRANCE). It is made of natural quartz (99 % of silica). The grains have been washed and are rounded in shape.

3.6.1.6 Tap water

All of the cob specimens were made with local tap water. Table 3.18 shows the chemical composition of the tap water used as mixing water. The measured pH is 7,69.

Table 3.18 Chemical composition of tap water and seawater used in concrete mixtures

Element	Concentration in mg/l
Calcium (Ca)	88.7
Magnesium (Mg)	38.4
Sodium (Na)	42.9
Chloride (Cl)	52.0
Potassium (K)	9.1
Phosphor (P)	2.6
Fluoride (F)	0.3
Zinc (Zn)	0.2
Iron (Fe)	<0.1
Copper (Cu)	<0.1
Manganese (Mn)	<0.1
Sulfates (SO_4^-)	8.4
Nitrite (NO_3^-)	5.2

3.6.1.7 Mix design

The mixture compositions are presented in Table 3.19. Soil and algae are first mixed dry by hand. The required amount of water is added and mixed with the algae until the mixture reaches a liquid state. The fibers are then gradually added to the PROVITEQ concrete mixer for 120 s. The soil algae mixture is manually compacted and stored at a controlled temperature (20 ± 1 °C) for 24 hours. After these 24 hours, the mixture is compacted manually in oiled moulds. The respective weights of all mixtures were calculated to get the same density. Taking into account the amount of water, the mass required to fill the mould is then 2,628 kg. After mixing, the cob samples were filled into cylindrical moulds (diameter Ø 11 cm x height 22 cm) for mechanical analysis and into prismatic moulds (30 x 30 x 4 cm^3) for thermal tests (Figure 3-13). The moulds are left at room temperature (20 ± 1 °C) for 48 hours and then placed in an oven at 40°C for 48 hours. The drying process takes 3 weeks. Three replicates were made for each selected composition. After the drying phase, the samples were exposed to ambient conditions (20 ± 1 °C and 50% relative humidity). Sample characterizations began once equilibrium was reached, i.e., when the mass difference between two daily weighing is less than 0.1 %. Generally, this equilibrium is reached after 48 hours.

It is important to note that no cracking was observed, and the shrinkage is still very low (<2%) for all cob samples after 28 days. Another important point to note is that we also elaborated and studied the structural cob specimen SC15, but this one had a particle breakage. For this reason, we present in this study only the performances of SC0, SC5 and SC10 specimens.

Table 3.19 Mixture proportion of the formulated structural and insulation cob with algae.

Insulation cob (IC)				
Algae in weight	0%	10%	15%	20%
Clay (kg)	4,120	3,708	3,502	3,296
Reed (kg)	1,03	1,03	1,03	1,03
Algae (kg)	0	0,412	0,618	0,824
Water (kg)	4,12	4,12	4,12	4,12

Structural cob (SC)			
Algae in weight	0%	5%	10%
Silty soil (kg)	5.927	5.485	5.042
Algae (kg)	0	0,442	0.885
Sand (kg)	2.919	2.919	2.919
Straw (kg)	0,177	0,177	0.177
Water (kg)	2.654	2.654	2.654

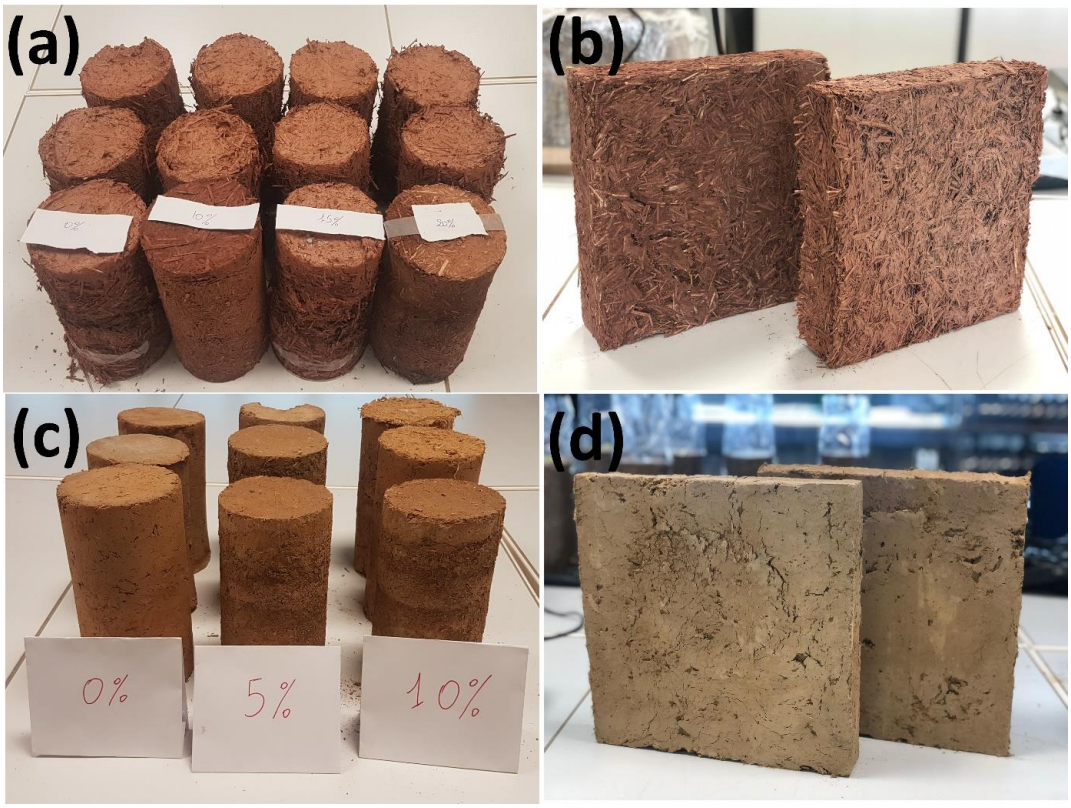

Figure 3-13 Insulation cob samples used for (a) mechanical tests (Ø11 cm × 22 cm) and (b) thermal tests (30×30×4 cm^3). Structural cob samples used for (c) mechanical tests (Ø11 cm × 22 cm) and (d) thermal tests (30×30×4 cm^3)

3.6.2 Characterization techniques

Soil composition analyses were performed using X-ray fluorescence (XRF) spectroscopy. XRF spectra were recorded using an Inel Equinox 3500 spectrometer (equipped with a Cu microfocus source, a multilayer parabolic mirror in the primary beam and an Amptek X123SDD silicon). Drift detectors were placed vertically 10mm above the sample to ensure high sensitivity even for low atomic number elements). Data were collected with an integration time of 400 s.

XRD: An incident beam Ge (111) monochromator on a D8 Advance Vario 1 Bruker instrument (2-circles diffractometer, -2 Bragg-Brentano mode) was used to collect the XRD diagram using copper radiation (λ = 1.54059). From 10° to 80°, the X-ray diffraction pattern of soil is acquired for 1sec at each 0.01° step (16 h/scan). Quantification and crystalline phase identification were done with the Full-Pattern Search-Match (FPSM) technique and the Crystallography Open Database, while Rietveld quantification was done with the MAUD software [40].

ThermoScientific DIONEX ICS3000 CC ion chromatography was used to examine the chemical elements present in tap water. The ion chromatography consists of a double pump module, an eluent generator module, a detector chromatography module and an autosampler. Column pressure and eluent flow rate of 1.0 ml/min. The ionic species were identified and quantified using interpolation over an appropriate calibration curve. All tests were carried out at room temperature.

The thermal conductivity was measured using a NETZSCH Heat Flow Meter device (Model HFM 436 Lambda). The samples have prismatic dimensions of 30x30x7 cm^3 and are positioned between the cooling plate and the heater plate; heat passes from the heater plate through the sample to the cooling plate, where it is transported away. A Peltier cryostat adjusts the cooling and heater plate temperatures to create a temperature gradient of 10 ÷ 40°C from the heater plate across the specimen.

The ability of a substance to hold thermal energy is characterized by its specific heat capacity (Cp). Cp measurements are taken using a Differential Scanning Calorimetry technique (DSC, NETZSCH STA 449 F3) in accordance with ISO 11357-4 [42]. Data is continually recorded from -20 °C to 40 °C at a heating rate of 1 °C/min.

The BET method [120] was used to measure the specific surface area of the cob specimens, and a Helium pycnometer was used to determine the absolute density

(Accupyc II 1340). The Atterberg limits, as defined by the standard NF P94-051 [121], are used to calculate the plasticity of the used soil.

Apparent porosity of cob samples was measured using the gravimetric method according to ISO 5017 [43]. The sample was saturated by water. First, the saturated sample is weighed suspended on a scale and submerged in water (M_w). Then, it is weighed while in the air (M_o). The sample is then dried in an oven before being weighed dry (M_d). The different weights are measured and equation 3-9 is used to calculate the apparent porosity.

$$\rho_d = M_d \frac{\rho_w}{(M_o - M_w)} \qquad \textbf{3-9}$$

ρ_d = apparent density of the cob sample.

The compressive test was performed on cylindrical samples with dimensions of Ø11 cm x 22 cm in accordance with the standard NF EN-12390-3 [44]. The uniaxial compression test was performed on a 100 kN INSTRON SCHENCK press. The testing was conducted at a controlled force with an applied loading rate of 0.05 kN/s. This study presents compressive strength at 4% longitudinal deformation percentages since this value is more reflective of building behaviour.

3.7 Results and discussion

3.7.1 Moisture sorption isotherm of cob specimens

The moisture sorption curves are comparable for all specimens and have a sigmoidal form (Figure 3-14). These hysteretic loops curves are classified as the Type II-isotherm (IUPAC, 1985) according to the IUPAC (International Union of Pure and Applied Chemistry). The Type II-isotherm is characteristic of porous materials, such as the soil-straw and the soil-reed mix investigated in this study. The moisture content of the IS mixtures is about half that of the CS mixtures (Figure 3-14). This effect is due to the significantly higher porosity of the insulating cob compared to the structural cob (Figure 3-15). The mass differential value increases also from SC0 to SC15 and from IC0 to IC20 specimens, as well. This phenomenon is caused by a number of reasons, including the specimen's porosity. The moisture content of raw soils, reed, flax straw, and *Laminaria digitata* algae was measured, as shown in Figure 3-15 (b) and Figure 3-15 (d). The results indicated that marine algae absorb a high quantity of moisture in IC and SC mixes. With the incorporation of algae, IC and SC mix improve their hygroscopic properties. The presence of organic components such as alginate

contributes to *Laminaria digitata*'s high absorbed moisture. Alginate is a polysaccharide hydrocolloid that is a very important hydrophilic element by its ability to absorb and retain a considerable quantity of water inside its structure [122,123]. Figure 3-14 shows the typical mass change for adsorption and desorption processes at various RH percentage stages. At 90% RH, the mass changes for algae, the IC and the SC specimen are around 45%, 12% and 6 %, respectively. Though *since Laminaria digitata* algae has a high sorption capacity, it will inhibit surface condensation (mildew) when incorporated to the soil-straw-water mix.

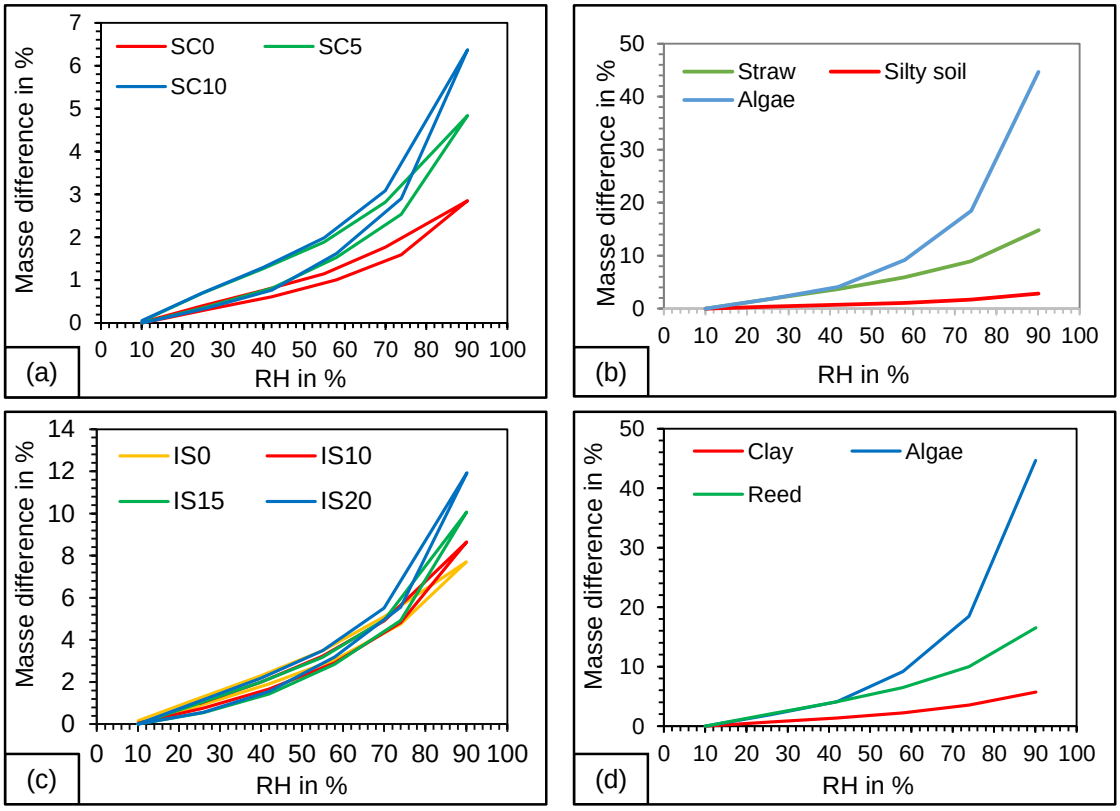

Figure 3-14 (a) Moisture sorption-desorption isotherm of the structural cob specimens at room temperature, (b) Moisture sorption isotherm of structural soil, flax straw and *Laminaria digitata* algae, (c) Moisture sorption-desorption isotherm of the insulting cob specimens at room temperature and (b) Moisture sorption isotherm of insulating soil, reed straw and *Laminaria digitata* algae.

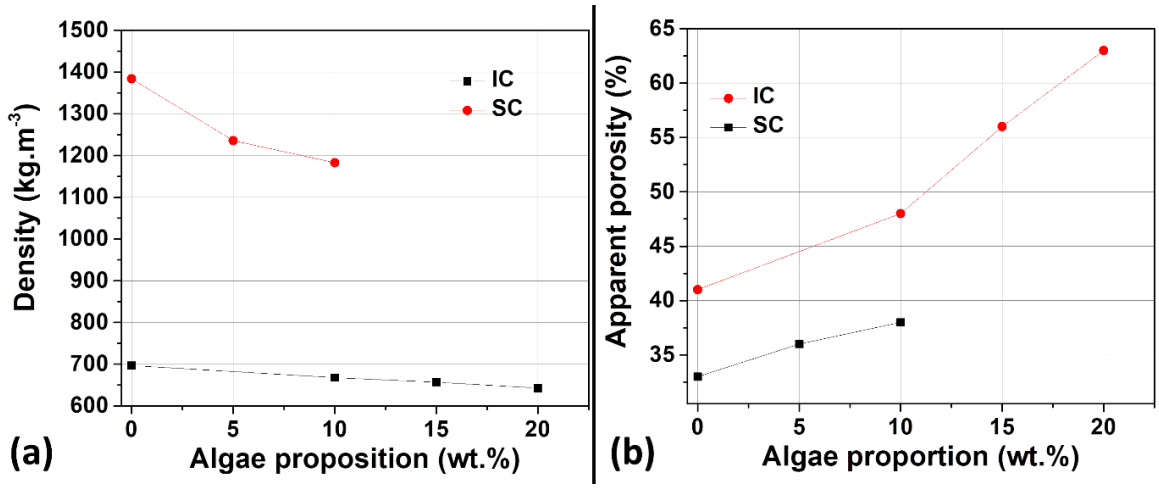

Figure 3-15. (a) Density of structural and insulating cob for different proportions of algae and (b) Apparent porosity of structural and insulating cob for different proportions of algae.

3.7.2 Specific Heat Capacity of IC and SC specimens

The specific heat capacity values for the IC mix range from 950 to 1210 $J.kg^{-1}.K^{-1}$, while those for the SC mix range from 200 to 800 $J.kg^{-1}.K^{-1}$. At all temperatures, the Cp values of specimens with algae are significantly higher than those of the standard cob specimens, i.e., IC0 and SC0 Figure 3-16. This increase of specific heat capacity is due to the increase of algae. Indeed, *Laminaria digitata* has a low thermal conductivity with a high specific heat capacity (λ=0.073 $W.m^{-1}.K^{-1}$, C_p= 1700 at 20°C) [26] which is comparable to that of hemp straw-based thermal insulators. (λ=0.038 to 0.059 $W.m^{-1}.K^{-1}$, C_p= 1400 $J.kg^{-1}.K^{-1}$ at 20°C) [124,125].

In construction industry, building with materials with high calorific capacity performance is crucial in terms of energy efficiency. Furthermore, the C_p of building materials is an important parameter to appreciate the occupants' indoor comfort. In the summer, walls with a high C_p maintain rooms cold with no energy supply inside houses for an extended period and in winter, they keep the heat in the building longer. In conclusion, our results are very promising. Indeed, they show that the soil-straw-algae mixtures produce an improved hydric performance than the standard cob with a simple soil-straw combination.

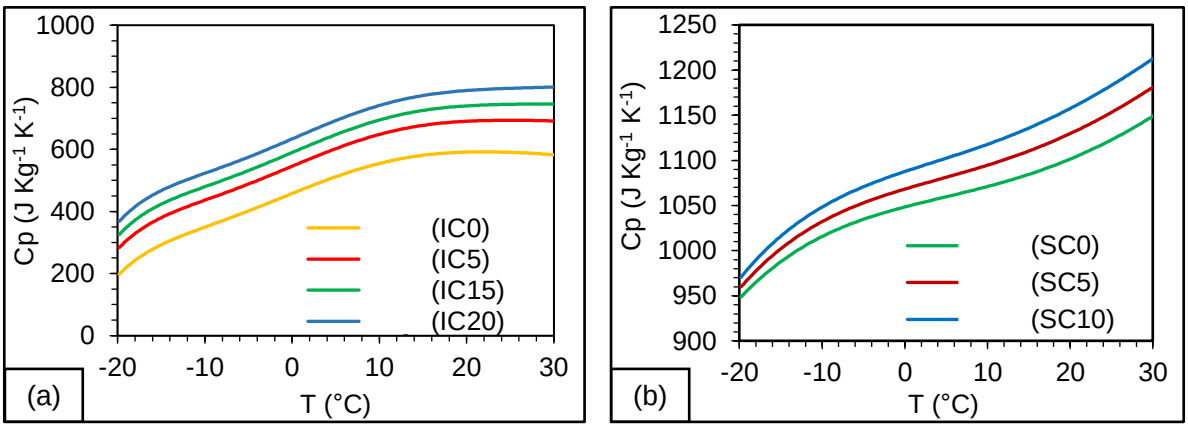

Figure 3-16 Specific heat capacity of (a): IC specimens at different substitution of soil by algae and (b): SC specimens at different substitution of soil by algae.

3.7.3 Thermal conductivity of IC and SC specimens

As shown in Figure 3-17, the thermal conductivity of the IC specimens prepared without algal incorporation is between 0.113 and 0.148 $W.m^{-1}.K^{-1}$ for temperatures ranging from 10°C to 40°C. Thermal conductivity values range from 0.113 $W.m^{-1}.K^{-1}$ at 10°C to 0.127 $W.m^{-1}.K^{-1}$ at 40°C for cob specimens with 20% algae. The decrease in thermal conductivity is very significant even at 10% of the substitution. These findings suggest that introducing algae into the soil matrix decreases the thermal conductivity of the insulating cob. The most effective algal content for improving the thermal insulation of the insulating cob material is with 20% of clay substitution. Indeed, as compared to standard insulating cob (IC0), the addition of 20% algae decreased the thermal conductivity by 26% at 20 °C. For the structural cob, the same phenomenon is observed with a significant decrease in thermal conductivity with the addition of 5% algae. Indeed, as compared to standard structural cob (SC0), the addition of 5% algae decreased the thermal conductivity by 44% at 20 °C. The low thermal conductivity of SC compared to IC specimens is due to the increase in porosity caused by the quantity of straw fibers.

The insulating potential of cob increases with the porosity of the body soil matrix. The organic additives such as algae were beneficial for pore-forming in the soil body, and the cob exhibited high insulating performance with satisfactory mechanical characteristics. The decrease of thermal conductivity is also due to the high specific heat capacity of cob with algae addition which is an important factor that allows this new material to reduce the thermal gradient. The thermal conductivity of the exterior wall is an essential parameter. It is well known that the moisture level of cob materials has a significant impact on their thermal conductivity. Furthermore, the water in cob

wall has latent heat effects, which change the thermal conductivity and thermal capacity of the material.

The use of the algae in cob construction improves its thermal properties, reducing the transfer of heat and presenting best thermal comfort. algae is a thermal insulator (λ=0.073 $W.m^{-1}.K^{-1}$). It is reasonable to correlate energy and environmental concerns with the efficiency of the cob thermal analysis. In constructions with less insulation, the energy required to heat or cool an environment is significantly higher. As a result, a structure made of cob connected with algae will require less energy to maintain thermal comfort, requiring less fuel and energy.

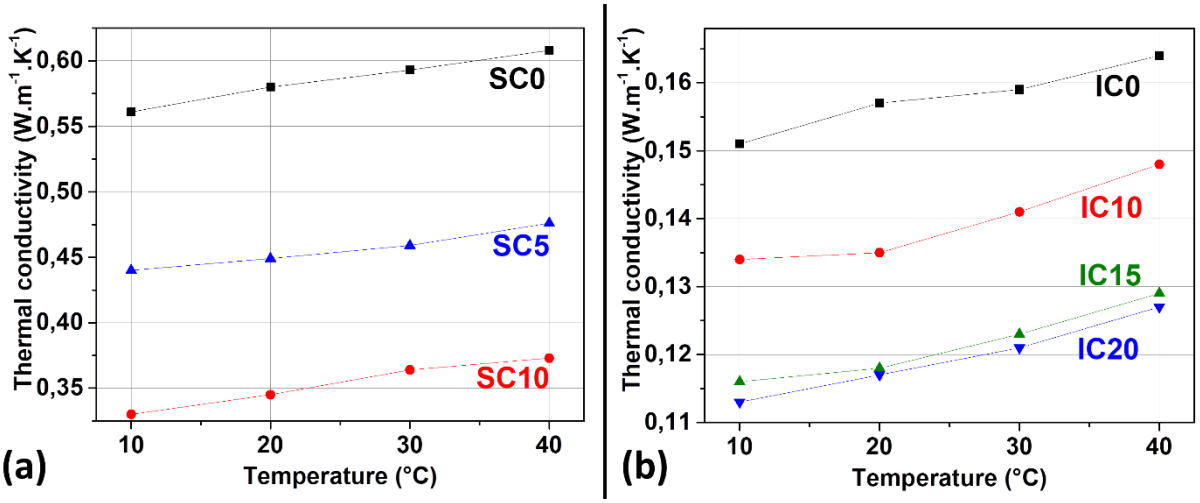

Figure 3-17 (a) Thermal conductivity vs temperature of structural cob with different substitution of soil by algae and (b) Thermal conductivity vs temperature of insulating cob with different substitution of clay by algae.

3.7.4 Mechanical properties of IC and SC specimens

The visual observations indicated that the gel-like properties of the alginate resulted in higher consistency and plasticity during mixing compared to the mix with water alone. Apart from the lack of adhesion between the components of the mix, no grain rupture was observed in the compression tests. As a result, the highest stress recorded cannot be used to evaluate the compressive strength of these ductile materials [126]. Recent studies have identified the maximum compressive strength for a range of longitudinal deformation percentages ranging from 1.5 to 7.5 % [126]. In this study, we chose the corresponding compressive strength at 4 % strain (Figure 3-18). Algae addition produced the greatest compressive strength values, which were statistically greater than the control cob. The increased of compressive strength is explained by the structuring, strengthening, and high cohesion between the algae, the fibers and soil matrix that prevented the cracks spreading. This effect is generated by the alginate's

stabilization [26]. The increase of mechanical properties is also due the decrease of bulk density of the cob specimens with algal addition (Figure 3-15). Indeed, the algae has a much lower density (136 Kg.m^{-3}) than the soils used in IC and SC samples. The reduction in bulk density of materials is beneficial for improved workability in construction and increased efficiency in transportation. Another component that contributes to the decrease in apparent density is the frame given by the algal addition, which reduces shrinking of the cob specimens throughout the drying process.

The only sample showing a reduction in compressive strength is the structural cob containing 10 % algae (SC10). This is most likely due to the fact that the observed high viscosity of the SC10 sample results in poor mixing with high polymer contents. This also explains the observed defects. The lowest compressive strength is observed with the high polymer dosage and the SC5 mixture offers the most favourable results among the alginate-silica soil mixtures.

Our results are in agreement with those reported by other studies, which report increasing strength values of clay-polymer with increasing polymer or alginates content [102,127,128]. These results back up the findings of [129], who found that adding alginate to montmorillonite clay transformed the discrete layered morphology into a co-continuous network, which enhanced the mechanical performance.

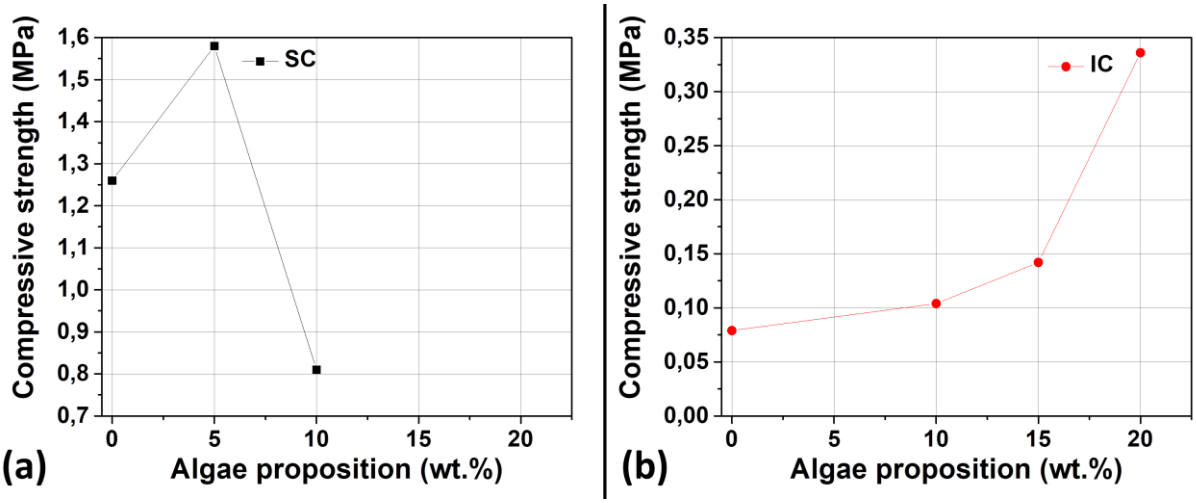

Figure 3-18 (a) Compressive strength of structural cob for different proportions of algae and (b) Compressive strength of insulating cob for different proportions of algae

To explain the influence of algae addition, the phase composition of cob specimen (SC5) was determined through XRD Table 3.20. The corresponding XRD pattern is shown in Figure 3-19. The XRD analysis show the disappearance of huntite combined to the decrease of the montmorillonite content in favour of the formation of gaylussite

(Table 3.17 and Table 3.20). Montmorillonite is the only expandable species found in the structural cob. The presence of kaolinite, muscovite and illite, as well as the reduction of montmorilonite, will decrease the shrinking behaviour. Indeed, these crystals have a weak intracrystalline swelling behaviour and contain a minor amount of water [47]. The formation of carbonate hydrates (gaylussite) is responsible for the increase of the strength properties [130].

The *Laminaria digitata* has a significant quantity of sodium oxide (Na_2O). The sodium oxide combines with atmospheric carbon dioxide to form Na_2CO_3 phases. The formation of gaylussite $Na_2Ca(CO_3)_2 5H_2O$ as show by Raman analysis [26] for the IC specimens and by XRD for the SC5 specimen (Figure 3-19 and Table 3.20). For the IC specimens, the calcium is originating from the clay (dissolution of calcite)) and the tap water. For the SC specimens, the calcium is originating from the silty soil (dissolution of huntite) and tap water. The decrease of the mechanical properties of the sample SC10 can be explained by the low quantity of calcium in the silty soil (1.27% of CaO) compared to the clay used for the IC samples (5.33% of CaO), which does not allow the formation of more gaylussite at high algae addition.

Therefore, as revealed by Galán-Marín et al., [131], the stabilizing effect of algae is due to ionic bridging between the high sodium alginate within algae and the divalent calcium cations originating from the soil and also from tap water (concentration of calcium is 88.7 mg/l) in our study. This ionic bridging results in the formation of gaylussite, which is responsible for the enhanced compressive strengths of SC and IC specimens as compared to standard cob.

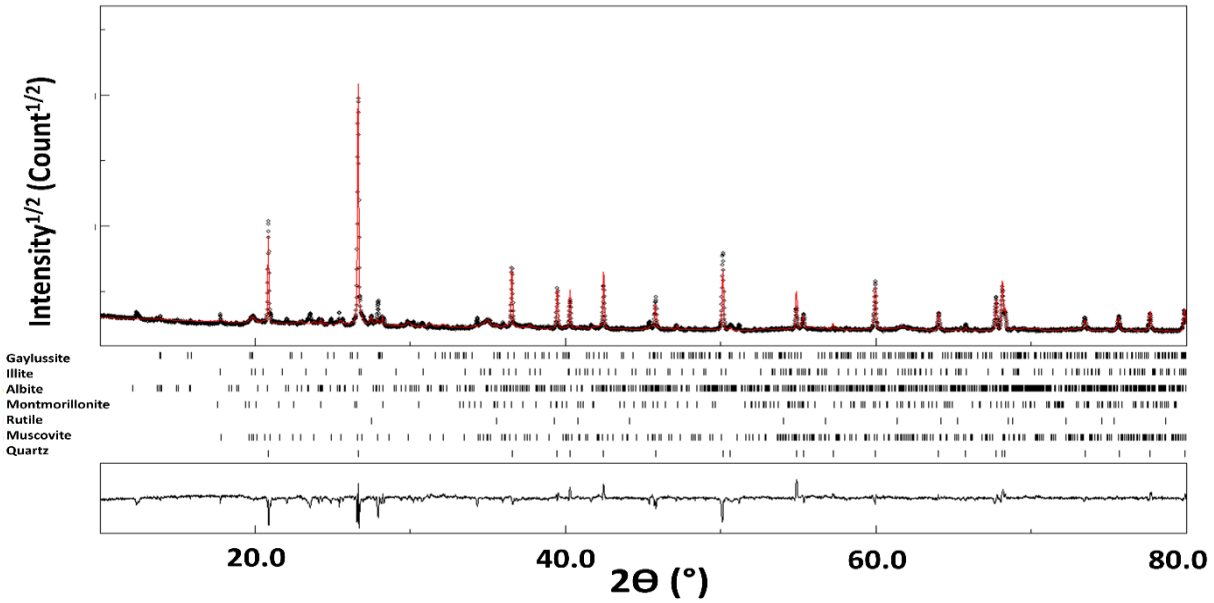

Figure 3-19 XRD pattern of SC5 specimens. On top of the observed profile, the computed pattern (red line) is superimposed (black dots). At the bottom is the difference curve ($I_{obs} - I_{calc}$).

Table 3.20 Refined values of lattice parameters, unit cell volume, average diameter and microstrain $<\varepsilon^2>^{1/2}$ used. One standard deviation is indicated in parenthesis on the last digit.

Phases	COD reference	V (%)	Lattice type + Space group	Lattice parameters (Å)	⟨D⟩ (nm)	$\langle\varepsilon^2\rangle^{1/2}$
Quartz SiO_2	1526860	53.8 (5)	Trigonal $P3_221$	a=4,914 (2) c=5,405 (2)	492 (10)	5. 10^{-4}
Muscovite $KAl_2(AlSi_3O_{10})(F,OH)_2$	1100011	33.5 (5)	Monoclinic C2/c:b1	a=5,194 (1) b=9,005 (2) c=19,995(1) β=95.782 (1)	34(5)	6. 10^{-3}
Montmorillonite $(Na,Ca)_{0.3}(Al,Mg)_2Si_4O_{10}(OH)_2$	1100106	3.0 (2)	Monoclinic C2/c:b1	a=5,382 (2) b=9,056 (2) c=10,229 (2) β=99.98 (2)	96 (6)	6. 10^{-4}
Albite $NaAlSiO_3$	1556999	3.1 (2)	Triclinic P1	a=8,166 (1) b=12,845 (1) c=7,188 (1) α=94.240 (1) β=116.590 (1) γ=87.715	44 (5)	6. 10^{-3}
Rutile TiO_2	1532819	1.5 (3)	Tetragonal P42/mnm	a=4.582 (1) c=3.014 (2)	92 (5)	8. 10^{-4}
Illite $(K,H_3O)(Al,Mg,Fe)_2(Si,Al)_4O_{10}[(OH)_2,(H_2O)]$	2300190	1.1 (2)	Monoclinic C2/m:b1	a=5,197 (1) b=8,961 (1) c=10,159(1) β=100.970 (1)	100 (5)	6. 10^{-4}
Gaylussite $Na_3Ca(CO_3)_2.5.H_2O$	9009890	4.9 (1)	Monoclinic C2/c:b1	a=14,416 (1) b=7,724 (1) c=11,424(1) β=128.281 (1)	99 (5)	6. 10^{-4}

3.8 Discussion

3.8.1 Insight into the mechanism of earth stabilization by algae

The ionic bridging between the high sodium alginate from *Laminaria digitata* algae and the divalent calcium cations originating from the soil and the water is related to the mechanism of *Laminaria digitata* algae stabilization. The gelation characteristics of alginate at room temperature also contribute to soil stabilization [132]. *Laminaria digitata* contains sodium alginate, which is soluble in water but generates an insoluble gel when exposed to a calcium-rich environment [132]. Furthermore, sodium alginates derived from brown Algae are recognized to be non-toxic hydrogels with outstanding biocompatibility attributes, promoting their use in the pharmaceutical sector [133]. This reveals algae's great effectiveness in the stabilization and conservation of earth-straw based materials.

3.8.2 Comparison with literature

The findings here are compared to previous research on the hydrothermal performance of earth-fiber based materials. Table 3.21 illustrates the reported densities, thermal conductivities, specific heat capacity, and the maximum isotherm sorption.

Regardless of the fact that all of the data are from the similar light earth material, the hygroscopic values indicate a broad range of variance. With example, for a dry density of 637 to 702 $kg.m^{-3}$, the thermal conductivity values range from 0.113 $W.m^{-1}.K^{-1}$ (in this study) to 0.22 $W.m^{-1}.K^{-1}$ [134]. Thermal conductivity is 0.065 $W.m^{-1}.K^{-1}$ for dry densities less than 300 kg m^{-3} [135]. This density difference may help to explain why our IC specimens have a somewhat higher conductivity than those described in the literature [135–137]. Indeed, it is acknowledged that heat conductivity decreased with density [135,138]. As a result, the thermal conductivity values observed in this study are in the lower range of thermal conductivities measured in accordance with dry density.

There are very few investigations on specific heat capacity compared to those of thermal conductivity. Our insulating cob specimens have a lower Cp value than those described in the literature for light earth with hemp straw or in the presence of PCM, but it is still greater than that of standard cob materials. The improvement provided by PCMs is only visible around the phase change temperature (24°C). The increased hemp straw mass content (33.7%) may explain the difference in Cp between our IC

specimens and those of Colinart et al., [136]. In terms of sorption value, clay-reed-algae combinations outperform the literature values.

For the structural cob, the hygroscopic values indicate also a broad range of variance. for a dry density of 1107 to 1583 kg.m^{-3}, the thermal conductivity values range from 0.32-0.33 W.m^{-1}.K^{-1} (in this study) to 0.76 W.m^{-1}.K^{-1} [134]. This shows that our SC5 sample has one of the lowest thermal conductivities in the literature with a similar composition.

The results clearly indicates a low Cp when compared to the results reported by Zeghari et al [134] and those obtained for mud-based materials. For the mud, this phenomena might be attributable to a variety of factors, including specimen density, porosity, and the amount of clay minerals present in the mud sample [74]. In terms of sorption value, soil-flax-algae combinations outperform the literature values.

In conclusion, the improvement produced by algae is apparent on thermal conductivity and on the sorption of cob specimens.

Table 3.21 Hygrothermal properties for different insulated soil-fiber walls

Soil	Composition	Density (Kg.m^{-3})	Conductivity (W.m^{-1}.K^{-1})	C_p (J.Kg^{-1}.K^{-1})	Sorption max (%)	Reference
Clay	Clay (0-20% algae), 25% Reed	643 - 697	0.113 – 0.157	1150 – 1240 at 30°C	7.8 - 12	This study
	Clay, 25% Reed	637 - 664	0.16 – 0.18	x	x	[33]
	Clay, 25% Hemp	654 - 702	0.18 – 0.20	x	x	[33]
	Clay, 33.7% Hemp	272	0.09	1050 at 40°C	4.3 – 5.6	[136]
	Clay, 20-33% Typha *Australis*	323 - 586	0.065 – 0.112	x	12.9	[135]
	Commercial Straw-clay	241 -531	0.071 -0.12	x	12	[137]
	Clay (0-20%, Phase Change Materials), 25% Reed	650 - 700	0.134 – 0.156	537 - 2130 at 24 °C	6 - 7.7	[139]
	Clay, 25% Reed	<700	0.19	1500 – 3000 at room temperature	-	[134]
	Clay, 25% Hemp shiv	<700	0.22	1500 – 3000 at room temperature	-	[134]
Mud	Mud, 0-6% Hemp	1271 - 1519	0.25 – 0.55	1500 -1600 at 40°C	3.4	[140]
	Mud, 0-6% Corn Cob	1565 - 1671	0.35 – 0.55	1500 -1600 at 40°C	3.1	[140]
Soil	Silty soil (0-10% algae), 2% Wheat straw	1183 - 1395	0.33 – 0.61	550 – 850 at 30°C	3.1 - 6.4	This study

	Silty soil (0-10% Phase Change Materials), 2.5% wheat straw	1400 -1500	0.64 – 0.76	1164 – 3862 at 24°C	2 – 2.5	[141]
	Silty soil, 2.5% hemp straw	1107 - 1583	0.75	1205 at room temperature	-	[134]
	Silty soil, 2.5% wheat straw	1107 - 1583	0.32	1205 at room temperature	-	[134]
	Silty soil, 2.5% Flax straw	1107 - 1583	0.42	1205 at room temperature	-	[134]
	Silty soil, 2.5% Reed	1107 - 1583	0.36	1205 at room temperature	-	[134]

Thermal conductivity can be established as a linear function of density, as several authors indicate [33,134,138,140,142]. When the density is low, generally less than 1300 kg.m^{-3}, heat transport is mostly driven by resistance in the air bulks, which is especially noticeable in materials strongly filled with fibers. However, when the density exceeds 1300 kg.m^{-3}, the thermal conductivity no longer varies linearly with density. The material structure involves few bulk components, and the transfer is mostly driven by conduction in aggregate materials, which is highly dependent on the composition of the aggregate utilized.

The correlation between density and thermal conductivity of the structural and insulation cob specimens is presented in Figure 3-20. The established linear relationship between thermal conductivity and density is given by the equation 3-10:

$$\lambda = 0.603.10^{-3}\rho - 0.273 \quad \textbf{3-10}$$

with correlation coefficients (R^2) of 0.9995

where ρ is the density in (Kg.m^{-3}) and λ the thermal conductivity in (W.m^{-1}.K^{-1}).

Zeghari et al [134] reported the cob thermal conductivity for similar cob specimens, which is estimated by the equation 3-11:

$$\lambda=0.0002\ \rho+0.05 \quad \textbf{3-11}$$

However, the here studied cob have a low thermal conductivity than expected in accordance with density. This is due to the algal effect, which are known to influence the moisture content, the specific heat capacity, the porosity and thus the thermal conductivity of cob.

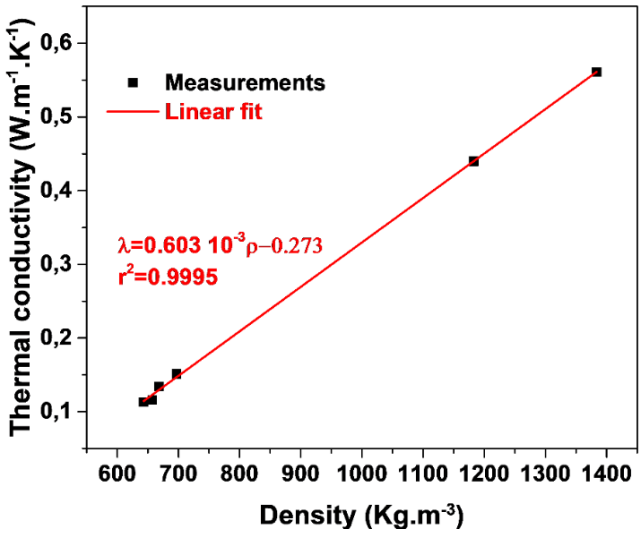

Figure 3-20 Density of the cob specimens versus thermal conductivity

3.9 Perspectives

This study can contribute to a global environmental and economic issue, i.e. the valorization of brown algae on a large scale. Indeed, the world knows the largest sea of *sargassum* algae, which measures over 8850 km. Scientists have dubbed it the Great Atlantic Sargassum Belt [143]. This huge mass of brownish algae is expanding every year, and now covers an area from Africa to the Caribbean. It weighs more than 20 million tons and extends from the Gulf of Mexico to the West coast of Africa.

The findings of this study clearly show that stranded algae, which are considered as wastes, have the ability to improve the mechanical and hygrothermal performance of cob-based material.

Earthen building is gaining popularity as a potential means of establishing local value chains with minimal environmental effect. However, the growth of this historically existing construction technology in a significant portion of France is still limited due to the high cost and construction time imposed by the considerable workforce, as well as the time of the material drying. It could be beneficial to make earth material benefit from concrete formulation progress, particularly in terms of rheology control. The use of dispersants and gelling agents such as alginates, provides improved control of the material's initial rheology and subsequent solidification.

The earth-straw-based materials proposed in this study would thus be more suitable for the construction of external walls that postpone heat transmission from outdoor to interior.

3.10 Conclusions

The mechanical and hygrothermal evaluation of cob walls incorporating *Laminaria digitata* seaweed was the main focus of this work. Promising results from the experiments are outlined in the following paragraphs:

- Algae increases the cob ability to store heat, its degree of insulation, and its compressive strength.
- The incorporation of 20% of algae to the insulation cob matrix reduced the thermal conductivity by 26%.
- The incorporation of 5% of algae to the structural cob enhanced the compressive strength by 22%.

Specimens with algae had proven to be a successful material in earthen construction, leading to the reduction of the wall thickness and contributing to the energy saving due to its thermal properties. To offer an architecturally optimized design for interior and/or exterior walls in order to achieve good energy efficiency during the winter and good comfort during the summer. It is also necessary to assess the energy savings predicted from the incorporation of algae into the soil for cob buildings structures.

3.11 References

[1] Jaquin, P., 2012, “12 - History of Earth Building Techniques,” *Modern Earth Buildings*, M.R. Hall, R. Lindsay, and M. Krayenhoff, eds., Woodhead Publishing, pp. 307–323.

[2] Houben, H., and Guillaud, H., 1989, *Traité de construction en terre*, Parenthèses.

[3] Oti, J. E., Kinuthia, J. M., and Bai, J., 2009, “Engineering Properties of Unfired Clay Masonry Bricks,” Engineering Geology, **107**(3), pp. 130–139.

[4] Daoudi, L., Rocha, F., Costa, C., Arrebei, N., and Fagel, N., 2018, “Characterization of Rammed-Earth Materials from the XVIth Century Badii Palace in Marrakech, Morocco to Ensure Authentic and Reliable Restoration,” Geoarchaeology, **33**(5), pp. 529–541.

[5] Schroeder, H., 2015, *Sustainable Building with Earth*.

[6] Allinson, D., and Hall, M., 2010, “Hygrothermal Analysis of a Stabilised Rammed Earth Test Building in the UK,” Energy and Buildings, **42**(6), pp. 845–852.

[7] Adegun, O. B., and Adedeji, Y. M. D., 2017, “Review of Economic and Environmental Benefits of Earthen Materials for Housing in Africa,” Frontiers of Architectural Research, **6**(4), pp. 519–528.

[8] F. Henry, A., G.Elambo, N., J.h.m, T., E.N.Fabrice, O., and M.Blanche, M., 2014, “Embodied Energy and CO_2 Analyses of Mud-Brick and Cement-Block Houses,” AIMSE, **2**(1), pp. 18–40.

[9] Sharma, V., Marwaha, B. M., and Vinayak, H. K., 2016, “Enhancing Durability of Adobe by Natural Reinforcement for Propagating Sustainable Mud Housing,” International Journal of Sustainable Built Environment, **5**(1).

[10] Alausa, S. K., Adekoya, Bolarinwa. J., Aderibigbe, J. O., and Nwaokocha, C. F., 2013, “THERMAL CHARACTERISTICS OF LATERITE-MUD AND CONCRETE-BLOCK FOR WALLS IN BUILDING CONSTRUCTION IN NIGERIA,” **4**, pp. 1–4.

[11] Thapa, V. B., Waldmann, D., Wagner, J.-F., and Lecomte, A., 2018, “Assessment of the Suitability of Gravel Wash Mud as Raw Material for the Synthesis of an Alkali-Activated Binder,” Applied Clay Science (TOP10 Journal in Mineralogy), **161**(C).

[12] Thapa, V. B., Waldmann, D., and Simon, C., 2019, “Gravel Wash Mud, a Quarry Waste Material as Supplementary Cementitious Material (SCM),” Cement and Concrete Research, **124**(105833).

[13] 2019, “UNPG - French Aggregates Industry” [Online]. Available: http://www.unpg.fr/wp-content/uploads/stat-unpg-chiffres-2017-web.pdf. [Accessed: 22-Jun-2022].

[14] Rakhimova, N. R., and Rakhimov, R. Z., 2019, “Literature Review of Advances in Materials Used in Development of Alkali-Activated Mortars, Concretes, and Composites,” Journal of Materials in Civil Engineering, **31**(11), p. 03119002.

[15] Zami, M. S., and Lee, A., 2009, “Contemporary Earth Construction in Urban Housing– Stabilised or Unstabilised?,” School of the Built Environment, University of Salford.

[16] Brady, N. C., and Weil, R. R., 2002, *Nature and Properties of Soils, The 13th Edition*, Pearson Education, Inc, New Jersey.

[17] Gu, S., Kang, X., Wang, L., Lichtfouse, E., and Wang, C., 2019, “Clay Mineral Adsorbents for Heavy Metal Removal from Wastewater: A Review,” Environmental Chemistry Letters, **17**(2), pp. 629–654.

[18] Gallipoli, D., Bruno, A. W., Perlot-Bascoules, C., and Mendes, J., 2017, “A Geotechnical Perspective of Raw Earth Building,” Acta Geotechnica, **12**(3), p. 463.

[19] Rose, C. M., and Stegemann, J. A., 2018, “From Waste Management to Component Management in the Construction Industry,” Sustainability, **10**(1), p. 229.

[20] Villamizar, M. C. N., Araque, V. S., Reyes, C. A. R., and Silva, R. S., 2012, “Effect of the Addition of Coal-Ash and Cassava Peels on the Engineering Properties of Compressed Earth Blocks,” Construction and Building Materials, **36**, pp. 276–286.

[21] Lima, S. A., Varum, H., Sales, A., and Neto, V., 2012, “Analysis of the Mechanical Properties of Compressed Earth Block Masonry Using the Sugarcane Bagasse Ash.”

[22] Thomas, J., Jose, J., Mathew, N., and Reji, R., 2019, “Mud Bricks Using Oyster Shells.”

[23] Cabrera, J., and Rojas, M. F., 2001, “Mechanism of Hydration of the Metakaolin–Lime–Water System,” Cement and Concrete Research, **31**(2), pp. 177–182.

[24] Gameiro, A., Santos Silva, A., Veiga, M., and Velosa, A., 2012, “Lime-Metakaolin Hydration Products: A Microscopy Analysis,” Materiali in Tehnologije, **46**.

[25] Gameiro, A., Santos Silva, A., Veiga, R., and Velosa, A., 2012, “Hydration Products of Lime–Metakaolin Pastes at Ambient Temperature with Ageing,” Thermochimica Acta, **535**, pp. 36–41.

[26] Bouasria, M., El Mendili, Y., Benzaama, M.-H., Pralong, V., Bardeau, J.-F., and Hennequart, F., 2021, “Valorisation of Stranded Laminaria Digitata Seaweed as an Insulating Earth Material,” Construction and Building Materials, **308**, p. 125068.

[27] Vichan, S., Rachan, R., and Horpibulsuk, S., 2013, “Strength and Microstructure Development in Bangkok Clay Stabilized with Calcium Carbide Residue and Biomass Ash,” ScienceAsia, **39**(2), p. 186.

[28] Horpibulsuk, S., Phetchuay, C., and Chinkulkijniwat, A., 2012, “Soil Stabilization by Calcium Carbide Residue and Fly Ash,” Journal of Materials in Civil Engineering, **24**(2), pp. 184–193.

[29] Siddiqua, S., and Barreto, P. N. M., 2018, “Chemical Stabilization of Rammed Earth Using Calcium Carbide Residue and Fly Ash,” Construction and Building Materials, **169**, pp. 364–371.

[30] Zierold, K. M., Sears, C. G., Hagemeyer, A. N., Brock, G. N., Polivka, B. J., Zhang, C. H., and Sears, L., 2020, “Protocol for Measuring Indoor Exposure to Coal Fly Ash and Heavy Metals, and Neurobehavioural Symptoms in Children Aged 6 to 14 Years Old,” BMJ Open, **10**(11), p. e038960.

[31] Kampala, A., Horpibulsuk, S., Prongmanee, N., and Chinkulkijniwat, A., 2014, “Influence of Wet-Dry Cycles on Compressive Strength of Calcium Carbide Residue–Fly Ash Stabilized Clay,” Journal of Materials in Civil Engineering, **26**(4), pp. 633–643.

[32] Lekshmi, M. s., Vishnudas, S., and Nair, D. G., 2017, “An Investigation on the Potential of Mud as Sustainable Building Material in the Context of Kerala,” International Journal of Energy Technology and Policy, **13**(1–2), pp. 107–122.

[33] Goodhew, S., Boutouil, M., Streiff, F., Le Guern, M., Carfrae, J., and Fox, M., 2021, “Improving the Thermal Performance of Earthen Walls to Satisfy Current Building Regulations,” Energy and Buildings, **240**, p. 110873.

[34] 2012, “NF EN 450-1. Fly ash for concrete - Part 1 : definition, specifications and conformity criteria.”

[35] Bouasria, M., Khadraoui, F., Benzaama, M.-H., Touati, K., Chateigner, D., Gascoin, S., Pralong, V., Orberger, B., Babouri, L., and El Mendili, Y., 2021, “Partial Substitution of Cement by the Association of Ferronickel Slags and Crepidula Fornicata Shells,” Journal of Building Engineering, **33**, p. 101587.

[36] Phung, T. A., Le Guern, M., Boutouil, M., and Louahlia, H., 2019, “Hygrothermal Behaviour of Cob Material,” *Earthen Dwellings and Structures*, D.V.; A.D. Theocharis (Eds), ed., Springer, Singapore, pp. 345–356.

[37] El Mendili, Y., Vaitkus, A., Merkys, A., Gražulis, S., Chateigner, D., Mathevet, F., Gascoin, S., Petit, S., Bardeau, J.-F., Zanatta, M., Secchi, M., Mariotto, G., Kumar, A., Cassetta, M., Lutterotti, L., Borovin, E., Orberger, B., Simon, P., Hehlen, B., and Le Guen, M., 2019, “Raman Open Database: First Interconnected Raman–X-Ray Diffraction Open-Access Resource for Material Identification,” J Appl Crystallogr, **52**(3), pp. 618–625.

[38] Caglioti, G., Paoletti, A., and Ricci, F. P., 1958, “Choice of Collimators for a Crystal Spectrometer for Neutron Diffraction,” Nuclear Instruments, **3**(4), pp. 223–228.

[39] Gražulis, S., Daškevič, A., Merkys, A., Chateigner, D., Lutterotti, L., Quirós, M., Serebryanaya, N. R., Moeck, P., Downs, R. T., and Le Bail, A., 2012, “Crystallography Open Database (COD): An Open-Access Collection of Crystal Structures and Platform for World-Wide Collaboration,” Nucleic Acids Research, **40**(D1), pp. D420–D427.

[40] Lutterotti, L., Matthies, S., Wenk, H.-R., Schultz, A. S., and Richardson, J. W., 1997, “Combined Texture and Structure Analysis of Deformed Limestone from Time-of-Flight Neutron Diffraction Spectra,” Journal of Applied Physics, **81**(2), pp. 594–600.

[41] 2016, “NF EN ISO 12572. Hygrothermal Performance of Building Materials and Products - Determination of Water Vapour Transmission Properties - Cup Method.”

[42] 2021, “NF EN ISO 11357-4. Plastics - Differential Scanning Calorimetry (DSC) - Part 4 : Determination of Specific Heat Capacity.”

[43] “NF ISO 5017. Dense Shaped Refractory Products - Determination of Bulk Density, Apparent Porosity and True Porosity.”

[44] 2019, “NF EN 12390-3. Testing Hardened Concrete - Part 3 : Compressive Strength of Test Specimens.”

[45] Barton, C. D., 2002, “Clay Minerals,” pp. 187–192.

[46] Mookherjee, M., Mainprice, D., Maheshwari, K., Heinonen, O., Patel, D., and Hariharan, A., 2016, “Pressure Induced Elastic Softening in Framework Aluminosilicate- Albite (NaAlSi3O8),” Sci Rep, **6**(1), p. 34815.

[47] Andrade, F. A., Al-Qureshi, H. A., and Hotza, D., 2011, “Measuring the Plasticity of Clays: A Review,” Applied Clay Science, **51**(1), pp. 1–7.

[48] Biagioni, C., Merlino, S., and Bonaccorsi, E., 2015, “The Tobermorite Supergroup: A New Nomenclature,” Mineralogical Magazine, **79**(2), pp. 485–495.

[49] Komarneri, S., Roy, D. M., and Roy, R., 1982, “Al-Substituted Tobermorite: Shows Cation Exchange,” Cement and Concrete Research, **12**(6), pp. 773–780.

[50] Komarneni, S., Roy, R., Roy, D. M., Fyfe, C. A., Kennedy, G. J., Bothner-By, A. A., Dadok, J., and Chesnick, A. S., 1985, “27Al And29Si Magic Angle Spinning Nuclear Magnetic Resonance Spectroscopy of Al-Substituted Tobermorites,” J Mater Sci, **20**(11), pp. 4209–4214.

[51] Faucon, P., Petit, J. C., Charpentier, T., Jacquinot, J. F., and Adenot, F., 1999, “Silicon Substitution for Aluminum in Calcium Silicate Hydrates,” Journal of the American Ceramic Society, **82**(5), pp. 1307–1312.

[52] Paradiso, P., Santos, R. L., Horta, R. B., Lopes, J. N. C., Ferreira, P. J., and Colaço, R., 2018, “Formation of Nanocrystalline Tobermorite in Calcium Silicate Binders with Low C/S Ratio,” Acta Materialia, **152**, pp. 7–15.

[53] Luo, F., Wei, C., Xue, B., Wang, S., and Jiang, Y., 2013, “Dynamic Hydrothermal Synthesis of Al-Substituted 11 Å Tobermorite from Solid Waste Fly Ash Residue-Extracted Al2O3,” Res Chem Intermed, **39**(2), pp. 693–705.

[54] Bernstein, S., and Fehr, K. T., 2012, “The Formation of 1.13 Nm Tobermorite under Hydrothermal Conditions: 1. The Influence of Quartz Grain Size within the System CaO–SiO2–D2O,” Progress in Crystal Growth and Characterization of Materials, **58**(2), pp. 84–91.

[55] Michel, M., Georgin, J.-F., and Ambroise, J., 2012, “Improving the Mechanical Performance of High-Grade Slag Cement by the Addition of Portland Cement and Sulfoaluminate Cement,” Construction and Building Materials, **C**(37), pp. 291–300.

[56] Ismail, I., Bernal, S. A., Provis, J. L., Hamdan, S., and van Deventer, J. S. J., 2013, “Drying-Induced Changes in the Structure of Alkali-Activated Pastes,” J Mater Sci, **48**(9), pp. 3566–3577.

[57] Ma, B., Liu, X., Tan, H., Zhang, T., Mei, J., Qi, H., Jiang, W., and Zou, F., 2018, “Utilization of Pretreated Fly Ash to Enhance the Chloride Binding Capacity of Cement-Based Material,” Construction and Building Materials, **175**, pp. 726–734.

[58] Marsh, A., Heath, A., Patureau, P., Evernden, M., and Walker, P., 2018, “Alkali Activation Behaviour of Un-Calcined Montmorillonite and Illite Clay Minerals,” Applied Clay Science, **166**, pp. 250–261.

[59] Stolboushkin, A. Y., Ivanov, A. I., Syromyasov, V. A., and Fomina, O. A., 2016, “A Study on Sintering of Ceramic Bricks Made from Waste Coal,” IOP Conf. Ser.: Earth Environ. Sci., **45**, p. 012018.

[60] Elkhalifah, A. E., Maitra, S., Azmi Bustam, M., and Murugesan, T., 2012, “Thermogravimetric Analysis of Different Molar Mass Ammonium Cations Intercalated Different Cationic Forms of Montmorillonite,” Journal of thermal analysis and calorimetry, **110**(2), pp. 765–771.

[61] Laskou, M., Margomenou-Leonidopoulou, G., and Balek, V., 2006, “Thermalcharacterization of Bauxite Samples,” J Therm Anal Calorim, **84**(1), pp. 141–146.

[62] Dollimore, D., Tong, P., and Alexander, K. S., 1996, “The Kinetic Interpretation of the Decomposition of Calcium Carbonate by Use of Relationships Other than the Arrhenius Equation,” Thermochimica Acta, **282–283**, pp. 13–27.

[63] Barba, A., Beltrán, V., Feliu, C., García, J., Ginés, F., Sánchez, E., and Sanz, V., 1997, “Raw Materials for Fabrication of Supports to Clay Ceramics,” AICE/ITC: Castellón, Spain.

[64] Carty, W., and Senapati, U., 1998, “Porcelain—Raw Materials, Processing, Phase Evolution, and Mechanical Behavior.”

[65] El Mendili, Y., Chateigner, D., Orberger, B., Gascoin, S., Bardeau, J.-F., Petit, S., Duée, C., Le Guen, M., and Pilliere, H., 2019, “Combined XRF, XRD, SEM-EDS, and Raman Analyses on Serpentinized Harzburgite (Nickel Laterite Mine, New Caledonia): Implications for Exploration and Geometallurgy,” ACS Earth Space Chem., **3**(10), pp. 2237–2249.

[66] Ait Chaou, A., Abdelouas, A., Mendili, Y. E., Bouakkaz, R., Utsunomiya, S., Martin, C., and Bourbon, X., 2015, “Vapor Hydration of a Simulated Borosilicate Nuclear Waste Glass in Unsaturated Conditions at 50 °C and 90 °C,” RSC Adv., **5**(79), pp. 64538–64549.

[67] Plummer, L. N., and Busenberg, E., 1982, “The Solubilities of Calcite, Aragonite and Vaterite in CO2-H2O Solutions between 0 and 90°C, and an Evaluation of the Aqueous Model for the System CaCO3-CO2-H2O,” Geochimica et Cosmochimica Acta, **46**(6), pp. 1011–1040.

[68] Bouasria, M., Babouri, L., Khadraoui, F., Chateigner, D., Gascoin, S., Pralong, V., Benzaama, M.-H., Orberger, B., and El Mendili, Y., 2020, “Insight into the Partial Replacement of Cement by Ferronickel Slags from New Caledonia,” European Journal of Environmental and Civil Engineering, **0**(0), pp. 1–19.

[69] Garbev, K., Stemmermann, P., Black, L., Breen, C., Yarwood, J., and Gasharova, B., 2007, “Structural Features of C–S–H(I) and Its Carbonation in Air—A Raman Spectroscopic Study. Part I: Fresh Phases,” Journal of the American Ceramic Society, **90**(3), pp. 900–907.

[70] Grangeon, S., Claret, F., Roosz, C., Sato, T., Gaboreau, S., and Linard, Y., 2016, “Structure of Nanocrystalline Calcium Silicate Hydrates: Insights from X-Ray Diffraction, Synchrotron X-Ray Absorption and Nuclear Magnetic Resonance,” J Appl Crystallogr, **49**(Pt 3), pp. 771–783.

[71] Liao, W., Li, W., Fang, Z., Lu, C., and Xu, Z., 2019, “Effect of Different Aluminum Substitution Rates on the Structure of Tobermorite,” Materials, **12**(22), p. 3765.

[72] Minke, G., 2000, *Earth Construction Handbook: The Building Material Earth in Modern Architecture*, WIT Press: Boston, Southampton.

[73] Sing, K. S. W., 1985, “Reporting Physisorption Data for Gas/Solid Systems with Special Reference to the Determination of Surface Area and Porosity (Recommendations 1984),” Pure and Applied Chemistry, **57**(4), pp. 603–619.

[74] van Oss, C. J., and Giese, R. F., 1995, “The Hydrophilicity and Hydrophobicity of Clay Minerals,” Clays Clay Miner., **43**(4), pp. 474–477.

[75] Volhard, F., 2016, *Light Earth Building: A Handbook for Building With Wood and Earth*, Birkhauser.

[76] Esfanjary Kenari, E., 2017, *Persian Historic Urban Landscapes Interpreting and Managing Maibud over 6000 Years*, Edinburgh University Press.

[77] Jaquin, P. A., Augarde, C. E., and Gerrard, C. M., 2008, “Chronological Description of the Spatial Development of Rammed Earth Techniques,” International Journal of Architectural Heritage, **2**(4), pp. 377–400.

[78] El Mendili, Y., Bouasria, M., Benzaama, M.-H., Khadraoui, F., Le Guern, M., Chateigner, D., Gascoin, S., and Bardeau, J.-F., 2021, “Mud-Based Construction Material: Promising Properties of French Gravel Wash Mud Mixed with Byproducts, Seashells and Fly Ash as a Binder,” **14**(20), p. 6216.

[79] Medvey, B., and Dobszay, G., 2020, “Durability of Stabilized Earthen Constructions: A Review,” Geotech Geol Eng, **38**(3), pp. 2403–2425.

[80] Minke, G., 2006, *Building With Earth: Design And Technology Of A Sustainable Architecture*, Birkhäuser - Publishers for Architecture, Berlin, Germany.

[81] Mardiana, A., and Riffat, S. B., 2015, “Building Energy Consumption and Carbon Dioxide Emissions: Threat to Climate Change,” J Earth Sci Clim Change, **s3**.

[82] Miccoli, L., Müller, U., and Fontana, P., 2014, “Mechanical Behaviour of Earthen Materials: A Comparison between Earth Block Masonry, Rammed Earth and Cob,” Construction and Building Materials, **61**, pp. 327–339.

[83] Hall, M., and Djerbib, Y., 2004, “Rammed Earth Sample Production: Context, Recommendations and Consistency,” Construction and Building Materials, **18**(4), pp. 281–286.

[84] Bekhiti, M., Trouzine, H., and Rabehi, M., 2019, “Influence of Waste Tire Rubber Fibers on Swelling Behavior, Unconfined Compressive Strength and Ductility of Cement Stabilized Bentonite Clay Soil,” Construction and Building Materials, **208**, pp. 304–313.

[85] Irani, N., and Ghasemi, M., 2019, “Effect of Scrap Tyre on Strength Properties of Untreated and Lime-Treated Clayey Sand,” European Journal of Environmental and Civil Engineering, **25**(9), pp. 1609–1626.

[86] Kalkan, E., 2013, “Preparation of Scrap Tire Rubber Fiber–Silica Fume Mixtures for Modification of Clayey Soils,” Applied Clay Science, **80–81**, pp. 117–125.

[87] Chang, I., Lee, M., Tran, A. T. P., Lee, S., Kwon, Y.-M., Im, J., and Cho, G.-C., 2020, “Review on Biopolymer-Based Soil Treatment (BPST) Technology in Geotechnical Engineering Practices,” Transportation Geotechnics, **24**, p. 100385.

[88] Georgees, R. N., Hassan, R. A., Evans, R. P., and Jegatheesan, P., 2015, “Effect of the Use of a Polymeric Stabilizing Additive on Unconfined Compressive Strength of Soils,” Transportation Research Record, **2473**(1), pp. 200–208.

[89] Williamson, S., and Cortes, D. D., 2014, “Dimensional Analysis of Soil–Cement Mixture Performance,” Géotechnique Letters, **4**(1), pp. 33–38.

[90] Chang, I., Im, J., and Cho, G.-C., 2016, “Introduction of Microbial Biopolymers in Soil Treatment for Future Environmentally-Friendly and Sustainable Geotechnical Engineering,” Sustainability, **8**(3), p. 251.

[91] Estabragh, A. R., Beytolahpour, I., and Javadi, A. A., 2011, “Effect of Resin on the Strength of Soil-Cement Mixture,” Journal of Materials in Civil Engineering, **23**(7), pp. 969–976.

[92] Khatami, H. R., and O’Kelly, B. C., 2013, “Improving Mechanical Properties of Sand Using Biopolymers,” Journal of Geotechnical and Geoenvironmental Engineering, **139**(8), pp. 1402–1406.

[93] Soltani, A., Deng, A., Taheri, A., and O'Kelly, B. C., 2019, "Engineering Reactive Clay Systems by Ground Rubber Replacement and Polyacrylamide Treatment," Polymers, **11**(10), p. 1675.

[94] Ben-Hur, M., Malik, M., Letey, J., and Mingelgrin, U., 1992, "Adsorption of Polymers on Clays as Affected by Clay Charge and Structure, Polymers Properties, and Water Quality," Soil Science, **153**(5), pp. 349–356.

[95] Letey, J., 1994, "Adsorption and Desorption of Polymers on Soil," Soil Science, **158**(4), pp. 244–248.

[96] Slaný, M., Jankovič, Ľ., and Madejová, J., 2019, "Structural Characterization of Organo-Montmorillonites Prepared from a Series of Primary Alkylamines Salts: Mid-IR and near-IR Study," Applied Clay Science, **176**, pp. 11–20.

[97] Rehm, B. H. A., 2009, "Alginates: Biology and Applications," *Microbiology Monographs*, Springer Berlin Heidelberg, pp. 1–53.

[98] Draget, K. I., Smidsrød, O., and Skjåk-Bræk, G., 2005, "Alginates from Algae," *Polysaccharides and Polyamides in the Food Industry: Properties, Production, and Patents*, John Wiley & Sons, Ltd, pp. 1–30.

[99] Arab, M. G., Mousa, R. A., Gabr, A. R., Azam, A. M., El-Badawy, S. M., and Hassan, A. F., 2019, "Resilient Behavior of Sodium Alginate–Treated Cohesive Soils for Pavement Applications," Journal of Materials in Civil Engineering, **31**(1), p. 04018361.

[100] Peng, C., Zheng, J., Huang, S., Li, S., Li, D., Cheng, M., and Liu, Y., 2017, "Application of Sodium Alginate in Induced Biological Soil Crusts: Enhancing the Sand Stabilization in the Early Stage," J Appl Phycol, **29**(3), pp. 1421–1428.

[101] Zhao, Y., Zhuang, J., Wang, Y., Jia, Y., Niu, P., and Jia, K., 2020, "Improvement of Loess Characteristics Using Sodium Alginate," Bull Eng Geol Environ, **79**(4), pp. 1879–1891.

[102] Dove, C. A., Bradley, F. F., and Patwardhan, S. V., 2019, "A Material Characterization and Embodied Energy Study of Novel Clay-Alginate Composite Aerogels," Energy and Buildings, **184**, pp. 88–98.

[103] López-Contreras, A. M., Geest, M. van der, Deetman, B., Burg, S. van den, Brust, H., and Vrije, T. de, 2021, *Opportunities for Valorisation of Pelagic Sargassum in the Dutch Caribbean*, Wageningen Food & Biobased Research.

[104] Widera, B., 2014, "Possible Application of Seaweed as Building Material in the Modern Seaweed House on Laesø," Ahmedabad, India.

[105] Perrot, T., Rossi, N., Ménesguen, A., and Dumas, F., 2014, "Modelling Green Macroalgal Blooms on the Coasts of Brittany, France to Enhance Water Quality Management," Journal of Marine Systems, **132**, pp. 38–53.

[106] 2012, "CEVA - Etude et suivi des marées vertes en Normandie," CEVA [Online]. Available: https://www.ceva-algues.com/. [Accessed: 23-Jun-2022].

[107] Grossman, M., 2000, "Nitrates From Agriculture in Europe: The EC Nitrates Directive and Its Implementation in England," Boston College Environmental Affairs Law Review, **27**(4), p. 567.

[108] Lemesle, S., Mussio, I., Rusig, A.-M., Menet-Nédélec, F., and Claquin, P., 2015, "Impact of Seaweed Beachings on Dynamics of Δ15N Isotopic Signatures in Marine Macroalgae," Marine Pollution Bulletin, **97**(1), pp. 241–254.

[109] Lapointe, B. E., Brewton, R. A., Herren, L. W., Wang, M., Hu, C., McGillicuddy, D. J., Lindell, S., Hernandez, F. J., and Morton, P. L., 2021, "Nutrient Content

and Stoichiometry of Pelagic Sargassum Reflects Increasing Nitrogen Availability in the Atlantic Basin," Nat Commun, **12**(1), p. 3060.

[110] May Tzuc, O., Rodríguez Gamboa, O., Aguilar Rosel, R., Che Poot, M., Edelman, H., Jiménez Torres, M., and Bassam, A., 2021, "Modeling of Hygrothermal Behavior for Green Facade's Concrete Wall Exposed to Nordic Climate Using Artificial Intelligence and Global Sensitivity Analysis," Journal of Building Engineering, **33**, p. 101625.

[111] Tijskens, A., Roels, S., and Janssen, H., 2019, "Neural Networks for Metamodelling the Hygrothermal Behaviour of Building Components," Building and Environment, **162**, p. 106282.

[112] Tijskens, A., Roels, S., and Janssen, H., 2021, "Hygrothermal Assessment of Timber Frame Walls Using a Convolutional Neural Network," Building and Environment, **193**, p. 107652.

[113] Bouasria, M., Benzaama, M.-H., Pralong, V., and El Mendili, Y., 2022, "Mechanical and Hygrothermal Performance of Fly-Ash and Seashells Concrete: In Situ Experimental Study and Smart Hygrothermal Modeling for Normandy Climate Conditions," Archiv.Civ.Mech.Eng, **22**(2), p. 100.

[114] Goodhew, S., Boutouil, M., Streiff, F., Le Guern, M., Carfrae, J., and Fox, M., 2021, "Improving the Thermal Performance of Earthen Walls to Satisfy Current Building Regulations," Energy and Buildings, **240**, p. 110873.

[115] Köbbing, J., Thevs, N., Zerbe, S., Wichtmann, W., and Couwenberg, J., 2013, "The Utilisation of Reed (Phragmites Australis): A Review," Mires and Peat.

[116] Zhang, X., Chen, B., and Riaz Ahmad, M., 2021, "Characterization of a Novel Bio-Insulation Material for Multilayer Wall and Research on Hysteresis Effect," Construction and Building Materials, **290**, p. 123162.

[117] Meinhold, G., 2010, "Rutile and Its Applications in Earth Sciences," Earth-Science Reviews, **102**(1), pp. 1–28.

[118] Hillel, D., 2008, "SOIL PHYSICAL ATTRIBUTES," *Soil in the Environment*, D. Hillel, ed., Academic Press, San Diego, pp. 55–77.

[119] Miranda-Trevino, J. C., and Coles, C. A., 2003, "Kaolinite Properties, Structure and Influence of Metal Retention on PH," Applied Clay Science, **23**(1), pp. 133–139.

[120] Brunauer, S., Emmett, P. H., and Teller, E., 1938, "Adsorption of Gases in Multimolecular Layers," J. Am. Chem. Soc., **60**(2), pp. 309–319.

[121] 1998, "NF P94–051. Soils : Investigation and Testing - Determination of Atterberg's Limits. Liquid Limit Test Using Cassagrande Apparatus."

[122] Ahmed, E. M., 2015, "Hydrogel: Preparation, Characterization, and Applications: A Review," Journal of Advanced Research, **6**(2), pp. 105–121.

[123] Vauchel, P., Kaas, R., Arhaliass, A., Baron, R., and Legrand, J., 2008, "A New Process for Extracting Alginates from Laminaria Digitata: Reactive Extrusion," Food Bioprocess Technol, **1**(3), pp. 297–300.

[124] Nováková, P., 2018, "Use of Technical Hemp in the Construction Industry," MATEC Web Conf., **146**, p. 03011.

[125] Gaujena, B., Agapovs, V., Borodinecs, A., and Strelets, K., 2020, "Analysis of Thermal Parameters of Hemp Fiber Insulation," Energies, **13**(23), p. 6385.

[126] Laborel-Préneron, A., Aubert, J. E., Magniont, C., Tribout, C., and Bertron, A., 2016, “Plant Aggregates and Fibers in Earth Construction Materials: A Review,” Construction and Building Materials, **111**, pp. 719–734.

[127] Dove, C., 2014, “The Development of Unfired Earth Bricks Using Seaweed Biopolymers,” Siena, Italy, pp. 219–230.

[128] Ohta, S., and Nakazawa, H., 1995, “Porous Clay-Organic Composites: Potential Substitutes for Polystyrene Foam,” Applied Clay Science, **9**(6), pp. 425–431.

[129] Cheng, Y., Lu, L., Zhang, W., Shi, J., and Cao, Y., 2012, “Reinforced Low Density Alginate-Based Aerogels: Preparation, Hydrophobic Modification and Characterization,” Carbohydrate Polymers, **88**(3), pp. 1093–1099.

[130] Valencia-Saavedra, W., Robayo-Salazar, R., and Mejía de Gutiérrez, R., 2021, “Alkali-Activated Hybrid Cements Based on Fly Ash and Construction and Demolition Wastes Using Sodium Sulfate and Sodium Carbonate,” Molecules, **26**(24), p. 7572.

[131] Galán-Marín, C., Rivera-Gómez, C., and Petric, J., 2010, “Clay-Based Composite Stabilized with Natural Polymer and Fibre,” Construction and Building Materials, **24**(8), pp. 1462–1468.

[132] Kulshreshtha, Y., Vardon, P. J., Du, Y., Habert, G., Vissac, A., Morel, J.-C., Rao, S. M., van Paassen, L., van Loosdrecht, M. C. M., Mota, N. J. A., and Jonkers, H. M., 2021, “Biological Stabilisers in Earthen Construction: A Mechanistic Understanding of Their Response to Water-Ingress,” Construction Technologies and Architecture, **1**, pp. 529–539.

[133] Rhein-Knudsen, N., Ale, M. T., Ajalloueian, F., and Meyer, A. S., 2017, “Characterization of Alginates from Ghanaian Brown Seaweeds: Sargassum Spp. and Padina Spp.,” Food Hydrocolloids, **71**, pp. 236–244.

[134] Zeghari, K., Gounni, A., Louahlia, H., Marion, M., Boutouil, M., Goodhew, S., and Streif, F., 2021, “Novel Dual Walling Cob Building: Dynamic Thermal Performance,” Energies, **14**(22), p. 7663.

[135] Niang, I., Maalouf, C., Moussa, T., Bliard, C., Samin, E., Thomachot-Schneider, C., Lachi, M., Pron, H., Mai, T. H., and Gaye, S., 2018, “Hygrothermal Performance of Various Typha–Clay Composite,” Journal of Building Physics, **42**(3), pp. 316–335.

[136] Colinart, T., Vinceslas, T., Lenormand, H., Menibus, A. H. D., Hamard, E., and Lecompte, T., 2020, “Hygrothermal Properties of Light-Earth Building Materials,” Journal of Building Engineering, **29**, p. 101134.

[137] Labat, M., Magniont, C., Oudhof, N., and Aubert, J.-E., 2016, “From the Experimental Characterization of the Hygrothermal Properties of Straw-Clay Mixtures to the Numerical Assessment of Their Buffering Potential,” Building and Environment, **97**, pp. 69–81.

[138] Al Rim, K., Ledhem, A., Douzane, O., Dheilly, R. M., and Queneudec, M., 1999, “Influence of the Proportion of Wood on the Thermal and Mechanical Performances of Clay-Cement-Wood Composites,” Cement and Concrete Composites, **21**(4), pp. 269–276.

[139] Alassaad, F., Touati, K., Levacher, D., and Sebaibi, N., 2021, “Impact of Phase Change Materials on Lightened Earth Hygroscopic, Thermal and Mechanical Properties,” Journal of Building Engineering, **41**, p. 102417.

[140] Laborel-Préneron, A., Magniont, C., and Aubert, J.-E., 2018, “Hygrothermal Properties of Unfired Earth Bricks: Effect of Barley Straw, Hemp Shiv and Corn Cob Addition,” Energy and Buildings, **178**, pp. 265–278.

[141] Alassaad, F., Touati, K., Levacher, D., Mendili, Y. E., and Sebaibi, N., 2022, “Improvement of Cob Thermal Inertia by Latent Heat Storage and Its Implication on Energy Consumption,” Construction and Building Materials, **329**, p. 127163.

[142] Barnaure, M., Bonnet, S., and Poullain, P., 2021, “Earth Buildings with Local Materials: Assessing the Variability of Properties Measured Using Non-Destructive Methods,” Construction and Building Materials, **281**, p. 122613.

[143] Wang, M., Hu, C., Barnes, B. B., Mitchum, G., Lapointe, B., and Montoya, J. P., 2019, “The Great Atlantic Sargassum Belt,” Science, **365**(6448), pp. 83–87.

Chapter 4. Artificial intelligence modelling of hygrothermal behaviour of buildings

4.1 Introduction

Building hygrothermal behavior is influenced by a number of variables, some of which are uncontrollable. Given the complex and non-linear mechanisms that drive the building environment, developing a trustworthy model to describe the hygrothermal behavior of a building is a difficult undertaking. To analyse and enhance energy performance, an accurate hygrothermal model is required. Many techniques are utilized to simulate the behaviour of materials, artificial intelligence based on data-driven approaches, notably the artificial neural network (ANN) is now getting momentum [1]. Due to its capacity to learn and adapt to changing settings, neural network modelling is particularly good at predicting system behaviour. The ANN model is based on the human body's organic neural network, in which neurons are linked and interact optimally with one another [2]. ANN has been frequently employed in the civil engineering area to predict inherent features of concrete, such as mechanical resistance [3–5] and hygrothermal behaviour. The use of a data-driven model to model hygrothermal behavior has not been substantially investigated [6]. It is not guaranteed that the user will test all potential combinations with this procedure, and there may be some other sets that result in a higher FIT. Three algorithms (Levenberg-Marquart, scaled conjugate Gradient, and resilient backpropagation) were tested in this study to assure the correct setting and increase the accuracy of our model. To our knowledge, no research has been conducted on the application of the ANN model to hygrothermal behavior at the building scale and in real-world climate circumstances (without control).

4.2 Hygrothermal modelling review

Building hygrothermal behavior is influenced by a number of variables, some of which are uncontrollable. Finding a credible model to describe a building's hygrothermal behavior is a difficult task. Indeed, complex and non-linear systems governed by their surroundings define their dynamics. However, in order to analyse and enhance energy performance, an accurate hygrothermal model is required. Models can be divided into two categories [6]:

- *Comsol Multiphysics®, Fluent®, WUFI®,* and *EnergyPlus®* tools are used to create physical models based on physical techniques such as conservation of energy and mass.
- Data driven models, that are based solely on input/output data and have no physical interpretation.

Several physical models for predicting the physical processes of hygrothermal transport in porous materials have been presented in the literature [7]. The building envelope is subjected to a variety of factors. For example, we can consider the exterior environment (temperature, rain, radiation, wind, and so on) in addition to the internal environment (ventilation, heating, different sources of heat and humidity, etc.). Numerical modeling is a useful tool for analyzing the behavior of the building envelope. The modeling of completely coupled heat and mass transfers in envelopes is based on a variety of phenomenological methodologies that differ mostly in the transfer potentials employed. The temperature, for example, is referred to as a conventional transfer potential in heat transfer. Water content [7], vapor pressure [8,9], vapor content [10,11], and relative humidity [12,13] are some of the mass transfer driving forces used in moisture transfer models.

The calculation of the model's parameters by dissociating the liquid and vapor phases during transfer, as well as the estimation of the thermal gradient coefficient, present the greatest challenges. Indeed, in the case of hydric features, such as sorption isotherm curves with hysteresis effect and water vapor permeability, the input parameters characterisation of these models is very chronological, with testing lasting up to a year. Furthermore, heavy experimental procedures are required to determine the sorption isotherm curves, which explain the material's hydric behavior in respect to its surroundings.

4.2.1 Fundamentals of coupled heat and mass transfer

In the discipline of construction physics, building materials are treated as porous systems where diverse phenomena of mass and heat transmission and exchange occur. Building energy behavior modeling methods are based on physical principles that do not adequately account for all real settings and circumstances. The entire hygrothermal load from inside and outside has not been taken into account by many building simulation tools. For the bulk of the simulation software available today, it is seen as being less important [14,15]. Although it is challenging to take into account the entire heat, air, and moisture equilibrium model, the interior relative humidity is almost kept exhibiting freely and uncontrolled [6]. The energy of the vapor phase change is considered in the general form of the heat transfer equation for porous media, but not the energy of the liquid's diffusion. the heat transfer is presented in the equation 4-1.

$$\rho \cdot c_p \cdot \frac{\partial T}{\partial t} = \nabla(\lambda \cdot \nabla T) + \nabla(L_v \cdot \nabla j_v) \quad \textbf{4-1}$$

ρ [kg/m^3] = Density
c_p [$J.kg^{-1}.K^{-1}$] = Specific heat at constant pressure,
λ [$W.m^{-1}.K^{-1}$] = Thermal conductivity,
L_v [J/kg] = Latent heat of evaporation,
j_v [$W.m^{-2}$] = Mass flow density of moisture vapor diffusion,
T [K] = Temperature.

4.2.2 Fundamentals of heat transfer

Heat transfer is defined as a change in a material's enthalpy induced by a change in temperature. A body heating or cooling action causes a change in the amount of heat transported and the spatial temperature distribution. This process is known as transient heat conduction. Heat flow in space is impacted by thermal conductivity as well as temperature gradient. Fourier's law describes the heat flow generated by a material's temperature variation in equation 4-2. Remaining in the one-dimensional frame, the spatial coordinate is x.

$$q = \lambda \nabla T = \lambda \frac{\partial T}{\partial x} \quad \textbf{4-2}$$

q [W/m^2] = Heat flux density

4.2.3 Fundamentals of mass transfer

According to Fourier's law, there is a relationship between the heat flux density gradient and the material's conductivity and temperature gradient. In the general heat equation, the moisture flux is a source term that may also transmit the heat flux gradient [16]. This effect is frequently overlooked while working with continuous environment. However, it may be considered when dealing with hygroscopic materials permeable to moisture adsorption. The equation 4-3 is how the mass diffusion rate, is defined.

$$m = -S \cdot D \cdot \frac{dC}{dx} \quad \textbf{4-3}$$

m [Kg/s] = Mass diffusion rate,
S [m^2] = Area through which the mass diffuses,
D [m^2/s] = Diffusion coefficient,
C [Kg/m^3] = Mass concentration.

When a concentration gradient arises, the quantity of material that moves across a unit area in a unit of time is referred to as the diffusion coefficient in physics. Diffusion coefficients are commonly computed using experimental techniques. Because molecules in fluids flow easily, the diffusion coefficient of gases is greater than that of

solids. Diffusion in liquids and solids is more challenging to produce because of the impact of molecular force fields and greater collisions.

4.2.4 Coupled heat and mass transfer

In order to solve both the heat and the water equation, a hybrid solution method was consequently suggested. With each iteration, the physical characteristics are updated and the procedure is repeated. The physical characteristics (thermal and vapour conductivities, heat and hydric capacities, etc.) as well as the saturation vapour pressure and the source term are updated after each iteration. This cycle of iteration is continued until convergence is obtained. Models for heat and moisture movement are created using the laws of mass and energy conservation. Commonalities among the various hygrothermal models for porous building envelopes and materials include the forces that drive the transport of moisture.

- **Model of Künzel**

Künzel produced a new model in 1995 that was based on Kiel's theorem but otherwise relatively comparable to others created in earlier decades. Künzel define the combined heat and moisture transmission in building elements using the terms relative humidity and temperature T as defined the equation 4-4 [14].

$$\frac{dw}{d\varphi}.\frac{\partial \varphi}{\partial t} = \nabla\left(D_{\varphi}\nabla\varphi + \delta_p \nabla(\varphi p_{sat})\right) \qquad \textbf{4-4}$$

$\frac{dw}{d\phi}$ = Moisture storage capacity,

D_{φ} [$m^2.s^{-1}$] = Liquid conduction coefficient,

δ_p [$kg.\ s^{-1}.m^{-1}.Pa^{-1}$] = Water vapor permeability,

φ = Relative humidity,

p_{sat} [Pa] = Water vapor saturation pressure.

Künzel suggests the equation 4-5 for heat transfer.

$$\frac{dH}{dT}.\frac{\partial T}{\partial t} = \nabla(\lambda \nabla T) + h_v \nabla\left(\delta_p \nabla(\varphi p_{sat})\right) \qquad \textbf{4-5}$$

h_v [$J.\ kg^{-1}$] = Evaporation enthalpy of water,

$\frac{dH}{dT}$ = Porous materials' capacity to Heat storage.

- **Model of Mendes**

Using the equations of Philip and De Vries as a foundation, Mendes suggested a novel hygrothermal model in 1999. The linked heat and moisture transport equations were instead driven by the volumetric moisture content and the temperature gradient,

respectively [17]. The moisture transfer equation's current model is expressed in the equation 4-6.

$$\frac{\partial \theta}{\partial t} = \nabla(D_T \nabla T + D_\theta \nabla \theta) \quad \textbf{4-6}$$

Θ = Volumetric moisture content,
D_θ = Total moisture diffusion coefficient (the vapor and liquid phases associated to the moisture gradient),
D_T = Total moisture diffusion coefficient (the vapor and liquid phases associated to the temperature gradient).
Mendes suggests the equation 4-7 for heat transfer:

$$\rho . c_p . \frac{\partial T}{\partial t} = \nabla(\lambda \nabla T) + L_v . \nabla\left(D_{T,vap} \nabla T + D_{\theta,vap} \nabla \theta\right) \quad \textbf{4-7}$$

$D_{T,vap}$ = Vapor diffusion coefficient associated to the temperature gradients,
$D_{\theta,vap}$ = Vapor diffusion coefficient associated to the moisture content.

4.2.5 Hygrothermal behavior at building scale: physical approach-based

The nodal method is premised on the notion that every construction zone is a single volume that can be described as a combination of physical variables in a steady state. The common representations of a node are a room, a floor, or a specific volume. However, a node may also represent something more complicated, such as an internal load, like the heat generated by an HVAC system, equipment, or a person using the space. Thus, each zone is generally comparable to a node with its own set of physical characteristics, such as temperature, humidity, and pressure. The heat and moisture balance equations may be solved using a matrix computing technique for each node of the entire building volume. TRNSYS and EnergyPlus are the most popular building energy simulation software, they use the nodal technique, a one-dimensional methodology. The performance of the envelope as well as energy consumption may be significantly impacted by rain absorption and moisture accumulation inside building walls.

4.2.6 Historical evolution of knowledge surrounding the issues of hygrothermal behavior of materials

A Scientometric analysis is performed in this section. The current status and historical evolution of knowledge surrounding the issues of hygrothermal behavior of materials were exposed by analyzing several bibliometric aspects of all the acquired papers. First, the database "Scopus" was searched for the term "hygrothermal." VOSviewer [18] was used to input the results collected. The origin nations of the primary writers of

3435 publications can be provided, as well as the origin countries of the other co-authors (Figure 4-1). China, France, the United States, Canada, India, Italy, Algeria, Morocco, and other countries have all conducted extensive research on this hygrothermal phenomenon.

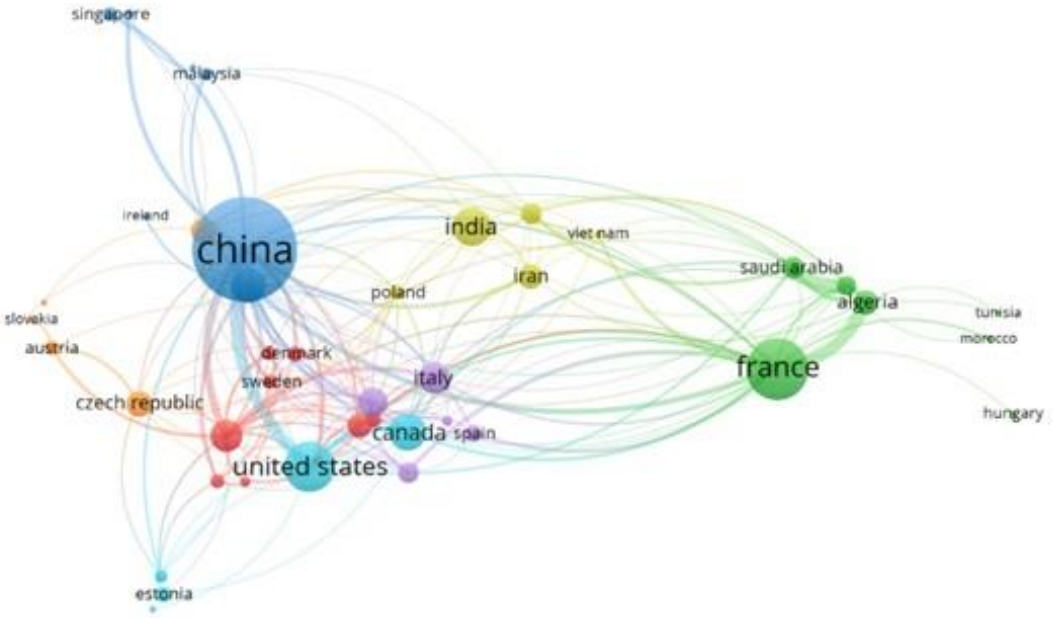

Figure 4-1 Origin countries of the article's autors [19]

As shown in Figure 4-2, the most cited topics in the literature are: (i) the investigation of the mechanical/hygrothermal coupling to analyse laminated composite materials, (ii) the characterization of the intrinsic properties of hygrothermal transfer, and (iii) the study of the hygrothermal behavior of building envelopes and their durability.

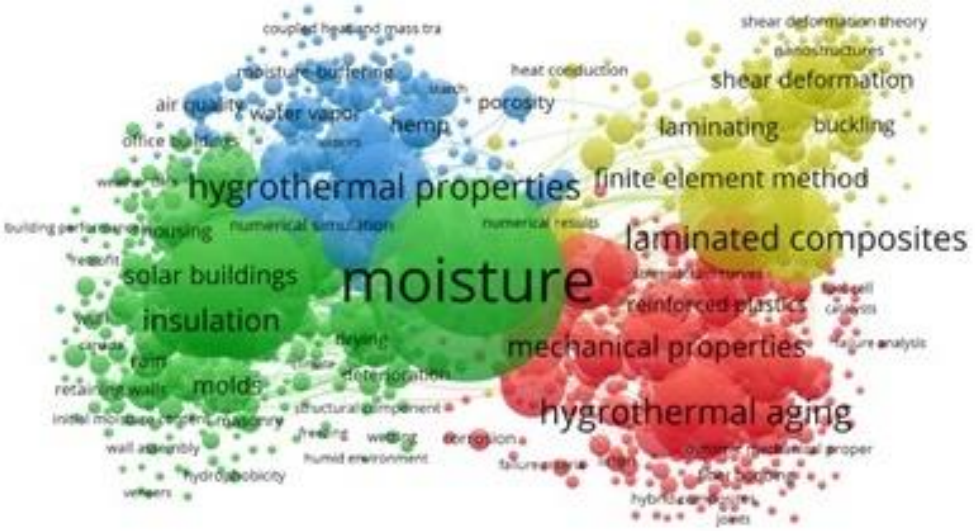

Figure 4-2 Network of keywords found [19].

Furthermore, a normalizing of unclear phrases was required for the tools employed in the analysis of hygrothermal behavior. Following this, six keywords were investigated:

"hygrothermal", "transfer", "building", "material", "heat and mass", and "modeling". This study was conducted using three software programs: "Comsol Multiphysics®," "WUFI ®," and "EnergyPlus ®." Only peer-reviewed journals were regarded as a source of publications.

Table 4.1 Comparison between three most used numerical tools [19]

Software	HAM model	Approach	Benefits	Limit
Comsol Multiphysics®	Luikov [20], Kenzel [21] and Philips & De vries [22]	Finite element Method.	Ability to couple several phenomena.	Paying software.
EnergyPlus®	Kenzel model [21]	Simplified (EMPD)Finite Difference Method.	Open access, ability to module develop by the users, BIM.	Lack of a formal and effective user interface.
WUFI Plus®	Kenzel model [21]	Implicit Finite Volume Method.	Database: building envelope material properties and climates.	Constant input, paying software, high computing time.

4.2.7 Limitations of physical simulation and the use of ANN modeling

Several constraints can be stated based on the literature under the following issues:

- Resolving the partial differential equations that regulate coupled heat and mass flow necessitates a large number of calculations and a long calculation time.
- The difficulty of co-simulation between mass transfer models (such as Comsol) and building energy tools (BES) [23–25].
- Each material's experimental characterization (thermal and hydric) is required to supply inputs to the model.
- A scarcity of trustworthy thermophysical input data for diverse components of the envelope, such as heritage buildings [26].
- Most mathematical models employed in simulations are simplified due to the difficulty of the dynamic hygrothermal reaction of bio-based materials.

In the case of data-driven models, the literature [27] identified three primary categories for creating thermal prediction: RC (resistor-capacitor), TF (discrete-time transfer functions), and AI models with a deep learning method (Artificial Neural Network, ANN) [28,29]. Indeed, ANN models have the ability to detect complicated nonlinear relationships among inputs and outputs [30]. Wang et al. [27] demonstrated that the ANN model outperforms the RC model as well as an exogenous terms-based autoregressive model (ARX models) in most cases.

Furthermore, only three research [31–33] highlight the use of data-driven models to study the hygrothermal behaviour of building materials. However, their studies were done only at the wall scale under controlled climatic conditions. To predict the hygrothermal behaviour of building components, the authors employed ANN, CNN (Convolutional neural networks), and LSTM (Long short term memory) [34]. The hygrothermal performance, on the other hand, is not tested on bio-based materials. These authors looked at three different types of materials: (i) large masonry walls [31], (ii) wood frame walls [31], and (iii) concrete walls with a second vegetation skin [33]. ANN modelling, unlike physical models, is an effective tool for simulating the hygrothermal behaviour of building products with a minor number of inputs, according to the authors. The hygrothermal activity of this material is less visible when compared to bio-based materials. Table 4.2 provide a summary of the work on data driven models [19].

Table 4.2 Summary of work using ANN, LSTM and CNN models.

Study	Approach	Materials	Validation
May Tzuc et al. [35]	ANN	Double-skin green facades	RMSE / MAPE / R^2
Tijskens et al. [31]	CNN	Timber frame wall with brick veneer and sidings	RMSE / MAPE
Tijskens et al. [32]	CNN and LSTM	Massive masonry wall	RMSE / MAPE / R^2

Most hygrothermal softwares require climate data such as exterior air temperature and relative humidity, as well as solar radiation impacting on the building [6]. Solar radiation, on the other hand, was not taken into account in the three-research listed above. Furthermore, the model parameters, including the number of neurons, were adjusted manually in these investigations without any justification for their selection.

The basic ANN design utilized in [36] consisted of five neurons in the input layer, one hidden layer, and two neurons in the output layer, all of which were controlled by humidity and temperature. It is not guaranteed that the user will test all potential combinations with this procedure, and there may be some other sets that result in a higher FIT. Three algorithms (Levenberg-Marquart, scaled conjugate Gradient, and resilient backpropagation) were tested in this study to assure the correct setting of our model and to increase the model's accuracy. Furthermore, the model will be trained and validated at the lab-scale and under real climate conditions.

4.3 Artificial neural network modeling

4.3.1 Introduction

The artificial neural network (ANN) is the most often utilized data-driven model for the study of the energy efficiency of geothermal systems in the literature where a biological neuron is simplified into an artificial neuron. This neuron is modeled after a mathematical function dedicated to information processing [37]. Its architecture is separated into three types of layers, all of which are linked as: the input layer, which introduces the model inputs; the output layer, which obtains the trained model's outputs; and the hidden layers, which are each of the intermediate layers between the previous ones as shown Figure 4-3. The neuronal approach is based on three elements: (i) Synapses or connecting links that are associated to weights; (ii) A processing unit called “summing junction” that sums the input signals weighted by the synaptic weight and adjusts them by adding a bias value (b_k); (iii) An activation function (φ) that limits the signal amplitude at the neuron's output.

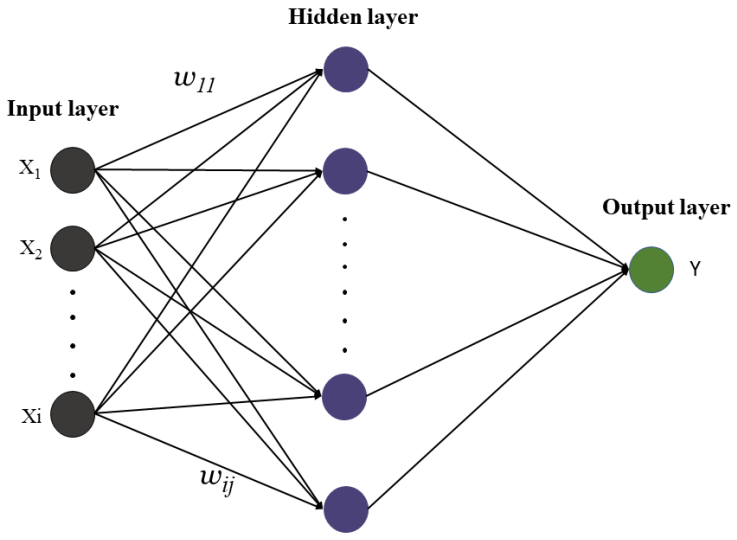

Figure 4-3 Simplified representation of an artificial neural network.

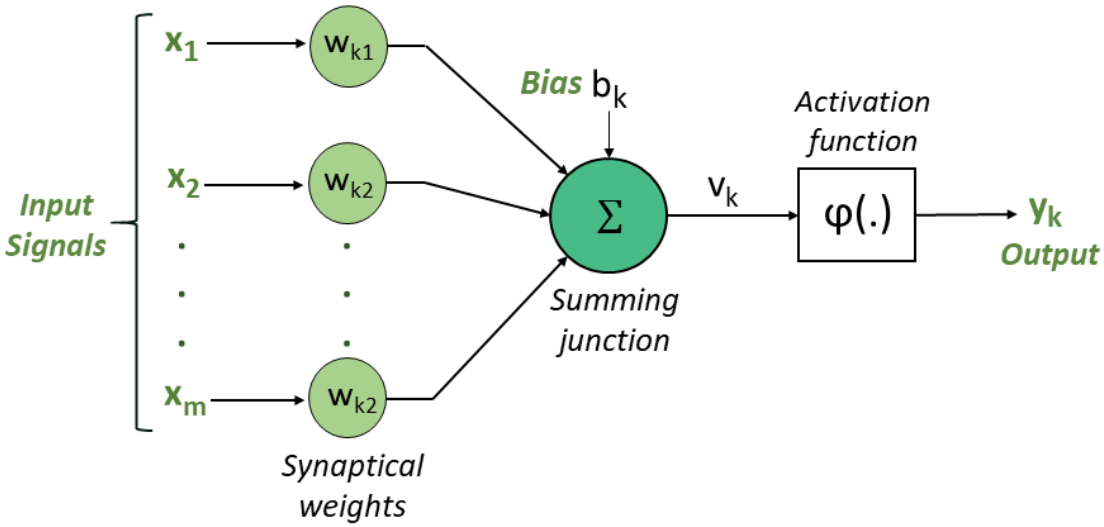

Figure 4-4 Simplified illustration of a neural function.

The neuron k can be described mathematically by the equations 4-8 et 4-9:

$$u_k = \sum_{j=1}^{m} x_j \times w_{kj} \qquad \textbf{4-8}$$

$$v_k = u_k + b_k \qquad \textbf{4-9}$$

Where u_k is the linear combiner of the inputs signal and v_k is the weighted sum of the input values adjusted by the b_k.

4.3.2 Activation functions

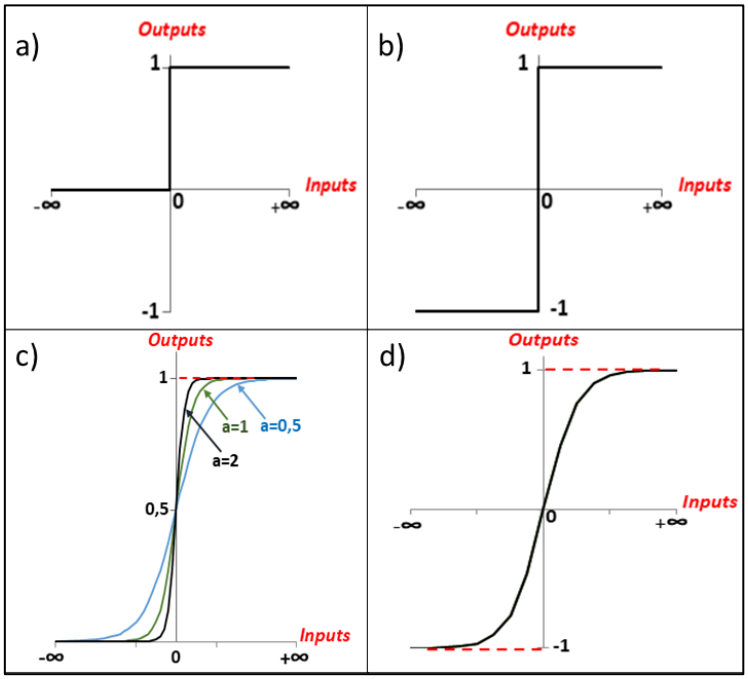

Figure 4-5 (a) Binary threshold function. (b) Bipolar threshold function. (c) Logistic function. (d) Hyperbolic tangent function.

The activation function is a set of mathematical equations that define the output signal of the neuron k. The sum of the weighted and bias-corrected inputs passes through the activation function φ to obtain the final output signal (y_k) as shown in equation 4-10 below:

$$y_k = \varphi\left(\sum_{j=1}^{m} x_j \times w_{kj} + b_k\right) \quad \textbf{4-10}$$

We can classify the Activation function into four categories as shown in Figure 4-5 [38]:

- **Threshold function**: Figure 4-5 **(a)** shows the binary version of this function, which returns a number between 0 and 1 (equation 4-11), and Figure 4-5 **(b)** shows the bipolar version, which returns a value between -1 and 1 (equation 4-12).

  a) Binary threshold

  $$Y = \varphi(v) = \begin{cases} 1 \; if \; v \geq 0 \\ 0 \; if \; v < 0 \end{cases} \quad \textbf{4-11}$$

  b) Bipolar threshold

  $$Y = \varphi(v) = \begin{cases} 1 \; if \; v \geq 0 \\ -1 \; if \; v < 0 \end{cases} \quad \textbf{4-12}$$

- **Sigmoidal function:** The sigmoidal function is mostly an S-curved nonlinear function. The function most frequently used in neural network design are the logistic function (Figure 4-5 ***(c)***) and the hyperbolic tangent function (Figure 4-5 ***(d)***). The logistic function may be used to maintain output values between 0 and 1 (equation 4-13), whereas the hyperbolic tangent function can include negative values (equation 4-14).

  c) Logistic function: (with a is the slope parameter)

  $$Y = \varphi(v) = \frac{1}{1+e^{-av}} \quad ; \quad 0 \leq \varphi(v) \leq 1 \quad \textbf{4-13}$$

  d) Hyperbolic tangent function:

  $$Y = \varphi(v) = \tanh(v) \quad ; \quad -1 \leq \varphi(v) \leq 1 \quad \textbf{4-14}$$

4.3.3 Artificial neural network methodology

Three steps are involved in the implementation of the artificial neural network model as illustrated in the Figure 4-6. The model must first be trained in order to lower the error function. The weighting parameters can be changed depending on comparisons between experimental and model output to reduce error. To make the comparison, the

correlation coefficient and the root mean square error are employed. The validation stage comes next. The goal is to evaluate a model that fits the training data set while changing its hyper parameters objectively. In the final stage, the model's results are evaluated for relevance.

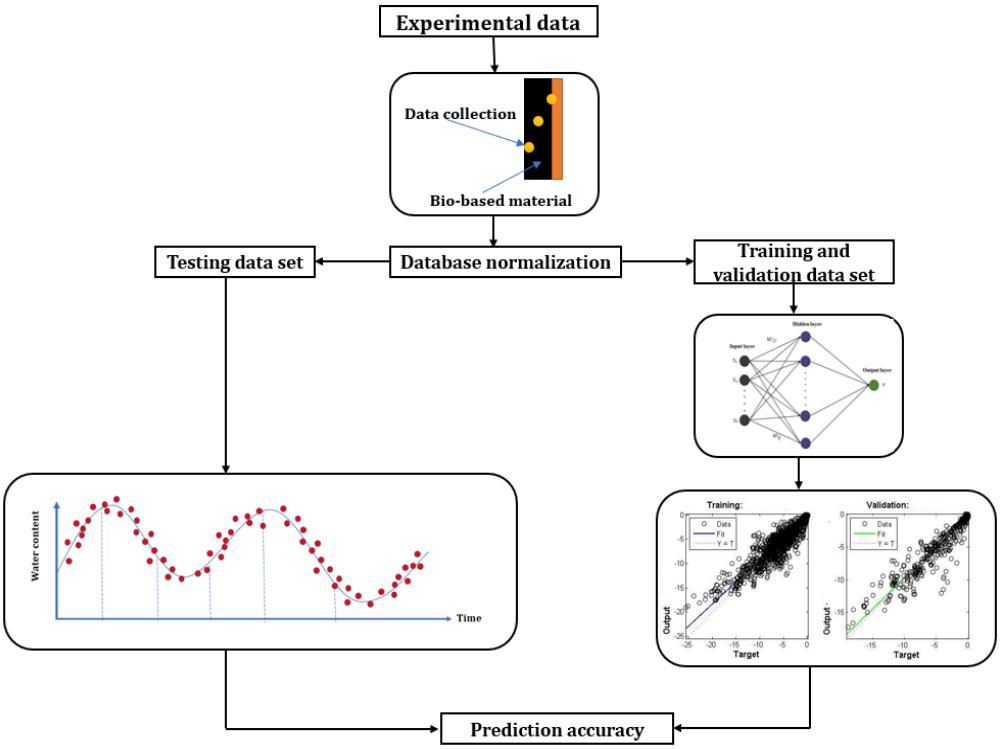

Figure 4-6 Procedures for hygrothermal modeling using ANN

The determination coefficient (R^2), the Root Means Square Error (RMSE), and the Mean Squared Error (MSE) are all performance measures that are often used to assess the effectiveness of built models. The meanings of these indicators are given in the form of equations (4-15 to 4-17).

$$R^2 = 1 - \frac{\sum_{i=1}^{n}(yi-\hat{y}i)^2}{\sum_{i=1}^{n}(yi-\bar{y})^2} \quad \textbf{4-15}$$

$$RMSE= \sqrt{\frac{1}{n} \times \sum_{i=1}^{n}(\hat{y}i - yi)^2} \quad \textbf{4-16}$$

$$MAPE= (\frac{1}{n} \times \sum_{i=1}^{n} \left|\frac{yi-\hat{y}}{yi}\right|)\times 100\% \quad \textbf{4-17}$$

A multi-criteria optimization involves selecting and adjusting the parameters that influence the accuracy of the model. The decision variables are the values that the optimization algorithm governs. The algorithm must find the convergence value as rapidly as possible. There are various optimization algorithms, including Levenberg-

Marquart, scaled conjugate Gradient, and resilient backpropagation. Each algorithm's advantages and disadvantages are as follows:

- The Levenberg-Marquardt algorithm is a good procedure for locating minima that works well for the majority of test functions.
- A number of variables influence the algorithm's efficiency.
- The optimal values of these variables are heavily influenced by the test function.
- Incorporating delayed gratification within the algorithm improves success rates while decreasing the amount of jacobian assessments.
- Acceleration is effective, but only under limited circumstances; performance is strongly dependent on the initial guess.
- While deferred gratification is frequently sufficient to establish a successful and trustworthy fit, acceleration can be highly useful in certain circumstances.
- The conjugate gradient approach has a basic restriction in that it takes n cycles to attain the minimum.
- A strategy should be devised to execute the majority of the function minimization in the first few cycles.
- Resilient back propagation (Rprop) does not require you to supply any free parameter values (and generally an optional momentum term) for the learning rate.
- Rprop's main disadvantage is that it is a more difficult method to develop.

However, the main limitations of artificial neural network models are: The models don't need a physical explanation (black box). In other terms, the results obtained by neural networks are derived from mathematics that are largely unknown and poorly understood. The models lack transparency and access to high-quality data. As a result, determining how distinctive occurrences are related using this class of models is extremely difficult.

4.4 Numerical results

4.4.1 Modelling of concrete prototype

4.4.1.1 Prototype

We developed a prototype of 70 cm length, 70 cm width, and 70 cm height to test the hygrothermal behavior. The walls are made of five centimeters of concrete and five centimeters of external thermal insulation. We used recycled cotton panels with a thermal conductivity of 0.039 $W.m^{-1}.K^{-1}$ as insulation. We built a 30×25 cm^2 opening to

meet the RE2020 recommandation, which requires at least 16 % of the living area to be glazed (see).

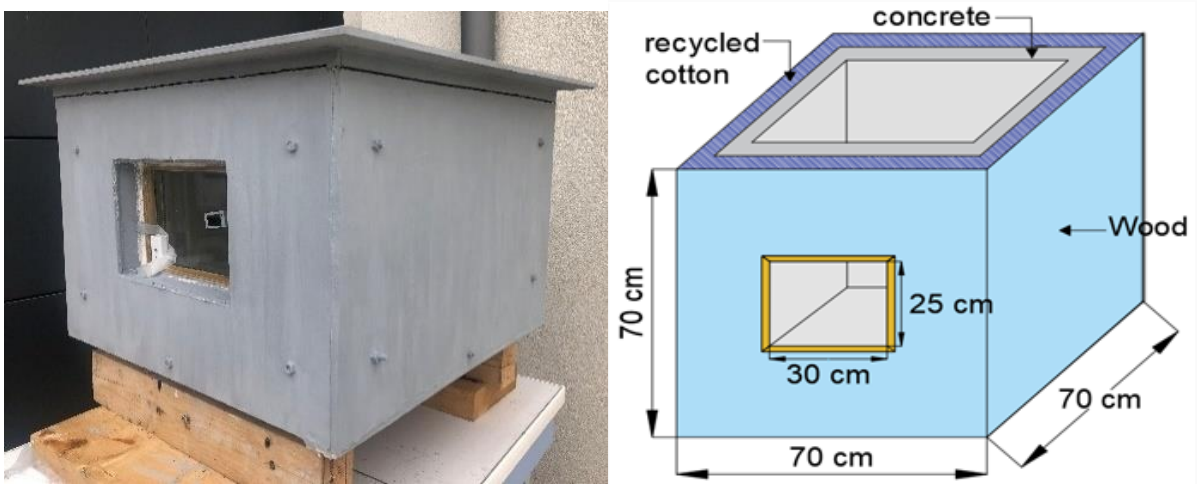

Figure 4-7 Design of the experimental prototype

We put one sun radiation sensor and three relative humidity and temperature sensors inside the prototype. The first sensor was installed in the middle, the second on the southbound glassing, and the third on the opposite wall (facing north). We installed a temperature/humidity sensor and a solar radiation sensor outside. The sensors are wireless and provide data to the Wibee using the Zigbee radio frequency standard. As shown in Figure 4-8, Wibee is a ZigBee controller capable of managing, controlling, and monitoring a set of ZigBee objects. It includes an Ethernet connectivity with a database and web server. In Table 4.3, the technical specifications of the sensors are listed.

Table 4.3 Technical characteristics of sensors

Humidity range	From 0 to 100%
Temperature range	From -40 °C to 125 °C
Accuracy	± 3% (max) between 0-80 % RH ± 0,4°C (max), from -10 °C to 85 °C
Radio coverage	100 m outdoor 20 m indoor

The temperature and relative humidity within the prototype were modeled using data collected over an eight-day period. To ensure an accurate distribution during the construction of the model, the data is randomly divided into two parts: 70% of the data is used for training, and 30% is utilized to test the model's performance. The goal is to put the model to the test using data that isn't the same as the training data. The data is also subjected to normalization between 0 and 1 in order to decrease the model's

complexity, facilitate gradient convergence, and improve interoperability (avoid disproportionate influence during the learning process).

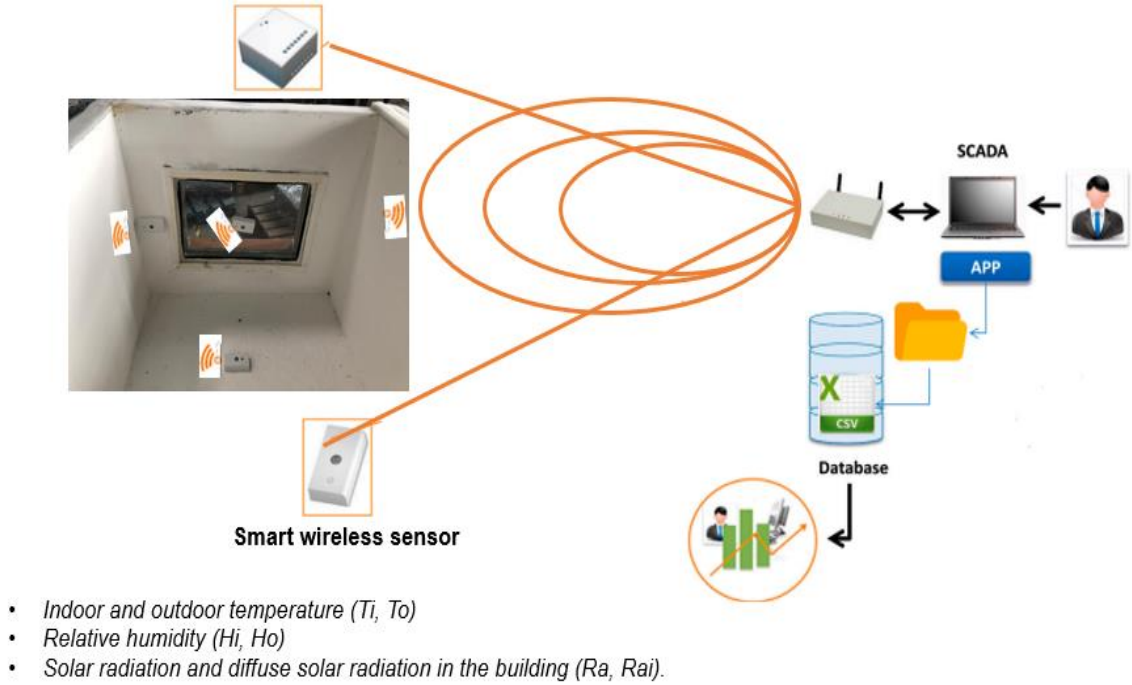

Figure 4-8 Smart wireless sensor and data collection system.

The model we trained has eight input data points, one hidden layer, and two output data points as shown in Figure 4-9. During the model's training, the number of neurons in the hidden layer is determined. External and indoor solar radiation, outdoor temperature and humidity, and indoor temperature and humidity measured on the glazing and on the northern wall are the parameters used as input data for the ANN hygrothermal model

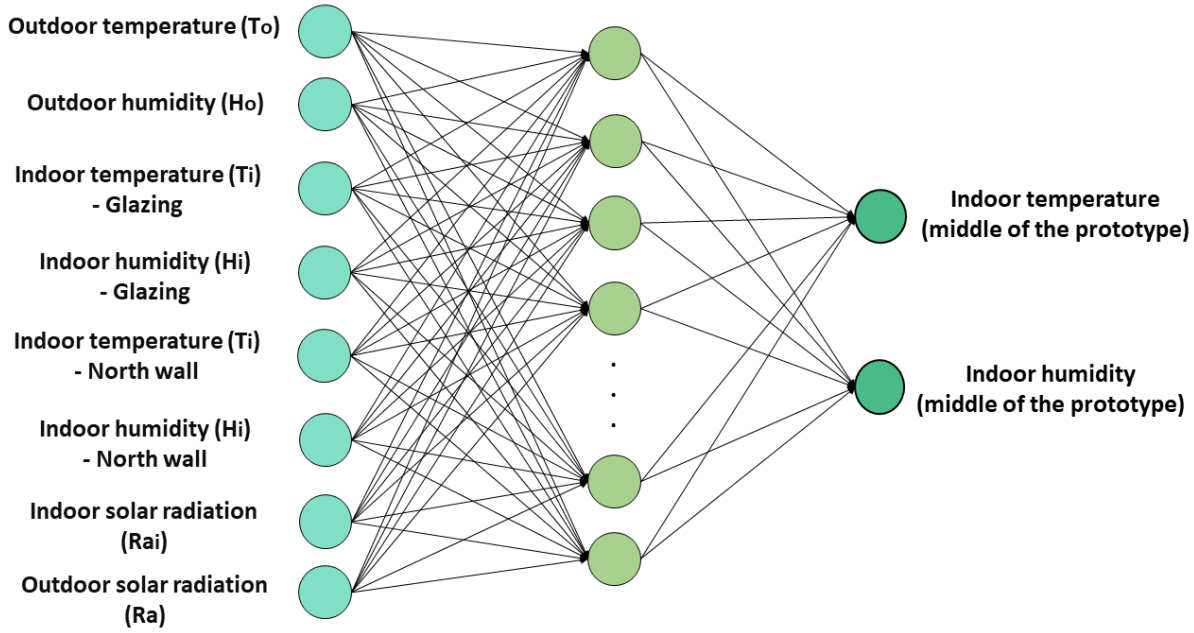

Figure 4-9 Topology of the artificial neural network

4.4.1.2 Numerical optimization

The process of improving a model's performance criteria and determining the ideal configuration is known as optimization. A multi-criteria optimization involves identifying and optimizing the parameters that influence the model's accuracy. The quantities that the optimization algorithm governs are known as decision variables. The algorithm needs to find the convergence value as soon as possible. Levenberg-Marquart, Scaled Conjugate Gradient, and resilient backpropagation are some of the optimization techniques available.

A small value for MAPE and RMSE indicates higher performance, while a value near to 1 for R^2 indicates better model performance. For each algorithm, we also chose the number of neurons in the hidden layer. We utilized a loop that returned model errors for each number of neurons between 1 and 60, allowing us to quickly select the number with the minimum mistake.

The errors acquired by varying the model learning algorithms and the number of neurons in the hidden layer are shown in Figure 4-10. We examined the training and validation performance indicators for each method when changing the number of neurons. The number of neurons in the hidden layer that corresponds to the smallest errors is the optimal number. We can see from the graph that the best number for Levenberg-Marquart is 22 neurons. for the Scaled Conjugate Gradient is 18 neurons, and for Resilient backpropagation is 21 neurons. The Levenberg-Marquart algorithm

exhibits the lowest RMSE and MAPE errors, as well as the closest determination coefficient to 1, among the three algorithms. The RMSE and MAPE for the temperature acquired using the Levenberg-Marquardt method with 22 neurons are respectively 0,2062 and 0,693 in training and 0,1567 and 0,7605 in validation.

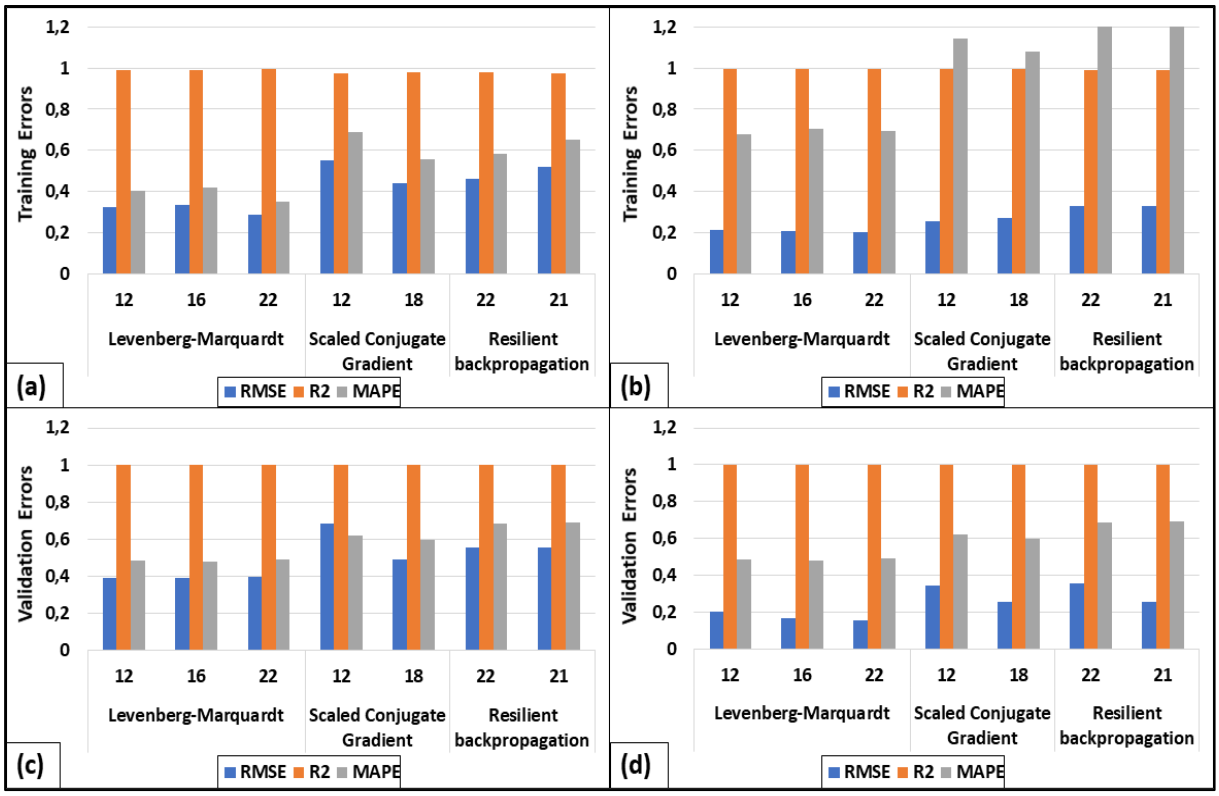

Figure 4-10 Errors generated by the various algorithms and by the different numbers of neurons in the hidden layer. (a) and (c) Relative humidity. (b) and (d) Temperature.

4.4.1.3 Evaluation of the model performance

The Levenberg-Marquardt algorithm with 22 neurons in the hidden layer was employed in this investigation. Figure 4-11 shows the temperature and relative humidity modelisations for the training, validation, and global phases. In all phases, the determination coefficients are greater than 0.99. (See RMSE and MAPE values in Figure 4-10). This graph depicts the neural network models' accuracy when compared to real-world data.

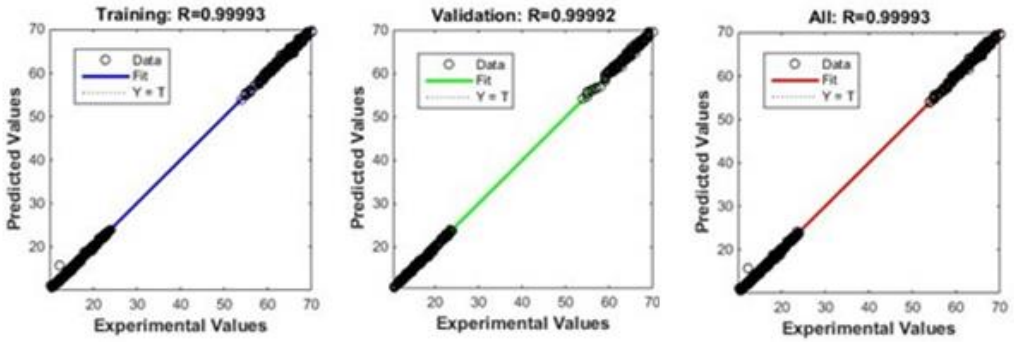

Figure 4-11 Coefficient of determination for modeled values of indoor relative humidity and temperature in traning, validation and overall phases.

In , the precision of the best data-driven models can also be seen. Indoor temperature and relative humidity modeled and experimental values are plotted as a function of time. The results demonstrate that the modeled and experimental values have fairly similar curves. This suggests that the model was able to learn and model the prototype's hygrothermal behavior.

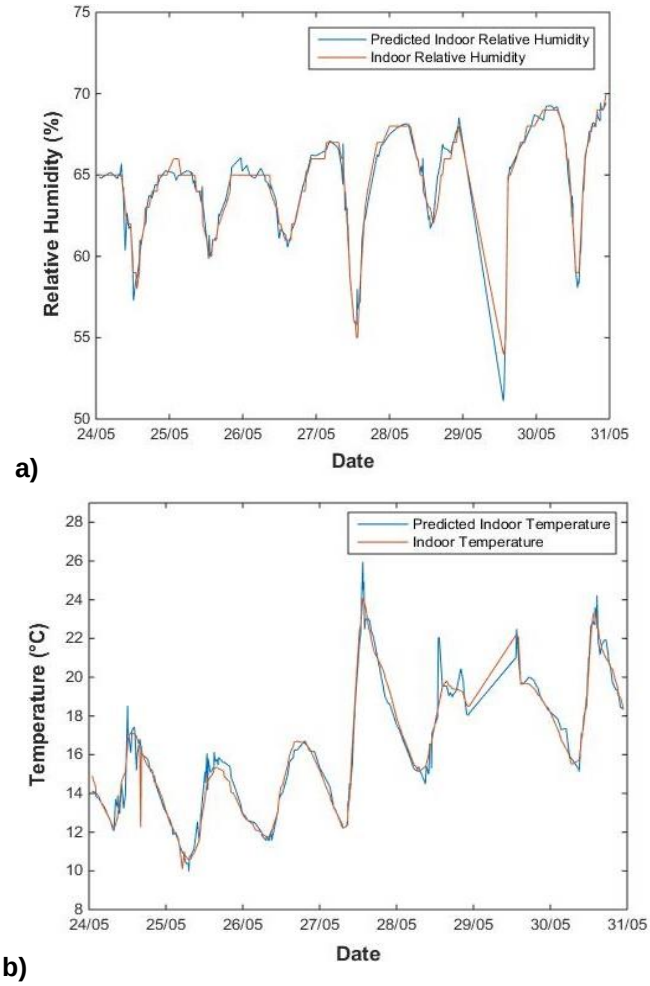

Figure 4-12 Comparision between modeled and experimenta values. (a) Indoor relative humidity. (b) Indoor temperature

In Figure 4-13, we also showed the relative humidity (Figure 4-13 (a)) and the temperature (Figure 4-13 (b)) within the prototype based on the weather conditions. For an external temperature ranging from 7 °C to 25 °C, the inside air temperature fluctuates between 10 °C and 26 °C. Furthermore, the relative humidity of the inside air ranges between 52 % and 68 %, whereas the relative humidity of the outside air varies between 45 % and 86 %. We have a good level of comfort in most circumstances, considering that relative humidity in habitable spaces should be kept between 30 % and 60 % (ASHRAE Handbook). Nevertheless, with a 8 % variation in regard to the humidity setpoint, optimal thermal comfort was not guaranteed for certain periods of time. The material appears to have reacted well to the humidity, based on the thickness of the wall. The difference in humidity between the outside and indoors might be as much as 20 %. The substantial disparity between the two parameters can be explained by the material's ability to absorb moisture. In the following part, we compute the risk of condensation to validate this method.

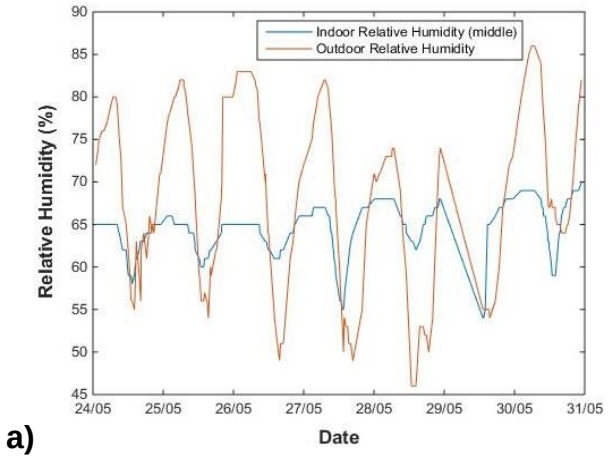

a)

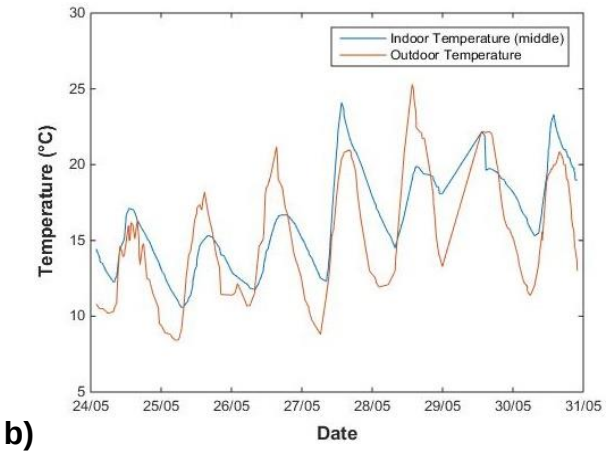

b)

Figure 4-13 Variation of indoor temperature and humidity according to outdoor conditions. (a) Relative humidity. (b) Temperature.

4.4.1.4 Condensation evaluation

Figure 4-14 shows the condensation risk indicator, which is a function of the internal vapor pressure (Pv) and internal saturation pressure (Ps). The Glazer method is used to calculate these two pressures, as described in [39]. We used the following formula 4-18 and 4-19 because the temperature and relative humidity data collection period was not during a cold spell and so did not contain any negative temperatures:

If T ≥ 273.15 K

$$Ps = \exp\left(-\frac{5800,22}{T} + 1.3915 - 0.04864.T + 4.17650.10^{-5}.T^2 - 1.445.10^{-8}.T^3 + 6.546.\ln(T)\right) \quad \textbf{4-18}$$

$$Pv = \frac{HR(\%).P_s(Indoor)}{100} \quad \textbf{4-19}$$

The location with the largest danger of condensation inside the prototype is where (Pvint-Psint) is greatest. There is no risk of condensation if (Pvint-Psint) is always negative or equal to zero. Figure 4-14 shows that Pvint-Psint values stay negative, indicating that condensation inside the prototype is not a concern.

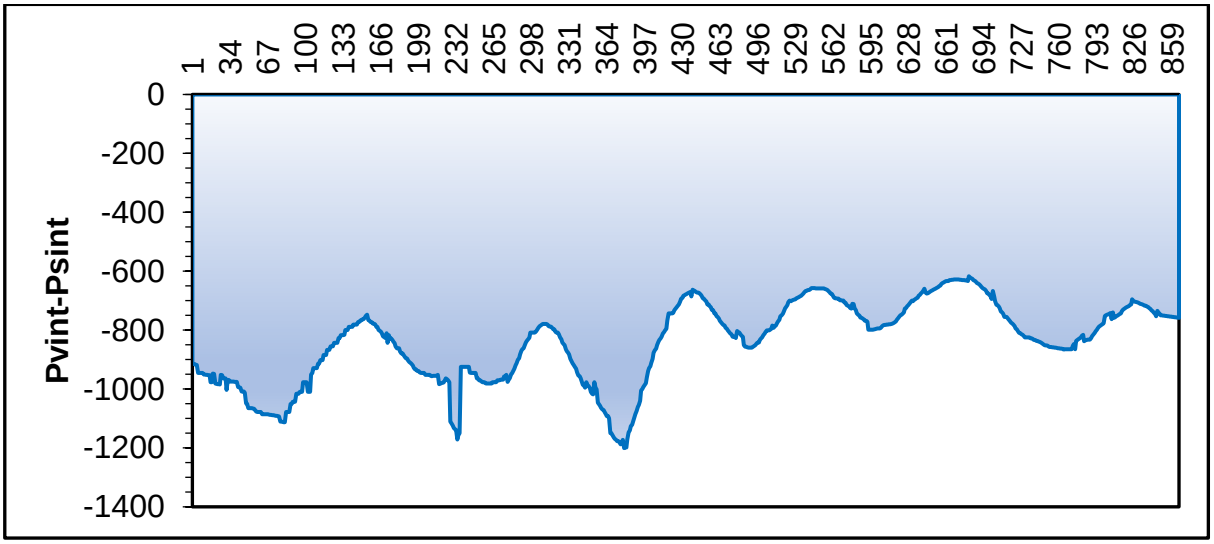

Figure 4-14 Risk of condensation

This means that our FA-CR concrete mixture absorbs moisture, explaining the changes in indoor and outdoor relative humidity seen in Figure 4-13 (a). The absorbed moisture aids the concrete's ongoing pozzolanic reaction by forming extra CSH and CSAH. Figure 4-15 depicts the compressive strengths of the developed concrete FA15-CR15 after 14, 28, and 300 days of curing under controlled conditions. The compressive strength of the concrete mixture at 300 days is 38 % more than the value obtained at 28 days. These findings demonstrate the creation of extra hydration products, which leads to an increase in mechanical strength.

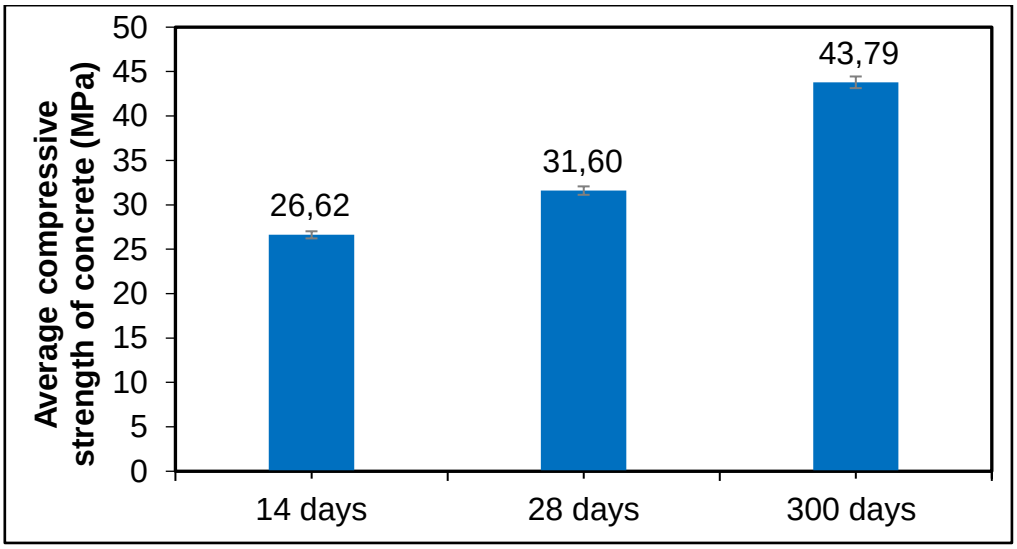

Figure 4-15 Average compressive strength at different ages of the mortar CR15-FA15.

4.4.2 Modelling of earthen prototype

4.4.2.1 Prototype

We developed a lab-scaled prototype of 59 cm length, 61 cm width, and 44 cm height to test the hygrothermal behavior as shown in the Figure 4-16. The prototype is composed of 6 cm of structural cob and coated with a 6 cm of insuation cob. The roof and floor are made with an insulation. We placed a 20 cm × 30 cm window to fit the RE2020 recommandation.

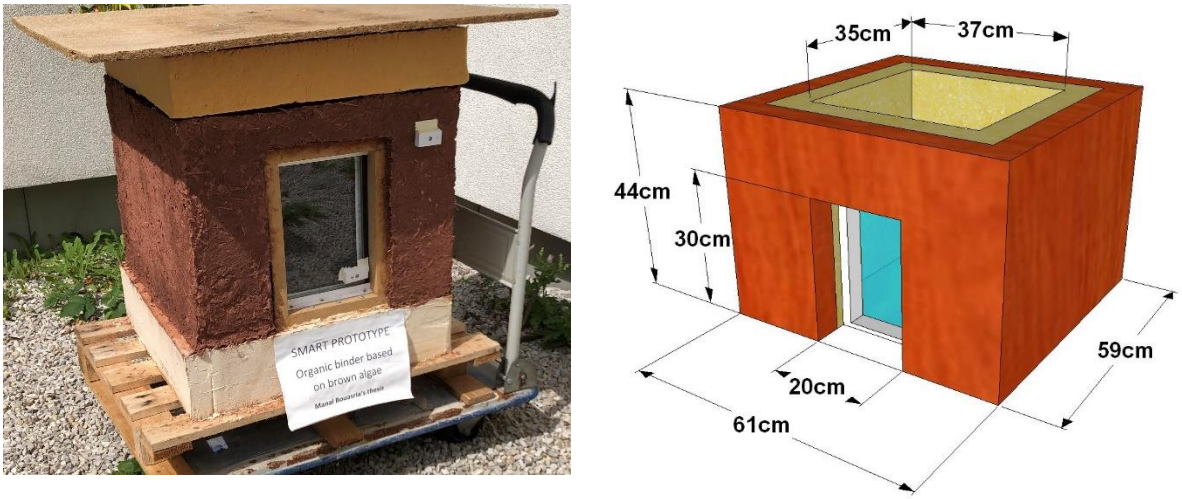

Figure 4-16 Design of the experimental prototype

The sensors of temperature/humidity placed inside the prototype were installed in the middle, south and north faces. The solar radiation sensor was placed in the middle of the floor. We placed the sensors also in the outdoor faces (north and south). The description and technical characteristic of the sensors system is given in the part II of the chapter 2 section 1.5. We kept the same architecture as announced in the figure

20 in the chapter 1 section 1.3. We used the collected data over nine days to model the temperature and relative humidity. The data is normalized between 0 and 1 and randomly divided between training and validation: 60% of the data is used for training, and 40% is utilized to the validation of model.

4.4.2.2 Numerical optimization

For the optimisation of the neural network model, we used MAPE, RMSE and R2 indicators to investigate the efficiency of the algorithms of Levenberg-Marquart, scaled conjugate Gradient, and resilient backpropagation. A small value for MAPE and RMSE indicates higher performance, while a value near to 1 for R^2 indicates a best model performance. We compared the performance of each algorithms with a number of hidden neuron ranging from 1 to 60. For each algorithm we chose three numbers of neurons in the hidden layer with the best performance and we compared them as shown in the Figure 4-17.

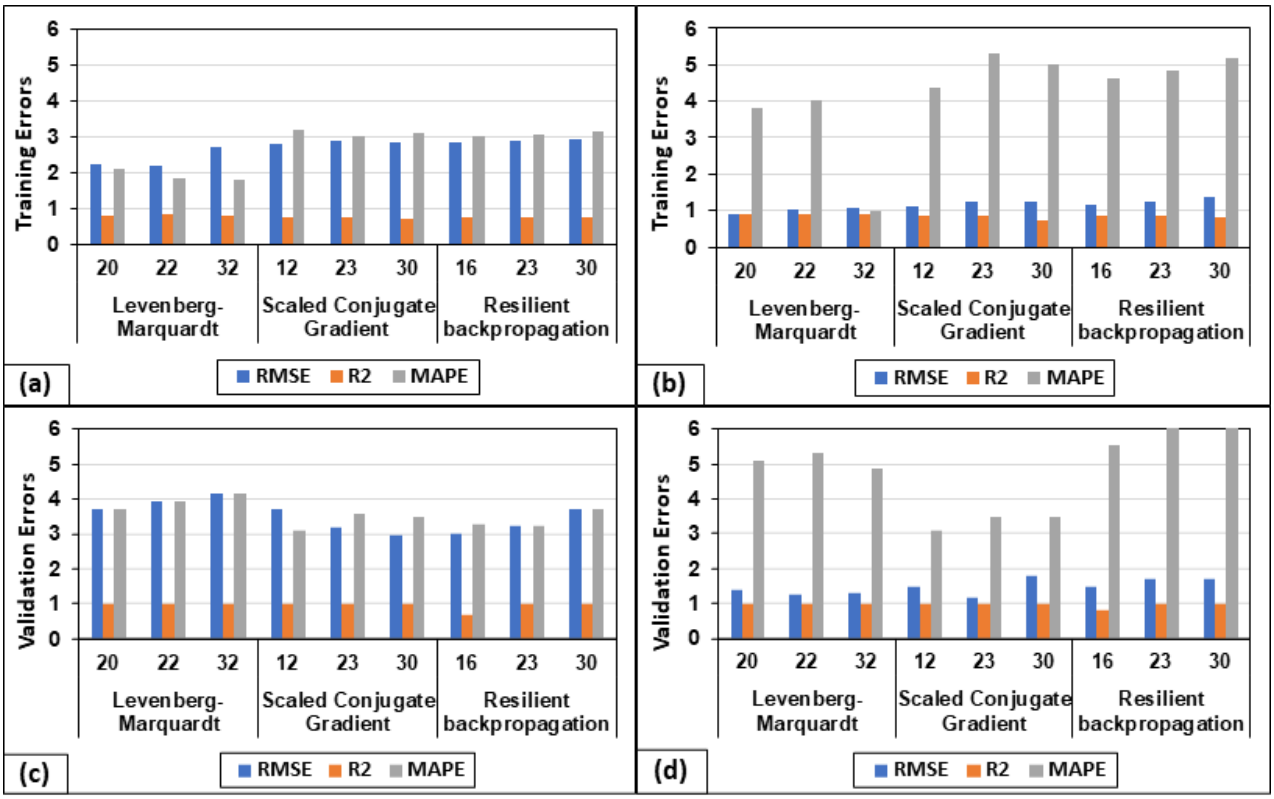

Figure 4-17 Errors generated by the various algorithms and by the different numbers of neurons in the hidden layer. (a) and (c) Relative humidity. (b) and (d) Temperature.

The comparaison of the training and validation errors between the different algorithms shows a similarity between the Levenberg-Marquart and the scaled conjugate gradient.

We finaly chose to use the Levenberg-Marquart which present better performance at the training level.

4.4.2.3 Evaluation of the model performance

We used the Levenberg-Marquart with 20 neurons in the hidden layer to model indoor temperature and relative humidity. For this combination the coefficient of determination for the training, validation, and global phases is given in Figure 4-18. The coefficient is equal to 0.99 (Figure 4-18) which demonstrate the accuracy of the developped neural network model.

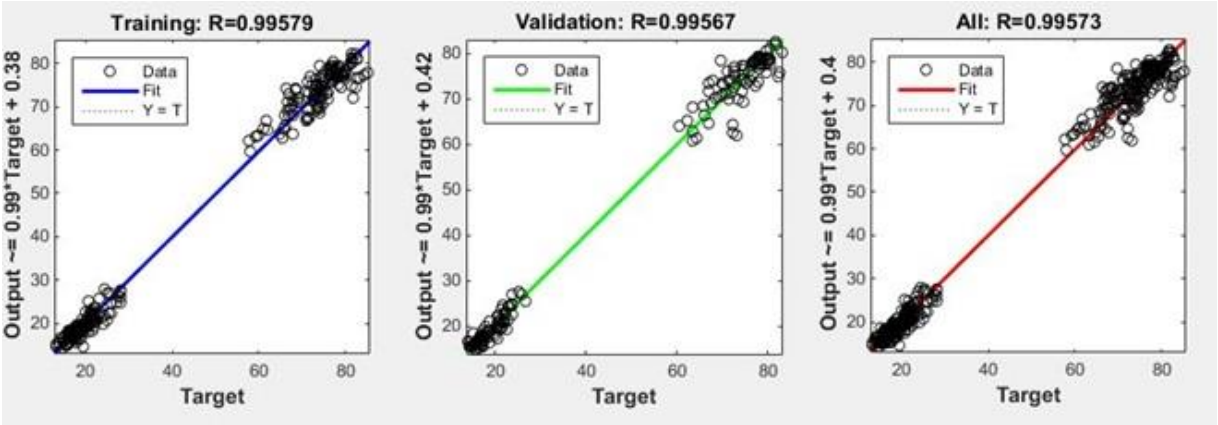

Figure 4-18 Coefficient of determination for modeled values of indoor temperature and relative humidity.

In Figure 4-19, by plotting the modeled and the experimental values of the indoor temperature and relative humidity depending on the time, we can observe the accuracy of the model. Indeed, the modeled and experimental values show plots of similar shape. This implies that the model was successful in learning and modeling the hygrothermal behaviour of the prototype.

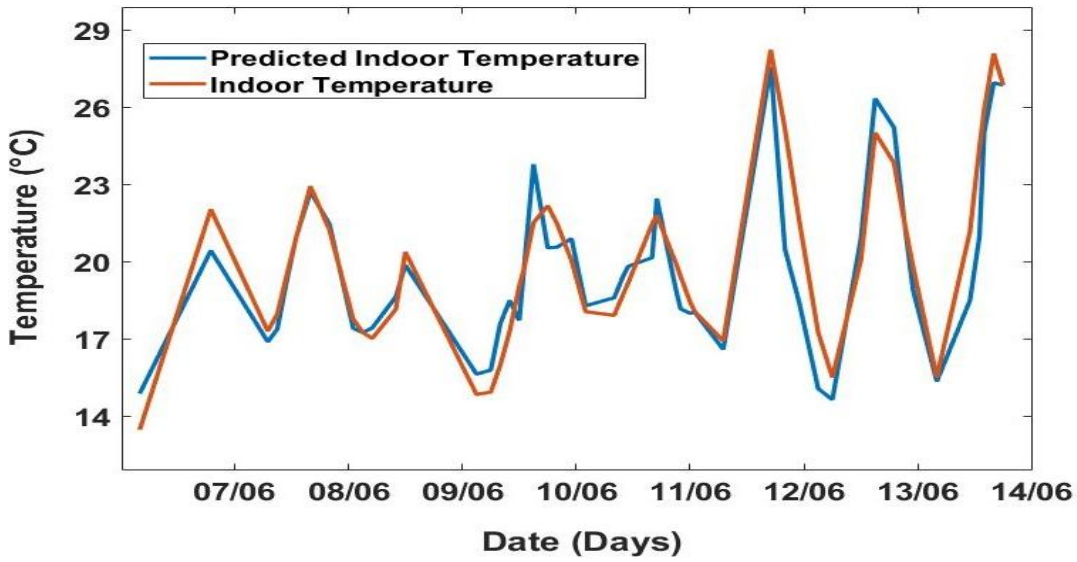

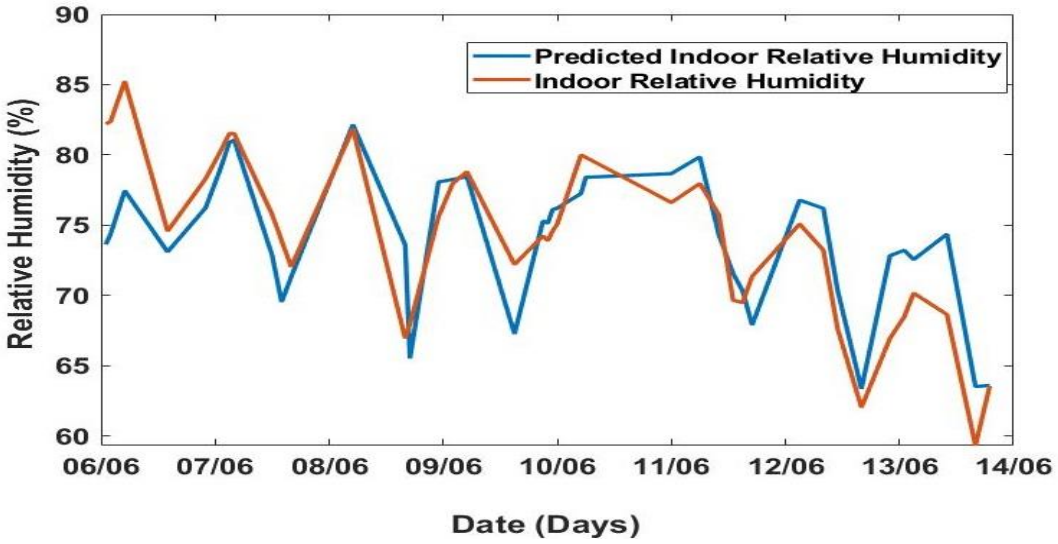

Figure 4-19 Experimental and modeled values of Temperature and Relative humidity.

In Figure 4-20, we plotted the indoor and outdoor values of temperature and relative humidity to observe their evolution in time. For an external temperature ranging between 11 °C to 37 °C, the indoor temperature is between 13 °C and 27 °C. The difference between the outside and inside temperature can reach 36 %. The outdoor relative humidity varies between 30 % and 98 % while indoor it varies between 58% and 85%. The difference in relative humidity can reach 50 % between the outside and inside.

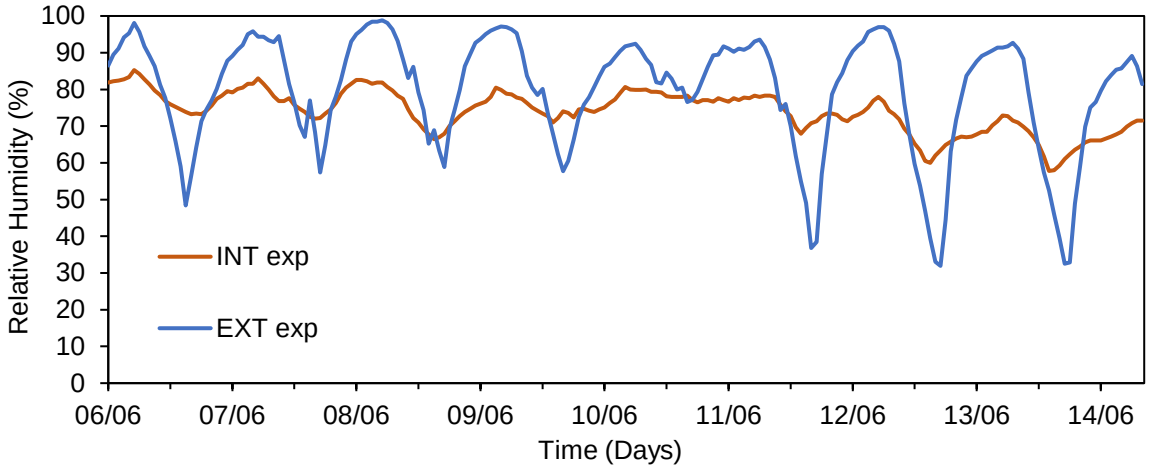

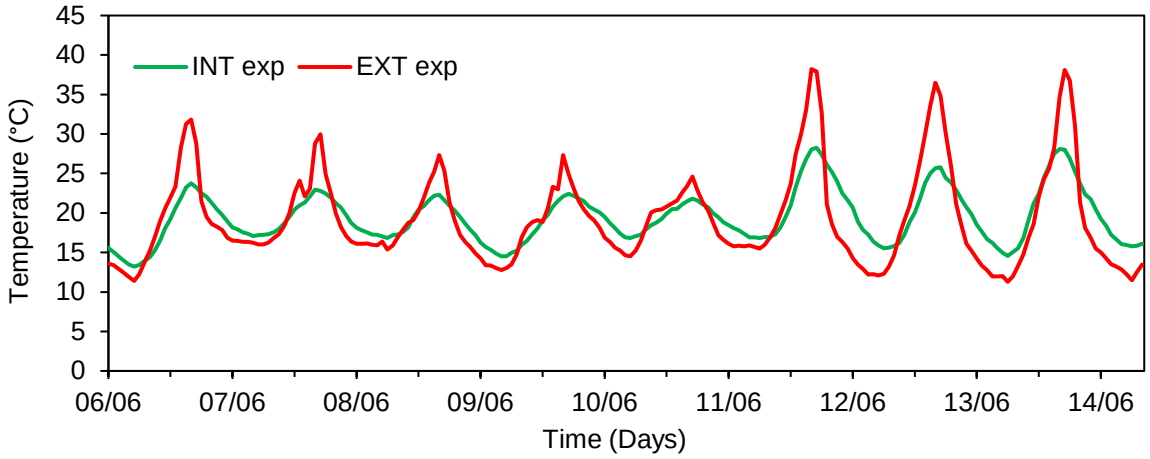

Figure 4-20 Variation of indoor relative humidity and temperature according to outdoor conditions.

4.5 Conclusion

For the first time, the ANN model is utilized to assess the hygrothermal behavior of a concrete prototype. Physical models for hygrothermal behavior require a large number of hygroscopic properties of the researched material, which might be difficult, if not impossible, to retrieve. The hyperparameters can be calculated quickly via genetic algorithm optimization. We were able to determine the best architecture after investigating the model's sensitivity to the algorithm and the number of neurons in the hidden layer. The results reveal that the ANN model learned and modeled the prototype's hygrothermal behavior. The suggested approach enables building engineers to quickly diagnose diverse circumstances and determine the building's hygrothermal comfort.

The insulation cob with 20% of algae and the structural cob with 5% are used to the construction of a lab scaled prototype which was instrumented by wireless sensors. The development of the artificial neural network to model the hygrothermal properties of the two-layered structure has shown positive results. The experimental and modeled findings of the artificial neural network displayed good similarity.

4.6 Reference

[1] Kandiri, A., Mohammadi Golafshani, E., and Behnood, A., 2020, “Estimation of the Compressive Strength of Concretes Containing Ground Granulated Blast Furnace Slag Using Hybridized Multi-Objective ANN and Salp Swarm Algorithm,” Construction and Building Materials, **248**, p. 118676.

[2] Behnood, A., and Golafshani, E. M., 2018, “Predicting the Compressive Strength of Silica Fume Concrete Using Hybrid Artificial Neural Network with Multi-Objective Grey Wolves,” Journal of Cleaner Production, **202**, pp. 54–64.

[3] Bilim, C., Atiş, C. D., Tanyildizi, H., and Karahan, O., 2009, “Predicting the Compressive Strength of Ground Granulated Blast Furnace Slag Concrete Using Artificial Neural Network,” Advances in Engineering Software, **40**(5), pp. 334–340.

[4] Boğa, A. R., Öztürk, M., and Topçu, İ. B., 2013, “Using ANN and ANFIS to Predict the Mechanical and Chloride Permeability Properties of Concrete Containing GGBFS and CNI,” Composites Part B: Engineering, **45**(1), pp. 688–696.

[5] Chithra, S., Kumar, S. R. R. S., Chinnaraju, K., and Alfin Ashmita, F., 2016, “A Comparative Study on the Compressive Strength Prediction Models for High Performance Concrete Containing Nano Silica and Copper Slag Using Regression Analysis and Artificial Neural Networks,” Construction and Building Materials, **114**, pp. 528–535.

[6] Hamdaoui, M.-A., Benzaama, M.-H., El Mendili, Y., and Chateigner, D., 2021, “A Review on Physical and Data-Driven Modeling of Buildings Hygrothermal Behavior: Models, Approaches and Simulation Tools,” Energy and Buildings, **251**, p. 111343.

[7] Abahri, K., Belarbi, R., Oudjehani, N., Issaadi, N., and Ferroukhi, M., 2013, “Total Pressure Gradient Incidence on Hygrothermal Transfer in Highly Porous Building Materials,” Advanced Materials Research, **772**, pp. 124–129.

[8] Ferroukhi, M. Y., Djedjig, R., Limam, K., and Belarbi, R., 2016, “Hygrothermal Behavior Modeling of the Hygroscopic Envelopes of Buildings: A Dynamic Co-Simulation Approach,” Build. Simul., **9**(5), pp. 501–512.

[9] Boukhelf, F., Trabelsi, A., Belarbi, R., and Bachir Bouiadjra, M., 2022, “Experimental and Numerical Modelling of Hygrothermal Transfer: Application on Building Energy Performance,” Energy and Buildings, **254**, p. 111633.

[10] Slimani, Z., Trabelsi, A., Virgone, J., and Zanetti Freire, R., 2019, “Study of the Hygrothermal Behavior of Wood Fiber Insulation Subjected to Non-Isothermal Loading,” Applied Sciences, **9**(11), p. 2359.

[11] Trabelsi, A., Slimani, Z., and Virgone, J., 2018, “Response Surface Analysis of the Dimensionless Heat and Mass Transfer Parameters of Medium Density Fiberboard,” International Journal of Heat and Mass Transfer, **127**, pp. 623–630.

[12] Alioua, T., Agoudjil, B., Chennouf, N., Boudenne, A., and Benzarti, K., 2019, “Investigation on Heat and Moisture Transfer in Bio-Based Building Wall with Consideration of the Hysteresis Effect,” Building and Environment, **163**, p. 106333.

[13] Alioua, T., Agoudjil, B., Boudenne, A., and Benzarti, K., 2021, “Sensitivity Analysis of Transient Heat and Moisture Transfer in a Bio-Based Date Palm Concrete Wall,” Building and Environment, **202**, p. 108019.

[14] Künzel, H. M., 1995, *Simultaneous Heat and Moisture Transport in Building Components: One- and Two-Dimensional Calculation Using Simple Parameters*, IRB-Verl, Stuttgart.

[15] Zirkelbach, D., Schmidt, T., Kehrer, M., and Künzel, H. M., "WUFI Pro 5 Manual."

[16] Mendes, N., Philippi, P. C., and Lamberts, R., 2002, "A New Mathematical Method to Solve Highly Coupled Equations of Heat and Mass Transfer in Porous Media," International Journal of Heat and Mass Transfer, **45**(3), pp. 509–518.

[17] Mendes, N., Ridley, I., Lamberts, R., Philippi, P. C., and Budag, K., 1999, "UMIDUS: A PC Program for the Prediction of Heat and Moisture Transfer in Porous Buildings Elements," Building Simulation, **6**, pp. 277–283.

[18] van Eck, N. J., and Waltman, L., 2013, "VOSviewer Manual," p. 28.

[19] Benzaama, M.-H., Rajaoarisoa, L., Boukhelf, F., and El Mendili, Y., 2022, "Hygrothermal Transfer Modelling through a Bio-Based Building Material: Validation of a Switching-Linear Model," Journal of Building Engineering, **55**, p. 104691.

[20] Luikov, A. V., 1966, "Application of Irreversible Thermodynamics Methods to Investigation of Heat and Mass Transfer," International Journal of Heat and Mass Transfer, **9**(2), pp. 139–152.

[21] Künzel, H. M., 1995, *Simultaneous Heat and Moisture Transport in Building Components One- and Two-Dimensional Calculation Using Simple Parameters .*

[22] Philip, J. R., and De Vries, D. A., 1957, "Moisture Movement in Porous Materials under Temperature Gradients," Transactions, American Geophysical Union, **38**(2), p. 222.

[23] Harish, V. S. K. V., and Kumar, A., 2016, "A Review on Modeling and Simulation of Building Energy Systems," Renewable and Sustainable Energy Reviews, **56**, pp. 1272–1292.

[24] Berger, J., Mazuroski, W., Mendes, N., Guernouti, S., and Woloszyn, M., 2016, "2D Whole-Building Hygrothermal Simulation Analysis Based on a PGD Reduced Order Model," Energy and Buildings, **112**, pp. 49–61.

[25] Steeman, M., Janssens, A., Steeman, H. J., Van Belleghem, M., and De Paepe, M., 2010, "On Coupling 1D Non-Isothermal Heat and Mass Transfer in Porous Materials with a Multizone Building Energy Simulation Model," Building and Environment, **45**(4), pp. 865–877.

[26] Akkurt, G. G., Aste, N., Borderon, J., Buda, A., Calzolari, M., Chung, D., Costanzo, V., Del Pero, C., Evola, G., Huerto-Cardenas, H. E., Leonforte, F., Lo Faro, A., Lucchi, E., Marletta, L., Nocera, F., Pracchi, V., and Turhan, C., 2020, "Dynamic Thermal and Hygrometric Simulation of Historical Buildings: Critical Factors and Possible Solutions," Renewable and Sustainable Energy Reviews, **118**, p. 109509.

[27] Wang, Z., and Chen, Y., 2019, "Data-Driven Modeling of Building Thermal Dynamics: Methodology and State of the Art," Energy and Buildings, **203**, p. 109405.

[28] Ghritlahre, H. K., and Prasad, R. K., 2018, "Application of ANN Technique to Predict the Performance of Solar Collector Systems - A Review," Renewable and Sustainable Energy Reviews, **84**, pp. 75–88.

[29] Gairaa, K., Khellaf, A., Messlem, Y., and Chellali, F., 2016, “Estimation of the Daily Global Solar Radiation Based on Box–Jenkins and ANN Models: A Combined Approach,” Renewable and Sustainable Energy Reviews, **57**, pp. 238–249.

[30] Wang, Z., and Srinivasan, R. S., 2017, “A Review of Artificial Intelligence Based Building Energy Use Prediction: Contrasting the Capabilities of Single and Ensemble Prediction Models,” Renewable and Sustainable Energy Reviews, **75**, pp. 796–808.

[31] Tijskens, A., Roels, S., and Janssen, H., 2021, “Hygrothermal Assessment of Timber Frame Walls Using a Convolutional Neural Network,” Building and Environment, **193**, p. 107652.

[32] Tijskens, A., Roels, S., and Janssen, H., 2019, “Neural Networks for Metamodelling the Hygrothermal Behaviour of Building Components,” Building and Environment, **162**, p. 106282.

[33] May Tzuc, O., Rodríguez Gamboa, O., Aguilar Rosel, R., Che Poot, M., Edelman, H., Jiménez Torres, M., and Bassam, A., 2021, “Modeling of Hygrothermal Behavior for Green Facade’s Concrete Wall Exposed to Nordic Climate Using Artificial Intelligence and Global Sensitivity Analysis,” Journal of Building Engineering, **33**, p. 101625.

[34] Somu, N., Raman M R, G., and Ramamritham, K., 2021, “A Deep Learning Framework for Building Energy Consumption Forecast,” Renewable and Sustainable Energy Reviews, **137**, p. 110591.

[35] May Tzuc, O., Rodríguez Gamboa, O., Aguilar Rosel, R., Che Poot, M., Edelman, H., Jiménez Torres, M., and Bassam, A., 2021, “Modeling of Hygrothermal Behavior for Green Facade’s Concrete Wall Exposed to Nordic Climate Using Artificial Intelligence and Global Sensitivity Analysis,” Journal of Building Engineering, **33**, p. 101625.

[36] May Tzuc, O., Rodríguez Gamboa, O., Aguilar Rosel, R., Che Poot, M., Edelman, H., Jiménez Torres, M., and Bassam, A., 2021, “Modeling of Hygrothermal Behavior for Green Facade’s Concrete Wall Exposed to Nordic Climate Using Artificial Intelligence and Global Sensitivity Analysis,” Journal of Building Engineering, **33**, p. 101625.

[37] Haykin, S. S., 2009, *Neural Networks and Learning Machines*, Prentice-Hall, New York Munich.

[38] Rajaoarisoa, L., 2020, “Large-Scale Building Thermal Modeling Based on Artificial Neural Networks: Application to Smart Energy Management,” *Artificial Intelligence Techniques for a Scalable Energy Transition*, Springer International Publishing, Cham, pp. 15–44.

[39] Nervetti, G., and Soma, F., 1982, *La verifica termoigrometrica delle pareti*, Hoepli, Milano.

CONCLUSION

This thesis investigated the efficiency of new cementitious and bio-organic binders. In the first part of this research project, we studied the effect of cement replacement.

We started by substituting the cement by FNS and FNS+CR and sudied the mechanical and hydrothermal properties of cement paste and mortar. The obtained conclusions can be summerized below:

• A partial substitution of cement by FNS-CR mix, up to 30 %, has no effect on the workability of mortar in its fresh state. Workability is reduced above this substitution rate due to the water absorption of these admixtures with high SSA.

• Increasing FNS-CR addition in cement results in lower compressive and flexural strengths. As a result, the use of FNS and CR, which are less dense than cement, is limited to moderate rates.

• However, mechanical strengths remain close to those of the control mortar at up to 20% of cement substitution by FNS+CR.

• At 2 days curing time, the addition of 10% FNS-CR improves mechanical behavior due to the cement setting acceleration.

• The combination of FNS and CR has two major advantages: (i) FNS's high silica content promotes polymerization in the C-S-H structure; (ii) the dissolved CO_3^{2-} ions originating from CR induces the formation of carboaluminates, which reduce the system's porosity and increase its strength.

• The results show a clear potential for using FNS-CR by-products as a partial replacement of cement at an optimal rate of 20 %.

However, the thermal resistance was not satisfactory due to the presence of magnesium-rich FNS. To overcome this shortcoming, we replaced FNS by FA and examined the behavior of mortar and concrete with cement substituted by FA and CR.

The effect of partial cement replacement with an FA and CR mixture on the mechanical and hygrothermal properties of mortar and concrete is examined. The use of CR and FA result in significant cost savings in cement manufacturing. It has the potential to significantly contribute to the attainment of sustainable development goals and, as a result, the reduction of CO_2 emissions. As a consequence of the pozzolanic reaction, the high silica and calcium content of FA and CR, respectively, lead to development of extra C-S-H and C-S-A-H components, resulting in a reduction of porosity and increased strengths. Furthermore, as the substitution amount is increased, the

concrete's thermal conductivity reduces dramatically. It has been demonstrated that these by-products have a real potential for partial cement replacement at a rate of 30 % (FA15-CR15).

The FA and CR mix is also used, but this time as stabilizer of French gravel wash mud (GWM) for cob construction. The thermal and mechanical performance of GWM mixed with these by-products, as well as the study of the hydrated products, reveal some encouraging outcomes, which are outlined as follows:

- The combination of GWM-FA-CR significantly contribute to the achievement of sustainable development goals and, as a result, carbon emission reduction.
- Tobermorite and Al-tobermorite are the main hydration products responsible of the excellent mechanical performance properties.
- The increased compressive strength compared to traditional cob building materials will result in a reduction in cob wall thickness and, as a result, a decrease in the amount of raw materials employed in cob construction.
- There are two advantages to using FA and CR:
  - The high silica and calcium contents of these two by-products react with clays, resulting in the formation of CSH and CASH systems (tobermorite and Al-tobermorite) as a result of pozzolanic reaction, and thus the reduction in porosity and the increase of mechanical performances.
  - When compared to the traditional cob construction materials used in Normandy, the GMW-FA-CR has a lower thermal conductivity and a higher specific heat capacity.

The mechanical and hygrothermal evaluation of cob walls incorporating *Laminaria digitata* algae was the main focus of the second part of this research project. Promising results from the experiments are outlined in the following paragraphs:

- Algae increases the cob ability to store heat, its degree of insulation, and its compressive strength.
- The incorporation of 20 % of algae to the insulation cob matrix reduced the thermal conductivity by 26 %.
- The incorporation of 5 % of algae to the structural cob enhanced the compressive strength by 22 %.

Specimens with algae had proven to be a successful material in earthen construction, leading to the reduction of the wall thickness and contributing to the energy saving due to its thermal properties. To offer an architecturally optimized design for interior and/or exterior walls in order to achieve good energy efficiency during the winter and good comfort during the summer. It is also necessary to assess the energy savings predicted from the incorporation of algae into the soil for cob buildings structures.

In this thesis, we have shown the possibility of using available resources to bring new performances to both concrete and earthen construction. The conclusions also prove that our approach is in line with the sustainable development goals and CO_2 reduction.

For the first time, the ANN model is utilized to assess the hygrothermal behavior of a concrete prototype. Physical models for hygrothermal behavior require a large number of hygroscopic properties of the researched material, which might be difficult, if not impossible, to retrieve.

The hyperparameters can be calculated quickly via genetic algorithm optimization. We were able to determine the best architecture after investigating the model's sensitivity to the algorithm and the number of neurons in the hidden layer. The results reveal that the ANN model learned and modeled the prototype's hygrothermal behavior. The suggested approach enables building engineers to quickly diagnose diverse circumstances and determine the building's hygrothermal comfort. The insulation cob with 20 % of algae and the structural cob with 5 % are used to the construction of a lab scaled prototype which was instrumented by wireless sensors. The development of the ANN to model the hygrothermal properties of the two-layered structure has shown encouraging results. The experimental and modeled findings of the ANN displayed good similarity.

This thesis opens up the possibility of the chemical stabilisation of different earth construction techniques. We tested the addition of seaweed powder to compressed earth bricks. The compressive strength doubled with the addition of 20% of seaweed powder. Indeed, the ability of algae to improve the thermomechanical behaviour is interesting. To this end, the construction of a real earth building stabilised by algae will allow the study of energy consumption, thermal comfort and air quality (absorption, mould on the interior walls). Concerning the modelling of hygrothermal behaviour with artificial neural networks, it is interesting to use the LSTM (Long Short Term Memory). An artificial neural network capable of both learning and predicting future behaviour.

APPENDIX

SCIENTIFIC RESEARCH PRODUCTION:

JOURNAL PAPER

1- BOUASRIA, Manal, BABOURI, Laidi, KHADRAOUI, Fouzia, CHATEIGNER, Daniel, GASCOIN, Stéphanie, PRALONG, Valérie, BENZAAMA, Mohammed-Hichem, ORTBERGER, Beate, EL MENDILI, Yassine. Insight into the partial replacement of cement by ferronickel slags from New Caledonia. European Journal of Environmental and Civil Engineering, 2022, vol. 26, no 8, p. 3662-3680.

2- BOUASRIA, Manal, KHADRAOUI, Fouzia, BENZAAMA, Mohammed-Hichem, TOUATI, Karim, CHATEIGNER, Daniel, GASCOIN, Stéphanie, PRALONG, Valérie, ORBERGER, Beate, BABOURI, Laidi, EL MENDILI, Yassine. Partial substitution of cement by the association of Ferronickel slags and Crepidula fornicata shells. Journal of Building Engineering, 2021, vol. 33, p. 101587.

3- BOUASRIA, Manal, BENZAAMA, Mohammed-Hichem, PRALONG, Valérie, EL MENDILI, Yassine. Mechanical and hygrothermal performance of fly-ash and seashells concrete: in situ experimental study and smart hygrothermal modeling for Normandy climate conditions. Archives of Civil and Mechanical Engineering, 2022, vol. 22, no 2, p. 1-22.

4- BOUASRIA, Manal, EL MENDILI, Yassine, BENZAAMA, Mohammed-Hichem, PRALONG, Valérie, BARDEAU, Jean-François, HENNEQUART, Franck. Valorisation of stranded *Laminaria digitata* seaweed as an insulating earth material. Construction and Building Materials, 2021, vol. 308, p. 125068.

5- EL MENDILI, Yassine, BOUASRIA, Manal, BENZAAMA, Mohammed-Hichem, KHADRAOUI, Fouzia, LE GUERN, Malo, CHATEIGNER, Daniel, GASCOIN, Stéphanie, BARDEAU, Jean-François. Mud-Based Construction Material: Promising Properties of French Gravel Wash Mud Mixed with Byproducts, Seashells and Fly Ash as a Binder. Materials, 2021, vol. 14, no 20, p. 6216.

CONFERENCE PAPER

1- BOUASRIA, Manal, BENZAAMA, Mohammed-Hichem, PRALONG, Valérie, EL MENDILI, Yassine. Smart Technology for Hydrothermal Performance of Low Carbon Material Using an Artificial Neural Network Model. ICCEFCSD 2022: 16. Environment-Friendly Construction for Sustainable Development, 2022, p. 1-5, Vienna. (**Best presentation**)

2- BOUASRIA, Manal, BENZAAMA, Mohammed-Hichem, PRALONG, Valérie, EL MENDILI, Yassine. Insight into the use of seaweed ash as a soil stabilizing material for earthen construction. 2nd International conference on green energy and environmental technology 2022, Rome, Italy

Résumé

DÉVELOPPEMENT ET CONTRÔLE DES PERFORMANCES MÉCANIQUES ET HYGROTHERMIQUES DES MATÉRIAUX À FAIBLE TENEUR EN CARBONE PAR UNE TECHNOLOGIE INTELLIGENTE

La distribution des émissions de gaz à effet de serre et de la consommation d'énergie des bâtiments a été estimée à 30 % en phase de construction, 70 % en phase d'exploitation et d'entretien et 1 % en phase de démantèlement. Pendant la phase de construction, les matériaux utilisés représentent 56 % des émissions de CO_2. Par conséquent, de nombreuses mesures sont prises en compte lors de la construction, telles que : l'émergence du concept de l'économie circulaire, le choix des matériaux à faible teneur en carbone, l'utilisation des déchets, l'utilisation de matériaux intelligentes, réutilisation des matériaux lors de la démolition.

Ainsi, l'objectif de cette thèse est de développer des matériaux à faible impact environnemental. Des essais de caractérisation physique, chimique, hygrothermique et mécanique sont réalisés à différentes échelles. Un prototype sera créé et une preuve de concept sera créée pour vérifier l'efficacité des matériaux bas carbone développés dans cette thèse.

Dans ce contexte, nous avons d'abord étudié le comportement de mélanges cimentaires incluant des sous-produits. Nous avons substitué le ciment par plusieurs déchets, à savoir les laitiers de ferronickel (FNS) associé à des coquilles de crépidule (CR) et des cendres volantes (FA) associés à des coquilles de crépidule. Des études mécaniques, thermiques ont été menés à la fois à l'échelle du matériaux (mortier et béton) et aussi sur un prototype à l'échelle du laboratoire. Les propriétés mécaniques du mortier avec une utilisation de FA-CR en substitution du ciment se sont avérées supérieures à celles du mortier et du béton ordinaires. Le prototype à base de ce nouveau matériau bas carbone a été développé pour surveiller le comportement hygrothermique avec des modèles des réseaux de neurones artificiels. Les résultats de l'expérience sur le risque de condensation et le développement de moisissures révèlent que le mélange de béton choisi peut empêcher la condensation.

Dans ce travail de thèse, nous nous sommes intéressés aussi à la stabilisation de la construction en terre par un liant cimentaire et ensuite par un liant organique. Dans la première partie, nous avons étudié la pertinence de la boue de lavage de gravier et

des coquillages comme matériau de construction en terre non cuite tout en utilisant des cendres volantes comme liant et stabilisateur cimentaire. Nos résultats montrent que ce mélange conduit à une réduction de la porosité, une augmentation des performances mécaniques, une diminution de la conductivité thermique avec une capacité thermique spécifique plus élevée. Dans la deuxième partie, nous avons utilisé de la poudre d'algues comme stabilisateur de la bauge. Nous avons étudié l'impact de la substitution de la terre par de la poudre d'algues (liant organique). Pour ce nouveau matériau à base d'algues, nous avons observé une amélioration de la capacité de stockage de la chaleur et de la conductivité thermique sans impacter les propriétés mécaniques. Le développement du réseau neuronal artificiel pour prédire les propriétés hygrothermiques du prototype terre-algues-fibres a montré une bonne similarité entre les résultats expérimentaux et le modèle. Enfin, le mécanisme de stabilisation de la terre a été étudié à l'aide de techniques d'analyse microstructurale (DRX et spectroscopie Raman).

Mots clés : Liants bas carbone, béton, stabilisation de la construction en terre, propriétés microstructurales, mécaniques et hygrothermiques, modèles ANN.

Abstract

The distribution of energy consumption and greenhouse gas emissions in buildings has been estimated at 30% during the construction phase, 70% during the use and maintenance phase, and 1% during the demolition process. During the construction phase, the materials used represent 56% of the CO2 emissions. The long term use of a building, difficult to control, depends on a large number of variables. Numerous levers are therefore studied to act during construction: low-carbon materials, waste reduction, promoting the circular economy, optimized design, intelligent material saving, construction and demolition waste, etc.

Therefore, the objective of this PhD is to develop new low carbon materials. Physical, chemical, hygrothermal and mechanical characterization experiments are carried out at different scales. A prototype will be designed and a proof of concept will be created to verify the effectiveness of the eco-materials developed in this research.

In this context, we started by studying the behaviour of cementitious mixtures including by-products. We substituted cement by several wastes, i. e. ferronickel slag (FNS) associated with *Crepidula* shells (CR) and fly ash (FA) associated with *Crepidula*

shells. Mechanical and thermal properties of the mortar and concrete were studied at the material scale and also on a lab-scale prototype. The mechanical properties of the mortar with the use of FA-CR in substitution of cement were found to be superior to those of ordinary mortar and concrete. The prototype based on this new low carbon material was developed to monitor the hygrothermal behaviour with artificial neural network models. The results of the experiment on the risk of condensation and mold growth reveal that the chosen concrete mix can prevent condensation. Indeed, the high silica, aluminate, and calcium content of the smart Fly ash-*Crepidula* mixture reacts with water from humid ambient air to produce additional hydrates as a result of pozzolanic reaction, resulting in continual strength enhancement.

In this thesis work, we were also interested by the stabilization of earthen construction using a cementitious binder and then by an organic binder. In the first part, we investigated the suitability of gravel washing sludge and seashells as an unfired earth construction material while using fly ash as a binder and cementitious stabilizer. Our results show that this mixture leads to a reduction in porosity, an increase in mechanical performance and a decrease in thermal conductivity with a higher specific heat capacity. In the second part, we used seaweed powder as a stabilizer for the cob construction. We studied the impact of substituting soil with seaweed powder (organic binder). For this new algae-based material, we observed an improvement in heat storage capacity and thermal performance without impacting mechanical properties. The development of the artificial neural network to model the hygrothermal properties of the earth-algae-fiber prototype showed a good similarity between the experimental results and the model. Finally, the stabilization mechanism of the soil was studied using microstructural analysis techniques (XRD and Raman spectroscopy).

Keywords: Low-carbon binders, concrete, earth construction stabilization, microstructural, mechanical and hygrothermal properties, ANN model.